Surfactant templated mesostructured titania films: A comparison of three methods

Hawley, Adrian

Award date:
2008

Awarding institution:
University of Bath

Surfactant Templated Mesostructured Titania Films
A comparison of three methods

Adrian Marcus Hawley
A thesis submitted for the degree of Doctor of Philosophy
University of Bath
Department of Chemistry
August 2008

Acknowledgements

Foremost I would like to thank Karen Edler for her enthusiastic and indefatigable support during my postgraduate work. Her support during my application as an overseas student was of great assistance and her egalitarian research group and excellent supervision have been of fundamental importance throughout the PhD.

I would also like to thank previous and continuing members of staff in the Department of Chemistry who have helped me learn new experimental methods and developed my theoretical understanding over the past three years. In particular I would like to thank Steve Roser for his explanations of reflectivity theory and Ben O'Driscoll for pushing me to be a more well rounded scientist, be it providing opportunities to operate scattering instruments or helping me appreciate a tidy laboratory.

Additionally, I am grateful to all the members of the Edler Research group who have made working in the group enjoyable socially and have helped develop a harmonious environment in which to work.

The financial support, for fees and subsistence, generously provided by the University of Bath and the Overseas Research Student Award Scheme have also been vital. I am deeply grateful for this assistance, without which I would have been unable to undertake postgraduate research in the UK. I would also like to thank BASF and DuPont for the generosity in providing chemicals without which this work would not have been possible. Furthermore, I would like to both acknowledge and thank the ISIS, ESRF and ILL research facilities, and the tireless and ever dependable beamline scientists employed therein, who have helped facilitate much of the key research involved in my PhD.

Finally, on a personal note I would like to thank my friends and family both in Australia and in England who have been supportive ever since my initial application. Such support has made relocation half a world away much easier to adjust to than would otherwise have been the case and has been of great importance in helping me stay focused during the more trying times of my research. Last, but by no means least, I would like to thank my girlfriend, Emily, for her patience and encouragement during many times of considerable stress and for her perennial ability to make me a happier person.

Table of Contents

Abstract

Surfactant Templated Titania Films

The development of mesoporous titania films is a considerable research goal in the field of mesoporous material development due to proven applicability in photochemical and photovoltaic applications. The formation of thick, robust, mesoporous titania films is of particular interest and the focus of this thesis has been the study and comparison of the surfactant templated formation of such materials by three methods. Film structure has been studied using TEM and small angle X-ray and neutron scattering while formation was studied using Brewster angle microscopy and X-ray and neutron reflectometry.

Repetitive dip-coating was used to produce films for development into dye sensitized solar cells allowing development of cells of reasonable efficiency when four depositions were used. This research showed that repetitive deposition does not necessarily lead to a linear increase in film thickness, as subsequent depositions may be thinner making the future application of this method for solar cells problematic.

In contrast to dip-coating, a fluorinated surfactant was used in a largely alcohol solvent to produce mesostructured films at the air-solution interface. Film formation occurred by a surface driven mechanism via addition of individual precursors and micelles producing a lamellar structure in-situ. After removal from the interface a cubic phase developed after drying of the film. Although films are not stable to calcination the calcined material remains porous. The surfactant templated formation of ZnO films at the air-solution interface was also studied.

The di-block copolymer $PEPEG_{2250}$ was also used to template titania films at the air-solution interface from alcoholic solvent. Film formation occurred via a bulk driven mechanism. Although these films were found to be disordered at the interface and not stable to calcination they were unusually robust and self supporting after removal from the interface. Studies of subphase development allowed the first time-resolved observation of surfactant templated titania particle formation.

Chapter 1
Introduction

1.1 Templated mesoporous materials

The development of materials possessing an ordered, porous structure, larger than the micropores typically achieved in zeolites, has been a persistent research goal in recent years. This is particularly true for materials possessing structure on the mesoscale that have shown application in catalysis, sensing and photochemistry among other areas.[1-7] The mesoporous size range is defined as 20 - 500Å, in adsorption studies as the range in which capillary condensation, with a characteristic hysteresis loop between adsorption and desorption, occurs.[8,9] Below 20Å, the microporous range, adsorption is dominated by interactions with the pore walls due to their close proximity. In the larger than 500Å, macroporous, range channels are sufficiently large that adsorption processes are comparable to the condensation in the bulk. However, the designated size limits for mesostructure are somewhat arbitrary as interactions and limiting distances vary between different solids.[8]

Mesoporous materials have been area that has seen a large expansion since the publication of the molecular sieve, MCM-type materials by researchers from Mobil in 1992.[10] These novel materials generated a wealth of international interest and a great deal of research has been conducted into both new materials and the formation mechanisms that lead to them. It was noted at the time that some natural materials possess an intricate structure of both organic and inorganic material and some processes used presently are regarded as mimicking biology.[9-11] Recent research has noted, among other things, the high strength of inorganic-organic materials in nature. One such example is Nacre, a material that makes up seashell, that is formed of layers of calcium carbonate and protein material and is both considerably less brittle and more robust than pure calcium carbonate as a result.[11]

Although recent advances in understanding the role and benefits of these hybrid materials show great advantages for many desired applications a purely inorganic material is also desirable. A wider range of application conditions, such as higher temperature and varied pH, are accessible with an inorganic material. The formation mechanisms used in natural systems provide instruction and inspiration for new materials however, as the organic phase may be removed after formation to yield an ordered, porous inorganic material. Self-assembly is perhaps the most prevalent class of mechanisms used in nature and has been defined by Brinker as, "the spontaneous organisation of materials through non-covalent interactions without external intervention".[12] Such a process is clearly desirable for a biological organism as it requires minimal energy input and is similarly desirable for research and application as it can provide a one-step process that does not require time consuming repetition to produce a functional material.[13]

Using self-assembly to form ordered materials is not necessarily straightforward as the structure and ordering, or lack thereof, in the product is highly sensitive to the initial reaction conditions.[1,14] Being able to direct the formation to a desired final structure is a valuable research goal and has been achieved since 1992 using an increasingly wide range of surface active compounds as templates for the final structure.[1,2,10] A number of different approaches have been used to form ordered materials possessing an internal structure on the mesoscale with a wide range of particle shapes reported up to 1cm in size and film materials also becoming accessible.[14,15]

1.2 Surfactant Templated Self-Assembly

1.2.1 Ionic, block copolymer and fluorinated surfactants

Surface active compounds, surfactants, are amphiphilic molecules that find use in many everyday and esoteric applications. Properties arising from the combined hydrophilic - hydrophobic nature of surfactants give rise to uses in fields as wide ranging as laundry detergent to industrial explosives. The competing stabilisation and destabilisation of the respective hydrophilic and hydrophobic domains in water drives the complex behaviour of surfactants and as surfactant concentration increases a point is reached where well defined structure begins to appear in solution. Hydrophobic domains group together to form a water-free environment leading, initially, to spherical micelle formation.[16] Defined as the critical micelle concentration (cmc), the point at which micelles appear depends upon a range of factors such as the surfactant, solvent, temperature and ions in solution. As surfactant concentration increases beyond the cmc, a range of liquid crystals can form including cylindrical micelles, cubic and hexagonal phases and lamellar sheets as shown in *Figure 1-1*.

Although aqueous surfactant solutions represent the most common and most studied area within surfactant chemistry, surfactants may produce micelles and liquid crystal phases in other solvent systems. In non-polar solvents micelle formation is similar to, but the reverse of, that occurring in aqueous media with many surfactants producing reverse micelles where hydrophilic headgroups gather together to exclude the solvent. Mixed solvent systems of polar and non-polar solvents can also be used to create or enhance the surface activity of compounds that possess more limited surface activity in either system alone.[17]

Surfactants have been used to direct the structure formation in self-assembled materials since the early 1990's when Mobil researchers reported the use of the cationic surfactant cetyltrimethylammonium chloride (C_{16}TAC) in water for the formation of MCM-41.[10] In 1992 these materials were proposed to form by a Liquid Crystal Templating (LCT) mechanism, see § 1.2.2, in which inorganic material forms around a surfactant liquid crystal phase that is extant in solution.[18] The organic, surfactant phase

may then be removed to leave a porous inorganic solid with the inverse structure of the liquid crystal phase.

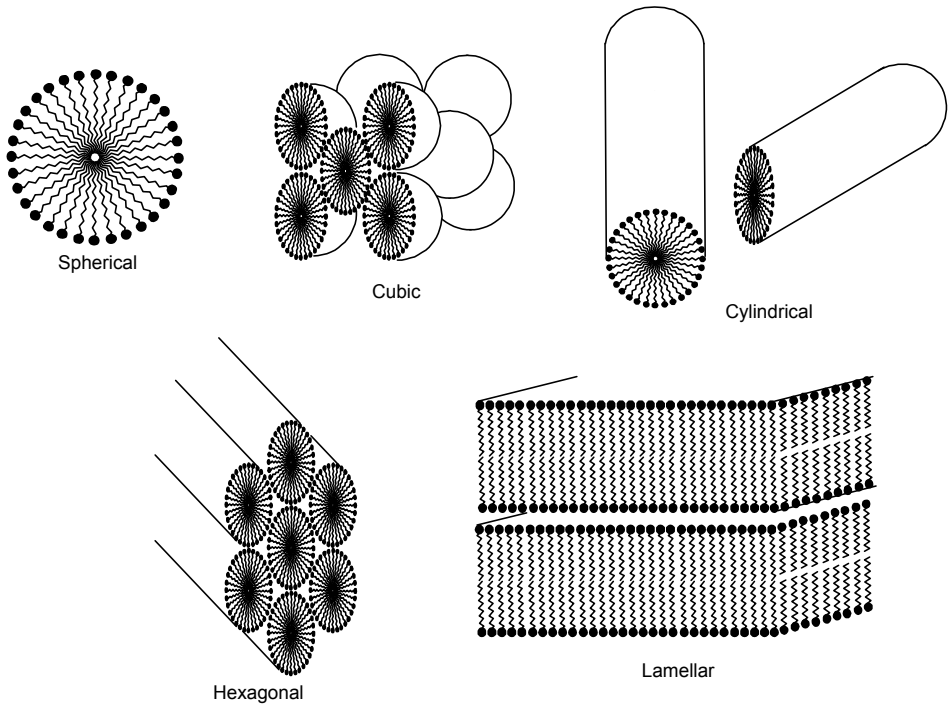

Figure 1-1 : *Diagrams of different micelle phases (after Clint).*[19] *Hexagonal and cubic structures are of particular interest for mesoporous material formation.*

Following on from the publication of MCM-41 a wider range of surfactants have been successfully used in forming mesoporous materials with initial research continuing to use ionic surfactants. Typically featuring a hydrophobic hydrocarbon tail and hydrophilic, charged headgroup cationic surfactants provided well studied materials as templates and provided strong electrostatic interactions with anionic silica oliogmers at high pH to form materials. After the 1992 publication of MCM-41 cationic surfactants remained dominant in the production of mesoporous materials for some time. A reversal of the cationic surfactant – anionic oligomer interaction allowed an anionic surfactant at low pH to be used as a template for the first time in 1994 and neutral surfactant use soon followed in both acidic and basic conditions.[20]

Subsequently Pluronic tri-block copolymers of the form $PEO_xPPO_yPEO_x$ began to be used as amphiphilic surfactant templates with the first mesoporous silica material using such a surfactant reported in 1995.[21] The block copolymers possess a surface active

nature due to their regions of differing hydrophobicity and it has been argued that their relative biological safety, cheapness and ability to form micelles at low concentration makes them desirable material templates.[21] Furthermore the materials formed using Pluronic surfactants, a widely used class of block copolymer surfactants, were found to have thicker inorganic walls and longer structural length scales. These factors make such materials more robust in addition to allowing access to larger pore sizes than those possible using short chain ionic surfactants.[6,15,22,23]

However, although block copolymers have been widely used as material templates in aqueous and mixed alcohol-water systems, the difference in hydrophobicity between the PPO and PEO segments is insufficient to generate ordered micelle phases as a template in very low water systems in which critical micelle concentrations are considerably higher.[17,24] Increasing the hydrophobicity of the hydrophobic block by using a poly-(butylene oxide) or a long polyethylene segment are recommended approaches to creating more ordered micelles[17,25] although neither have yet been very widely used. It has been shown that short polyethylene-poly(ethylene-oxide), Brij, surfactants can template silica materials in aqueous conditions[21,23,26] and KLE polymers, derived from Krayton liquids, may be used in mesoporous material and films formation[27-29] however the use of high alcohol systems remains relatively rare.

Fluorinated surfactants, on the other hand, possess considerable surface activity in any non-fluorinated solvents, a range that includes aqueous and non-aqueous conditions such as alcohols and supercritical CO_2.[26] Perfluorocarbons, in which all hydrogen atoms have been replaced with fluorine, and derived surfactants, develop the same micelle phases as other surfactants but are more surface active and more thermally stable than hydrocarbon surfactants.[27-29] The fluorine – carbon bond, one of the strongest covalent bonds known, and greater size of fluorine make fluorocarbon chains very rigid and unable to freely dissolve in aqueous or alcohol systems, creating their surfactant nature.[30] Less environmentally harmful than CFCs, fluorocarbon surfactants have been attracting considerable attention recently and represent an area of ongoing research.[31]

Although less is known about the characteristics of partially fluorinated surfactants it has been reported that the highly hydrophobic nature of the fluorinated chain favours the formation of the bilayer structures of lamellar sheets and vesicles.[32]

Fluorinated surfactants have, however, been used in the successful synthesis of ordered silica materials. [28,32] In 2003 the use, in combination with the Pluronic surfactant P-123, of a fluorinated surfactant to form mesoporous silica materials at low and high temperatures was reported.[29] Subsequently fluorinated surfactants alone have since been reported in the formation of silica materials, including films, and a mixed titania and silica analogue to MCM-41 has been reported using an aqueous system.[33-36]

1.2.2 Surfactant Templating Mechanisms

During the formation of mesoporous materials the precursors undergo a series of reactions during their growth into a uniform, solid network as shown in *Figure 1-2,* in which the reactions of silica precursors are displayed, since these are more straightforward than those of titania precursors. Although comparable occur for titania precursors the rates of reaction are considerably higher, see § 1.4.

Initially the precursors undergo hydrolysis reactions to form hydroxide species that subsequently undergo alkoxolation and condensation with neighbouring silica species to form oligomers that ultimately condense into a continuous network.[37] Molecular dynamics simulation of silica formation has shown that steric considerations and reverse reactions are not of particular importance during the early formation of materials.[38]

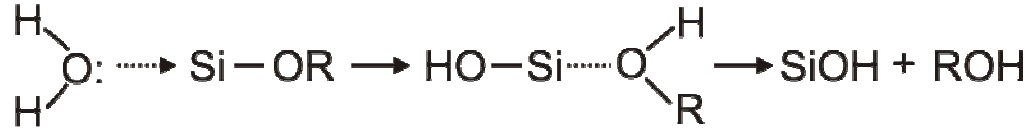

Hydrolysis

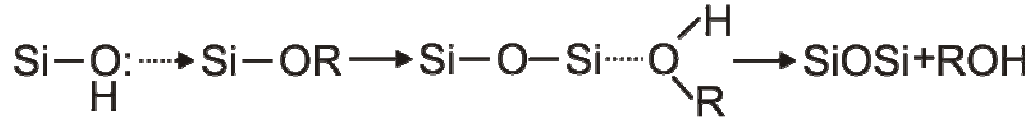

Alkoxolation

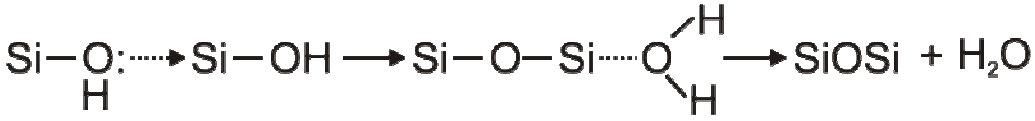

Condensation

Figure 1-2 : Inorganic precursors undergo hydrolysis and condensation reactions prior to and during the formation of mesoporous materials[37]

The mechanism by which ordered mesoporous materials are formed and templated by surfactants has also been the subject of considerable research in recent years and a variety of different mechanisms have been suggested and investigated.[6,39] These investigations have often been hampered by the rapid precipitation of silica-surfactant composite materials within the terminal stages of the reaction.[6] Liquid crystal templating, LCT, a schematic of which is shown in *Figure 1-3*, was the first mechanism proposed for the formation of MCM-41 formation in 1992 and describes a process of true liquid crystal templating.[18] It was suggested that surfactant in solution formed an ordered liquid crystal phase, hexagonal in the case of MCM-41, around which inorganic material, silica in this case, occupying the solvent region gathers and creates inorganic walls between the micelles. Growing silica continues to undergo condensation to form a uniform solid around the micelle. Subsequent calcination removes the organic, surfactant phase to leave a porous silica solid with the inverse structure to the original liquid crystal phase.

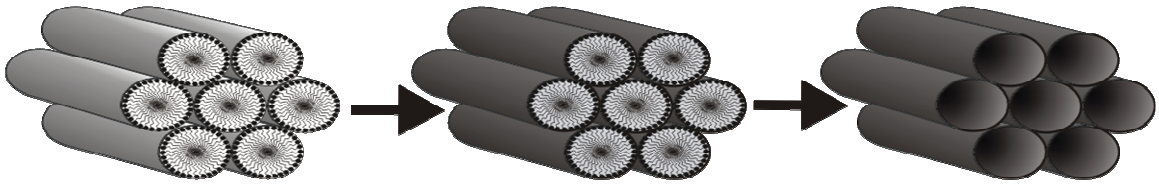

Figure 1-3 : The Liquid Crystal Templating mechanism proposed by Kresge, et. al. in 1992 (after Kresge, et. al.).[18] Inorganic material forms around a surfactant micelle phase. Removal of the surfactant by calcination produces a stable inorganic material.

However, the mechanism was not fully understood at this time. It was suggested that micelle encapsulation occurs due to the anionic inorganic species balancing the charge of the cationic surfactant or that it may be the inorganic material itself that mediates the hexagonal ordering.[18] In this case micelles may exist freely in the reaction solution and the encapsulation by inorganic material acts to induce the ordering of the micelles into a hexagonal array.

Studies in 1993 utilising in situ ^{14}N and ^{29}Si NMR found that the hexagonal phase, H_1, does not exist in solution during the CTAB templated formation of MCM-41 and that it could not be directing the structure as proposed in the LCT mechanism.[40] This seemed reasonable given that the concentration of surfactant used in forming MCM-41 (14% wt.) was much closer to the 17% wt. at which cylindrical micelles form in solution

than the 34% wt. at which a hexagonal phase appears. Chen, et. al. reported that randomly oriented cylindrical micelles interact with silica species to become encapsulated by 2-3 layers of silica around the exterior of the micelles.[40] During the subsequent condensation of the silica precursors, enhanced by their close proximity around the micelles, the composite species interact to form the hexagonal structure of MCM-41, see *Figure 1-4*.[40] It is thus possible to form materials with structure corresponding to liquid crystal phases observed at much higher surfactant concentration than that used in the precursor solution of the reaction. The same researchers also reported that the electrostatic interactions between anionic inorganic species (I^-) and cationic surfactants (S^+) and the development of charge balancing are the driving forces behind material formation. As a consequence, in alkaline preparations, complete condensation of the silica does not occur until heat is applied as SiO^- species persist to maintain charge matching.

Molecular dynamics simulations support this mechanism of development into composite species followed by joining of the growing silica clusters once they exceed 40 silica monomer units.[38] Subsequent research in 1994 extended the electrostatic charge matching mechanism to the use of anionic surfactants (S^-) and cationic inorganic (I^+) precursors and also reported ion mediated processes in which surfactants and inorganic species shared a common charge ($S^-X^+I^-$ and $S^+X^-I^+$).[41]

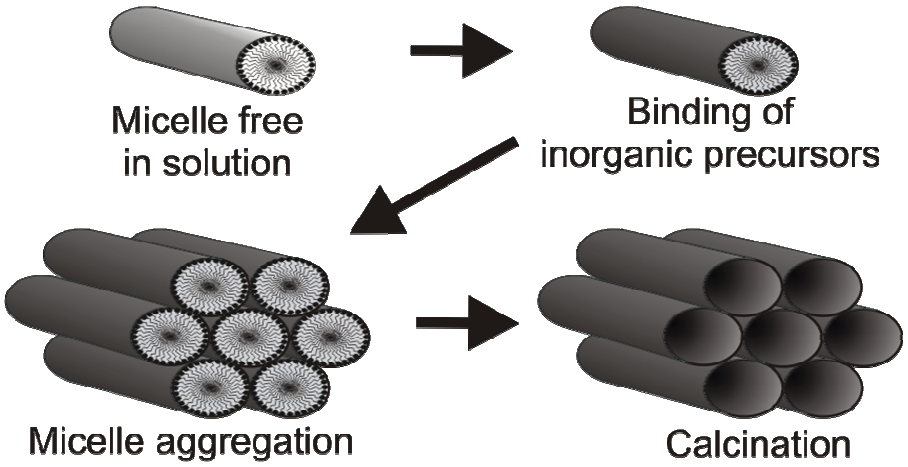

Figure 1-4 : The formation mechanism for MCM-41 reported by Chen, et. al. in 1993.[40] *Micelles free in solution are encapsulated by silica precursors and the composites subsequently order into a hexagonal phase.*

Development of mesostructured materials without the use of electrostatic interactions was published in 1995 when neutral amine surfactants (S^0) were utilised with neutral inorganic (I^0) precursors in the formation of mesoporous solids.[42,43] The authors reported that hydrogen bonding interactions between the surfactant and growing inorganic species led to the development of ordered materials. When block copolymer surfactants became used in mesoporous material formation, hydrogen bonding was also suggested as the driving force for interaction between the surfactant and inorganic groups.[21] More recently, a counter-ion mediated interaction between the silica precursor species (X^-I^+) and the surfactants headgroups (S^0H^+) has been described, as the ethylene oxide groups of the surfactant are argued to become positively charged in the acidic conditions used in such syntheses.[6,17,44] However, this mechanism is has been conclusively argued to be unlikely as there remains insufficient evidence to support it.[45,46]

The research of Flodström et al., investigating the formation of silica materials in acidic systems using copolymer surfactants, has found that adsorption of hydrolyzed silica species onto disordered micelles is followed by the gathering of these micelles into conglomerates.[22] Subsequent precipitation of these conglomerates occurs concurrently with coalescence of micelles into long cylinders prior to the formation of a hexagonal phase. Hydrogen bonding between conglomerates of micelles was reported to be inconsequential as it is in competition with water in the aqueous system. Recent research has suggested that aggregation of micelles and conglomerates is due to micelle collisions after cooperative phase separation has occurred.[47] As aggregates combine and grow the assembly process can form materials with structure comparable to liquid crystal phases of higher surfactant concentrations than those used.[1,6]

In general the formation of mesoporous materials using copolymer surfactants at concentrations below liquid crystal formation and in acidic conditions may be considered to occur in three phases as outlined over the page.[6] However, only the first of these phases is specific to non-ionic surfactants as similar processes occur in the development of aggregates and formation of a final structure when ionic surfactants are used as material templates.

1. Silica precursors and surfactant micelles cooperatively assemble due to hydrogen bonding and hydrophobic interactions between silica species and PEO groups of the surfactant.
2. Collisions between micelles and van Der Waals forces between silica-surfactant conglomerates create larger aggregates as silica condensation connects the conglomerates. This gives rise to a new liquid-crystal phase that separates from the water phase of the solution as it becomes denser, corresponding to the first observation of precipitation in the solution.
3. Energy competition between the free energy of mesophase formation and surface free energy occurs and determines the final particle structure and morphology.

As with the use of ionic surfactants, the structure of materials produced using copolymer surfactants has been found to vary greatly with the reaction conditions. Of particular importance are the size ratio of the hydrophilic EO headgroup to the hydrophobic region (usually PPO) and the surfactant concentration in the reaction.[48,49] A very large EO headgroup has been found to produce disordered wormlike structures while a small EO group produces materials with small pores and no order.[49] Changing the surfactant concentration is found to produce materials of varied order as concentration increases as outlined below:[1,49]

$$\text{Disordered} \rightarrow \text{Hexagonal} \rightarrow \text{Wormlike} \rightarrow \text{Hexagonal} \rightarrow \text{Disordered}$$

The initial disordered phase corresponds to surfactant molecules free in solution, too dilute for ordered materials to form. A higher concentration is able to yield ordered materials as outlined in the three steps above while a still higher concentration reaches a boundary on the surfactant phase diagram and a disordered, wormlike phase is formed. Further surfactant creates a hexagonal phase and corresponds to true liquid crystal templating of silica material around a hexagonal phase present in the solution. At the highest concentration disordered materials are again formed as a surfactant – water phase

is formed that partially excludes the silica materials. Further research using liquid nitrogen to freeze solutions at different times during material formation supports this transition.[50] Inorganic material was found to form around an existing micelle phase at high surfactant concentration while at lower concentrations, at which micelles are present but liquid crystal phases are not, the inorganic precursors drive the formation of ordered materials.

However, unlike ionic and block copolymer surfactants no extensive work has been undertaken examining the mechanisms of mesoporous material formation utilising perfluorinated and partially fluorinated surfactants. Although recent work has proven the utility of such surfactants in producing ordered materials, formation mechanisms have only been described from phase diagrams and compared to those for copolymer surfactants rather than receiving specific research attention.[33-35]

Additionally, work on mesoporous materials using non-aqueous solvents remains limited.[6] The use of surfactants that micellise in ethanol, such as fluorinated surfactants or novel block copolymer surfactants, allows research to utilise non-aqueous solvents. This is of particular interest as such solvents allow for greater control of the high reactivity of transition metal precursors that would otherwise prevent the formation of ordered materials, see § 1.4.

1.3 Surfactant Templated Thin Films

Early mesoporous materials were formed as structured particles and powders and throughout the expansion of this area, particulate materials have continued to represent the majority of materials.[2] However, for applications such as membranes, sensors, coatings and solar cell technology the production of a continuous mesoporous film is preferable.[14,51-53] The first surfactant templated silica films were reported in 1996 and since that time many further thin films have been reported on a substrate or, less commonly, at the air-liquid interface.[14,54,55] Film formation on substrates often utilises dip or spin-coating processes in which film formation process are designated as the Evaporation Induced Self Assembly (EISA) technique published in the late 1990's and described in greater detail later, § 3.1.[12]

Remarkably straightforward in premise, the dip-coating process consists of dipping a substrate into a reaction solution, using mixed solvent of ethanol and water, and withdrawing the substrate at a controlled speed. The reaction solution drains away from the substrate to leave a coating of a thickness dependent upon evaporation, viscosity and dipping/withdrawing speed.[12] Spin-coating is a comparable process in which the layer of film material is deposited by placing a drop of solution on a substrate and spinning the substrate to spread out the solution. In both cases no ordered phase is present in the bulk reaction solution and it is during aging of the film at elevated temperature, generating the preferential evaporation of alcohol from the solution, that leads to the development of a surfactant liquid crystal phase as the relative surfactant concentration increases as shown in *Figure 1-5*.[56]

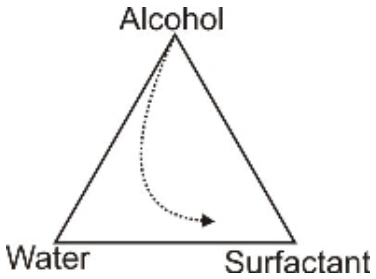

Figure 1-5 : Progression along the ternary phase diagram of a reaction solution during evaporation induced self assembly

Concurrent to the evaporation of the solvent, the inorganic precursors in the film react to form small inorganic oligomers that bind to surfactant micelles. Once a surfactant liquid crystal phase has formed in the film, the network becomes coated by the inorganic precursors that subsequently bind together due to their increased proximity to each other and the film formation is an example of Liquid Crystal Templating as shown in *Figure 1-3*, § 1.2.2. It is also noted that this formation mechanism requires a specific series of reactions that is brought about by the careful aging, under controlled conditions, of the films after dip or spin coating.

The aging steps of the EISA process are the most problematic part of technique as the presence or absence of a final structure, and its type, are highly dependant upon the temperature and humidity to which the film is exposed to.[56] If inorganic precursors form solid networks before the solvent has evaporated sufficiently for an ordered liquid crystal phase to form, a disordered material results. Furthermore, crystalline titania formed in the films may be unable to match the curvature of the surfactant structure and the material may collapse upon calcination.[57] High temperatures and long calcination times may also lead to the development of larger crystals destroying a pore network as a result.

These effects demand fine control over the temperature and humidity conditions during film aging as the surfactant structure is not established until the final aging steps. The technique is also limited to producing films no thicker than several hundred nanometres, as in thicker films the difference in solvent loss from the surface and from deeper within the film becomes more pronounced.[57] As the films shrink as they dry, if this difference becomes too great, the films crack as the surface contracts. Nevertheless, dip-coating has become a well established method of film formation and recently repetitive dip-coating has been extended to develop titanium dioxide films and has established films of sufficient thickness for the development of solar cells.[58,59]

Recent developments in film formation on a substrate by dip-coating suggest that, using a rather painstaking process, thick films may be formed but in general films formed on substrates are of limited thickness and are often subject to cracking as the inorganic phase dries and contracts.[14,57] However, film formation at an air-solution interface does not present these drawbacks and the development of interface formation therefore represents a promising area of research.[14] Formation at the air-liquid interface may occur

via a number of different mechanisms that are often related to the formation mechanisms described in § 1.2.2.

For example, the formation of surfactant – silica films at the air-solution interface has been shown to occur via two different mechanisms as shown in *Figure 1-6*. A bulk driven mechanism, consisting of the development of a number of silica coated micelles into silica-surfactant aggregates in solution, followed by the rapid joining of aggregates to form a uniform film at the interface has been observed under specific concentration conditions.[60-63] This proceeds by a liquid-liquid phase separation process analogous to that discussed above for silica particle formation. X-ray reflectometry experiments showed the rapid loss of specular reflection after a concentration dependent induction time, showing film formation to be a rapid process, an observation supported by Brewster Angle Microscopy images taken during film formation.[61]

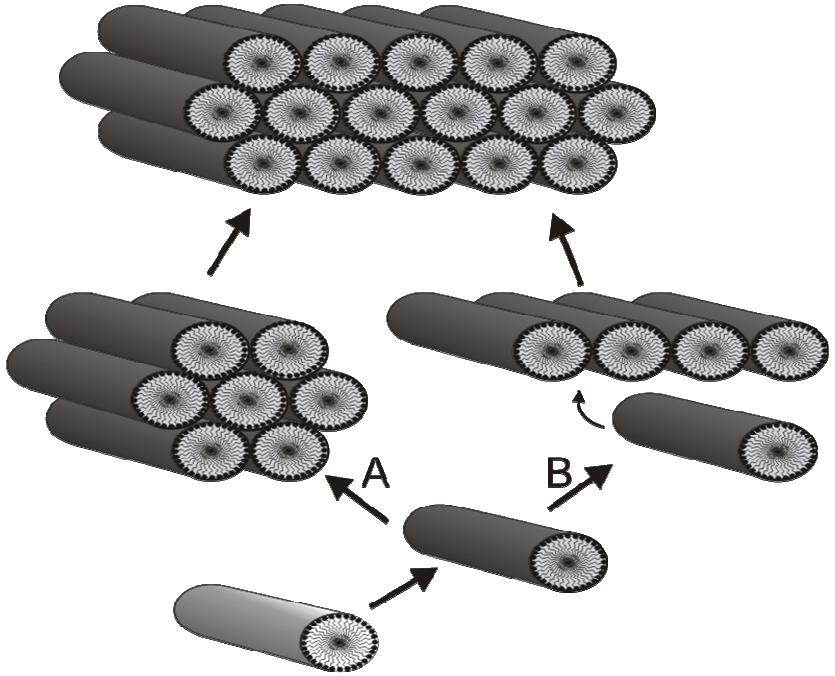

Figure 1-6 : The bulk driven, (a), and interface driven, (b), formation mechanisms observed for silica-surfactant films at the air-liquid interface.

Experiments have used both ionic and block copolymer surfactants and the formation processes appears to be similar to that for the formation of ordered particulate materials using copolymer surfactants. Interactions between the inorganic precursor and

surfactant are driven by charge density. The elongation from spherical to cylindrical micelles prior to film formation is also comparable to the developments that occur in the solution phase development of copolymer templated materials.[63]

Outside the specific concentration region in which a bulk-driven mechanism operates, film formation is reported to occur by a slower, gradual, surface-driven formation mechanism. At higher and lower inorganic precursor concentrations reported reflectometry results show the narrowing of an initially broad peak due to Bragg reflection from the film.[61] This is what would be expected for a thin film of micelles getting thicker very slowly due to addition of individual micelles to an existing ordered structure, rather than aggregates of micelles coming to the surface, then packing to make a continuous film. In the case of a disordered film becoming ordered, it is expected that specular reflection will be lost first followed by the narrowing of a broad peak. The retention of the specular peak during structure formation, and ripples observed in the specular peak, show a very smooth film of increasing thickness suggesting a thin film getting thicker, rather than a thick but disordered film becoming ordered.

Similar observations of peak development and narrowing have subsequently been reported for formation of a titania-surfactant film at the air-water interface.[64,65] In this case the narrowing of the peak was assigned to the development of additional repeat units at the interface as no evidence was found for the existence of a coacervate phase prior to film formation. This is analogous to the second, surface driven, mechanism of development for silica films described above.

1.4 Titanium Dioxide Materials

As the development of silica materials began, the potential utility of mesoporous transition metal-based materials was also rapidly realised for applications such as catalysis and photochemistry.[58,66] Due to the greater challenges in using transition metal precursors, the development of such materials has persistently lagged behind that of silica materials and the first successful materials were developed as mixed transition metal – silica structures.[67] Solely transition metal oxide powders were subsequently developed with the production of a range of lamellar powders and structured tungsten oxide materials followed by the first thermally stable titanium dioxide based material.[20,67,68] A similar delay has also been present between the development of silica and transition metal film materials. Nonetheless a wide range of film materials containing and formed from transition metals have now been achieved, predominantly via evaporation induced self assembly.[2,20]

Titanium dioxide is arguably the most promising transition metal material for widespread application as it is biologically and chemically inert, stable to corrosion, is inexpensive and its band gap of 3.2 eV holds great potential for photochemical and photoelectric applications.[69-71] Indeed, titanium dioxide-based mesoporous materials have been successfully studied for use in sensors, catalysts for pollutant decomposition and solar cells among other areas.[53,58,59,66,72] The development by Gratzel et. al. of titanium dioxide particles into dye sensitized solar cells has been one development of particular significance and improving the efficiency to such cells to rival that of silicon solar cells remains a considerable research goal.[53,66,73] Already it has become possible to create titanium dioxide solar cells that are more efficient than silicon cells at high temperatures and low solar angles.[74]

However, the continued development of new titanium dioxide materials has been hampered by the highly reactive nature, particularly in the presence of water, of the Titanium (IV) chlorides and alkoxide that are most commonly used precursor materials.[75] The reactivity of these materials is partially derived from a low electronegativity and a desire to fill the metal coordination sphere of Titanium (IV), as the precursors typically posses four ligands rather than the preferred six.[3,13,37,75-77] Alkoxides represent a

particularly common reagent for the formation of both silica and transition metal materials, however transition metal alkoxides are an order of magnitude more reactive than their silica equivalents.[75,76] The precursors readily undergo hydrolysis, alcoxolation and hydrolysis reactions, comparable to those of silica precursors, shown in *Figure 1-2*, leading to disordered inorganic polymers that precipitate from solution.[13,37]

In organic solvents, such as alcohols with little water present, alkoxides undergo alcohol exchange reactions in which the metal ligands are replaced with solvent as below:

$$M(OR)_z + xR'OH \rightarrow M(OR)_{z-x}(OR')_x + xROH$$

Alcohol exchange reactions also occur with metal chloride species which are also commonly used precursors. Silicon chlorides typically react completely in excess alcohols, while larger metals undergo partial reactions, forming species such as $TiCl_2(OEt)_2 \bullet EtOH$, in the case of titanium.[37]

Additionally, the drive to fill the coordination sphere of the metal leads to formation of metal alkoxides oligomers, with alkoxides acting as bridging ligands that are considerably more stable in solution than monomer species, such as $Ti_3(OR)_{12}$ shown in *Figure 1-7*. Titanium alkoxides with primary alkoxide ligands form trimeric species in solution while secondary and tertiary alkoxides are restricted to tetrahedral monomers due to steric hindrance.[3] Such oligomers slow hydrolysis reactions due to the stability of the bridging alkoxides.

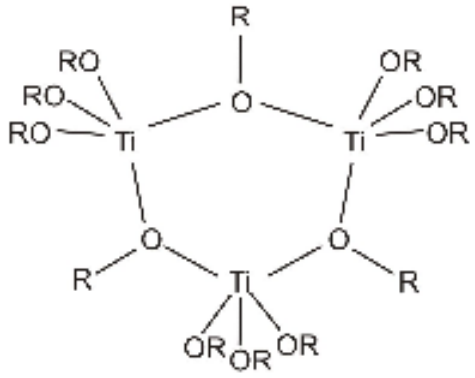

Figure 1-7 : Molecular structure of the $Ti_3(OR)_{12}$ trimeric alkoxides oligomer (After Sanchez, et. al. 1990).[3]

The use of competing ligands with alkoxide precursors, of which trimer formation is an example, is one way to slow and control the reaction of titanium precursor compounds. Reactions may also be slowed by other means such as limiting the availability of water, to restrict hydrolysis, and by using highly acidic conditions.[2] The presence of acids acts to catalyse the hydrolysis of alkoxides, but slows the subsequent condensation. Protonation of the alkoxide ligands generates good leaving groups, as shown below, thus hastening hydrolysis.[37]

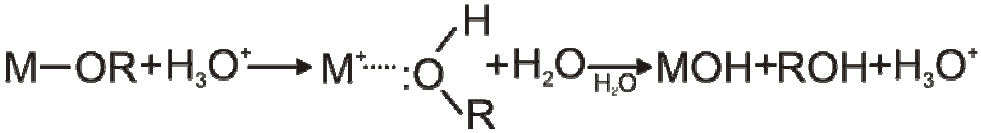

Acid catalysis is directed to the ends of growing inorganic chains, leading to the formation of extended polymers with limited branching, however, when the H^+ to Ti ratio is greater than one, the highly acidic conditions slow all condensation considerably.[37] This combination is ideal for the formation of mesostructured materials for many applications, as fully hydrolysed precursors most readily lead to the formation of crystalline TiO_2. When hydrolysis and condensation occur concurrently the formation of $Ti(OH)_x(OR)_{4-x}$ species and presence of alkoxides ligands can prevent the generation of pure TiO_2 and amorphous products become predominant.[3] However, at high acid and low water concentrations there is greater polydispersity in the titanitum oxide oligomers formed in solution.[78]

Therefore, controlling both the hydrolysis and condensation reactions of the titanium (IV) precursors is of fundamental importance in the generation of ordered titanium dioxide-based materials. However, these demands must also be balanced with the knowledge that the surface activity of the surfactant templates, and therefore the final morphology of materials produced, depend upon factors such as solvent composition, water content and acidity.[6,17] Unfortunately the high reactivity of the precursor materials means that little information is presently available about the mechanisms that exist in titanium dioxide material formation and debates in this area are ongoing.[6]

Some mechanistic information has been reported for the use of metal oxides and copolymer surfactants in which charged metal ion species were found to associate preferentially with hydrophilic PEO blocks.[6,79] Subsequent aggregation and organisation occurs based upon the hydrophobic and hydrophilic regions of the copolymer surfactant. However, the interactions between titanium species and copolymer surfactants have been found to vary considerably with the hydrolysis ratio, the ratio of water to titanium. When little water is present, the desired expansion from 4 to 6 coordination can lead to strong chelation between the titanium metal and ethylene oxide groups and alkoxylation can create a covalent bond between the hydroxide terminal group of the surfactant and the metal.[75] Both of these interactions with the polymer are capable of disrupting ordering of the surfactant due to hydrophobicity considerations resulting in disordered products.

The presence of water reduces the metal – surfactant interactions and allows greater freedom to form micelles. In this case hydrogen bonding is reported to become of greater importance and the relatively hydrophilic nature of hydroxide groups in growing titania oligomers present multiple sites for interaction and leads to the formation of an inorganic layer around surfactant micelles.[75] Subsequent joining together of the coated micelles by inorganic condensation allows the formation of a structured inorganic network.[75] These results further emphasise the importance of the amount of water present in solution during the formation of titanium dioxide materials.

It has been reported that the complexity added by having water present in the reaction makes non-aqueous preparations the most promising for transition metal materials including titania.[80] However, completely non-aqueous preparations typically require rigorous control of reaction conditions, elevated temperatures and produce disordered materials.[17,75,80] Therefore it is probable that the inclusion of a limited amount of water to an otherwise non-aqueous preparation has the greatest chance of forming mesoporous titania materials under mild reaction conditions leading to the present research.

1.5 References

(1) Palmqvist, A. *Current Opinion in Colloid & Interface Science* **2003**, *8*, 145-155.

(2) Soler-Illia, G. d. A.; Sanchez, C.; Lebeau, B.; Patarin, J. *Chemical Reviews* **2002**, *102*, 4093-4138.

(3) Sanchez, C.; Livage, J. *New Journal of Chemistry* **1990**, *14*, 513-521.

(4) Corma, A. *Chemical Reviews* **1997**, *97*, 2373-2419.

(5) Corma, A.; Fornes, V.; Garcia, H.; Miranda, M. A.; Sabater, M. J. *Journal of the American Chemistry Society* **1994**, *116*, 9767-9768.

(6) Edler, K. *Australian Journal of Chemistry* **2005**, *58*, 627-643.

(7) Flanigen, E. M. *Pure & Applied Chemistry* **1980**, *52*, 2191-2211.

(8) Gregg, S. J.; Sing, K. S. W. *Adsorption, Surface Area and Porosity*; 2nd ed.; Academic Press: London, 1982.

(9) Everett, D. H. *Pure & Applied Chemistry* **1972**, *31*, 577-638.

(10) Beck, J. S.; Vartuli, J. C.; Roth, W. J.; Leonowicz, M. E.; Kresge, C. T.; Schmitt, K. D.; Chu, C. T.-W.; Olson, D. H.; Sheppard, E. W.; McCullen, S. B.; Higgins, J. B.; Schienker, J. L. *Journal of the American Chemistry Society* **1992**, *114*, 10834-10843.

(11) Sellinger, A.; Weiss, P. M.; Nguyen, A.; Lu, Y.; Assink, R. A.; Gong, W.; Brinker, C. J. *Nature* **1998**, *394*, 256-260.

(12) Brinker, C. J.; Lu, Y.; Sellinger, A.; Fan, H. *Advanced Materials* **1999**, *11*, 579-585.

(13) Livage, J.; Henry, M.; Sanchez, C. *Progress in Solid State Chemistry* **1988**, *18*, 259-341.

(14) Edler, K.; Brennan, T.; Roser, S. J. *Thin Solid Films* **2006**, *495*, 2-10.

(15) Zhao, D.; Yang, P.; Huo, Q.; Chmelka, B. F.; Stucky, G. D. *Current Opinion in Solid State & Materials Science* **1998**, *3*, 111-121.

(16) Evans, D. F.; Wennerstrom, H. *The Colloidal Domain: where physics, chemistry, biology and technology meet*; VCH Publishers, Inc.: New York, 1994.

(17) Soler-Illia, G. d. A.; Scolan, E.; Louis, A.; Albouy, P.; Sanchez, C. *New Journal of Chemistry* **2001**, *25*, 156-165.

(18) Kresge, C. T.; Leonowicz, M. E.; Roth, W. J.; Vartuli, J. C.; Beck, J. S. *Nature* **1992**, *359*, 710-712.

(19) Clint, J. E. *Chemistry in Britain* **1990**, *26*, 333-336.

(20) Huo, Q.; Margolese, D. I.; Ciesla, U.; Feng, P.; Gier, T. E.; Sieger, P.; Leon, R.; Petroff, P. M.; Schuth, F.; Stucky, G. D. *Nature* **1994**, *368*, 317-321.

(21) Bagshaw, S. A.; Prouzet, E.; Pinnavaia, T. J. *Science* **1995**, *269*, 1242-1244.

(22) Flödstrom, K.; Teixeira, C. V.; Amenitsch, H.; Alfredsson, V.; Linden, M. *Langmuir* **2004**, *20*, 4885-4891.

(23) Guo, Q.; Thomann, R.; Gronski, W. *Polymer* **2007**, *48*, 3925-3929.

(24) Bharatiya, B.; Guo, C.; Ma, J.; Hassan, P.; Bahadur, P. *European Polymer Journal* **2007**, *43*, 1883 - 1891.

(25) Yu, C.; Yu, Y.; Zhao, D. *Chemical Communications* **2000**, 575-576.

(26) Abe, M. *Current Opinion in Colloid & Interface Science* **1999**, *4*, 354-356.
(27) Hoffmann, H.; Wurtz, J. *Journal of Molecular Liquids* **1997**, *72*, 191-230.
(28) Mele, S.; Ninham, B. W.; Monduzzi, M. *Journal of Physical Chemistry B* **2004**, *108*, 17751-17759.
(29) Han, Y.; Li, D.; Zhao, L.; Song, J.; Yang, X.; Li, N.; Di, Y.; Li, C.; Wu, S.; ZXu, X.; Meng, X.; Lin, K.; X, F.-S. *Angewandte Chemie International Edition* **2003**, *42*, 3633-3637.
(30) Kekicheff, P.; Tiddy, G. *Journal of Physical Chemistry* **1989**, *93*, 2520-2526.
(31) Patel, N.; Marlow, M.; Lawrence, M. J. *Journal of Colloid and Interface Science* **2003**, *258*, 345-353.
(32) Ravey, J.; Stebe, M.; Sauvage, S.; Elmoujahid, C. *Colloids and Surfaces A* **1995**, *99*, 221-231.
(33) Blin, J.; Lesieur, P.; Stebe, M. *Langmuir* **2004**, *20*, 491-498.
(34) Blin, J.; Stebe, M. *Microporous and Mesoporous Materials* **2005**, *87*, 67-76.
(35) Meng, X.; Di, Y.; Zhao, L.; Jiang, D.; Li, S.; Xiao, F.-S. *Chemistry of Materials* **2004**, A-I.
(36) Di, Y.; Meng, X.; Li, S.; Xiao, F.-S. *Microporous and Mesoporous Materials* **2005**, *82*, 121-127.
(37) Brinker, C. J.; Scherer, G. W. *Sol-Gel Science*; 1 ed.; Academic Press: London, 1990; Vol. 1.
(38) Yamahara, K.; Okazaki, K. *Fluid Phase Equilibria* **1998**, *144*, 449-459.
(39) Patarin, J.; Lebeau, B.; Zana, R. *Current Opinion in Colloid & Interface Science* **2002**, *7*, 107-115.
(40) Chen, C.-Y.; Burkett, S. L.; Li, H.-X.; Davis, M. E. *Microporous Materials* **1993**, *2*, 27-34.
(41) Huo, Q.; Margolese, D. I.; Ciesla, U.; Demuth, D.; Feng, P.; Gier, T. E.; Sieger, P.; Firouzi, A. *Chemistry of Materials* **1994**, *6*, 1176-1191.
(42) Tanev, P. T.; Pinnavaia, T. J. *Science* **1995**, *267*, 865-867.
(43) Niederberger, M.; Garnweitner, G. *Chemistry A European Journal* **2006**, *12*, 7282-7302.
(44) Yang, B.; Guo, C.; Chen, S.; Ma, J.; Wang, J.; Liang, X.; Zheng, L.; Liu, H. *Journal of Physical Chemistry B* **2006**, *110*, 23068-23074.
(45) Cassiers, K.; Van Der Voort, P.; Linssen, T.; Vansant, E. F.; Lebedev, O.; Van Landuyt, J. *Journal of Physical Chemistry B* **2003**, *107*, 3690-3696.
(46) Epping, J. D.; Chmelka, B. F. *Current Opinion in Colloid & Interface Science* **2006**, *11*, 81-117.
(47) Linton, P.; Alfredsson, V. *Chemistry of Materials* **2008**, *20*, 2878-2880.
(48) Soni, S.; Brotons, G.; Bellour, M.; Narayanan, T.; Gibaud, A. *Journal of Physical Chemistry B* **2006**, *110*, 15157-15165.
(49) Blin, J.; Leonard, A.; Su, B. L. *Chemistry of Materials* **2001**, *13*, 3542-3553.
(50) Baute, D.; Frydman, V.; Zimmermann, H.; Kababya, S.; Goldfarb, D. *Journal of Physical Chemistry B* **2005**, *109*, 7807-7816.

(51) Vendamme, R.; Onoue, S.-y.; Nakao, A.; Kunitake, T. *Nature Materials* **2006**, *5*, 494-501.
(52) Ogawa, M. *Chemical Communications* **1996**, *1996*, 1149-1150.
(53) Huo, K.; Tian, B.; Li, F.; Bian, Z.; Zhao, D.; Huang, C. *Journal of Materials Chemistry* **2005**, *15*, 2414-2420.
(54) Yang, H.; Kuperman, A.; Coombs, N.; Mamiche-Afara, S.; Ozin, G. A. *Nature* **1996**, *379*, 703-705.
(55) Yang, H.; Coombs, N.; Sokolov, I.; Ozin, G. A. *Nature* **1996**, *381*, 589-592.
(56) Brinker, C. J.; Dunphy, D. R. *Current Opinion in Colloid & Interface Science* **2006**, *11*, 126-132.
(57) Chen, W.; Geng, Y.; Sun, X.-D.; Cai, Q.; Li, H.-D.; Weng, D. *Microporous and Mesoporous Materials* **2008**, *111*, 219-227.
(58) Zhao, L.; Yu, Y.; Song, L.; Hu, X.; Larbot, A. *Applied Surface Science* **2005**, *239*, 285-291.
(59) Zukalova, M.; Zukal, A.; Kavan, L.; Nazeeruddin, M. K.; Liska, P.; Gratzel, M. *Nano Letters* **2005**, *5*, 1789-1792.
(60) Edler, K.; Goldar, A.; Hughes, A. V.; Roser, S. J.; Mann, S. *Microporous and Mesoporous Materials* **2001**, *44-45*, 661-670.
(61) Brennan, T.; Hughes, A. V.; Roser, S. J.; Mann, S.; Edler, K. *Langmuir* **2002**, *18*, 9838-9844.
(62) Edler, K.; Brennan, T.; Roser, S. J.; Mann, S.; Richardson, R. M. *Microporous and Mesoporous Materials* **2003**, *62*, 165-175.
(63) Fernandez-Martin, C.; Roser, S. J.; Edler, K. *Journal of Materials Chemistry* **2008**, *18*, 1222-1231.
(64) Henderson, M. J.; King, D.; White, J. W. *Langmuir* **2004**, *20*, 2305-2308.
(65) Henderson, M. J.; Gibaud, A.; Bardeau, J.-F.; White, J. W. *Journal of Materials Chemistry* **2006**, *16*, 2478-2484.
(66) Gratzel, M. *Nature* **2001**, *414*, 338-344.
(67) Antonelli, D. M.; Ying, J. Y. *Angewandte Chemie International Edition* **1995**, *34*.
(68) Ciesla, U.; Demuth, D.; Leon, R.; Petroff, P. M.; Stucky, G. D.; Unger, K.; Schuth, F. *Journal of the Chemistry Society Chemical Communications* **1994**, *94*, 1387-1388.
(69) Yun, H.-s.; Miyazawa, K. c.; Zhou, H.; Honma, I.; Kuwabara, M. *Advanced Materials* **2001**, *13*, 1377-1380.
(70) Deshpande, A. S.; Shchukin, D. G.; Ustinovich, E.; Antonelli, M.; Caruso, R. A. *Advanced Functional Materials* **2005**, *15*, 239-245.
(71) Hoffmann, M. R.; Martin, S. T.; Choi, W.; Bahnemann, D. W. *Chemical Reviews* **1995**, *95*, 69-96.
(72) Shchukin, D. G.; Caruso, R. A. *Advanced Functional Materials* **2003**, *13*, 789-794.
(73) Malfatti, L.; Falcaro, P.; Amenitsch, H.; Caramori, S.; Argazzi, R.; Bignozzi, C. A.; Enzo, S.; Maggini, M.; Innocenzi, P. *Microporous and Mesoporous Materials* **2006**, *88*, 304-311.

(74) Vargas-Florencia, D.; Edvinsson, T.; Hagfeldt, A.; Furo, I. *Journal of Physical Chemistry C* **2007**, *111*, 7605-7611.

(75) Soler-Illia, G. d. A.; Sanchez, C. *New Journal of Chemistry* **2000**, *24*, 493-499.

(76) Bradley, D. C.; Mehotra, R. C.; Guar, D. P. *Metal Alkoxides*; Academic Press: London, 1978; Vol. 1.

(77) Facca, F.; Puccetti, G.; Leblanc, R. *Colloids and Surfaces A* **1999**, *149*, 89-98.

(78) Blanchard, J.; Ribot, F.; Sanchez, C.; Bellot, P. V.; Trokiner, A. *Journal of Non-Crysatlline Solids* **2000**, *265*, 83-97.

(79) Yang, P.; Zhao, D.; Margolese, D. I.; Chmelka, B. F.; Stucky, G. D. *Chemistry of Materials* **1999**, *11*, 2813 - 2826.

(80) Antonietti, M.; Niederberger, M.; Smarsly, B. *Dalton Transactions* **2008**, 18-24.

Chapter 2
Experimental

2.1 Principles of Analysis

2.1.1 Specular Reflection

The scattering of radiation from a sample surface provides a number of powerful analytical tools for research, among which specular reflection is particularly useful for the study of thin films. Comprehensive discussions of the theory of specular reflection exist in the literature[1-4] and this section is restricted to a brief overview. The basis of reflectometry is measuring the intensity, or reflectivity, of radiation from an interface during specular reflection, at which the angles of incidence and reflection are equal. This reflection is associated with a change in the refractive index. The reflectivity, R, measured in these techniques is defined as reflectance, r, multiplied by its complex conjugate, r^*.

Rigorous mathematical calculations of scattering include both the real and imaginary components, due to scattering and absorption respectively, of the refractive index. However, if the imaginary component is excluded as being much smaller than the real component, as is the case in our experiments,[1] the refractive index, n, of a material is given by:

$$n = 1 - \frac{\lambda^2}{2\pi} N_b \qquad (2\text{-}1)$$

where λ is the wavelength of the radiation and N_b is the scattering length density. The scattering length density is dependent upon the different interactions of different types of radiation. Thus it is understood that when N_b is greater than zero the refractive index is dependent upon the type of radiation. In the case of neutron radiation scattering occurs

due to interactions with the nuclei of atoms in the sample and the scattering length density is given by the relationship

$$N_b = \sum_{i=1}^{N} b_i \times \frac{\rho N_A}{MW} \tag{2-2}$$

where ρ is the physical density, N_A is Avogadro's number, MW is the molecular weight of the atom and b_i is the neutron scattering length of the element. Across the periodic table b_i varies randomly and variation between both different elements and isotopes gives rise to a range of experimental techniques including contrast matching. Tables of atomic neutron scattering lengths may be readily found in the literature.[2] For X-rays, on the other hand, scattering length density is given by the equation

$$N_b = r_e \times \rho_e \tag{2-3}$$

where ρ_e is the electron density of the scattering species or atom and r_e is the radius of the electron cloud. In this case the scattering length density is observed to increase steadily with atomic number across the periodic table. As differences in refractive index are dependent upon differences in scattering length density the contrast typically referred to during analysis of neutron and X-ray scattering results is the difference in scattering length density. A summary of the neutron and X-ray scattering length densities (SLD) of the materials used in this work is shown in **Table 2-1**.

Table 2-1 : Summary of X-ray and neutron scattering length densities of materials used.

Compound	Neutron SLD	X-ray SLD
TiO_2	2.59 x10^{-6} Å^{-2}	3.42 x10^{-5} Å^{-2}
ZnO	4.76 x10^{-6} Å^{-2}	4.26 x10^{-5} Å^{-2}
$(C_2F_4)_n$	2.94 x10^{-6} Å^{-2}	1.11 x10^{-5} Å^{-2}
$(C_2H_4)_n$	-3.57 x10^{-7} Å^{-2}	9.80 x10^{-6} Å^{-2}
$(C_2H_4O)_n$	5.66 x10^{-7} Å^{-2}	9.28 x10^{-6} Å^{-2}
C_2H_5OH	-3.44 x10^{-7} Å^{-2}	7.58 x10^{-6} Å^{-2}
C_2H_5OD	7.14 x10^{-7} Å^{-2}	7.58 x10^{-6} Å^{-2}
C_2D_5OD	5.39 x10^{-6} Å^{-2}	7.58 x10^{-6} Å^{-2}

For specular reflectivity techniques calculations of interfacial scattering utilise Snell's law

$$n_1 \sin\theta_1 = n_2 \sin\theta_2 \tag{2-4}$$

where n_1 and n_2 are the refractive indices of the first and second media and θ_1 and θ_2 are the angles of incidence and transmission respectively as illustrated in *Figure 2-8*.

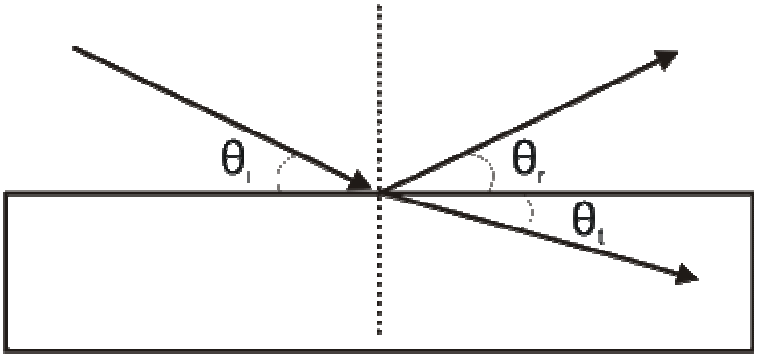

Figure 2-8 : Reflection and transmission from an interface transiting from a higher to a lower refractive index. Angles of incidence and reflection are observed to be equal.

The magnitude of the propagation number of the wave vectors, k_i, k_r and k_t shown in *Figure 2-8* are defined such that θ

$$|k| = \frac{2\pi}{\lambda_i} \tag{2-5}$$

The information gained from a specular reflection scattering curve corresponds to depth profile perpendicular to the interface, along the z-axis, as it is horizontal interfaces at various depths through the sample that give rise to the reflection. Thus it is the z-component, k_z, of the wave vectors incident to and reflected from the surface, that are of particular significance. These components may be calculated geometrically as

$$k_z = \frac{2\pi}{\lambda}\sin\theta \tag{2-6}$$

Interfacial structures are probed by specular reflectivity by plotting reflectivity, *R*, against the scattering vector, *Q* that is defined as the difference between the incident and reflected wave vectors

$$Q = k_r - k_i \tag{2-7}$$

This relationship may be shown diagrammatically as in *Figure 2-9* where it is observed that, if the scattering is considered to be elastic, only the z-components of the wave vectors are different and it is, therefore, Q_z that is of particular interest.

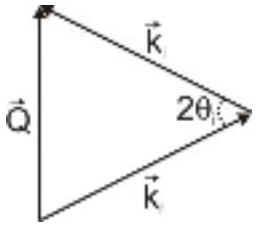

Figure 2-9 : Derivation of the scattering vector Q. Z-components of k_r *and* $-k_i$ *add while the other components are canceled.*

As only the sign of the z-component has changed between the incident and reflected wave vectors it is readily found that

$$k_z(reflected) = -k_i(incident) \tag{2-8}$$

and, after consideration of equation (2-6), that

$$Q_z = 2k_z = \frac{4\pi \sin\theta_i}{\lambda} \tag{2-9}$$

It is seen from this definition that scattering vector varies with both the angle of incidence and the wavelength of the radiation allowing two different approaches to reflectivity measurements, angle dispersive and energy dispersive. However, the mathematical treatment of reflectivity is also commonly considered in two different ways. Fresnel reflectivity provides more exactly represents reflectivity while the

kinematic approximation is a simplification that is only valid at higher values of Q_z, both methods are detailed below.

Fresnel reflectivity, arising from a difference in scattering length densities between two media, is observed to show total reflection below a certain critical angle that varies depending upon the media. Specifically, the critical angle, θ_c, is given by the relationship

$$\theta_c = \sqrt{16\pi\Delta N_b} \tag{2-10}$$

where ΔN_b is the change in scattering length density between the two media. As noted earlier the mathematical definition of the real number quantity reflectivity, R, is the complex quantity reflectance, r, multiplied by its complex conjugate, r^*. For reflection from an interface the reflectance is defined by the Fresnel equation

$$\left| r = \frac{n_i \sin\theta_i - n_t \sin\theta_t}{n_i \sin\theta_i + n_t \sin\theta_t} \right| \tag{2-11}$$

where n_i and n_t are the refractive indices of the incident and transmitting media respectively while θ_i and θ_t are the angles of incidence and transmittance. The increased loss of reflection for a rough interface may also be accounted for through multiplication by the Debye – Waller factor in which σ represents the roughness of the interface.

$$e^{\frac{Q^2\sigma^2}{2}} \tag{2-12}$$

The kinematic approximation, on the other hand, does not establish a critical angle for an interface and is only valid at higher Q, beyond the critical edge of a reflectivity profile. Above this critical angle reflectivity from interfaces within the sample may be considered, as some radiation is refracted. Furthermore, reflectivity is less than one and is approximated in the kinematic method by

$$R_F = \frac{16\pi^2 \Delta N_b}{Q^4} \tag{2-13}$$

and is found to be proportional to the change in scattering length density and is observed to drop away with a Q^{-4} relationship for an ideally smooth interface, as shown in *Figure 2-10*. For both rougher and poorly defined interfaces reflectivity drops away more steeply.

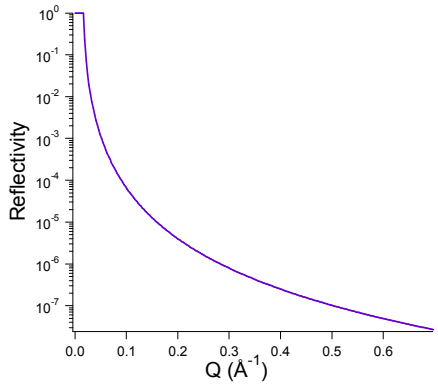

Figure 2-10 : Calculated reflectivity profile from an ideal interface without surface roughness. Reflectivity drops away with a Q^{-4} dependence.

Although reflection from a single, smooth interface is relatively straightforward, the reflectivity profile of an interface becomes more complex if a sample has multiple layers of different scattering length density. In this case scattering occurs at each interface requiring a more complex mathematical description, illustrated in *Figure 2-11*.

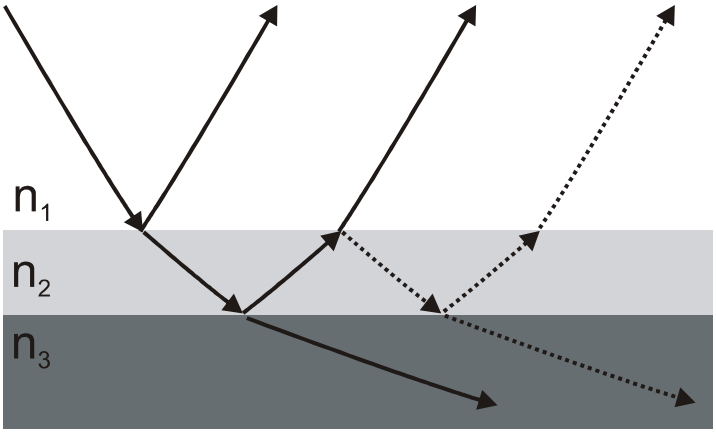

Figure 2-11 : Scattering occurs at each interface between media of different refractive index giving rise to a series of reflected and transmitted wave vectors.

A special case of this scattering from multiple layers is when long range order of a periodic structure, such as hexagonal, cubic or lamellar, exists in the sample. In such cases the regular spacing of the layers leads to constructive interference of the radiation reflected from subsequent layers as shown over the page in *Figure 2-12*.

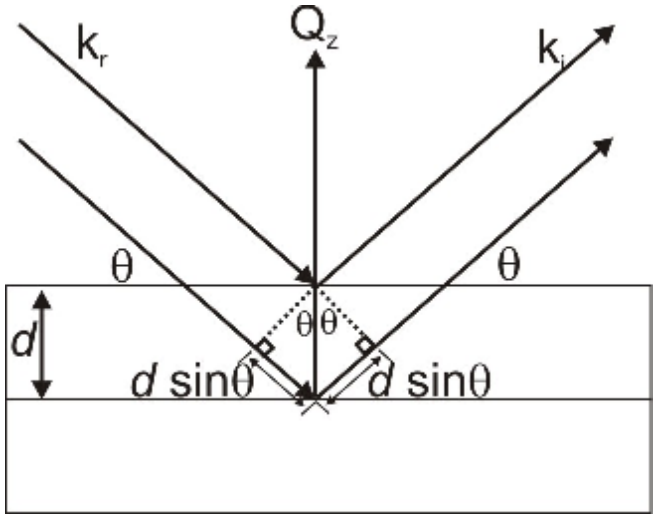

Figure 2-12 : Diagram of Bragg diffraction. Rays reflected from subsequent layers traverse a path length $2d\sin\theta$ longer than those reflected from the previous layer.

As the path length differs between subsequent layers, radiation reflected from each layer becomes out of phase by $2d\sin\theta$ which gives the requirement for constructive interference as Braggs' law

$$n\lambda = 2d\sin\theta \qquad (2\text{-}14)$$

where n is the order of diffraction (an integer), λ is the radiation wavelength, θ is the angle of incidence and d is the spacing between repeat layers in angstroms. This constructive interference gives rise to Bragg peaks in a reflectivity profile if there are sufficient repeat layers. As demonstrated in *Figure 2-13*, for a single layer, fringes are visible in reflectivity profile while peaks develop with an increased number of layers and greater long range order.

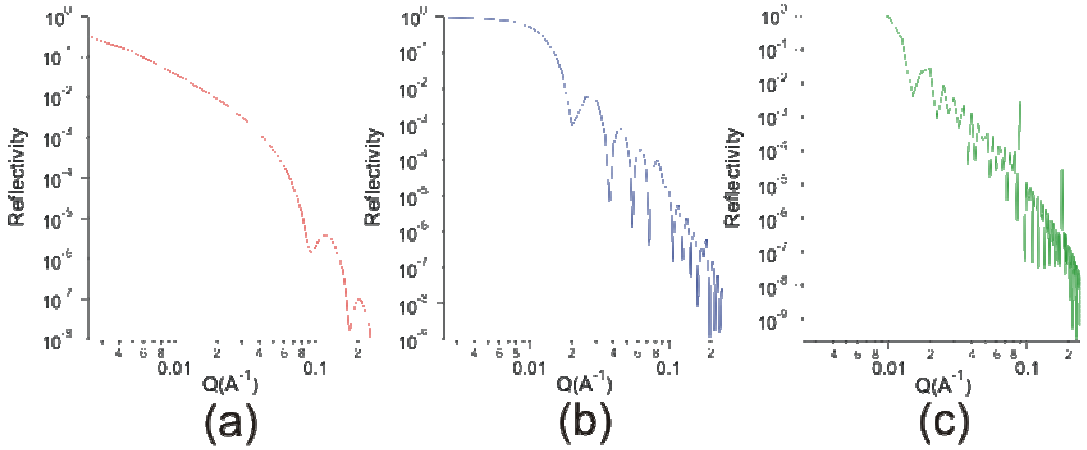

Figure 2-13 : Calculated reflectivity profiles for 1, 5 and 50 layers of TiO_2 and fluorinated surfactant shown in (a), (b) and (c) respectively.

If peaks are observed in a reflectivity profile it is possible to calculate a layer spacing within the sample without recourse to data modeling. By combining Equations (9) and (14) it is possible to calculate the interlayer distances using

$$Q_z = \frac{2\pi}{d} \tag{2-15}$$

From the definition of scattering vector in Equation (9) it follows that there are two possible methods for obtaining a reflectivity profile, energy dispersive and angle dispersive. In energy dispersive reflectometry a fixed geometry is established and a range of incident radiation energies, and therefore wavelengths, is utilized to cover the Q_z range studied. On the other hand, the angle dispersive technique, suitable for monochromatic radiation sources, uses a single incident radiation wavelength and uses changes in the

reflection geometry to change θ and thereby vary Q_z. Both techniques have been used in this research for neutron and X-ray reflection and scattering experiments.

Neutron and X-ray scattering are complementary techniques as the different radiation interactions yield the ability to gain different information. Modern X-ray sources are capable of generating orders of magnitude greater fluxes than neutron sources and as such X-ray techniques are suitable for the rapid collection of data in time-resolved experiments. A high flux is also suitable for scattering experiments in which low reflectivity conditions are present.

However, the atomic number dependence of X-ray scattering due to interaction with the electron cloud mean that light elements are weak scatters. The nuclear interactions of neutron scattering vary considerably with different isotopes for some elements, including hydrogen. This allows the possibility of studying different interfaces to X-ray techniques as lighter elements can produce considerable scattering. Additionally, it is possible, through use of a mixture of isotopes, to reduce the contrast of a specific interface to zero (contrast matching) and eliminate the scattering arising from it to allow the study of specific interfaces within a sample. Furthermore the uncharged nature of neutrons makes them deeply penetrating radiation and this allows for the study of a sample over long length scales.

2.1.2 Small Angle Scattering

Small angle X-ray and neutron scattering (SAXS and SANS) provide an additional tool for sample analysis. As with specular reflection, a full derivation of the principles of small angle scattering is beyond the scope of this section which is restricted to a brief overview, however detailed discussions of scattering theory are freely available in the literature.[3-6] In the case of powdered materials and particles in solution, small angle scattering may be regarded as being directly related to specular reflection techniques as scattering from the particles may be regarded theoretically as ‘reflection’ from a series of planes.[7] The numerous randomly oriented particles of powdered samples and particles in solution present different scattering geometries to the incident radiation, effectively covering an angularly disperse scattering range. If a range of incident radiation

wavelengths is utilised, as is often the case, the scattering range may be covered in an energy dispersive manner.

As shown in *Figure 2-14* some particles in a scattering sample will have the correct orientation for a periodic structure, if one is present, to be observed in a similar manner to reflectivity. In addition to internal ordering, the external ordering between particles and of the particles themselves may be examined.

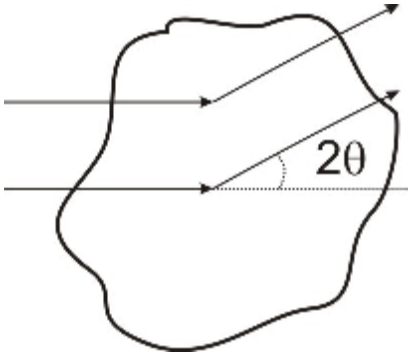

Figure 2-14 : Geometry of scattering from a particle in small angle scattering.

For liquid and solution samples a similar combination of properties are observed in small angle scattering. Scattering occurring from molecules in solution may be due to individual molecules, such as polymer coils, or from structures formed in solution such as surfactant micelles and liquid crystal phases. A small angle scattering profile thus consists of both a component, known as the Form Factor, due to scattering from individual species and a Structure Factor due to scattering from interactions between the individual species in the sample as given below:

$$I(Q) = NV^2(\Delta p)^2 P(Q)S(Q) + bgd \qquad (2\text{-}16)$$

where *I(Q)* is the intensity of the scattered radiation, *NV* is the number volume of scattering species, or concentration, and the scattering intensity is observed to increase linearly as concentration increases. *V* is the sample volume and Δp is the contrast between the scattering species and solvent. *P(Q)* is the form factor, representing scattering from single particles and *S(Q)* is the structure factor arising from structure in the sample due to interparticle interactions while *bgd* is the background.[8]

More specifically, the form factor, *P(Q)*, represents interference effects between radiation scattered from different parts of a single scattering body (such as a surfactant micelle or particle) in which atoms are treated as point sources of scattering. If the scattering body has regions of different scattering power, such as different atoms or molecules, the form factor may be highly dependent upon the shape and orientation of the scattering body. This may be defined in general in terms of particle volume and a shape parameter averaged for all orientations, however this may be simplified as expressions exist for the most common shapes such as that for spheres of radius R_s

$$P(Q) = \left[\frac{3(\sin(QR_s) - QR_s \cos(QR_s)}{(QR_s)^3} \right]^2 \qquad (2\text{-}17)$$

In addition to the size and shape of the scattering bodies the degree of uniformity of shape has a considerable impact upon the form factor. Cusps are observed to appear in systems with a large number of uniform particles. Variation, or polydispersity, of the particle dimensions, such as the radius, R_s, in Equation 2-17, makes the cusps less sharp as the range of particle dimensions leads to scattering from multiple sizes of particles and makes the pattern less clear as it is disrupted. At higher polydispersities cusps may be lost completely as shown in *Figure 2-15* (c).

In comparison the interparticle structure factor, *S(Q),* represents interference effects between radiation scattered from different scattering bodies and is therefore dependent upon local order in the scattering system. For non-interacting particles *S(Q)* becomes important due to the exclusion of one body from the space occupied by another while in interacting bodies a specific arrangement or exclusion may be favoured such as that imposed by repulsive interactions between like charged particles. In non-interacting bodies, the simplest case, the structure factor depends upon the number of scattering bodies, *N*, and their volume, *V*, and is defined in general as

$$S(Q) = 1 + \frac{4\pi N_p}{QV} \int_0^\infty [g(r) - 1] r \sin(Qr).dr \qquad (2\text{-}18)$$

where *r* is the distance outward radially from any particle. It is observed that as *N* approaches zero, *S(Q)* approaches 1 and that for dilute or weakly interacting systems the structure factor is 1, as interparticle interactions are minimal. Additionally, if the system is sufficiently disordered, interparticle effects may not be apparent in the scattering pattern. Although a structure factor should always be considered in analysis of small angle scattering, no information on long range order may be gained from the structure factor in dilute systems in which interparticle interactions are minimal. At higher concentrations and for highly interacting systems the structure factor has a considerable effect and must be considered. Approximations for the structure factor have been derived for various types of systems offering an expedient alternative to derivation from Equation 2-18.

The calculated small angle neutron scattering profiles in *Figure 2-15* show some of the differences in scattering patterns arising from different shapes in solution, *P(Q)*, and from different structure factors due to different interparticle interactions, *S(Q)*. Some effects of different form factors, corresponding to different particle shapes, are shown in *Figure 2-15 (a)* and *Figure 2-15 (b)* which display the differences between spherical and ellipsoidal particles in otherwise identical samples. The effect of polydispersity, also part of form factor considerations, is shown in *Figure 2-15 (c)* that shows scattering from spheres with a polydispersity of 0.2 otherwise identical to those in *Figure 2-15 (a)*.

In comparison, some effects on the small angle scattering pattern arising from different structure factors are shown in *Figure 2-15 (d)*, *(e)* and *(f)*. Diffraction peaks begin to be observed due to the effect of the structure factor for a 0.6 volume fraction of non-interacting 60 Å TiO_2 spheres shown in *Figure 2-15 (d)* while the effect of a 'sticky hard spheres' structure factor in which the 0.6 volume fraction of TiO_2 spheres have a very high stickiness parameter is shown in *Figure 2-15 (e)*. The final example, *Figure 2-15 (f)* shows the effect of moderately charged particles in which like – like repulsion between 120 x 60 Å prolate ellipsoids is observed to significantly reduce low angle scattering.

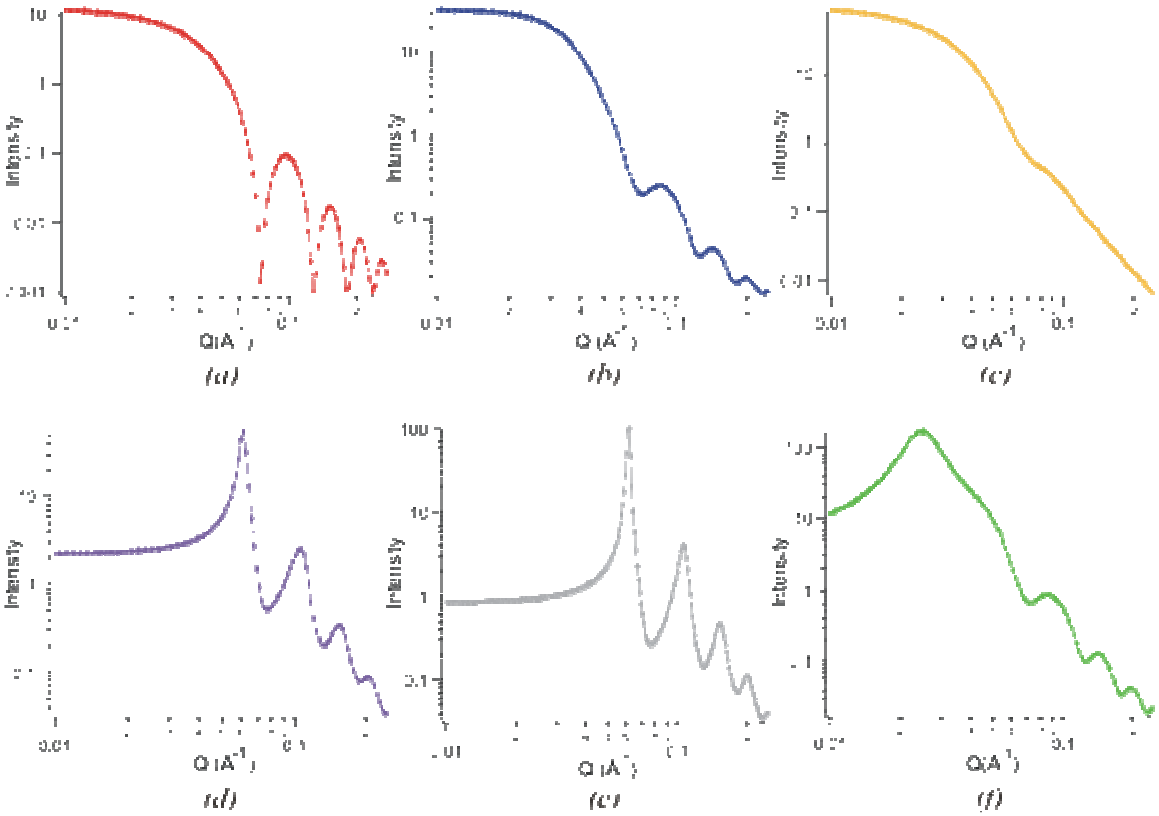

Figure 2-15 : Theoretical SANS patterns from TiO_2 particles. Profiles for 60Å TiO_2 spheres, 120 x 60 Å TiO_2 ellipsoids and 60 Å TiO_2 spheres with a polydispersity of 0.2, (a), (b) and (c) respectively, show the effects of different form factor, P(Q). Structure factors, S(Q), effects are shown in (d), 0.6 volume fraction 60Å hard spheres, (e) 0.6 volume fraction sticky hard spheres and (f), charged ellipsoids.

Although consideration of the form factor and structure factor allow detailed information to be gained from small angle scattering profiles it is also possible derive some information directly. The two most relevant examples of such analyses are Guinier analysis and calculation of the Porod slope.[3] The first of these, Guinier analysis, allows the estimation of the size of scattering bodies. At low concentrations, i.e. where $S(Q) = 1$, and assuming spherical particles and for small values of Q the scattering intensity, I, may be approximated as

$$I(Q) = I(0)\exp\left(\frac{-R_g^2 Q^2}{3}\right) \qquad (2\text{-}19)$$

where R_g is the radius of gyration of the scattering body. Therefore a plot of *ln(I)* vs. Q^2 will have a slope of $-\frac{1}{3}R_g^2$ allowing the straightforward calculation of R_g. However, this analysis is only valid where $R_gQ_{max} < 1$ where Q_{max} is the highest value of Q used in the analysis. R_g Defined as the root mean square of the distances of all scattering species (electrons for X-rays, atomic nuclei for neutrons) from the centre of gravity of the particle and provides a measure of the size of the scattering particles. If the shape of the scattering body is known dimensions such as radius or volume may subsequently be calculated.

Whereas Guinier analysis is only valid for small values of Q calculation of the Porod slope is only valid at high values of Q and allows analysis of the roughness of the interface or surface or a rough estimate of the shape of scattering bodies. The Porod law states that

$$I(Q) \propto SQ^{-4} \tag{2-20}$$

in the limit of $Q \rightarrow \infty$ where S represents the surface area of the scattering body. After consideration of fractal surfaces, where the scale of the measurement may change the result, the equation becomes

$$I(Q) \propto SQ^{-(6-d)} \tag{2-21}$$

where d is a measure of how fractal the surface is. It follows from the Porod law that a plot of *ln(I)* vs. *ln(Q)* the slope is indicative of the surface roughness. Smooth two dimension and three dimensional surfaces give slopes of -2 and -4 respectively while a slope in the range -3 – -4 is indicative of a fractal, or rough, surface.

Calculation using Guinier analysis and Porod slope provides some information about the scattering system, however, the most detailed information from both reflectivity and small angle scattering profiles is gained by modelling of an overall scattering pattern. Such modelling can provide information on solution phases that may be present in addition to information on the size, shape and interactions of species or particles in solution.

2.1.3 Reflectivity and Small Angle Scattering Data Modelling

For both reflectivity and small angle scattering data, computer modelling of the data is a recognised method to gain detailed information about the system. In both cases this is undertaken by using a computer to vary the parameters of a predefined model to generate the best agreement between theoretical and experimental data, typically by using a least squares error analysis. Fresnel reflection may be modelled in the case of reflectometry while modelling of small angle scattering models the form factor and structure factor of a sample, although the structure factor may be excluded as equal to 1 in sufficiently dilute, non-interacting systems.

Although model fitting provides a tool for gaining information from experimental data, care must be taken to confirm that the values for produced by a model are both physically possible and realistic for the sample system. To this end it is preferable to fix as many variables as possible prior to data modeling and to place limits on the range of values that other variables to ensure their values are physically realistic. The results of the models may be further confirmed by trying alternative models and trying different starting conditions for a model to check that a given model has not become stuck in a local minima of the error analysis. In the case of neutron scattering data further confirmation may be achieved by fitting multiple data sets simultaneously in which the physical structure of the samples is the same but scattering lengths densities of layers, or parts of a particle, have been varied.

Modelling of a reflectivity profile is typically undertaken by one of two methods both of which treat the sample as a series of uniform layers of different scattering length density. Such an approximation is valid in the reflectometry case as the observed Q_z wave provides only information perpendicular to the interface. The first method is that of the recursion modelling of the series of reflected and transmitted waves generated at a series of interfaces. Although an accurate method this rapidly becomes cumbersome as a larger number of interfaces and reflected waves are considered. A second widely used method, as used in this work, is the matrix method proposed by Abeles in 1950 that assigns a characteristic matrix to describe individual layers and treats the sample as a sequence of uniform layers and as shown in *Figure 2-16*.[9]

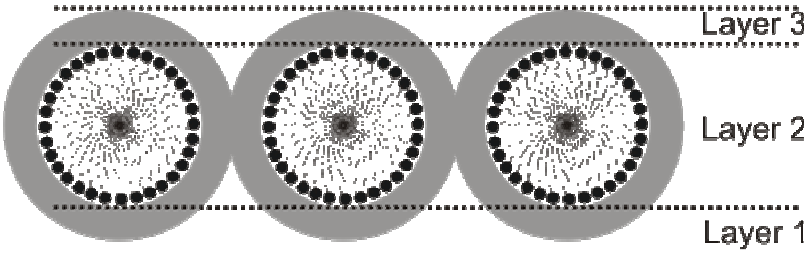

Figure 2-16 : The matrix method of reflectivity modeling treats samples as a series of uniform layers.

If it is not possible to divide a sample into layers of uniform composition the contents of a non-uniform layer may be averaged and a characteristic matrix derived. Utilising a complex exponential the Abeles method defines a characteristic matrix, M_i, for a uniform layer of refractive index n_i as

$$M_i = \begin{bmatrix} e^{i\beta_{i-1}} & r_i e^{-i\beta_{i-1}} \\ r_i e^{i\beta_{i-1}} & e^{i\beta_{i-1}} \end{bmatrix} \tag{2-22}$$

Where r_i is the reflectance as defined by the Fresnel equation and β_i is a phase factor for the incident light. The phase factor is used to calculate interference between light reflected from different layers by taking account of the distance travelled in each layer. As such it depends upon the layer thickness, d_i, the angle of incidence, θ_i, and the refractive index of the previous medium, n_{i-1}, and is defined as

$$\beta_i = \frac{2\pi d_i}{\lambda}\sqrt{n_i^{\,2} - n_{i-1}^{\,2}\cos^2\theta_i} \tag{2-23}$$

For reflection from a number of layers, l, above a substrate a characteristic matrix for the sample, M_S, is derived through multiplication of the characteristic matrices for each layer

$$M_S = \begin{bmatrix} C_1 & C_2 \\ C_3 & C_4 \end{bmatrix} = M_l \times M_{l-1} \ldots \times M_2 \times M_1 \tag{2-24}$$

where C denotes a matrix element in the characteristic matrix of the sample. This matrix multiplication is well suited to computer calculation and the reflectivity, R, from the sample may be calculated as

$$R = \frac{\left(n_0 C_1 - n_s C_4\right)^2 + \left(n_0 n_s C_2 - C_3\right)^2}{\left(n_0 C_1 + n_s C_4\right)^2 + \left(n_0 n_s C_2 + C_3\right)^2} \tag{2-25}$$

where n_0 and n_s are the refractive indices of the medium above the sample and the substrate respectively. This matrix multiplication calculation is frequently used in the fitting of both X-ray and neutron reflectometry data and is the model used in the reflectometry fitting program Motofit used in this work.[10] In the case of reflectometry data it is noted that comparatively small errors for low Q data points, due to a high number of counts, may dominate a least squares analysis of the data modeling leading to incorrect analysis at higher Q.

For small angle scattering data, on the other hand, data modeling requires the definition of a three dimensional particle shape for modeling of the form factor, *P(Q)*, and definition of interparticle interactions to model the structure factor, *S(Q)*. The form factor models the three dimensional geometry and size range of the particles in solution and may, in the case of polydisperse spheres, be given by

$$\left\langle V \right\rangle = \frac{4\pi}{3}\left\langle r^3 \right\rangle \tag{2-26}$$

where $\langle V \rangle$ is the average volume and $\langle r^3 \rangle$ is, in turn, given by

$$\left\langle r^3 \right\rangle = \frac{\left(z+3\right)\left(z+2\right)}{\left(z+1\right)}\left\langle R \right\rangle^3 \tag{2-27}$$

in which R is the total radius of the particle and z is a width parameter describing the particle size distribution as below. Additionally, a similar calculation for the form factor may be used when describing and core – shell particle in which case R is the combined radius given by the core radius and shell thickness.

When considering a range of particle sizes in solution the two most commonly used distributions for polydispersity considerations are the Gaussian distribution and the Schulz distribution, an example of which is shown in *Figure 2-17*, with the latter of these two being the most relevant to this work. As larger particles scatter more than small particles they are more noticeable in small angle scattering and this is reflected in the Schulz distribution, used in this work, shown below:

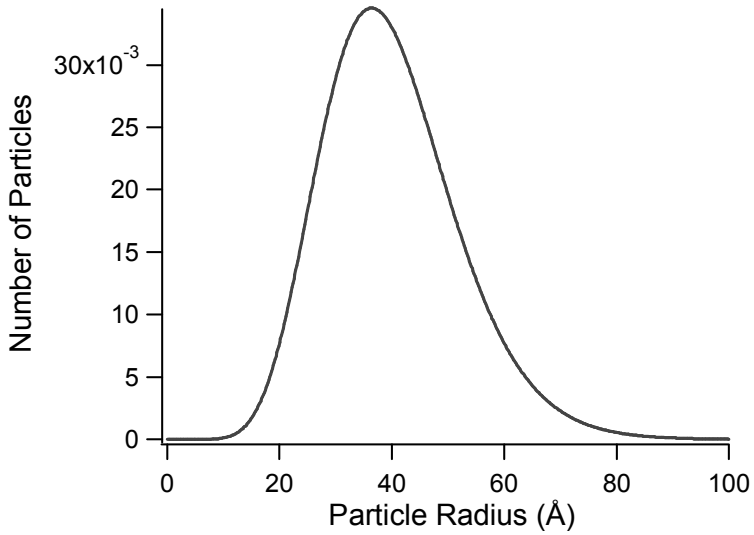

Figure 2-17 : Shultz distribution for polydisperse spheres with a mean radius of 40Å and a polydispersity of 0.2.

In the Schulz distribution the probability of a particle of radius a is given by $f(a)$ such that[11]

$$f(a) = (z+1)^{z+1}\left(\frac{a}{\bar{a}}\right)^{z} \frac{e^{-(z+1)\frac{a}{\bar{a}}}}{\bar{a}(z+1)} \tag{2-28}$$

where, $\bar{a}$ is the average radius, and z is the width parameter related to the variance, σ^2, of the distribution by

$$z = \frac{1-\left(\frac{\sigma}{\bar{a}}\right)^2}{\left(\frac{\sigma}{\bar{a}}\right)^2} \tag{2-29}$$

In addition to the effects of the particle shape and varied size range that are considered in terms of the form factor the presence of interactions between the particles must be considered for their influence on the distribution of scattering species and the resulting scattering pattern. The simplest model for the structure factor is that of a hard sphere model that assumes the particles in solution do not interact other than to provide physical exclusion to the area they occupy in solution. Although simple this model is sufficient for dilute systems in which there are weak interparticle interactions. Alternatively an assumption may be made that there are no interparticle interactions at all and that $S(Q) = 1$.

Once models have been settled upon for the form factor and the structure factor a calculation of the theoretical small angle scattering profile may be undertaken using Equation (13), see § 2.1.2 and *Figure 2-15*. This model may then undergo refinement, typically using a least squares analysis, to find the closest match between theoretical and experimental scattering profiles.

2.1.4 The Brewster Angle

Light is known to have both a magnetic and an electric component, perpendicular to each other, and in unpolarised light these components may be of any orientation with respect to the direction of travel. The Brewster Angle, also referred to as the polarisation angle, θ_P, is the angle at which only light with an electric vector perpendicular to the plane of incidence is reflected, as shown in *Figure 2-18* in which only the electric vector of the light is shown.[12,13] This selective reflection of the incident light means that plane polarisation occurs as light with an electric vector not perpendicular to the plane of incidence is refracted.

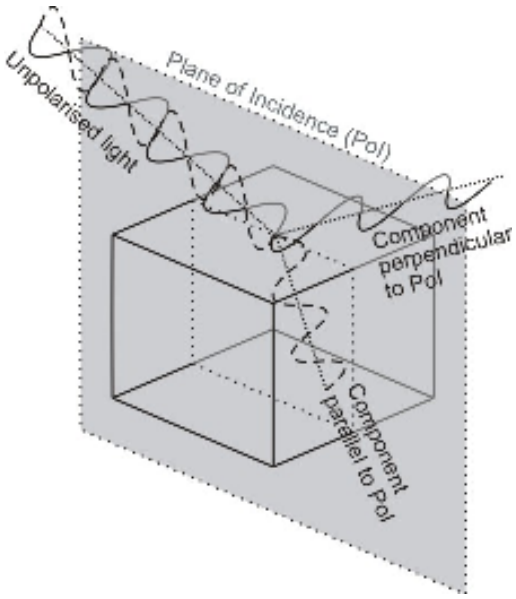

Figure 2-18 : Diagram of polarization by reflection at the Brewster Angle.

The condition at which polarization by reflection occurs is given by

$$\theta_P + \theta_t = 90° \text{ or } \theta_t = 90° - \theta_P \tag{2-30}$$

where θ_P is the polarization angle and θ_t is the angle of transmission or refraction. It is possible to combine this equation with Snell's law, shown in Equation 4, to give

$$n_i \sin\theta_P = n_t \sin(90° - \theta_P) \tag{2-31}$$

where n_i and n_t are the refractive indices of the incident and transmission media respectively. Given that the functions of *cos* and *sin* are 90° out of phase it is possible to straightforwardly rearrange Equation 2-31 to give the familiar form of Brewster's Law, that

$$\tan\theta_P = \frac{n_t}{n_i} \tag{2-32}$$

The phenomenon of plane polarization has led to the use of the Brewster Angle in a number of devices such as Brewster windows for lasers that transmit a specific polarisation of light.

However, if the incident light is already plane polarised all incident light will either be reflected or refracted depending on the orientation of the electric vector. It is also noted from Brewster's Law that the polarization angle is dependent upon the refractive indices of the media involved and, therefore, that θ_p changes with changes in either the incident of transmission refractive index. It is this knowledge that has led to the examination of surfaces using Brewster Angle Microscopy (BAM), a technique developed in the 1990's.[14]

If plane polarized light is incident upon a sample at the Brewster angle such that no reflection occurs, a change in the refractive index of the sample leads to a change in the polarization angle and reflection begins to occur as the incident angle and polarization angles diverge. Thus changes in the sample media or the development of an interfacial layer may be observed and it is possible to distinguish between different areas of a sample with micrometer resolution. Both local and global changes such as the formation of monolayers or films and phase separation may be followed and imaged and the BAM technique has seen considerable use in research since its development.[15,16]

2.1.5 Electron Microscopy

Light microscopy has a resolution that is ultimately limited by wavelength. Visible light has a wavelength of hundreds of nanometres while shorter wavelengths frequently suffer great absorption or, as in the case of X-rays, are too weakly interacting to allow focussing and imaging. A way that this may be overcome arises from the hypothesis that all moving particles have an associated wave put forward by De Broglie in the 1920s and described as

$$\lambda = \frac{h}{mv}\sqrt{1-\frac{v^2}{c^2}}$$

where λ is the wavelength, h is Plank's constant, m is the mass of the particle, v is the velocity of the particle and c is the speed of light.

A beam of electrons with a wavelength less than a nanometre may be used to generate a considerably magnified image in a similar manner to light microscopy but

with greater magnification and depth of field.[17] The first electron microscope was developed in the 1930's and scanning electron microscopes (SEM) and transmission electron microscopes (TEM) are in frequent use today.

Scanning electron microscopy uses the scattering of secondary electrons from a sample to produce an image and this properly termed secondary electron imaging is the most commonly used SEM technique. Electrons in a beam incident upon the sample interact with weakly bound electrons of atoms in the sample and undergo inelastic scattering that may leave them with greatly reduced energy. They are then collected by using a high positive potential to deflect the scattered electrons to a scintillator and photomultiplier to produce a measurable signal. However, secondary electrons can also be produced in scattering events with the sample chamber walls and other area away from the sample. Collection of electrons from such scattering results in background noise during imaging and is a factor limiting the resolution.

Transmission electron microscopy offers greater resolution and magnification than SEM but is restricted to examining thin samples as electrons are passed through the sample, as shown in TEM schematic in *Figure 2-19*.

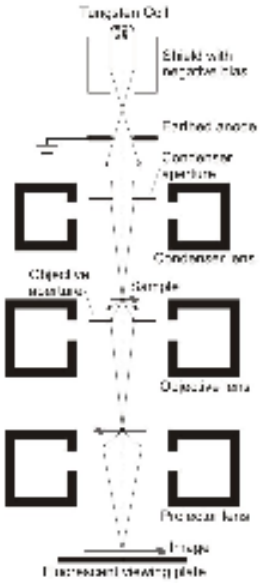

Figure 2-19[1] : Schematic diagram of a transmission electron microscope

[1] Figure based upon, and redrawn from, 2004 lecture notes of optical and electron microscopy course at the Research School of Biological Sciences (RSBS), Australian National University.

In a typical TEM, a tungsten hairpin wire filament within a shield that carries a high negative potential acts as a source of electrons as they are drawn from the heated filament by the potential of the shield. A largely unfocused beam of electrons then passes out of the shield and through a grounded anode. Many electrons are lost at this point due to collisions with the walls or exclusion by the condenser aperture, an adjustable opening that allows only a narrow beam of electrons to pass through. Concurrently the condenser lens provides beam focusing through the use of a magnetic field and can control the illumination of the sample by focusing a greater or lesser number of electrons through the aperture.

Electrons then reach the sample where they may be scattered, refracted or diffracted although in the case of TEM electrons passing through the sample are of interest. In this case an objective lens acts to exclude diffracted and widely scattered electrons. The objective lens then produces a magnified image of the sample with one or more projector lenses subsequently further enlarging the image to achieve very high magnification. The final image is typically viewed on a fluorescent screen or may be recorded with either a photographic plate or CCD camera.

The attainment of a magnified image of the sample represents only one of a range of observations that may be made using transmission electron microscopy. Periodic structure in a sample may be observed in an electron diffraction pattern and regions of different crystal orientation may be observed in a dark field image. These measurements involve moving or removing the objective aperture to allow diffracted electrons to be observed rather than being excluded.

Additionally, the electron beam used in electron microscopy may be used for elemental analysis of a sample using the electron probe microanalysis (EPMA) technique. This technique takes advantage of the fact that incoming electrons in the beam may interact with an inner shell electron in an atom of the sample and eject it from the atom as shown in *Figure 2-20*. The now ionised atom is left in an excited state and a higher shell electron drops down to fill the inner vacancy emitting an X-ray as it loses energy in the process.

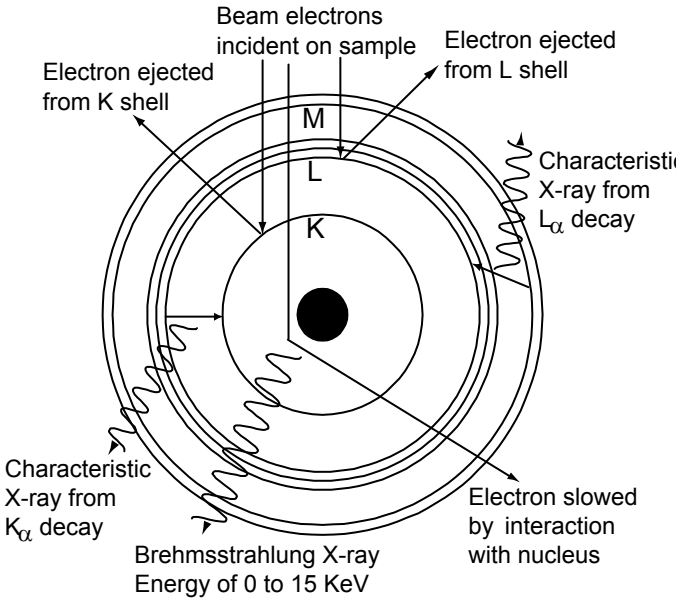

Figure 2-20[2] : Diagram of X-ray generation during EPMA

The energy of this emitted X-ray is characteristic to each electron transition and therefore characteristic to each element, allowing for the elemental analysis of a sample. Qualitative EPMA is a relatively straightforward process of observing the characteristic X-ray that are produced from a given region of a sample and therefore which elements are present. Quantitative measurements are also possible however they require a precise experimental setup and the use of a known standard of a known composition as close to that of the sample as possible. Thus quantitative measurements of new and unknown materials are problematic.

2.1.6 Nitrogen Adsorption

In 1777 it was noted that charcoal releases considerable volumes of gas when heated in a reversible process that is now understood in terms of adsorption. By the mid 19th Century it was becoming understood that surface area and porosity both play an important role in such processes and today the isothermic adsorption of gases, particularly nitrogen at 77 K, is the most commonly used technique for the determination of surface area and porosity for powdered materials and is detailed thoroughly

[2] Figure is based upon, and redrawn from, a series of figures in 2004 lecture notes of optical and electron microscopy course at the Research School of Biological Sciences (RSBS), Australian National University

elsewhere.[18] Adsorption, defined as the enrichment or depletion of an interfacial layer, is understood to be distinct from *absorption* in which atoms of gas penetrate into the mass of the solid.[19] As an adsorbate gas remains outside the physical mass of a sample the accurate measurement of the amount of gas adsorped to a sample can allow the calculation of surface area.

Simple adsorption, so called as it does not include polarity or electrostatic considerations, is understood to occur through dispersion forces. Fluctuations in the electron density of an atom can introduce a dipole in neighbouring atoms generating an attractive force. As the atoms near each other this is balanced by a repulsive force as the electron clouds begin to overlap giving a description of forces in adsorption as the Lennard-Jones potential in which a negative force is understood to be attractive[20]

$$\varepsilon(r) = -Cr^{-6} + Br^{-12} \tag{2-33}$$

Here C denoted an atom, r the radius, ε the force and B is a constant. It is readily observed that the forces in adsorption are highly distance dependant.

For ease of calculation it is useful to know the number of moles of gas adsorped to a sample and it is understood that the quantity of gas taken up by a sample is proportional to the mass of sample material, temperature, pressure and the nature of both the solid and the gas as shown by

$$n \propto P, T, gas, solid \tag{2-34}$$

where n is the number of moles of gas adsorped, T is the temperature and P is the pressure. If a specific gas is adsorped onto a particular sample under constant temperature a relationship for isothermal gas adsorption may be written as

$$n = f(p)_T \tag{2-35}$$

Furthermore, if the temperature is equal to or below the critical temperature of the gas the relationship may be written in terms of $p°$, the saturation vapor pressure, as

$$n = f(\frac{p}{p^\circ})_T \tag{2-36}$$

The equations, (2-35) and (2-36), define an adsorption isotherm, a relationship at constant temperature between the amount of gas adsorbed and the pressure. Although these relationships are understood in terms of the number of moles of gas adsorbed for practical measurement this may be expressed in terms of a mass or volume of gas, measured by monitoring the mass of a sample on a microbalance or monitoring a change in pressure.

It may be understood that if a monolayer of an adsorbate condenses to cover the surface of a sample, and the number of moles of gas in the monolayer, n_m, is known, the surface area may be calculated straightforwardly by the equation

$$A = n_m a_m N_A \tag{2-37}$$

where A is the surface area, a_m is the area of a single molecule of the adsorbate and N_A is Avogadro's number. Alternatively, this relationship may be expressed in terms of a measured quantity, such as the volume of adsorbate, by a simple conversion

$$A = \frac{v_m a_m N_A}{22414} \tag{2-38}$$

where v_m is the volume of adsorbed gas in the monolayer and 22414 is the volume of one mole of an ideal gas under STP conditions in mL. Division by the sample mass yields the surface area per gram for the material, typically expressed in square metres per gram, m^2g^{-1}.

Although the possibility of using the adsorption of gases to measure a surface area has been understood for many years and theoretical models continue to be advanced it is not yet possible to derive an accurate adsorption isotherm from modelling alone.[18] Arguably the most influential theory for the calculation of a surface area for adsorption was published by Brunauer, Emmett and Teller (BET) in 1938.[21] Despite being somewhat over simplified attempts to further this theory have been largely unsuccessful thus far and

the BET calculation remains the most widely used method of surface area calculation. For the such calculations a convenient form of the BET equation may be written as

$$\frac{\frac{p}{p^\circ}}{v(1-\frac{p}{p^\circ})} = \frac{1}{v_m} + \frac{c-1}{v_m c}(\frac{p}{p^\circ}) \qquad (2\text{-}39)$$

where $\frac{p}{p^\circ}$ is the relative pressure, v is the volume of absorbed gas, v_m is the volume of gas in a monolayer and c is a constant relating to the strength of the interaction between the adsorbate and adsorbtive. By plotting the adsorbed volume and relative pressure as in Equation (2-39) it is possible to calculate both v_m and c by solving the simultaneous equations for the slope and intercept shown below

$$slope = \frac{c-1}{v_m c} \text{ and } intercept = \frac{1}{v_m c} \qquad (2\text{-}40)$$

Using these equations it is readily shown, where s is the slope and i is the intercept, that

$$c = \frac{s}{i} + 1 \text{ and } v_m = \frac{1}{s+i} \qquad (2\text{-}41)$$

from which the surface area may be calculated as shown in Equation 2-38.

However, the simplifications used in generating the BET equation mean that the equation is only valid in the relative pressure range of $0.05 < p < 0.3$ and for adsorption isotherms showing a point of inflection at low relative pressure. If used to calculate an adsorption isotherm the BET equation produces a point of inflection at low relative pressure corresponding to the completion of an adsorbed monolayer. That a monolayer is completed prior to formation of any multilayer regions is one assumption of the BET equation and in samples where this is not the case the BET equation cannot be applied.[18]

More precisely the BET equation may be applied to Type II and Type IV isotherms corresponding to non-porous and mesoporous solids respectively. Since gas adsorption began to be used, many thousands of adsorption isotherms have been collected

and the vast majority of them may be classified into one of five different classes designated in 1940 and shown in *Figure 2-21*.[18,22] Type I isotherms are characteristic of microporosity, Type II and Type IV are characteristic of non-porous and mesoporous materials respectively and Type III and Type V isotherms are special cases corresponding to non-porous and porous materials with particularly weak interactions between the adsorbate and adsorptive.

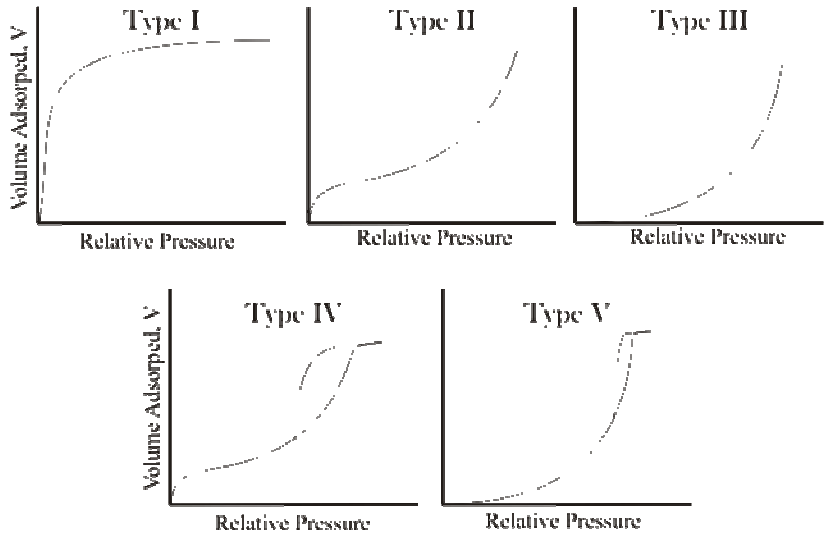

Figure 2-21 : Types of adsorption isotherm as classified in 1938. (After Brunauer[22]*)*

Hysteresis effects characteristic of Type IV isotherms vary between different samples but are due to reduced desorption at a given partial pressure compared with increased uptake at the same partial pressure due to capillary condensation. It is stated that the vapour pressure over a concave meniscus, such as that growing in a pore during adsorption, is less than the saturation vapour pressure, $p°$. Therefore liquid may condense at the meniscus of a pore when the pressure, p, is less than $p°$ and the relative pressure is less than one.

If, for simplification, the assumption is made that the contact angle of the adsorbing gas/liquid with the wall of pore is 0° the liquid meniscus will be hemispherical and the radius of curvature of the meniscus, r_m, is equal to the pore radius. This assumption allows the definition of the Kelvin equation

$$\ln \frac{p}{p^\circ} = \frac{-2\gamma V_L}{RT} \times \frac{1}{r_m} \tag{2-42}$$

where γ is the surface tension of the liquid, V_L is the molecular volume of the liquid, T is the temperature and R is a constant. This equation allows the calculation of the relative pressure at which capillary condensation will occur for a given pore size. It is also necessary to add the thickness of a monolayer to r_m when calculating pore size as capillary condensation does not occur until a monolayer has formed and the pores are therefore narrower during condensation.

Comparison of the amount of gas adsorbed at different relative pressures to the pore size corresponding to these pressures can then give an indication of a pore size distribution, the relative number of pores of different sizes, in a sample. Such calculations may be carried out in a number of ways but use of the Kelvin equation is the most common method for determination of pore size distribution. It is generally taken that the Kelvin equation is valid for pore sizes in the range of 10 – 250 Å although these limits are largely experimental limits. Few pores less than 10 Å, that may be considered mesoporous, have been observed and measurement of the pressure differences corresponding to different pore sizes greater than 250 Å are difficult to measure with sufficient accuracy. Unfortunately the Kelvin equation is subject to considerable inaccuracies and must be used with an acknowledgement of its limitations.

It is understood that for small pores the attractive forces between the gas will be higher due the close proximity of the pore walls, an interaction not accounted for in the Kelvin equation resulting in underestimated pore sizes. Studies have suggested that this error begins to appear for pore sizes less than 500 Å becoming more pronounced with small pores. This error has been calculated to be 10% for 100 Å and 30% by the time 20 Å pores are considered suggesting pores calculated to be of this size are actually 110 Å and 26 Å respectively.

Additionally, although it is predicted theoretically that a pore size distribution will be the same when calculated from either the adsorption or desorption branch on an isotherm this is rarely observed experimentally. In particular, the use of the desorption branch is likely to suffer error due to pore blocking and tensile strength effects. Pore

blocking arises when the diverse pores of a particle are interconnected but are not all directly open to the surface. If a larger pore is connected to the surface via a smaller pore the liquid in the large pore will be prevented from desorping until desorption occurs in the small pore at a lower partial pressure. The increased desorption at this lower partial pressure will be interpreted as a large number of pores corresponding to the smaller size and will create an artificially narrow pore size distribution.

The tensile strength error, on the other hand, arises from the finite tensile strength of the adsorbed liquid. As the partial pressure drops below unity tension is created across the meniscus of the condensed liquid in the pores. As the tension increases it eventually exceeds the tensile strength of the liquid that is then pulled apart into the gas phase. If not considered carefully this rapid desorption will be interpreted as a large number of pores of a size corresponding to the partial pressure at which the tensile strength is exceeded. For nitrogen, the most commonly used adsorbate, the tensile strength is exceeded at a partial pressure of roughly 0.40 corresponding to roughly 17 Å pores although this varies slightly for different adsorbants.

These effects provide a lower limit to the application of the Kelvin equation of approximately 17Å. Given that errors arising from pore blocking and tensile strength are of greater influence when considering the desorption branch of an isotherm it is recommended that the adsorption branch of an isotherm is used for the calculation of a pore size distribution.[18] This is in spite of the fact that the use of the desorption branch remains the most common in the literature.

2.1.7 Thermogravimetric Analysis

Thermogravimetric analysis (TGA) is an analytical technique that may be used to measure the thermal stability and composition of a sample by precisely monitoring the mass of a sample under increasing temperature. Given the limited use of TGA in the present work a brief overview only is provided here, however, detailed descriptions of TGA measurement are readily available from research institutions, textbooks and publications.[23-25] As a sample is heated a temperature will be reached at which solvent, e.g. water, in the sample is removed and at higher temperatures samples may partially or completely decompose as organics are burnt or a structure breaks down. By carefully

monitoring the mass of the sample during such decompositions it is possible to obtain a composition of a sample, in terms of relative mass. Common examples of such measurements are solvent content, organic content and decomposition temperature which may be measured in this manner.

A range of different experimental set-ups may be used for TGA measurements although perhaps the largest distinction is between experiments using horizontal balances and those using vertical balances. If a horizontal balance is used a sample is placed on one side of a balance and a reference is placed on the other. This allows additional measurements such as a comparison of temperature between the sample and reference and differential scanning calorimetry to be conducted. A vertical balance, in comparison uses a pan suspended from a balance arm to hold a sample and is a more straightforward, if more restricted, method of measurement. In both cases isolation from vibrations is important for accurate measurement given the sensitivity of the balances.

The rate of temperature increase is also of great importance in collecting accurate data as limited rate of heat transfer may create a difference between the programmed temperature and sample temperature. Additional errors may occur if rapid decomposition leads to a portion of a sample spitting out of the balance pan as this generates a misleading loss of mass. A heating rate of 5 °C/min may be considered a compromise between accuracy and reasonable measurement time, however slower rates allow greater accuracy. It is relatively common for analysis to be conducted in a low oxygen atmosphere, such as nitrogen or argon, to reduce the rate of decomposition for more accurate results.

2.2 Methods of Analysis

2.2.1 Neutron Reflectometry

Neutron reflectometry was performed at the ISIS pulsed spallation neutron source facility that is part of the Rutherford Appleton Laboratories. The energy dispersive reflectometer instruments SURF and CRISP, described in detail elsewhere and shown schematically in *Figure 2-22*, were used to conduct reflectometry experiments.[1,26,27] Both instruments have been established for the study of surfaces using specular neutron reflectivity and the SURF instrument has been specifically optimised for the study of liquid interfaces. The instruments are normally operated using 50 Hz pulses of neutrons in the 0.55 – 6.8 Å wavelength range to give a q range of 0.048 – 0.60 $Å^{-1}$. For both instruments a hydrogen moderator at 25 K is used to cool the neutrons in each pulse prior to travel down a flight path defined by four slits, two before and two after the sample. An optical laser is used as an aid during alignment of the sample height that is controlled on a sample stage with 0.05mm accuracy. The detectors in each case are a He^3 gas detector in which the destructive interactions of neutrons with the gas are observed.

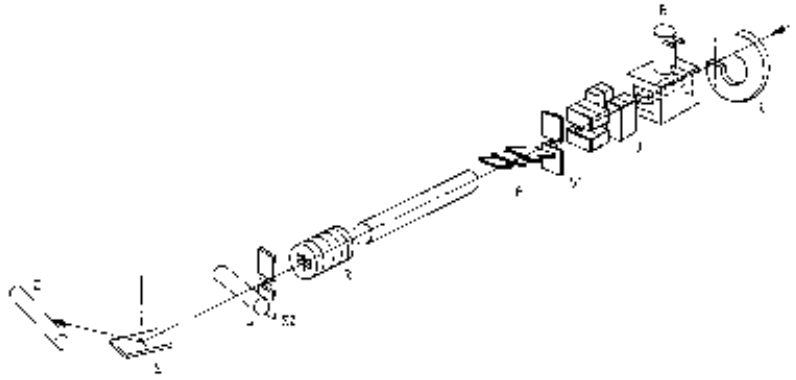

Figure 2-22[3] : Schematic diagram of the CRISP reflector at ISIS. c, chopper; B, beryllium filter; J, coarse collimating jaws; s2, collimating slit; F, frame overlap mirrors; R, downstream collimation; M, neutron beam monitor; s, sample; D, detector.

[3] Figure reproduced from Penfold, J.; Ward, R. C.; Williams, W. G. *Journal of Physics E-scientific Instruments* **1987**, *20*, 1411-1417 with the permission of IOP Publishing LTD; Dirac House; BS1 6BE.

For work on both instruments, scattering at the air-solution interface was performed by pouring a film precursor solution into a 4 x 15 cm PTFE trough to provide a meniscus above the edge of the trough. Reflection experiments from the interface were performed at 25°C, controlled by a Eurotherm controller, and a measured 35-45% relative humidity. In order to reduce the incoherent background air contrast matched ethanol (ACME) was used in the film solutions, prepared by addition of deuterated (33% wt. C_2H_5OD) and hydrogenated ethanol to produce a scattering length density (SLD) of zero. To aid in subsequent modeling of results a second solvent contrast, 3.26 x10^{-6} Å^{-2} using 60% wt. C_2D_5OD, was used to exceed the SLD of titanium dioxide, 2.59 x10^{-6} Å^{-2}.

2.2.2 Small Angle Neutron Scattering

Small angle neutron scattering (SANS) experiments were performed using the D11 instrument at the ILL in Grenoble, France.[26,28] D11 is a long, pinhole geometry instrument for small angle neutron scattering (SANS), designed for the study of large scale structures and suitable for observing particle development in solution. The ILL high flux reactor is the source of neutrons and a helical slot monochromator is used to reduce the polychromatic beam to a wavelength range of 4.5 – 40 Å prior to collimation. Neutron detection is via a 64 x 64 cm CERCA 3He multi-detector mounted on a moveable trolley within an evacuated tube to increase the accessible angular range. The sample to detector distance may thereby be varied to give an accessible Q_z range of 5 x 10^{-4} to 0.44 Å^{-1}. The layout of the D11 SANS instrument is shown in *Figure 2-23*.

Time resolved SANS experiments were performed with the use of 2 minute scans and detector positions of 1.1 m and 5 m giving Q_z ranges of 0.05 – 0.33 Å^{-1} and 0.01 – 0.07 Å^{-1} respectively. Reaction solutions were pipetted into 1 cm wide, 1 mm path length quartz cells and mounted on the D11 beamline. Experiments were conducted using 100% and 70% deuterated ethanol solvent in the reaction solutions to provide multiple contrasts for subsequent data modelling by simultaneous fitting.

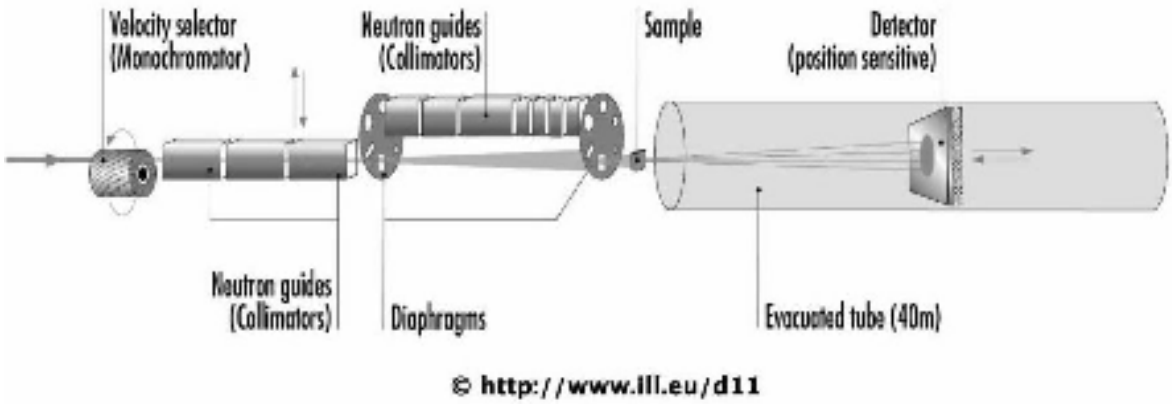

Figure 2-23[4] *: Schematic diagram of the D11 SANS instrument at the ILL.*

Detector distances of 1.1m, 5m and 10m were used in collecting SANS patterns from developed film material, removed from the air-solution interface and calcined to remove the surfactant phase and from surfactant solutions in ethanol. A range of surfactant solutions utilised a range of ethanol solvents of different deuterium percentages in order to establish the scattering length density of the surfactant. These experiments were performed using deuterated ethanol to provide contrast with the film material. In these experiments powdered film material was placed in sample cells that were subsequently filled with ethanol and placed on the beamline.

2.2.3 X-ray Reflectometry

X-ray reflectometry experiments were performed in the Department of Chemistry at the University of Bath and on the ID10B Tröika II beamline at the European Synchrotron Radiation Facility in Grenoble, France, a picture of which is shown in *Figure 2-24*.[29] The ID10B beamline is a high-brilliance undulator beamline at the ESRF designed for high resolution X-ray scattering and surface diffraction.[30] ID10B uses photons within the energy range of 8 keV and 22.2 keV provided by a diamond double-crystal monochromator. Study of thin film formation at the air-liquid interface was

[4] Figure reproduced from www.ill.eu/d11 with the permission of the Institut Laue-Langevin; BP 1566, rue Jules Horowitz; 38042 Grenoble Cedex 9; France

performed using time-resolved X-ray reflectometry as the flux of the synchrotron radiation was sufficient to allow short scans to be collected that maintained accuracy.

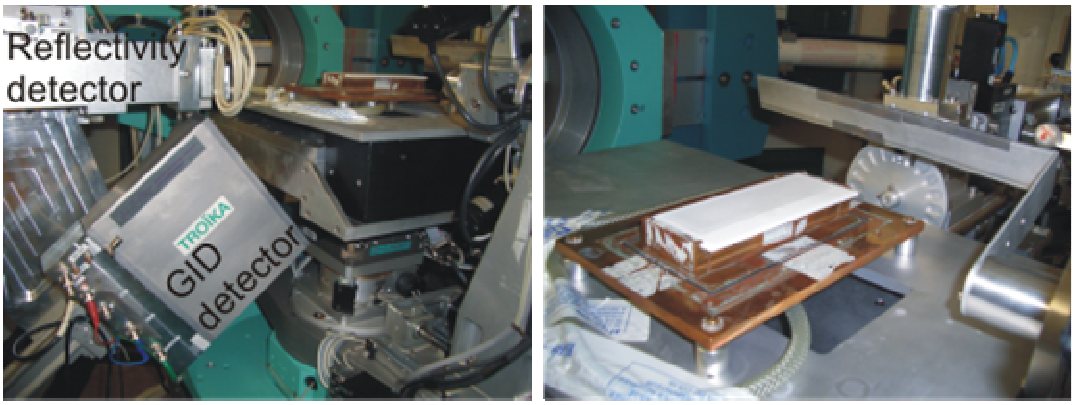

Figure 2-24 : Pictures of the IB10B Tröika II beamline at the ESRF showing, (a), the detectors and, (b), the sample environment.

Time-resolved experiments are able to cover a Q_z range of 0.085 – 0.25 Å^{-1} by using a linear detector with a vertical orientation to collect data over a range of reflected angles as described in the literature.[31] X-ray reflectometry and grazing-incidence diffraction experiments were performed upon developed materials. X-ray reflectometry patterns were collected over a Q_z range of 0.0014 – 0.3535 Å^{-1} and grazing-incidence diffraction patterns were collected over a Q_z range of 0.0014 – 0.89 Å^{-1} and a Q_{xy} range of 0 – 0.2 Å^{-1}. A linear detector with 1024 channels and with a vertical alignment was used to collect data during grazing-incidence diffraction experiments and was rotated incrementally in *xy* plane as shown in *Figure 2-25*.

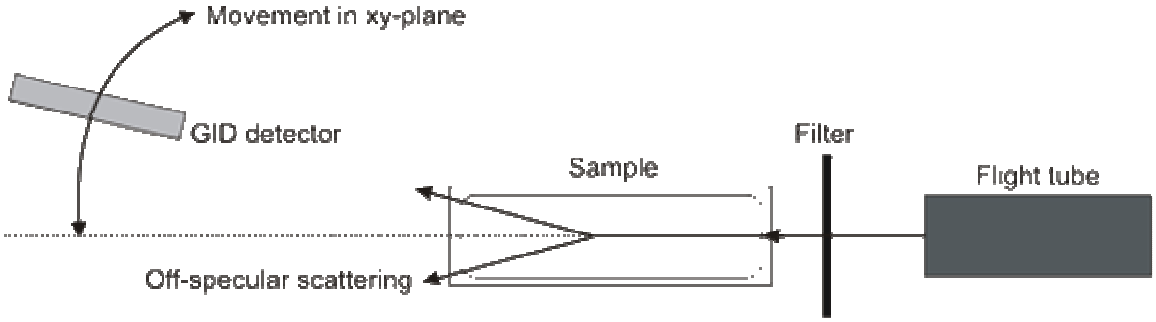

Figure 2-25 : Diagram of how off-specular scattering is collected on the ID10B beamline

Experiments at the air-solution interface were performed on the ID10B beamline by pouring a film preparation solution into a 4 x 15 cm PTFE trough identical to those used for neutron reflectivity experiments. X-ray reflection experiments from the interface were performed at 25°C, controlled by a water bath, and at 22 - 24% measured relative humidity. Development of films at the air-solution interface was observed using time-resolved X-ray reflectometry with a time resolution of less than one minute, varied depending upon the sample being studied. Angle dispersive X-ray reflectometry and grazing-incidence diffraction experiments were performed on fully developed films at the air-solution interface to observe the final film structure.

Also used, the reflectometer at the University of Bath is an energy dispersive instrument that uses a series of fixed geometries to collect a scattering profile over a Q range of 0.35 – 1 $Å^{-1}$, [32] a schematic of which is shown below in *Figure 2-26*. The X-ray source is a tungsten anode tube and a spectrum of Bremsstrahlung radiation is filtered by a Ni foil as the incident radiation. The path from the source to the Ge, Li detector is defined by four Huber X-ray slits, connected by two tubes that may be raised or lowered by actuators to change the incident and reflected angles. The height of the sample is established by a manually adjusted sample stage.

Experiments at the air-solution interface performed at the University of Bath by pouring a film preparation solution into a 4 x 15 cm PTFE trough as at the ID10B beamline. Experiments were performed at temperatures and humidity ranges measured to be 21 - 23°C and 22 - 24% respectively.

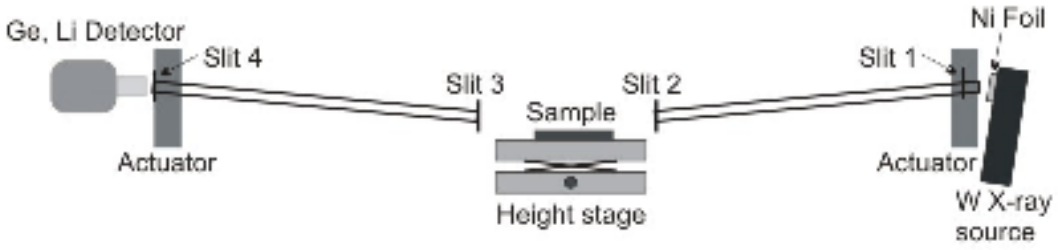

Figure 2-26 : The energy dispersive reflectometer at the University of Bath

Dip-coated films were studied at the University of Bath by aligning the reflectometer with a clean microscope slide placed in the beam footprint of the sample

position and obtaining a background profile. A microscope slide upon which a dip-coated film had been deposited was then placed in the sample position and the alignment confirmed before collecting a reflectivity profile.

2.2.4 Small Angle X-ray Scattering

An Anton Paar SAXSess small/wide angle X-ray scattering instrument with a measurable q range of 0.077 – 27.0 nm^{-1} was used to perform small angle X-ray scattering measurements. The X-ray source of the instrument is a long-fine focus sealed copper tube source with line focus operated at 40 kV and 50 mA. An elliptical focusing mirror is used to further enhance the flux. Collimation is achieved using a block collimator with a roughness of less than 0.14 μm/cm and the flight path from source to detector is in a chamber evacuated to below 5 mbar. Reusable 66 x 200 mm image plates with a 42.3 μm^2 pixel size are used for X-ray detection using the excitation of Europium in the image plate followed by emission detected by a Perkin Elmer cyclone reader using OptiQuant software.

SAXS profiles were generated using the SAXSquant 1.01 program and processing subsequent to measurement, including background subtraction, was performed using the Primary Data Handling (PDH) program. Desmearing from a line to a point source was performed using custom software provided by Anton Paar.

Solid films have been examined using two different sample preparation methods. Films produced on microscope slide substrates were scraped from the substrate to obtain a powder while films produced at the air-solution interface and removed using a plastic mesh were dried before cutting pieces of the film from the mesh. In both cases the film material was mounted in a sample holder between two pieces of sellotape and held in place by two copper plates.

Liquid samples of surfactants in solution have been examined by filling a 100 μL quartz capillary with solutions of surfactant in ethanol after flushing briefly with the sample solution. The capillary was then mounted in the temperature controlled sample holder provided. In both cases the temperature was maintained at 25°C.

2.2.5 Data Modelling

All data modelling has been conducted within the Wavemetrics scientific graphing, data manipulation and image processing program Igor Pro Version 6.0.2.4. The program is compatible with both Windows and Macintosh systems and is widely used in the research community for the modelling of scattering data.

X-ray and neutron reflectometry data have been modelled using the Motofit program written for the modelling of both X-ray and neutron data in 2006.[10] The program uses a least squares analysis for the assessment of the fit of a model to experimental data. In all cases the Abeles matrix modelling of method has been used for the modelling of reflectometry data.

Small angle X-ray and neutron scattering data have been modelled using Version 3 of the models available from the NIST Centre for Neutron Research (NCNR) website.[33,34] These routines provide models of form factor and structure factor for a wide range of shapes and interparticle interactions. For small angle scattering, the most frequently used model in this work is that entitled "*PolyCoreShellRatio*" that models polydisperse spherical core-shell particles and in which the ratio $R_{core}/R_{core+shell}$ is held to a constant. The polydispersity of the core size follows a Schulz distribution, see § 2.1.3, and the core radius : shell thickness ratio is maintained.

Models for oblate and prolate core-shell ellipsoids, cylinders and lamellar layers were also used in attempting to fit small angle scattering data and were modified such that the scattering length density of the core, shell and solvent were specifically modelled rather than modelling the contrast between them. In all cases the models used a model of hard sphere interparticle interactions as modelling different structure factors was not found to give superior fits to the experimental data.

2.2.6 Brewster Angle Microscopy Measurements

Brewster angle microscopy images were collected at the Department of Chemistry, University of Bath using a Nanofilm Technologies (NFT) I-Elli 2000 Imaging Ellipsometer used as a Brewster angle microscope. The I-Elli 2000 uses a frequency

doubled NdYAG diode laser with a wavelength of 532nm.[35] The angle of incidence and angle of reflection can be adjusted with an angular range of 45º to 80º and with an accuracy of 0.01º. The BAM image is viewed on a computer using a digital CCD camera with a high grade 768 x 572 pixel sensor featuring a lateral resolution of 2 μm. An automated system is used for image collection to remove the complication that a limited strip of the image is in focus that arises from the use of an inclined observation angle.

Film preparation solutions were observed in a live image as films development occurred and records of the time of film formation were taken manually using the live image to observe the point of film formation. Additionally, images of the reaction solutions before, during and after film formation were collected to observe a transition at the interface. Samples were prepared for BAM imaging by pouring a reaction solution into a 6 cm diameter Petri dish that was placed on an antivibration stage in the BAM field of view.

Given the surface area of the Petri dish was 28 cm^2 and that of the PTFE trough used for reflectometry experiments was 60 cm^2 the surface area : volume ratio is doubled in the BAM experiments which may effect film formation time. However, trends in formation time are expected to be comparable. In all BAM experiments, solutions were left in situ to continue development undisturbed, however, the samples were moved horizontally in some instances in order to confirm that the appearance of the interface was uniform over the whole sample.

Additionally, a separate series of experiments were conducted to establish the mass of solvent lost prior to film formation. In this case the Petri dish and solution were removed to a balance, accurate to four significant figures, at five minute intervals to observe the mass of solution remaining and manual records kept to accompany the BAM observations.

2.2.7 Scanning and Transmission Electron Microscopy

Scanning electron microscopy images were taken at the Centre for Electron Optical Studies at the University of Bath using a Japanese Electron Optics Laboratory JEOL JSM6480LV scanning electron microscope. The JSM6480LV is a modern instrument with a large sample chamber that allowed samples of dip-coated film material

mounted on microscope slides to be studied in situ as the complete microscope slide was mounted in microscope chamber. SEM images were collected with an operating voltage of 20 kV and to prevent charging of the samples they were sputter coated with gold prior to imaging in the SEM.

Additionally, transmission electron microscopy images were also taken at the Centre for Electron Optical Studies at the University of Bath. Images and diffraction patterns were collected using a Japanese Electron Optics Laboratory JEOL 1200 EX transmission electron microscope operated at 120 kV. Instrument settings and images were established using the fluorescent screen of the TEM instrument before final collection using a CCD camera. Electron diffraction patterns were also collected to establish the presence or absence of ordering within the sample film material. In all cases qualitative elemental analysis was performed using electron probe microanalysis to confirm the nature of the material before images were collected.

Samples were prepared for TEM study by scraping calcined film material from a microscope slide substrate using a clean scalpel. The resulting powder was placed in a test tube and dispersed in isopropanol by sonication for one minute. A clean pipette was then used to place a drop of this dispersion onto a carbon film mounted on a copper TEM grid. The dispersion was allowed to dry in air, thereby depositing film material on the TEM grid once the isopropanol had evaporated.

2.2.8 Surface Profilometry

Surface profiles and layer thicknesses of dip-coated films on microscope slide substrates were examined in the Department of Physics at the University of Bath. A Veeco Dektak 6M stylus profilometer with a step height resolution of 1 nm was used in a semi-clean room to minimise sample contamination. The instrument operates by moving the sample beneath the stylus with vertical deflections of the stylus measured with a linear differential transformer (LVDT). Changes in the voltage, due to movement of the stylus, are recorded and calculated to represent a surface profile.[36]

Dip-coated film samples were examined by scratching part of the film from the microscope slide substrate with a clean, dry scalpel to expose but not damage the substrate. Samples were positioned using a microscope and a profile measured over the

scratch with a 76 nm horizontal resolution. Repeated measurements were taken in each case and an average of four results from different areas of the sample was calculated.

2.2.9 Nitrogen Adsorption Measurements

Measurements of the nitrogen adsorption isotherms for powdered, calcined film material were conducted in the Department of Chemical Engineering at the University of Bath. A Micromeritics Accelerated Surface Area and Porosimetry Analyzer (ASAP) 2010 instrument was used for the automated measurement of nitrogen adsorption and desorption from powdered film material at 77 K. The instrument obtains the amount of gas absorbed by measuring a change in pressure and converting this to a volume of gas adsorped per gram of sample for each point collected on the isotherm.

Film samples were prepared by scraping film material from a microscope slide substrate and taking through calcination before placing approximately 0.1 g of the powder in the ASAP 2010 instrument. Material from approximately 30 film samples, made with identical reagent concentrations, was required to provide sufficient material for examination. Samples were degassed under vacuum overnight above 400 °C before measurement. Measurement was performed over a partial pressure cycle of 0 – 1 – 0 in 0.03 increments with an equilibration period of 45 seconds at each partial pressure.

2.2.10 Thermogravimetric Analysis Measurements

Analysis of the solvent content and organic content of film material, recovered from the air-solution interface and dried in air, was undertaken by thermogravimetric analysis using a Perkin Elmer TGA 7 thermogravimetric analyser. The instrument uses a vertical balance accurate to ± 0.005 mg to measure the change in the sample mass during heating, in an electrical furnace, and uses a dual nitrogen gas flows from above and below the sample to reduce the rate of decomposition and remove decomposition products. However, as the instrument was not isolated from vibrations or temperature variations within the laboratory and, as one gas flow regulator was damaged, the measurements cannot be considered fully accurate as an unstable gas flow will create errors in the mass measurement estimated to be 2-4%. A Perkin Elmer TAC 7/DX

thermal analysis controller and Puris software was used for instrument control and data collection in terms of percentage mass and sample temperature.

For both FSO-100 and $PEPEG_{2250}$ templated film material a sample of 1.5 – 3 mg of film material, within the 1 – 5 mg recommend sample size, was used for TGA experiments. FSO-100 – titania film material was recovered onto a microscope slide and allowed to dry in air while $PEPEG_{2250}$ – titania film material was removed from the air-solution interface to a $1cm^2$ plastic mesh to dry. In both cases the recovered film material was allowed to dry in air for 24 hours prior to measurement.

The limited supply of FSO-100 surfactant restricted measurement to a standard concentration, see § 2.3.3, while a range of samples templated by $PEPEG_{2250}$ varying the titania : surfactant molar ratio from 20 to 45 were studied. In all cases the film samples were heated from 25 °C to 600 °C at a heating rate of between 0.75 – 1.0 °C/min depending on the time available for the experiment. Both of these heating rates are expected to provide as accurate a measurement of sample decomposition as possible given the experimental problems detailed above.

2.3 Titanium Dioxide-based Film Synthesis

2.3.1 Materials

SURFACTANTS

The Pluronic surfactant P–123 with structure $H(C_2H_4O)_{20}(C_3H_6O)_{70}(C_2H_4O)_{20}H$, average molecular weight 5750 g/mol,[37] was generously supplied by BASF as a sample and the Pluronic surfactant F–127, $H(C_2H_4O)_{106}(C_3H_6O)_{70}(C_2H_4O)_{106}H$, average molecular weight 12600 g/mol,[38] was purchased from Sigma. The diblock copolymer surfactant polyethylene-poly(ethylene glycol), hereafter referred to as $PEPEG_{2250}$, with the structure $H(C_2H_4)_{20}(C_2H_4O)_{54}H$ and average molecular weight 2939 g/mol was purchased from Aldrich.[39] However, no information was available on the polydispersity of this surfactant.

The partially fluorinated surfactant Zonyl FSO–100 with the structure $F(C_2F_4)_4(C_2H_4O)_9H$, average molecular weight 725 g/mol,[40] was generously supplied by DuPont as free samples and all bottles supplied were from the same synthesis batch. For Zonyl FSO-100 the as-received inhomogeneous surfactant was centrifuged at 11000 rpm and 15 °C for 60 minutes and the golden brown liquid fraction separated for use in film formation. All other surfactants were used as supplied.

INORGANIC PRECURSORS

The inorganic precursor titanium tetrachloride, $TiCl_4$ (99.9% pure), was purchased from Acros Organics. The titanium alkoxides precursors technical grade (80% pure) titanium tetraethoxide, $Ti(OEt)_4$, and reagent grade (97% pure) titanium tetra *n*-butoxide, $Ti(OBu^n)_4$, were both purchased from Aldrich. Reagent grade (98% pure) zinc chloride, $ZnCl_2$, the inorganic precursor for zinc oxide-based film synthesis, was purchased from Sigma. In all cases the reagents were used as supplied.

OTHER REAGENTS

Poly(ethylene glycol), PEG, polymers of molecular weights of 10,000 and 600,000 g/mol were purchased from Aldrich. Absolute AR-grade (99.8% pure)

anhydrous ethanol solvent, C_2H_5OH, and analytical reagent grade (99+% pure) hydrochloric acid, HCl, 37% wt. in H_2O, were purchased from Fisher Scientific. A Milli-Q water purification system was used to produce pure water of resistance 18.2 MΩ/cm for all film preparations.

For neutron scattering experiments deuterated materials were also used. D_1 ethanol, C_2H_5OD and D_6 ethanol, C_2D_5OD, of 99.7% and 99.6% atomic purity respectively were purchased from CDN-Isotopes. Deuterated hydrochloric acid, DCl, 37% wt. in D_2O, of 99.5% atomic purity was purchased from Goss Scientific. Heavy water, D_2O, of 99.9% atomic purity was supplied by Aldrich. Reagents were used as supplied in all cases.

2.3.2 Dip-coated Films for Solar Cells

Dip-coated films were prepared based upon the work of Crepaldi, et. al. using reaction conditions reported in this work to produce film material with hexagonal structure.[41] 0.67 g (0.054 mmol) of Pluronic F-127 was placed in a plastic bottle and 18.43 g (400 mmol) of ethanol added prior to sealing and stirring for 30 minutes. 1.93 g (10.1 mmol) of $TiCl_4$ was then added dropwise and stirring continued until a uniform translucent yellow solution was obtained. Finally 1.80 g (100 mmol) of H_2O was added and stirring continued for 5 minutes to give a clear solution before pouring into a narrow (1 cm) vessel for dip-coating. The mole ratio of reagents used was 0.0054 F-127 : 40 C_2H_5OH : 1 $TiCl_4$: 10 H_2O.

Dip-coating was performed using a computer controlled Nima dip coater, model DSG-75, using microscope slides cleaned with water, Decon 90 and acetone as a substrate. During dip-coating a withdrawal speed of 90 mm/min (as used by Crepaldi et.al.) and at a temperature and relative humidity of 25 °C and 20-30% respectively. As soon as the withdrawal of the substrate from solution was complete each slide was placed in an oven maintained at 60 °C and 55% relative humidity and allowed to dry for 24 hours. The films were then aged for a further 24 hours at both 100 °C and then 130°C in an oven without humidity control before undergoing calcination from 25 – 600 °C with a 1 °C/min rate of temperature increase and maintained at 600 °C for 120 minutes before being allowed to cool naturally. Subsequent coats of film material were applied using the

same experimental procedure outlined above with up to four coats being applied in total. Films were carried through the full experimental procedure for each coating.

Experiments in producing dip-coated films at low temperatures have also been conducted based initially upon the work of Alberius, et. al.[42] For these films 1 g (0.172 mmol) of the Pluronic surfactant P-123 was dissolved in 12 g (260 mmol) of ethanol under stirring. Then an addition of 3.2 g of 37 % wt. HCl (32.5 mmol HCl, 110 mmol H_2O) was made and the solution stirred for 30 seconds before the addition 4.3 g (18.9 mmol) of $Ti(OEt)_4$. The final solution was stirred for a further minute before transferring into the narrow vessel for dip-coating. Microscope slide substrates, cleaned with water, Decon 90 and acetone, were dip-coated using a withdrawal rate of 60 mm/min (as used by Alberius et. al.) and placed into a fridge maintained at a temperature of 7 °C and 22% relative humidity for 24 hours. Films were then calcined from 25 - 400 °C using a heating rate of 1 °C/min and being maintained at 400 °C for 180 minutes before being allowed to cool naturally. The mole ratios of reagents used in this preparation was 0.0091 P-123 : 13.8 C_2H_5OH : 1.7 HCl : 5.8 H_2O : 1 $Ti(OEt)_4$

In addition to complete microscope slides a series of 10 slides for each technique were dip-coated a series of four times following the full procedure for each coating. An additional 10 – 15 mm of substrate was allowed to remain out of the precursor solution with each subsequent coat in order to produce a series of four tiers of film material to enable the thickness of progressive depositions to be analysed. A final series of experiments was conducted by the quadruple dip-coating glass segments (approximately 1.5 x 2.5 cm) that had a coating of a titanium dioxide blocking layer. These films were then further developed for testing as solar cells by the L.M. Peter research group within the Department of Chemistry at the University of Bath.

Films were developed into solar cells by being soaked in a solution of the Ruthernium-based solar dye cis-bis(isothiocyanato)bis(2,2'-bipyridyl-4,4'-dicarboxylato)-ruthenium(II) bis-tetrabutylammonium, commonly referred to as Ruthenium 535-bisTBA or N719. Cells were then dried, retaining some dye, and were developed into full solar cells by the addition of a counter electrode and drying with a heat gun.

The efficiency of the solar cells produced was tested by using a Xenon lamp and adjustable monochromator to measure the incident photon to electron conversion

efficiency (IPCE) over a 400 – 800 nm wavelength range. The photocurrent density was also measured by exposing the cells to artificial sunlight and measuring the current produced for a voltage range of 0 – 0.5 V.

2.3.3 TiO_2 – Fluorosurfactant Templated Films at the Air-Solution Interface

Titanium dioxide-based, fluorosurfactant templated films were initially produced at the air-solution interface using reagent concentrations similar to those reported to produce inorganic films in aqueous systems using anionic surfactants.[43] After initial tests found these to be excessively dilute the higher concentration film preparations described here were used for all studies.

20 g (434 mmol) of ethanol was added to 1.62 g (2.2 mmol) of the partially fluorinated surfactant Zonyl FSO-100 in a plastic bottle and sealed before stirring for five minutes to obtain a uniform solution. Separately 0.70 g (2.06 mmol) of $Ti(OBu^n)_4$ and was placed in a glass vial before the addition of 1.47 g of 37% wt. HCl (15 mmol HCl, 51 mmol H_2O). A white precipitate was observed to form upon mixing and the vial was shaken manually to produce a uniform pale yellow solution with no precipitate remaining after one minute. The molar ratio of reagents used in this baseline film preparation was:

1.07 FSO-100 : 210 C_2H_5OH : 1 $Ti(OBu^n)_4$: 7.3 HCl : 25 H_2O.

This yellow solution was then poured into the surfactant solution and the resulting film precursor solution was stirred for one minute. The final solution was then poured into a 6 cm diameter Petri dish or 4 x 15 cm PTFE trough, depending on the analytical technique being used, and allowed to develop unsealed at room temperature. The initially pale solution was observed to develop a deep yellow colour, associated with growing titania species, over a period of one hour and a thin, clear film could be observed by eye within 2-3 hours. Disturbance of the solution surface was observed to create lines of strain in the films that were clearly visible by eye.

Variation of the molecular ratio of reagents was used to observe the effects of different reagent concentrations on film formation and structure and preparations containing no acid were also tested. In each case the concentration of only one reagent was varied at any time. The range of concentrations used for these experiments is shown in Table 2-2 below. Precise details of the reaction conditions used are given with the

results of these experiments in Chapter 4. In all other respects the film preparation method remained the same throughout the experiments.

Table 2-2 : Mole ratios ranges used for different analytical techniques for titanium dioxide – based films at the air-solution interface

Technique	FSO-100	$Ti(OBu^n)_4$	HCl	H_2O	C_2H_5OH
BAM (initial test)	1	1.5	9.3	32	870
BAM (formation time)	0.55 – 1.88	0.07 – 1.64	1.84 – 9.03	6.3 – 32	210
X-ray reflectometry	0.8 – 1.6	0.43 – 1.45	3.7 – 10.5	12.6 – 36	210
Neutron reflectometry	1.07 – 1.6	0.5 – 1	3.7 – 9.2	12.7 – 31.5	210

2.3.4 ZnO – Fluorosurfactant Templated Films at the Air-Solution Interface

Following the formation of TiO_2 films at the air-solution interface similar preparations were examined with Zn and Zr precursor materials. Zirconium dioxide films were formed under identical conditions to those for titanium dioxide films, § 2.3.3. Zinc films were formed by adding 20 g (434 mmol) of ethanol 1.62 g (2.2 mmol) of Zonyl FSO-100 in a plastic bottle and stirring for five minutes to obtain a uniform solution. To this solution 1.47 g of 37% wt. HCl (15 mmol HCl, 51 mmol H_2O) was added and the solution stirred for 30 seconds. Finally, 0.28 g (2.05 mmol) of solid $ZnCl_2$ was added and the solution stirred for one minute in which time the solid was observed to completely dissolve. The mole ratio of reagents used in a standard preparation was 1.07 FSO-100 : 210 C_2H_5OH : 1 $ZnCl_2$: 7.3 HCl : 25 H_2O.

As with the titanium dioxide films, after the film precursor solution was prepared it was poured into a 6 cm diameter Petri dish or 4 x 15 cm PTFE trough depending on the analytical technique being used. Allowed to develop uncovered at room temperature and humidity a film could be observed by eye within 120 minutes. As shown in Table 2-3 the mole ratios of reagents were varied to study the effects of different reagent concentrations of film formation and structure. In each case the concentration of only one reagent was varied at any time.

Table 2-3 : Mole ratio ranges used for different analytical techniques for zinc oxide-based films at the air-solution interface

Technique	FSO-100	$ZnCl_2$	HCl	H_2O	C_2H_5OH
BAM (formation time)	0.53 – 1.6	0.53 – 2	2.5 – 9.7	8.4 – 33	210
X-ray reflectometry	0.53 – 1.6	0.5 – 3	2.5 – 8	8.4 – 28	210
Neutron reflectometry	1.07	0.51 – 1	3.7 – 7.3	12.5 – 25	210

2.3.5 Diblock Copolymer Templated Films at the Air-Solution Interface

Titanium dioxide – based films have been templated at the air – solution interface using the new method outlined here. 1 g (0.34 mmol) of the diblock copolymer surfactant PE-PEG_{2250} was dissolved in 20 g (434 mmol) of ethanol by stirring and heating at 45 °C for 60 minutes. Subsequently 0.45 g of 37% wt. hydrochloric acid (4.6 mmol HCl, 15 mmol H_2O) was added to the solution followed by 1.4 g (78 mmol) of H_2O and the solution stirred for 1 minute to ensure uniformity. Finally, 2.0 g (10.5 mmol) of titanium tetrachloride was added to the solution and stirring maintained for a further minute to obtain a pale yellow solution. The mole ratio of reagents used was:

0.032 $PEPEG_{2250}$: 41 C_2H_5OH : 0.44 HCl : 8.9 H_2O : 1 $TiCl_4$.

Once stirring was finished the film precursor solution was poured into either a 6 cm diameter Petri dish or a 4 x 15 cm PTFE trough depending upon the analytical technique being used. For Brewster angle microscopy and neutron reflectivity films were allowed to develop at room temperature and humidity uncovered while for X-ray reflectivity they were covered by a lid with a 2 cm diameter hole to reduce evaporation. In all cases an opaque, white film was observed by eye to develop at the surface within one hour. As in the case of fluorinated surfactant templated films disturbance of the interface was observed to highlight the presence of a film at the interface.

For small angle scattering experiments performed on developed film material preparation of the films was carried out as above and films were allowed to develop for 2 hours. After 2 hours the films were removed from the interface by placing a plastic mesh of 1 cm wide holes underneath the film and lifting free of the interface. Films were allowed to dry for 48 hours at room temperature and the now clear film material was cut

free from the plastic mesh for mounting as appropriate for X-ray or neutron scattering. In the case of SAXS experiments the films studied were the same as those studied in BAM with film material removed from the interface once the microscopy experiments were complete.

Additionally, small angle neutron scattering was performed on the subphase solution by making film precursor solutions as outlined above. As only a small sample volume was required for these experiments the solutions were made at a 1 : 20 mass ratio of the procedure outlined above and the molar ratio of reagents was maintained at 0.032 $PEPEG_{2250}$: 41 C_2H_5OH : 0.44 HCl : 8.9 H_2O : 1 $TiCl_4$.

Variation of the molecular ratio of reagents was used to observe the effects of different reagent concentrations on film formation and structure. In each case the concentration of only one reagent was varied at any time. The range of concentrations used for these experiments is shown in Table 2-4 below. Precise details of the reaction conditions used are given with the results of these experiments in Chapter 5. In all other respects the film preparation method remained the same throughout the experiments.

Additional experiments were conducted to observe the effects of polymer addition on film formation and film structure. For these experiments poly(ethylene glycol), PEG, of molecular weight 10,000 or 600,000 was added in a 1:10 or 1:5 mass ratio to the surfactant. The polymer was added to the dry surfactant in the plastic bottle prior to the addition of ethanol and dissolved concurrently, other reagent ratios remained constant.

Table 2-4 : Mole ratio ranges used for different analytical techniques for block copolymer templated titanium oxide-based films at the air-solution interface

Technique	**$PEPEG_{2250}$**	**$TiCl_4$**	**HCl**	**H_2O**	**C_2H_5OH**
BAM (formation time)	0.017 – 0.057	0.65 – 1.52	0.07 – 0.72	8.9	41
X-ray reflectometry	0.016 – 0.048	0.75 – 1.24	0.23 – 0.72	8.9	41
SAXS	0.017 – 0.057	0.65 – 1.52	0.07 – 0.72	8.9	41
Neutron reflectometry	0.04 – 0. 064	0.51 – 1.87	0.44	8.9	41
SANS	0.029 – 0.058	1 – 1.55	0.44	8.9	41
TGA	0.032 – 0.048	1 – 1.50	0.44	8.9	41

2.4 References

(1) Penfold, J.; Thomas, R. K. *Journal of Physics: Condensed Matter* **1990**, *2*, 1369-1412.

(2) Sears, V. F. *Neutron News* **1992**, *3*, 26-37.

(3) *Small Angle X-ray Scattering*; Glatter, O.; Kratky, O., Eds.; Academic Press: London, 1982; Available from: http://physchem.kfunigraz.ac.at/sm/Software.htm.

(4) King, S. M. *Small Angle Neutron Scattering*; Rutherford Appleton Laboratory, 1995; Available from: www.isis.rl.ac.uk/largescale/loq/documents/sans.htm.

(5) Hammouda, B. *Probing Nanoscale Structures - The SANS Toolbox [online]*; National Institute of Standards and Technology, 2008; Avilable from: www.ncnr.nist.gov/staff/hammouda/the_SANS_toolbox.pdf.

(6) Guinier, A. *X-ray Diffraction In Crystals, Imperfect Crystals and Amorphous Bodies*; Dover: New York, 1994.

(7) Porod, G. In *Small Angle X-ray Scattering*; Glatter, O., Kratky, O., Eds.; Academic Press: London, 1982.

(8) Heenan, R. K. *Introduction to SANS Part 1*, Rutherford Appleton Laboratories, 2006.

(9) Baumeister, P. W. *Journal of the Optical Society of America* **1962**, *52*, 1149-1152.

(10) Nelson, A. *Journal of Applied Crystallography* **2006**, *39*, 273-276.

(11) Wagner, N. J.; Krause, R.; Rennie, A. R.; D'Aguanno, B.; Goodwin, J. *Journal of Chemical Physics* **1991**, *95*, 494-508.

(12) Hecht, E. *Optics*; 4th ed.; Addison Wesley, 2002.

(13) Jenkins, F. A.; White, H. E. *Fundamentals of Optics*; 4th ed.; McGraw-Hill, 1976.

(14) Honig, D.; Mobius, D. *Journal of Physical Chemistry* **1991**, *95*, 4590-4592.

(15) Hobley, J.; Oori, T.; Kajimoto, S.; Hatanaka, K.; Kopitkovas, G.; Lippert, T.; Fukumura, H. *Colloids and Surfaces A* **2006**, *284-285*, 514-520.

(16) Nishida, J.; Brizard, A.; Desbat, B.; Oda, R. *Journal of Colloid and Interface Science* **2005**, *284*, 298-305.

(17) Hall, C. E. *Introduction to Electron Microscopy*; 2nd ed.; McGraw-Hill, 1966.

(18) Gregg, S. J.; Sing, K. S. W. *Adsorption, Surface Area and Porosity*; 2nd ed.; Academic Press: London, 1982.

(19) Everett, D. H. *Pure & Applied Chemistry* **1972**, *31*, 577-638.

(20) Lennard-Jones, J. E. *Physica* **1937**, *4*, 941-956.

(21) Brunauer, S.; Emmett, P. H.; Teller, E. *Journal of the American Chemistry Society* **1938**, *60*, 309-319.

(22) Brunauer, S.; Deming, L. S.; Deming, W. E.; Teller, E. *Journal of the American Chemistry Society* **1940**, *62*, 1723-1732.

(23) Hooker, S. *Thermogravimetric Analysis (TGA) [online]*; Materials Science and Engineering Laboratory, NIST, 2005 Available from: http://www.msel.nist.gov/Nanotube2/Practice%20Guide_Section%202_TGA.pdf.

(24) Jaroneic, M.; Gilpin, R. K.; Ramler, J.; Choma, J. *Thermochimica Acta* **1996**, *272*, 65-73.

(25) Duval, C. *Inorganic Thermogravimetric Analysis*; 2nd ed.; Elsevier: London, 1963.

(26) Schmatz, W.; Springer, T.; Schelten, J.; Ibel, K. *Journal of Applied Crystallography* **1974**, *7*, 96-116.

(27) Holt, S.; Webster, J. *SURF - Technical Specifications*; ISIS [online], 2008; Available from: http://www.isis.rl.ac.uk/LargeScale/surf/surf.htm.

(28) Lieutenant, K.; Lindner, P.; Gahler, R. *Journal of Applied Crystallography* **2007**, *40*, 1056-1063.

(29) Smilgies, D.-M.; Boudet, N.; Struth, B.; Konovalov, O. *Journal of Synchrotron Radiation* **2005**, *12*, 329-339.

(30) Konovalov, O.; Novak, J.; Singh, A.; Vorobiev, A.; Feder, P.; Lhost, K. *ID10B [online]*; ESRF, 2008; Available at:http://www.esrf.eu/UsersAndScience/Experiments/SCMatter/ID10B/id10b_manual.pdf .

(31) Edler, K.; Goldar, A.; Hughes, A. V.; Roser, S. J.; Mann, S. *Microporous and Mesoporous Materials* **2001**, *44-45*, 661-670.

(32) Hughes, A. V.; Goldar, A.; Gerstenberg, M.; Roser, S. J.; Bradshaw, J. *Physical Chemistry Chemical Physics* **2002**, *4*, 2371-2378.

(33) NCNR *Analysis Package*, 2008; Available from http://www.ncnr.nist.gov/programs/sans/data/data_anal.html.

(34) Kline, A. R. *Journal of Applied Crystallography* **2006**, *39*.

(35) *Imaging Ellipsometer I-Elli 2000 [online]*; Nanofilm Technologies; 2001; Available from http://web.archive.org/web/20010217114018/www.nanofilm.de/html/elli2000/i-elli2000.html.

(36) Chi, T. *The Fundamentals of Stylus Profiling*, Veeco, 2006.

(37) BASF *Technical Bulletin; Pluronic P123 Block Copolymer Surfactant*; [online], 2002; Available from: www.basf.com/performancechemical/pdfs/Pluronic_P123.pdf.

(38) BASF *Technical Bulletin: Pluronic F127 Block Copolymer Surfactant*; [online], 2004.

(39) Rajzer, B. *Certificate of Analysis: Polyethylene - block - poly(ethylene glycol)*; Sigma-Aldrch [online], 2005.

(40) DuPont *DuPont Zonyl FSO-100 fluorosurfactant*, DuPont Performance Chemicals, 2002.

(41) Crepaldi, E. L.; Soler-Illia, G. d. A.; Grosso, D.; Cagnol, F.; Ribot, F.; Sanchez, C. *Journal of the American Chemistry Society* **2003**, *125*, 9770-9786.

(42) Alberius, P. C. A.; Frindell, K., L.; Hayward, R. C.; Kramer, E. J.; Stucky, G. D.; Chmelka, B. F. *Chemistry of Materials* **2002**, *14*, 3284-3294.

(43) Henderson, M. J.; Gibaud, A.; Rennie, A. R.; White, J. W. *Physica B-Condensed Matter* **2005**, *357*, 27-33.

Chapter 3
Dip-coated Films for Solar Cells
A comparison of two techniques

3.1 Evaporation Induced Self Assembly: Dip-Coating

3.1.1 Film Formation During the EISA Technique

Arising in principle from the pioneering work of researchers at Mobil reported in the early 1990s[1] the EISA method of film formation was published in the late 1990's as a straightforward method to produce nanostructured materials.[2-4] Although dip-coating is primarily referred to in this section the discussion is equally relevant for the related techniques of dip-coating and spray deposition. These techniques are straightforward in principle but are highly sensitive to a wide range of reaction parameters such as reagent concentrations, solvent, temperature, humidity and aging, that offers both great customizability of products and challenges to consistency.[2,3,5] Initially developed producing mesoporous silica materials, the combination of CTAB and TMOS remains the largest single area of study in the EISA mechanism, although it has been extended to the formation of transition metal oxide materials and it is considered possible to template almost any metal oxide using the technique.[3,6] As a result the technique promises application in a wide range of fields and has attracted considerable research aiming for greater control over products by understanding of the processes involved.

Two different mechanisms have been considered to describe the formation processes during the EISA technique. Liquid crystal templating, similar to that suggested for MCM materials in 1992, has been proposed for mesoporous material formation using either ionic or block copolymer surfactants although it remains an issue of debate.[7,8] Cooperative self-assembly, in which inorganic precursors and surfactants for hybrid aggregates that subsequently form a structure, has also been proposed for the use of both types of surfactants.[9-11] In either case, in the EISA technique, the development of an ordered structure arises during the preferential evaporation of a solvent, commonly

ethanol, from the precursor solution creating a higher final surfactant and inorganic precursor concentration in the film.[3,5] A series of stages may be identified during film formation as evaporation continues and the stages of the surfactant-templated formation of a mesostructured film during dip-coating are shown in *Figure 3-27*.

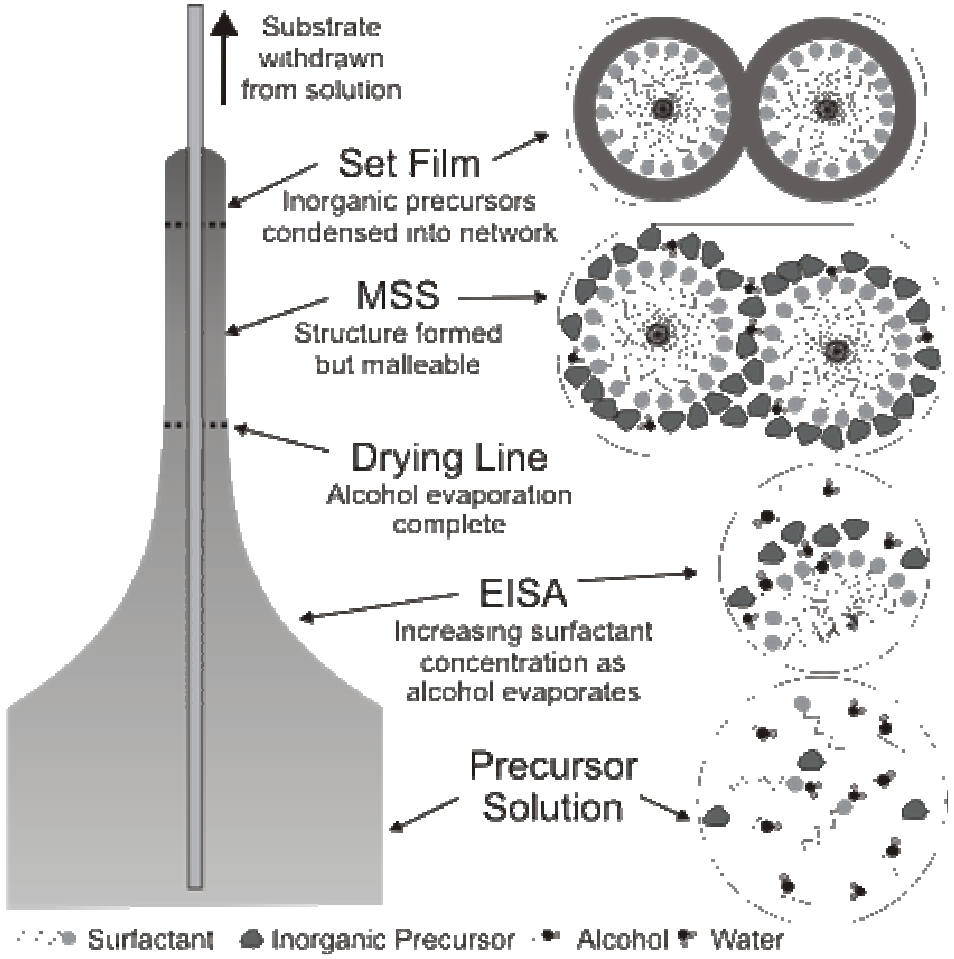

Figure 3-27[5] *: Mesostructured film formation during dip-coating.*

Evaporation during EISA is very rapid and is complete within 10 – 30 seconds from the substrate, leaving the precursor solution and a 'drying line', above which evaporation is complete, is typically 1 cm above the solution reservoir meaning that evaporation is completed and the film thickness is established during the dip-coating

[5] Grosso, D.; Cagnol, F.; Soler-Illia, G. d. A.; Crepaldi, E. L.; Amenitsch, H.; Brunet-Bruneau, A.; Bourgeois, A.; Sanchez, C.: Fundamentals of mesostructuring through evaporation induced self-assembly. *Adv. Funct. Mater.* 2004, *14*, 309-322 Copyright Wiley-VCH Verlag GmbH & Co. KGaA. Redrawn and reproduced with the permission of publisher and head author.

stage.[3,12,13] During evaporation, surfactant micelles rapidly form as the solution rapidly reaches the CMC and as evaporation continues, an ordered liquid crystal phase is formed. Once evaporation is complete, a modulable steady state, MSS, is reached, in which the reagents are in equilibrium in a solid but malleable film and the final structure of the film becomes fixed.[3] The MSS stage of film formation is similar to the true liquid crystal templating mechanism proposed in 1992, but differs in that cooperative self assembly occurs before the MSS is reached.

The MSS period typically persists for seconds or minutes depending upon the inorganic species, humidity and acidity. Although a structure is established at this point it may be changed during the MSS period if the equilibrium is disturbed, typically by the addition or removal of water. This is particularly relevant in the case of transition metal species such as titania, in which inorganic condensation, induced by the evaporation of HCl from the film, is slow and the MSS may persist for over an hour.[3]

After dip-coating is complete, a series of aging steps at elevated temperature are used to complete the development of the inorganic network and promote the formation of crystalline inorganic material. Although film structure is usually established by this stage, control over the temperature and humidity remain vital to prevent the formation of amorphous inorganic phases or collapse of the film, if condensation and crystal formation occur too rapidly.[5,6,14] Thus it may be readily concluded that the EISA technique is highly sensitive to a wide range of reaction conditions.

It is this sensitivity that offers the particular challenges and opportunities of the technique and since its publication it has become a large research field in its own right. Mesoporous silica films have been formed with a cubic, hexagonal or wormlike structure and the technique has been successfully extended to a number of transition metal oxides including W, Ti, Zr and Sn.[3,6,15-17] Titania films have been achieved with cubic, hexagonal and wormlike structures and have shown considerable promise for photochemical applications.[18-21]

The publication of titania-based, dye-sensitized solar cell development in 2001 has provided a clear research goal for templated film formation.[22] Initially produced using titania film layers produced from an emulsion of titania nanoparticles, DSSCs have been developed using dip-coated films aiming to increase dye uptake and provide

efficient electron transport.[20] DSSCs formed from nanoparticles have been reported with an efficiency of 10 – 20% and although that remains below the efficiency of silicon solar cells it is reported that DSSCs can exceed silicon solar cell efficiency in high temperatures and at low solar angles.[22-24] Research in this field continues to develop rapidly and it is in this light that the present research was conducted aiming to develop high surface area films to form enchanced DSSCs and contribute to the understanding of important factors governing film formation.

3.2 Results

3.2.1 Surface Profilometry

Dye sensitized solar cells developed to date often use a film approximately 10 μm thick and in the present work films of at least 0.5 μm were considered desirable.[22] This was achieved through repetitive dip-coating and the deposition of subsequent layers studied using surface profilometry. For both of the dip-coated films studied, using either Pluronic F-127 or P-123 as a structure directing agent, a series of four tiers was formed on a microscope slide as described in the experimental section. These samples were readily observed by eye to consist of a series of four layers as subsequent layers were found to preferentially diffract different colors, and therefore wavelengths, of light as shown in *Figure 3-28.* The layers were also observed to be highly uniform in the colour of the diffracted light suggesting a uniform thickness.

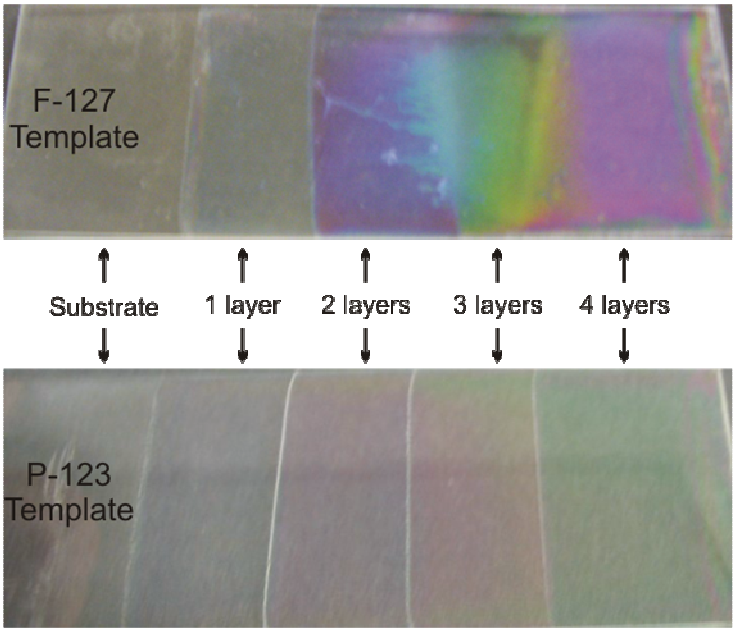

Figure 3-28 : Film tiers produced by dip-coating.
Different colors of light are observed for each layer.

Subsequent surface profilometry measurements confirmed this observation. The series of four pairs of measurements conducted in different areas of each layer were

found to have a standard error, Σ, of 11 nm or less, calculated for a mean of means.[25] As detailed in **Table 3-1**, uniform layers with a low variability in thickness were observed for each film deposition, in both film formation techniques. Additionally, the roughness of the films was observed to be less than 5 nm in all cases.

Table 3-1 : Thickness of film tiers from surface profilometry

F-127 Templated Tiers			**P-123 Templated Tiers**		
	Thickness	Σ		Thickness	Σ
1 Layer	180 nm	4.9 nm	1 Layer	170 nm	4.8 nm
2 Layers	304 nm	8.8 nm	2 Layers	293 nm	6.4 nm
3 Layers	386 nm	9.9 nm	3 Layers	444 nm	11.0 nm
4 Layers	437 nm	7.3 nm	4 Layers	584 nm	3.6 nm

However, although each tier of the samples was found to be highly uniform, surface profilometry showed, *Figure 3-29*, that the increase in film thickness varied with each deposition. In the case of F-127, templated films of sequential layers were found to be progressively thinner and four layers produced a 437 nm thick film, rather than the 720 nm thick film expected for identical layers. In comparison a single coat of the P-123 templated film was found to be thinner, while four layers were thicker, as deposited layers were found to have a more consistent thickness of approximately 150 nm, giving an overall thickness for four layers of 584 nm. There remained a decrease in thickness between the first layer and subsequent layers, however.

In addition to measuring the thickness of film tiers, surface profilometry studies showed no significant difference in thickness for multilayer P-123 templated films when a second layer was applied after the first layer had not been calcined. However, such films were observed to have a greater roughness of approximately 7 nm. A similar study of F-127 film multilayers without calcination was not possible, as the previously deposited layers were found to come away from the substrate during subsequent dip-coating.

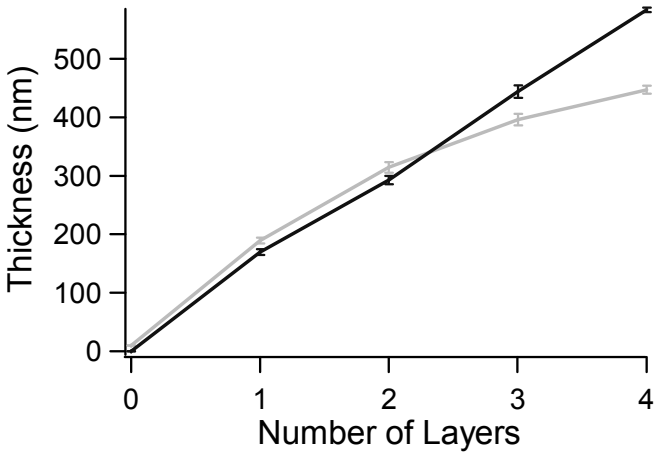

Figure 3-29 : Increase in film thickness with layer addition for F-127 (grey) and P-123 (black) templated films. F-127 data has been offset 10nm for clarity.

3.2.2 Electron Microscopy Imaging

Scanning electron microscopy was used to examine the surface structure of dip-coated films using F-127 as the template, to observe how uniform the films were. As shown in *Figure 3-30* a single coat of this film material was observed to have a uniform surface in which patches of film appear to be separated by 20 nm channels or deviations. However, these images are at the limit of the SEM resolution, leading to further examination by transmission electron microscopy.

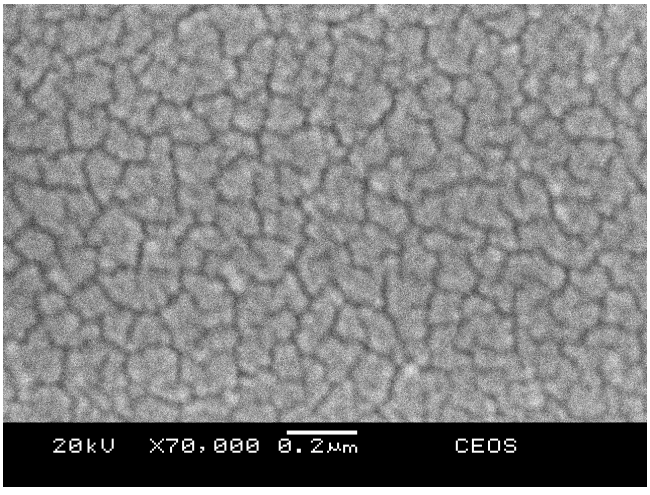

Figure 3-30 : SEM image of a dip-coated film using a F-127 template.

TEM images were collected from single and double layer films prepared using Pluronic F-127 as a template, to determine the structure of the material and to establish the presence and size of pores. As seen in *Figure 3-31*, these images showed the film material to be highly uniform and to consist of a porous matrix of titanium dioxide, confirmed by electron probe microanalysis, EPMA. Pores of 5 – 12 nm in diameter are observed in the material, however, although the film appears uniform, no hexagonal or cubic ordering is observed in the TEM images that are characteristic of a wormlike structure. No cracks comparable to those seen in SEM images were observed, although this may be due to film removal from the substrate.

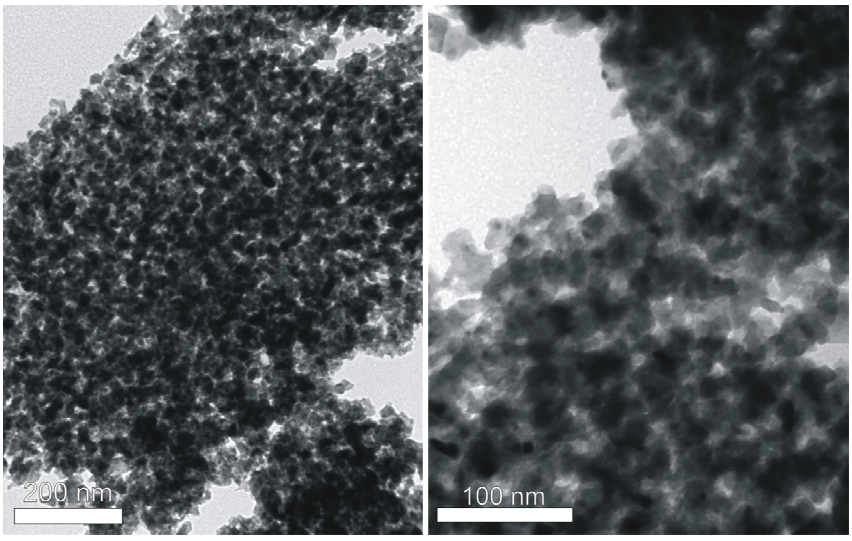

Figure 3-31 : TEM images from 1 layer of F-127 templated film material

Transmission electron microscopy images were also taken of film material after a second coat of F-127 film had been deposited shown in *Figure 3-32*. The surface and structure of the material is observed to be very similar to that for a single coat and also appears to have a wormlike structure. As in the single layer case, the porous titanium dioxide network is found to possess pores 5 – 12 nm in diameter, however there appear to be a greater number of smaller pores.

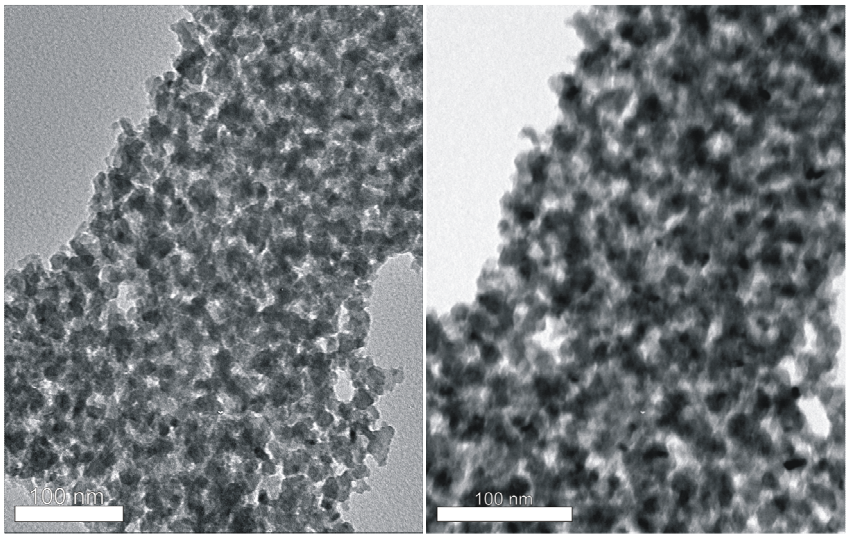

Figure 3-32 : TEM images from 2 layers of F-127 templated film material

For material from a two layer film, TEM imaging was complicated by the thickness of the sample as the majority of the sample was found to be too thick for successful imaging. Therefore, no TEM was conducted for materials produced with three or four layers of dip-coating. In the case of P-123 templated material, it was found to be difficult to obtain a sample thin enough for successful TEM imaging and images were only collected for material from a single film deposition.

These images, and electron probe microanalysis (EPMA) showed the titanium dioxide film to possess a uniform, regular structure with pores of 5 – 10 nm in diameter as shown in *Figure 3-33*. The material and pores appear more regular in both size and distribution in the P-123 templated film material than in the F-127 case, and the material appears to be free from cracking.

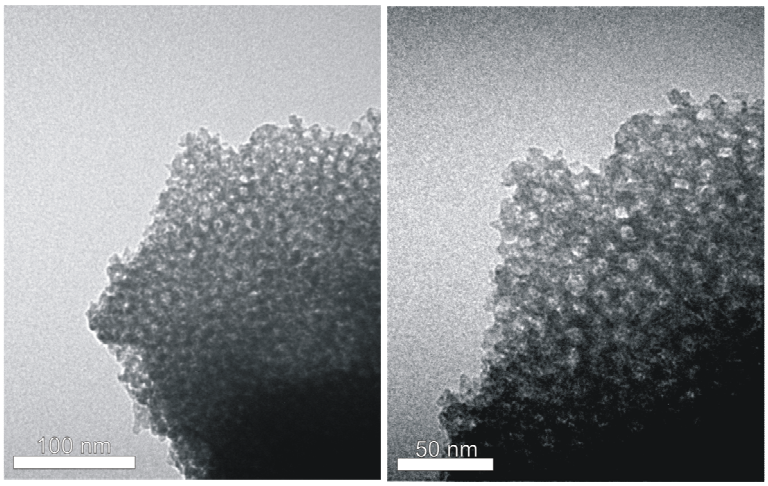

Figure 3-33 : TEM images from a single layer of P-123 templated film material

In addition to imaging, transmission electron microscopy was also used to collect electron diffraction patterns from the same samples used for imaging with results shown in *Figure 3-34*. A number of diffraction rings are observed for material from both one and two depositions of F-127 templated material, although fewer are observed once two layers have been deposited. Comparison of these diffraction patterns to crystallography data suggest that a *Pn3m* cubic phase is present in the F-127 templated film despite the lack of visible order in the TEM images.[26] On the other hand, despite the regular ordering apparent in images, no diffraction rings are observed for material templated with P-123 and it is possible that the material is too thick for electron diffraction to be successful.

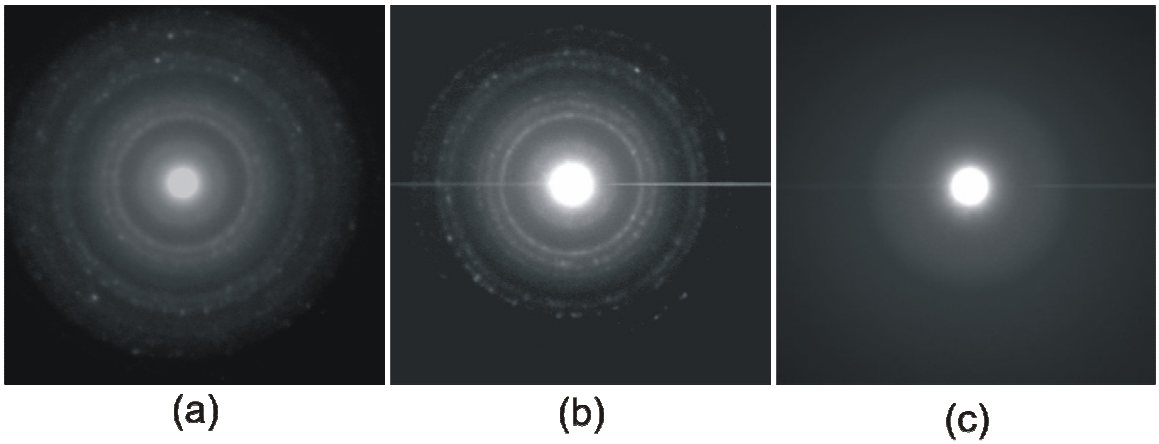

Figure 3-34 : Electron diffraction patterns from dip-coated film material. Patterns (a) and (b) correspond to a single and a double layer of F-127 templated film respectively. Diffraction from a single layer of P-123 templated film is shown in (c).

3.2.3 X-ray Scattering

The X-ray reflectometer at the University of Bath was used to collect reflectivity profiles from single depositions of dip-coated film material. In both of the F-127 and P-123 templated films attempts to collect a reflectivity profile from a multilayer film were not successful due to a very low intensity of the reflected radiation probably due to the mesoscale roughness of the multilayer film surface.

As shown in *Figure 3-35* a single layer of F-127 templated film calcined at 600 °C gave a reflectivity profile almost identical to that of a blank microscope slide and no structural peaks were identified. On the other hand, X-ray reflectometry performed on a single dip-coated layer of P-123 templated film calcined at 400 °C showed a single, broad peak at 0.14 $Å^{-1}$ corresponding to an interlayer spacing or ordering distance of 45Å, however, the peak position is uncertain. When an identical film was calcined at 600 °C no peak was observed, possibly due to the growth of titania crystals disrupting the film structure.[14,27]

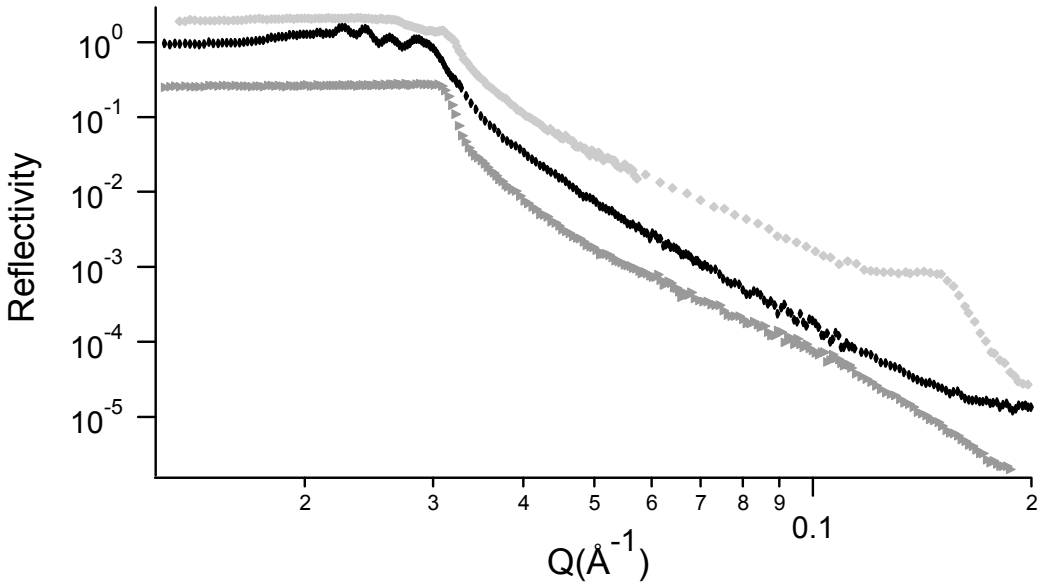

Figure 3-35 : X-ray reflectivity profiles from a blank microscope slide, dark grey, a single deposition of F-127 templated film, black, and a single deposition of P-123 templated film, light grey. Data offset for clarity.

Additionally, small angle X-ray scattering was performed on dip-coated film material scraped from the microscope slide substrate for both F-127 and P-123 templated films. As shown in *Figure 3-36* no structural peaks were observed in the F-127 templated film material while that using P-123 as a template, calcined at 400 °C, contained a single peak at $Q = 0.05$ Å^{-1} corresponding to a structural distance of 12.5 nm that is more well defined and more reliably observed than that in X-ray reflectivity. However when errors are considered no other features can be confidently identified. In both cases the background due to the Sellotape™ tape mounting of the samples has been subtracted and the data has been desmeared using the Lake program provided by the SAXS manufacturers as described in the Experimental section, § 2.2.4.

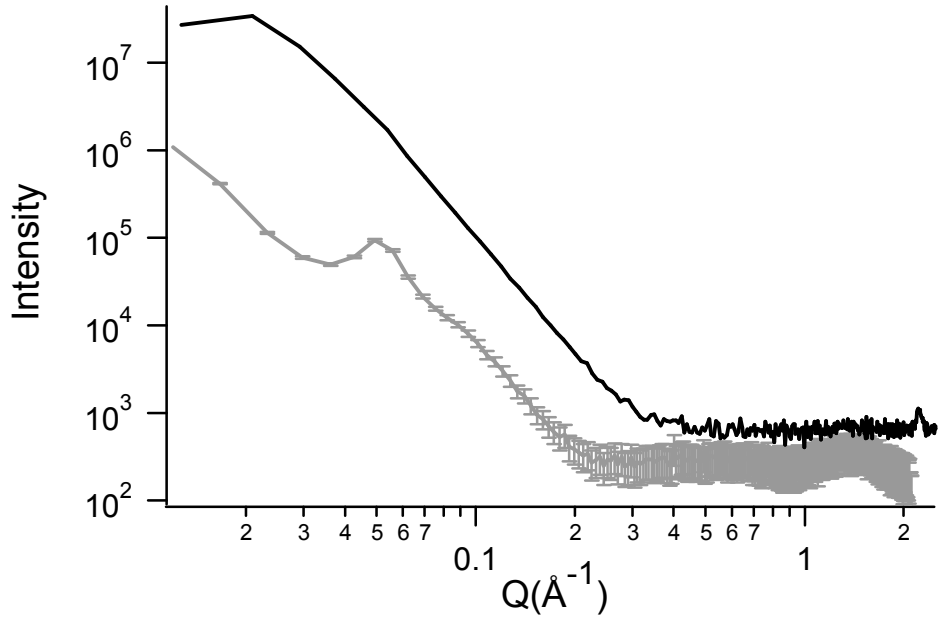

Figure 3-36 : SAXS profiles for film material templated with F-127, black, and P-123, grey. Data offset for clarity.

Small angle X-ray scattering data from F-127 templated material has been fitted with a polydisperse sphere model from the NCNR routines in which the polydispersity follows a Schulz distribution, see § 2.1.3.[28] The first data point has been excluded from the model, as it is unclear if it is affected by instrument alignment and, as shown in *Figure 3-37*, the resulting fit to the data has a χ^2 value, a measure of the accuracy of the fit, of 64 that is reasonable. Modeling yields a pore size, corresponding to the gaps and pores in the material in this case, with an average of 5 nm and a high polydispersity of

0.56. Attempts to fit an ellipsoid model to the pores of the F-127 templated film material resulted in worse fits, i.e. higher χ^2 values, than that of the spherical fit and in this case the best fit had radii of 5 nm and 15 nm and a χ^2 value of 84.

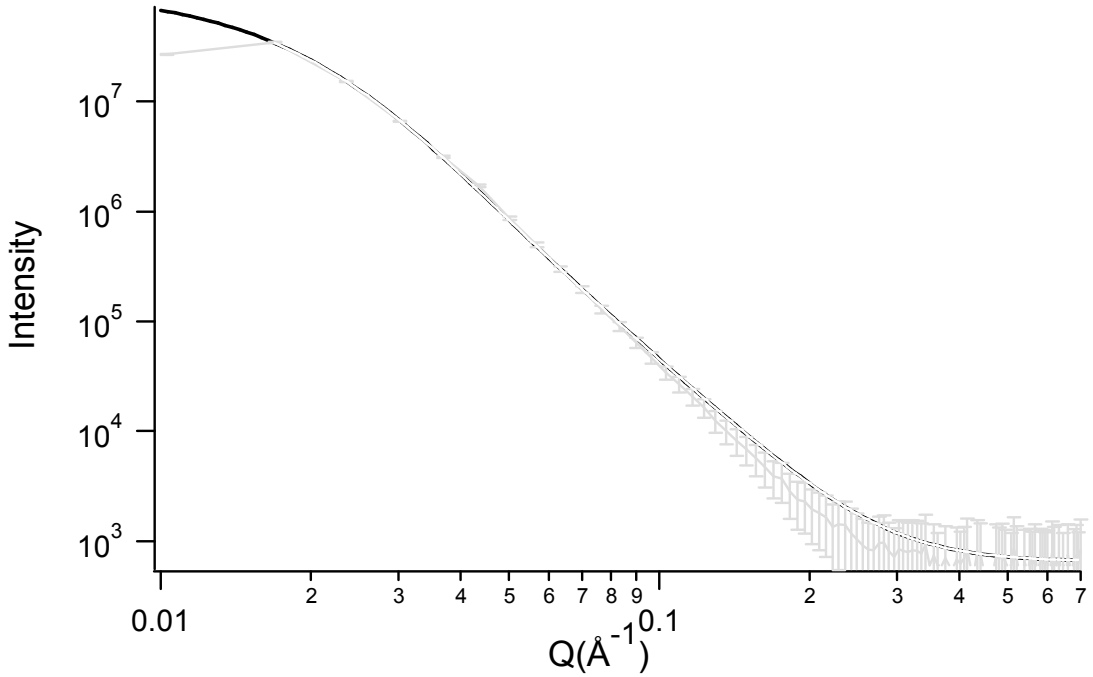

Figure 3-37 : Fit of polydisperse sphere model to SAXS pattern of F-127 templated film material. Data is shown in grey, the model in black.

Attempts to model the small angle X-ray scattering data from P-123 templated film material using either a spherical, ellipsoidal or hexagonal model were unsuccessful as all models produced very poor fits to the data. However, the peak observed in the scattering pattern of P-123 templated material at 0.05 $Å^{-1}$ corresponds to a distance of 12.5 nm. Assuming that the titania wall thickness is 20 – 40 Å thick, comparable to other reported systems,[27,29] this corresponds to a pore size of approximately 9 nm similar to TEM observations.

A Guinier analysis was unsuccessful in both cases as the calculated R_g multiplied by Q always exceeded 1 indicating that the analysis was outside the valid mathematical range, see § 2.1.3. Calculation of Porod slope was not possible as there was insufficient high angle data to obtain a reliable slope.

3.2.4 Solar Cell Testing

Development and efficiency testing of dip-coated films as dye sensitized solar cells (DSSC) was undertaken by the Peter research group at the University of Bath as detailed elsewhere, see § 2.3.2. A single deposition of F-127 templated film material was found to be very ineffective as a solar cell: no measurable results were obtained. Four layers of F-127 film material achieved greater success as shown in *Figure 3-38*. Solar cell efficiency in getting incident light to release electrons was measured over a wavelength range of 400 – 800 nm using a Xenon lamp. The peak incident photon to electron conversion efficiency (IPCE) was found to be 7% occurring for incident wavelengths of 510 – 525 nm. The directly measured photocurrent produced by the DSSCs using artificial sunlight was measured to be very low, however, barely above zero for most of the attracting potentials tested and gave unphysical, negative, results at high photovoltages.

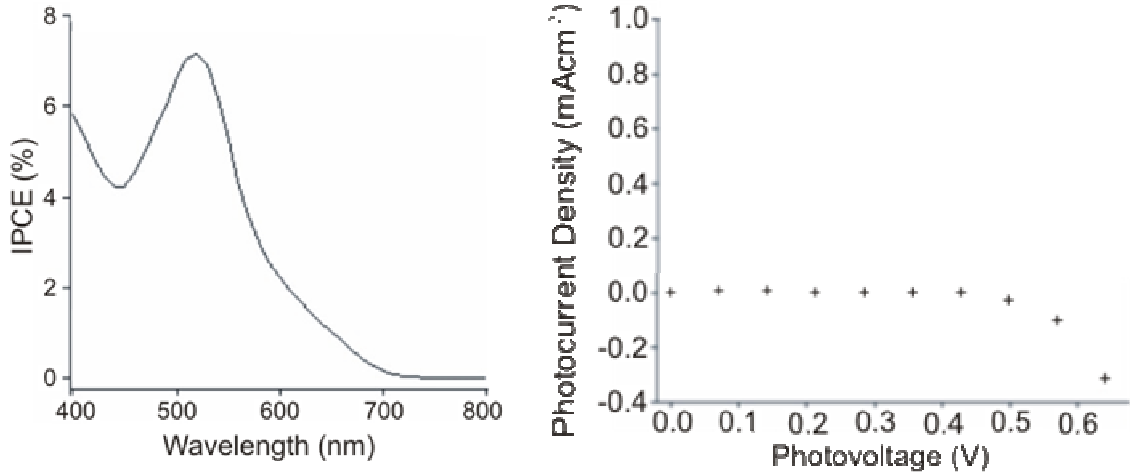

(a) (b)

Figure 3-38 : Measurements of IPCE, (a), and photocurrent density, (b), for DSSCs made using four layers of F-127 templated film

As one layer of F-127 templated film was unsuccessful in development into solar cells a single layer of P-123 templated film was not tested for solar cells. Instead, to allow even comparison, four layers of P-123 templated film were developed into DSSCs and

tested for their efficiency in both IPCE and current density produced as shown in *Figure 3-39*. Tested over a 400 – 800 nm wavelength range these cells were found to have a peak IPCE of 60% in the 480 – 500 nm wavelength range and tests of the cells at 0.1 of solar conditions produced a photocurrent density of 1.17 $mAcm^{-2}$. The photocurrent density is considered as linearly scalable, for different cell sizes or illumination conditions, for comparison with other results.

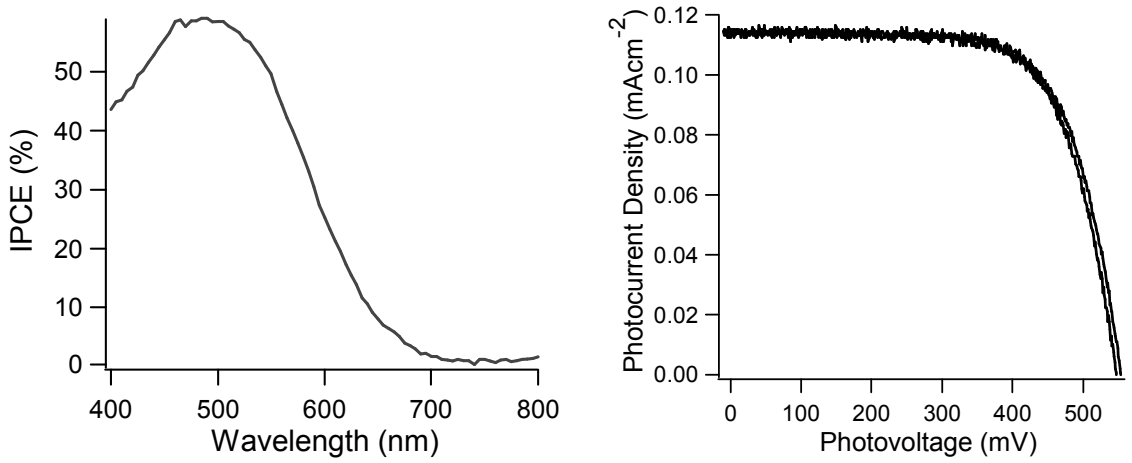

(a) (b)

Figure 3-39 : Measurements of IPCE, (a), and photocurrent density, (b), for DSSCs made using four layers of P-123 templated film.

3.3 Discussion

3.3.1 Film Thickness

Stylus profilometry measurements found dip-coated films templated with either block copolymer to be highly uniform and of a roughness of approximately 5 nm, a level that is not surprising as the dip-coating technique is recognized to produce smooth films of roughness even less than 1 nm.[6] A single repeat unit of a titanium-dioxde coated micelle is of the order of 5 nm thick thus, if some areas of the film have more repeat units than others, a 5 nm roughness is to be expected. Larger deviations with the appearance of channels observed in SEM images are not observed in surface profilometry measurements. As such deviations are observed to be of the order of 20 nm in width, less than the 76 nm horizontal resolution of the profilometry measurements, this is to be expected. As such the surface profilometry measurements of film thickness represent the average thickness over the film, as was intended, rather than providing a topographic map of the surface.

For F-127 templated films, a single coating was measured as 180 nm thick, considerably less than the 300 – 400 nm reported for similar preparations.[30] The reason for this deviation is unclear, given the similar reaction conditions however, given the precise control required during dip-coating it is possible that minor deviations in the reaction solution may be responsible. Subsequent measurements show that although the film thickness increases, as expected, it does not do so in a linear fashion. Rather, each subsequent dip-coated film deposition was found to be thinner than the proceeding one and, as shown in **Table 3-1** and *Figure 3-29*, these changes were too large to be accounted for by deviations in the measurement. This degradation of film thickness was found to be sufficiently pronounced that by the fourth deposition the added film was observed to be less than one third of the thickness of a single layer deposited under identical conditions.

Shrinkage of inorganic films under high temperatures has been noted for Si – Ti materials and similarly structured dip-coated films and titania particles have also been noted to contract at high temperatures as crystals form and contract the entire

structure.[23,30,31] However, in the maximum reported shrinkage is 20%, considerably less than that observed in the F-127 templated films, suggesting that although the films underwent multiple calcination steps, the reduction in film thickness is too great to be due to high temperature shrinkage. Furthermore, the thickness of dip-coated films is established during the dip-coating process, see § 3.1.1, and it is likely that thickness reduction results from differences in the deposition stage.

It is possible that the reduction in layer thickness is due to a decreasing interaction or wetability between the substrate, that varies from a silica microscope slide to a titania film, and the reaction solution during the dip-coating process, resulting in a thinner deposition initially. The effect of different substrates, such as glass and titanium metal sputter coated substrate, on the formation of titania films has been recently studied by Klotz, et. al.[32] Although a reduction in ordering was observed for a titanium substrate no reduction in thickness was reported. Furthermore, if a change in substrate – solution interactions was responsible for the change in thickness a change would be expected between the first and second deposited layers only. From the second layer onward all depositions are exposed to an identical titania substrate and the continued reduction in film thickness is unexplained.

Similarly, differences in the roughness of the substrate, a suggested explanation for substrate effects,[32] do not account for the decreasing layer thickness between the second and subsequent layers. The 5 nm roughness of the titania films is notably less the 30 nm roughness of the microscope slide and may cause some change, however, both are much smaller than the 200 nm roughness reported for a sputter coated titanium metal substrate for which no reduction in film thickness was reported.[32] Additionally, the roughness is constant after the first deposition and no further reduction in thickness is expected for identical substrates.[32]

In the case of uncalcined films, it has been noted that existing film layers partially dissolve when immersed in the reaction solution for application of a second layer. Although the dissolving of the film would reduce the thickness, no dissolving has been observed for the calcined titania films and it would result in a non-uniform film that does not concur with the profilometry results. Two further possible explanations for the

reduction in layer thickness are penetration of water or precursor solution into the substrate that is porous after one or more layers have been deposited.

Water is of particular importance for the hydrolysis reactions during titania precursor development and the water content of the reaction solution is one factor that must be controlled in the EISA technique.[30] Given this sensitivity to water it is possible that, after the first deposition, atmospheric water adsorbed into the pores of the substrate has an effect on the film thickness. In the high relative humidity conditions, above 40%, maintained during the aging of the films a substantial amount of water is known to persist in the freshly deposited films and it was therefore considered unlikely that water adsorbed into the substrate would have a significant impact upon film development.[30] It is possible that water is preventing the deposition of full thickness layers and, if so, this effect is expected to become more pronounced for subsequent layers although it is unclear why this should be the case.

A similar effect may be observed if the reaction solution for subsequent layers penetrates into the pores of the layers below. If the same volume of precursor solution is deposited for all dip-coated layers and some of this penetrates into the porous substrate, the layer that develops will be thinner than the proceeding one. As with the adsorption of water this would become more pronounced for later depositions, as a greater volume could be accommodated in the pores of the substrate. In addition to reducing the layer thickness, this process would be expected to reduce film ordering and reduce pore size as the pore network of previous depositions became filled with developing titania material. Such a change is not observed in TEM images or electron diffraction patterns taken for one and two layers of F127 templated film material suggesting that such interpenetration is not occurring. However, it is possible that the pores of the F-127 templated films are more open and accessible at the film surface than those of the P-123 templated films allowing the precursor solution to enter the system in greater amounts during subsequent depositions. As the P-123 surfactant is well known for the formation of cylindrical micelles that lie parallel to the substrate and ellipsoidal or spherical pores may form when the F-127 surfactant is used this seems possible.

In comparison to the F-127 templated films the P-123 templated films only show reduction in layer thickness between the first and subsequent depositions while the

thickness of the second, third and fourth layers is particularly consistent. In this case it appears clear that neither the adsorption of water into the pores of the substrate nor the interpenetration of reaction solution is occurring as these effects are expected to increase for later depositions. It is possible that the greater apparent viscosity of the reaction solution for the P-123 templated films than that for the F-127 templated films limits the effect of a porous substrate.

However, a reduced layer thickness is observed between the first layer and all subsequent depositions and it is likely that this results from differences during the dip-coating deposition. As discussed above, effects due to the different substrates of a glass slide and a deposited titania film are expected to produce differences between the first and later layers, with later depositions consistent with each other. Substrate roughness has been considered as likely to influence film development and it is possible that the lower 5 nm roughness of the titania films compared to the 30 nm roughness of the microscope slides reduces film thickness.[32] Although roughness effects were dismissed in the F-127 templated films, it is possible that the greater viscosity of the P-123 reaction solution makes these films more susceptible to differences in the substrate roughness. In particular, if the smoother titania film substrate is able to hold less reaction solution, it follows that the second and subsequent depositions will be thinner than the first layer but will be consistent with each other, as is observed.

In both cases reductions in the deposited film thickness suggest considerable implications for the further application of dip-coated materials. It appears that it may be difficult to achieve a desired thickness and precision in deposited layer thickness, and it shows that achieving thick dip-coated films may require an even greater number of repetitions of the coating process. It is clear that although regular layer deposition is possible, it cannot be taken for granted and must be studied whenever repetitive dip-coating is used.

Furthermore, recent results suggest that sintering of inorganic particles begins to occur after 5 repetitions of dip-coating and calcination, countering the gains of greater thickness for further depositions.[33] If a limited number of deposition cycles can be utilized, the thickness of a single layer is of key import. As the influence of substrate roughness and precursor solution viscosity appears to be of considerable influence in this

work in determining the volume of precursor solution deposited and thus film thickness, a specific study of this factor would be of considerable value.

3.3.2 Film Structure

It has been reported by Crepaldi, et. al. that the synthesis conditions used in the production of F-127 templated films produce hexagonally ordered materials,[30] however, slightly different concentrations are reported to yield cubic phases[30,34] that are more similar to results observed in the present work. Transmission electron microscopy images of the F-127 templated film material clearly show a somewhat disordered, porous structure of particles confirmed to be titania by EPMA. Furthermore, electron diffraction patterns from both single and double coats of the film material show diffraction rings that have been indexed to the *Pm3n* cubic structure that has been reported for other dip-coated films.[3,26] Although the body centered cubic *Im3m* phase is the most commonly reported cubic phase for dip-coated films using an F-127 template and has been reported for preparations similar to this work it is not exclusive and a *Pn3m* phase is reasonable.[3,30]

Neither X-ray reflectometry nor small angle X-ray scattering show any Bragg peaks that can be associated with a cubic structure but, as pores at the edges of particles observed in TEM are found to be varied in size and cover a 3 – 10 nm diameter range, it is possible that the lack of monodisperse pore size results in a lack of Bragg peaks. For Bragg peaks to appear in a scattering pattern a large amount of repeated, consistent structure must be present and it is not surprising that such peaks are not observed for the F-127 material. Modelling of the scattering data with a polydisperse sphere model confirms a high polydispersity of pore size that is expected to be responsible for the absence of peaks in the scattering pattern.

Polydispersity in micelle size may prevent regular packing of spheres and thus suppress the development of peaks. As such the assignment of a polydisperse cubic structure based on the electron diffraction results is reasonable. Although the surfactant micelles are expected to be monodisperse during film formation the disruption of the structure during calcination, due to the development of titania crystals, can reasonably be expected to create polydispersity in pore size.

Although X-ray scattering patterns from F-127 templated film material do not show peaks that can be analyzed, modeling of the data has been possible and is in good agreement with TEM imaging results. Modeling the pores in the material as polydisperse spheres produces a good fit to the data, see *Figure 3-37*, with an average pore radius of 5 nm and a high polydispersity of 0.56. Although at the high end of the 5 – 11 nm diameter range observed in TEM studies these results concur well and, furthermore, the *Pm3n* cubic structure, assigned from electron diffraction, is recognized as arising from templating around spherical micelles confirming the assignation of a spherical structure to the pores.[3]

Although similarities exist between models of ellipses and polydisperse spheres, it is confirmed that the pores are spherical in this case. The radii, particular the 3:1 aspect ratio, calculated in using an ellipsoid model, are outside the range of observations in the TEM images and are incompatible with the *Pn3m* structure and it is highly unlikely that pores in the F-127 templated material are ellipsoidal. Unfortunately no sufficiently long Porod region was observed to allow reliable calculation of the Porod slope as an indication of shape and smoothness.

Considerable differences are found in structural observations made for the P-123 templated film material, that shows a highly ordered and regular structure of 5-10 nm pores in TEM images but shows no order in electron diffraction patterns, however it was noted that the samples were largely too thick for TEM examination. Order is also observed in X-ray reflectometry, although peaks were considered unreliable in this case due to their poor resolution and possible errors in combining the reflectivity data, and small angle X-ray scattering patterns. Such observations further suggest that the lack of order in electron diffraction patterns is due to excessively thick, rather than disordered samples. It is also possible that the electron beam damages the sample, preventing further analysis by electron diffraction.

However, as it was not possible to accurately model the X-ray scattering data from the P-123 templated film material it is not possible to gain specific information this films in this manner. However, the peak observed at 0.05 $Å^{-1}$, *Figure 3-36*, and consideration of the wall thicknesses reported in other systems[27,29] suggests the pores of the film are approximately 9 nm in diameter, in good agreement with TEM observations.

Recently reported P-123 templated films used in the development of solar cells have been found to be highly successful although in this case no structure was assigned to the films which had the appearance of a wormlike structure in TEM images.[20] This suggests that, although an ordered phase is preferable, it is by no means a requirement for successful application of the films.

For both film materials, additional information on the overall pore size and distribution could be obtained by nitrogen adsorption isotherms, however, it was found to be impractical to conduct these experiments. Approximately 100 mg of film material is required for the adsorption experiments, whereas twenty dip-coated samples were found to produce less than one third of this mass of film material scraped from the substrate, indicating that producing a sufficient sample mass required excessive time.

3.3.3 Solar Cells

Tests of quadruple layer coatings of the F-127 and P-123 templated films as dye sensitized solar cells show that the peak IPCE of the F-127 templated films is 7% in the 510 – 525 nm wavelength range compared to 60% in the 480 – 500 nm wavelength range for the P-123 templated films. A large difference in the efficiency of the cells was also observed in the photocurrent density of the cells, as the F-127 templated films barely registered a current and the P-123 templated films produced 0.117 mA at 0.1 time solar conditions. The photocurrent density is a better indicator of solar cell efficiency and it is clear that the efficiency of the F-127 templated films as DSSCs is very low and does not compare favorably with titania or silica cells reported in the literature. Furthermore, it is clear that the P-123 templated films were considerably more successful in the development of dye sensitized solar cells.

Results of the development of P-123 templated titania films into solar cells have been recently reported by Zukalova, et. al. in which the cells were found to make a 50% improvement over cells made with films of randomly oriented titania nanoparticles.[20] The 950 nm thick films were produced by dip-coating three layers of film onto conductive glass and developing through to calcination for each deposition with pore sizes in the 5-10 nm range measured by nitrogen adsorption. The peak IPCE was reported as 49% at a wavelength of approximately 530 nm and the photocurrent density produced was 7

$mAcm^{-2}$ for 1.5 times solar conditions. This considerable improvement over cells using randomly oriented nanoparticle films of comparable thickness was assigned to the very high surface area of the mesoporous films, that allowed greater dye and electrolyte uptake.

Although the F-127 templated films produced in this work do not compare well to these films, the P-123 templated films represent a significant achievement. The peak IPCE of 60% is one fifth greater than that of the films in the literature, a significant improvment. However, the photocurrent produced from the films in this work, 1.75 $mAcm^{-2}$ at 1.5 times solar conditions, is considerably less the 7 $mAcm^{-2}$ reported by Zukalova, et. al. and the overall efficiency is also lower. This discrepancy in the IPCE and photocurrent density comparisons is possibly due to the different analyses used to determine IPCE and photocurrent density.

The IPCE analysis focuses on a very small area of a film and is less sensitive to the film thickness while the photocurrent produced is very sensitive to thickness due to its dependence on the amount of dye sensitizer adsorbed in the films. The lower photocurrent density suggests a lower uptake of the dye in the films produced in this work that may be due to the lower thickness or a lower surface area. Films produced in this work are thinner than those reported by Zukalova, et. al., probably due to the higher concentration, and therefore viscosity, of the precursor solution in that case.[20] It is, however, unfortunate that nitrogen adsorption isotherms were unable to be collected for the P-123 templated films in this work, as a comparison of surface area, as may be calculated using the BET equation, would clarify this. Nitrogen adsorption is therefore recommended as an area for further investigation.

Neither the films produced in this work nor those reported by Zukalova, et. al. surpass the efficiency achieved by solar cells using optimized films of randomly oriented nanoparticles, for which the film thickness is 18 μm.[35] Recent results also suggest that additional repetitions of the dip-coating procedure, although producing thicker films, does not yield any increase in solar cell efficiency due to a loss of surface area as particles sinter together.[33,36]

Although dip-coating may not presently be able to match randomly oriented nanoparticle films in thickness and efficiency, both sets of dip-coated films compare

favorably with nanoparticle films of a comparable, 1 μm, thickness. Such results confirm the potential of mesoporous materials, formed by the EISA technique in this case, in the production of high efficiency dye sensitized solar cells. It also suggests their utility in applications, such as coatings, in which a thin layer of material is required, a role that present dye-sensitized solar cells do not cover. Furthermore, the development of thicker dip-coated films in a single deposition may allow for new solar cells of even higher efficiency to be created.[14]

3.4 Conclusions and Future Work

Mesoporous titania films made using a dip-coating technique have indicated that repeated film deposition is not the straightforward process it is often assumed to be as subsequent layers may rapidly decrease in thickness. It is suggested that changes in substrate roughness may influence film thickness and a specific study of this factor is recommended as worthwhile.

Use of the F-127 surfactant as a template for film formation was found to produce the *Pm3n* cubic phase unusual in titania films, although repeated dip coating was found to be impractical in these films. Furthermore, their development into dye sensitized solar cells was largely unsuccessful, with very low efficiency cells produced. On the other hand, mesoporous films formed using a P-123 surfactant were found to produce regular deposition thicknesses for repeated coatings and formed promising solar cells, with an IPCE superior to that for dip-coated materials reported in the literature. Further comparison with materials reported in the literature may be achieved by calculation of the surface area of the films using nitrogen adsorption and this is recommended for future investigation.

These films were not competitive in overall cell efficiency, probably due to a low overall thickness and, therefore, a lesser amount of sensitizer dye being absorbed, however their successes demonstrates the potential of this technique. In light of recent reports of a maximum of 5 film layers yielding increased efficiency the development of this dip-coating technique to produce thicker films during each deposition is recommended as a pathway to the development of new, highly efficient dye sensitized solar cells. Larger surfactants or co-surfactants may allow thicker materials to be developed and this is recommended in addition to studying viscosity effects as a possible route to thicker materials.

3.5 References

(1) Beck, J. S.; Vartuli, J. C.; Roth, W. J.; Leonowicz, M. E.; Kresge, C. T.; Schmitt, K. D.; Chu, C. T.-W.; Olson, D. H.; Sheppard, E. W.; McCullen, S. B.; Higgins, J. B.; Schienker, J. L. *Journal of the American Chemistry Society* **1992**, *114*, 10834-10843.

(2) Brinker, C. J.; Lu, Y.; Sellinger, A.; Fan, H. *Advanced Materials* **1999**, *11*, 579-585.

(3) Grosso, D.; Cagnol, F.; Soler-Illia, G. d. A.; Crepaldi, E. L.; Amenitsch, H.; Brunet-Bruneau, A.; Bourgeois, A.; Sanchez, C. *Advanced Functional Materials* **2004**, *14*, 309-322.

(4) Yang, P.; Zhao, D.; Margolese, D. I.; Chmelka, B. F.; Stucky, G. D. *Nature* **1998**, *396*, 152-155.

(5) Brinker, C. J.; Dunphy, D. R. *Current Opinion in Colloid & Interface Science* **2006**, *11*, 126-132.

(6) Antonietti, M.; Niederberger, M.; Smarsly, B. *Dalton Transactions* **2008**, 18-24.

(7) Kresge, C. T.; Leonowicz, M. E.; Roth, W. J.; Vartuli, J. C.; Beck, J. S. *Nature* **1992**, *359*, 710-712.

(8) Boissiere, C.; Larbot, A.; Bourgaux, C.; Prouzet, E.; Bunton, C. A. *Chemistry of Materials* **2001**, *13*, 3580-3586.

(9) Brennan, T.; Hughes, A. V.; Roser, S. J.; Mann, S.; Edler, K. *Langmuir* **2002**, *18*, 9838-9844.

(10) Edler, K. *Australian Journal of Chemistry* **2005**, *58*, 627-643.

(11) Flödstrom, K.; Teixeira, C. V.; Amenitsch, H.; Alfredsson, V.; Linden, M. *Langmuir* **2004**, *20*, 4885-4891.

(12) Hurd, A. J.; Steinburg, L. *Granular Matter* **2001**, *3*, 19-21.

(13) Lee, C. H.; Yunfeng, L.; Shen, A. Q. *Physics of Fluids* **2006**, *18*, 1-11.

(14) Chen, W.; Geng, Y.; Sun, X.-D.; Cai, Q.; Li, H.-D.; Weng, D. *Microporous and Mesoporous Materials* **2008**, *111*, 219-227.

(15) Smarsly, B.; Grosso, D.; Brezesinski, T.; Pinna, N.; Boissiere, C.; Antonietti, M.; Sanchez, C. *Chemistry of Materials* **2004**, *16*, 2948-2952.

(16) Brezesinski, T.; Fattaakhova-Rohlfing, D.; Sallard, S.; Antonietti, M.; Smarsly, B. *Small* **2006**, *2*, 1203-1211.

(17) Brezesinski, T.; Fischer, A.; Limura, K.; Sanchez, C.; Grosso, D.; Antonietti, M.; Smarsly, B. *Advanced Functional Materials* **2006**, *16*, 1433-1440.

(18) Zhao, L.; Yu, Y.; Song, L.; Hu, X.; Larbot, A. *Applied Surface Science* **2005**, *239*, 285-291.

(19) Huo, K.; Tian, B.; Li, F.; Bian, Z.; Zhao, D.; Huang, C. *Journal of Materials Chemistry* **2005**, *15*, 2414-2420.

(20) Zukalova, M.; Zukal, A.; Kavan, L.; Nazeeruddin, M. K.; Liska, P.; Gratzel, M. *Nano Letters* **2005**, *5*, 1789-1792.

(21) Soni, S.; Henderson, M. J.; Bardeau, J.-F.; Gibaud, A. *Advanced Materials* **2008**, *20*, 1493.

(22) Gratzel, M. *Nature* **2001**, *414*, 338-344.

(23) Malfatti, L.; Falcaro, P.; Amenitsch, H.; Caramori, S.; Argazzi, R.; Bignozzi, C. A.; Enzo, S.; Maggini, M.; Innocenzi, P. *Microporous and Mesoporous Materials* **2006**, *88*, 304-311.

(24) Vargas-Florencia, D.; Edvinsson, T.; Hagfeldt, A.; Furo, I. *Journal of Physical Chemistry C* **2007**, *111*, 7605-7611.

(25) Chatfield, C. *Statistics for Technology*; Penguin Books Ltd: Middlesex, 1970.

(26) MacGillavry, C. H.; Rieck, G. D. e. *International tables for X-ray crystallography, Volume 3, Physical and chemical tables*; 2nd ed.; Dordrecht: London, 1968; Vol. 3.

(27) Sanchez, C.; Boissiere, C.; Grosso, D.; Laberty, C.; Nicole, L. *Chemistry of Materials* **2008**, *20*, 682-737.

(28) Kline, A. R. *Journal of Applied Crystallography* **2006**, *39*.

(29) Soler-Illia, G. d. A.; Crepaldi, E. L.; Grosso, D.; Sanchez, C. *Current Opinion in Colloid & Interface Science* **2003**, *8*, 109-126.

(30) Crepaldi, E. L.; Soler-Illia, G. d. A.; Grosso, D.; Cagnol, F.; Ribot, F.; Sanchez, C. *Journal of the American Chemistry Society* **2003**, *125*, 9770-9786.

(31) Brinker, C. J.; Scherer, G. W. *Sol-Gel Science*; 1 ed.; Academic Press: London, 1990; Vol. 1.

(32) Klotz, M.; Chouqnet, A.; Heitz, C.; Sondergard, E.; Albouy, P. *Thin Solid Films* **2006**, *495*, 40-44.

(33) Prochazka, J.; Kavan, L.; Shklover, V.; Zukalova, M.; Frank, O.; Kalbac, M.; Zukal, A.; Pelouchova, H.; Janda, P.; Week, K.; Klementova, M.; Carbone, D. *Chemistry of Materials* **2008**, *20*, 2985-2993.

(34) Grosso, D.; Soler-Illia, G. d. A.; Crepaldi, E. L.; Cagnol, F.; Sinturel, C.; Bourgeois, A.; Brunet-Bruneau, A.; Amenitsch, H.; Alberius, P. C. A.; Sanchez, C. *Chemistry of Materials* **2003**, *15*, 4562-4570.

(35) Nazeeruddin, M. K.; Pechy, P.; Renouard, T.; Zakeeruddin, S. M.; Humphry-Baker, R.; Comte, P.; Liska, P.; Cevey, L.; Costa, E.; Shklover, V.; Spiccia, L.; Deacon, G. B.; Bignozzi, C. A.; Gratzel, M. *Journal of the American Chemistry Society* **2001**, *123*, 1613-1624.

(36) Zukalova, M.; Prochazka, J.; Zukal, A.; Yum, J. H.; Kavan, L. *Inorganica Chimica Acta* **2008**, *361*, 656-662.

Chapter 4
Fluorinated Surfactant Templated Films

Novel use of a partially fluorinated surfactant
as a template for self-assembled films

4.1 Introduction

To a large degree the use of surface active molecules in the development of novel mesoporous materials has been due to their ability to form ordered micelles and liquid crystal phases in aqueous solution due to the different natures of their head and tail sections. Ionic surfactants were the first used,[1] followed by block-copolymer surfactants,[2] while more recently surfactants utilising a perfluorocarbon section, in which all hydrogen has been replaced by fluorine, have begun to be used.[3,4] Fluorinated surfactants are known to form similar micelles and liquid crystal phases to other surfactants in water, see § 1.2.1, and are well suited to mesoporous material templating.[5,6]

Molecules with a perfluorinated section are highly surface active in any non-fluorinated solvent allowing the formation of micelles and liquid crystal phases in a wide solvent range including water, alcohols, hydrocarbons and supercritical CO_2.[7] This surface activity, greater than that of hydrocarbon surfactants, arises from the rigid nature of the perfluorinated chain, due to the strong bond between fluorine and carbon and the comparatively large size of the fluorine.[3,8] It has been reported that partially fluorinated surfactants favour the formation of bilayer micelle structures such as vesicles and lamellar sheets in most solvent systems due to this high surface activity.[9]

Surface activity in non-aqueous solvents gives fluorinated surfactants the potential for use in limited water, high alcohol conditions in which the reaction of inorganic precursors can be controlled to prevent precipitation of disordered materials.[10,11] Furthermore such surfactants are more thermally stable than hydrocarbon surfactants and are less environmentally harmful than CFCs and recent work has reported the use of fluorosurfactants in mesoporous material formation from aqueous solution.[12,13]

In 2003 the use of a mixture of Pluronic and fluorinated surfactants was reported to template the formation of mesostructured silica at low and high temperatures.[14] The use of fluorosurfactants in mixed surfactant systems have been a growing area of research and the success of such systems has recently been demonstrated by the 2007 report of the synthesis of mesoporous SBA-16 silica particles among other materials.[6,15,16]

More recently the use of partially fluorinated surfactants alone has been reported in the formation of surfactant templated silica powders and films and structured mixed titania-silica powders has been reported using an aqueous solvent.[3,12,15,16] Materials include hexagonal and wormlike porous silica powders produced at elevated temperatures[3] and the production of thick walled mesoporous silica-titania powders using aqueous conditions and elevated temperatures over 2 days.[15] Additionally, the aqueous synthesis of mixed fluorosurfactant-silica powders with mesoscale lamellar structure has been recently reported by cooperative self-assembly in solution further demonstrating their potential in this field.[17]

Although the activity of fluorinated surfactants suggests their potential for templating pure transition metal oxide materials, such as titania, from systems using limited water content this remains a developing area. Fluorosurfactants have been used to form ordered pure titania particles in supercritical CO_2 emulsions however the formation of similar materials from milder conditions remain elusive.[4] In particular, the formation of continuous, uniform titania films at room temperature and atmospheric pressure is a goal for many applications, such as sensors and photochemistry, and is the motivation for the present research.

In addition to the development of titania materials, the use of other transition metals in mesoporous materials is desirable for applications such as catalysis and photochemistry.[18,19] Zinc is one such example as the 3.37 eV band gap of ZnO is suitable for development in photochemical applications such as decomposition of organics or solar cells.[20] Indeed, the use of zinc oxide in photovoltaic applications was reported as early as 1999 achieving an incident photon to electron conversion efficiency (IPCE) of 80%.[21] More recently the use of polymer-zinc oxide films have been used in Gratzel solar cells achieving a 0.20% efficiency, demonstrating the potential of zinc materials although it is not competitive with current TiO_2 materials.[22]

As the majority of present ZnO materials utilise chemical vapour deposition, chemical bath deposition or film formation from preformed powdered materials, the synthesis of pure, uniform, robust zinc oxide films using mild conditions is a significant research goal.[20,23] The potential utility of such materials represents the motivation behind the present work and this research into the partially fluorinated surfactant templated formation of zinc oxide films at the air-solution interface is the first of its kind, to our knowledge.

4.2 Fluoro-Surfactant Templated Titania Films - Results

4.2.1 Small Angle X-ray Scattering

To further the understanding of self-assembly in the subphase during film formation small angle X-ray scattering patterns were collected from samples in the range of 0% to 90% wt. of FSO-100 surfactant in ethanol. In the interest of clarity only some of the scattering patterns from this range are shown in *Figure 4-40.* Of these the 10% wt. sample is the closest to the concentration of the film precursor solutions and it is observed to show no structure in solution. No peaks appear corresponding to a highly ordered liquid crystal phase appear in solutions at any FSO-100 content, however, a broad peak is observed at 0.177 $Å^{-1}$, corresponding to 35 Å, developing above 70% wt. surfactant. Solutions were observed to remain fluid at all concentrations and no crystalline surfactant phase is expected.

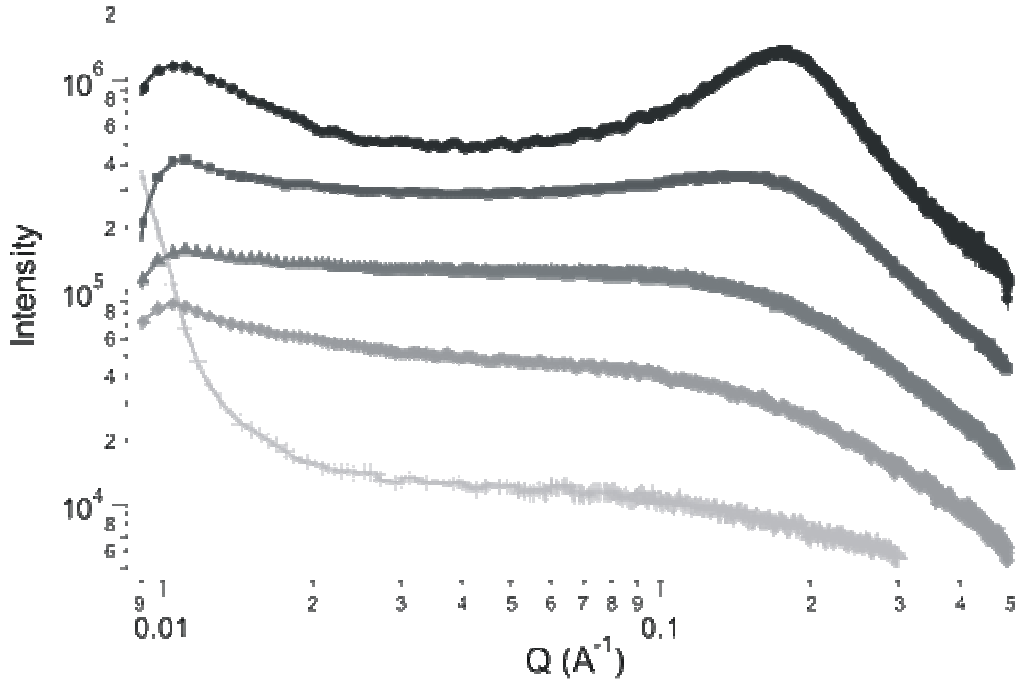

Figure 4-40 : SAXS patterns from different concentrations of FSO-100 surfactant in ethanol. Patterns corresponding to 10% (crosses), 20% (diamonds), 40% (triangles), 60% (squares) and 80% (circles) wt. are shown.

In the absence of structural peaks modelling of the data for all concentrations was undertaken with spherical, ellipsoidal, cylindrical and lamellar models tested as fits to the data using a hard sphere structure factor in all cases. There was found to be insufficient contrast between the ethanol solvent and the PEO chains of the surfactant for significant scattering, see **Table 2-1**, § 2.1.1, and, therefore, data fitting was conducted modelling the fluorinated tail of the surfactant only. The results of the best models (as assessed by χ^2 from analysis) are shown in **Table 4-2.**

Table 4-2 : Summary of SAXS models for FSO-100 surfactant in ethanol. R_a is the rotation axis of ellipsoids or the radius of a sphere as appropriate, R_b is the minor axis of ellipsoids and PD is the Schulz polydispersity.

FSO-100 (% wt.)	Micelle Shape	R_a (Å) ± 2	R_b (Å) ± 2	PD ± 0.05	Guinier R_g (Å)	R
10	Spherical	11	-	0.18	50	65
20	Spherical	10	-	0.10	35	46
30	Spherical	10	-	0.27	37	47
40	Ellipsoidal	10	9	-	33	-
50	Ellipsoidal	18	10	-	44	-
60	Ellipsoidal	30	10	-	52	-
70	Ellipsoidal	37	10	-	59	-
80	Ellipsoidal	35	10	-	58	-
90	Ellipsoidal	38	10	-	60	-

It was observed that for surfactant concentrations below 40% wt. FSO-100 forms polydisperse spherical micelles 10 Å in radius in solution. At concentrations above 70% the surfactant forms prolate ellipsoids approximately 36 x 10 Å in size with a peak developing in scattering patterns at this point due to hard sphere interactions between the micelles. In between these two extremes, 40% - 70% wt., FSO-100 micelles are observed become more ellipsoidal as the concentration increases.

In addition to data modelling, Guinier analysis was used to calculate the radius of gyration, R_g, of the FSO-100 micelles in solution with results shown in **Table 4-2**. The radius of gyration is observed to be constant for high and low FSO-100 concentrations and is observed to increase as the elliptical micelles rotation axis increases in size from 10 Å to 38 Å. In all cases R_g is considerably larger than the fitted radius as the fitted radius does not account for the PEO groups of the surfactant. It was not possible to

calculate Porod slopes for the data as no linear Porod region was observed in the scattering patterns.

As well as examination of the surfactant phase diagram, SAXS was used to study the structure of film material recovered from the air-solution interface after study in Brewster Angle Microscopy experiments, see § 4.2.2. After film formation was observed in BAM experiments solutions were left for an additional 2 hours before collecting the developed film material onto clean microscope slides. SAXS patterns collected from the collected material did not suggest an ordered structure and due to concerns about acid in the film material damaging the SAXS instrument further study was done after calcination.

Collected film material was allowed to dry overnight prior to calcination at 600°C to ensure solvent, acid and surfactant removal. SAXS patterns were then collected from the film material after the surfactant had been removed and, as shown in *Figure 4-41*, the scattering patterns for different reagent concentrations show some structural variation in the recovered film material. In all cases peaks observed at high angles are assigned to the anatase phase of titania,[24] however, in some cases the high angle intensity drops sharply due to the background subtraction.

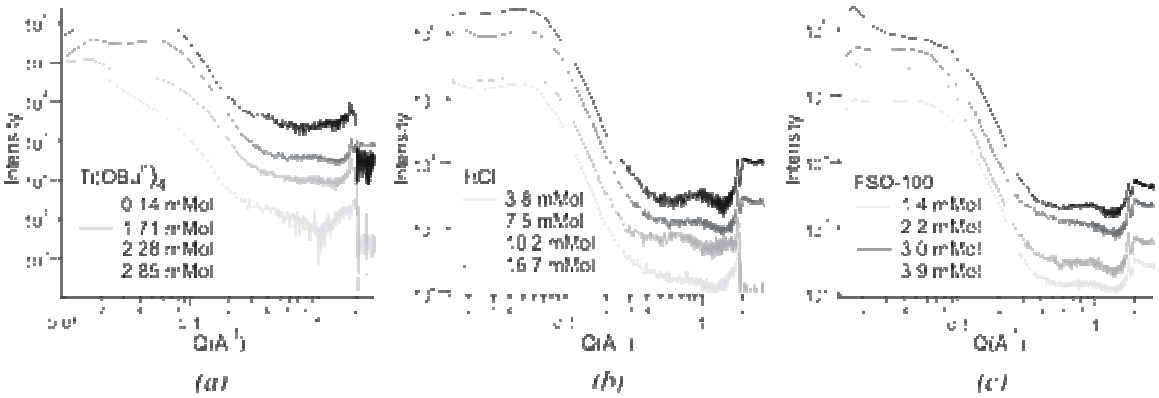

Figure 4-41 : SAXS patterns from FSO-100 templated titania film material after calcination showing the effect of Ti(OBu^n)$_4$, (a), HCl, (b), and FSO-100, (c), variation. Data is offset for clarity in all cases.

The structure of the film material after calcination was further studied by using NCNR routines,[25] see § 2.2.5, to model the SAXS patterns collected from the material. Models of spherical, ellipsoidal and cylindrical voids in a titania matrix were tested for

the scattering patterns with patterns from oblate ellipses providing the best fit in all cases with results shown in **Table 4-3**. As collection of the SAXS patterns was undertaken after surfactant removal it is expected that the particle size and shape observed during modelling reflect the size and shape of the voids in the material rather than the size of the particles. Scattering length densities used during modelling are listed in **Table 2-1**, § 2.1.1.

Table 4-3 : Summary of modeling of SAXS patterns from titania film material removed from the interface, dried and calcined. R_a and R_b are the rotation and minor axes of the ellipsoids respectively while the volume fraction is not listed as it was used to scale the SAXS patterns rather than as part of a structure factor.

Experiment	$Ti(OBu^n)_4$ (mMol)	FSO-100 (mMol)	HCl (mMol)	R_a (Å) ± 2	R_b (Å) ± 2
$Ti(OBu^n)_4$ Variation	0.14	2.25	14.9	17	133
	1.68	"	"	12	31
	2.00	"	"	15	32
	2.25	"	"	16	34
	2.57	"	"	17	33
	2.85	"	"	18	35
FSO-100 Variation	2.00	1.38	14.9	17	30
	"	2.25	"	15	32
	"	3.05	"	14	29
	"	3.88	"	12	25
HCl Variation	2.00	2.25	3.76	18	37
	"	"	7.51	16	32
	"	"	14.9	15	32
	"	"	18.6	13	27

4.2.2 Brewster Angle Microscopy

The formation of titania films at the air-solution interface using the partially fluorinated surfactant Zonyl FSO-100 was undertaken to observe the formation processes and effects of different reagent concentrations on film formation time in order to study the mechanism of film formation. Initial experiments showed that no film formed in the absence of the titanium precursor, $Ti(OBu^n)_4$ indicating that it was required in the formation mechanism for film development.

BAM experiments showed that when film precursors are initially mixed a uniform black image disrupted by stationary bright specks due to surfactant migration to the interface is observed, shown in *Figure 4-42 (a)*. Movement is observed as material passes through the field of view and passing in and out of focus as it moves toward or away from the focal plane. This movement was found to gradually decrease over time as a film developed at the air – solution interface and was observed to eventually cease completely and this was taken as indicative of film formation. BAM images taken for a standard film preparation noted a completely stationary surface, *Figure 4-42 (b)*, 160 minutes after the addition of the $Ti(OBu^n)_4$. Additionally, as the film forms it was observed that the subphase solution develops a yellow colour, associated with titanium oxide oligomers in other film preparations.[26,27]

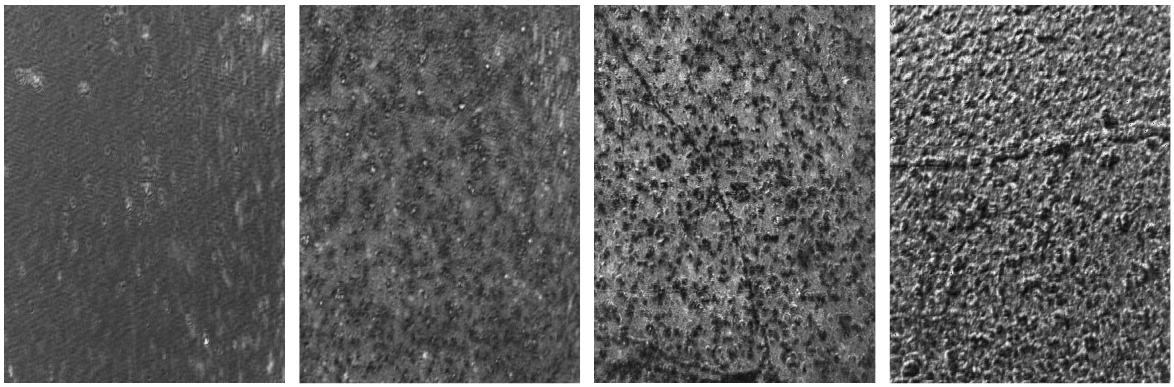

(a) *(b)* *(c)* *(d)*

Figure 4-42 : BAM images of a FSO-100 templated titania film developing at the air-solution interface. Image (a) shows the surface directly after mixing while images (b), (c) and (d) show the surface after 160 minutes, after a film has formed and after 305 minutes and 26 hours respectively. The BAM images are 477 x 385 μm in each case.

Further development of structure at the interface leads to an optically clear film present after an additional hour with additional surface structure becoming visible in BAM images. As seen in *Figure 4-42 (c)*, it was possible to observe fractures in the film at this point if it had been damaged by agitation when aligning the Brewster angle microscope. Films were observed to continue to develop over more than a day becoming visible by eye and with microscopy showing a rough interface, *Figure 4-42 (d),* with areas having the appearance of holes. Such areas are, however, may be due to poor surface packing at the interface or due to regions of different refractive index.

For observation of the effect of reagent concentration on film formation time the appearance of a completely stationary interface was taken as the point of film formation. *Figure 4-43* shows the changes in formation time as the concentration of HCl, the titania precursor $Ti(OBu^n)_4$ and FSO-100 surfactant concentrations are varied. The formation time was observed to decrease as either the acid concentration or surfactant concentration increased while films took longer to form at higher concentrations of titania precursor. Film formation at the upper and lower limits of the concentration ranges studied was observed to become increasingly uncertain as it became difficult to accurately observe the point of film formation. This gave rise to practical limits to the concentration range studied.

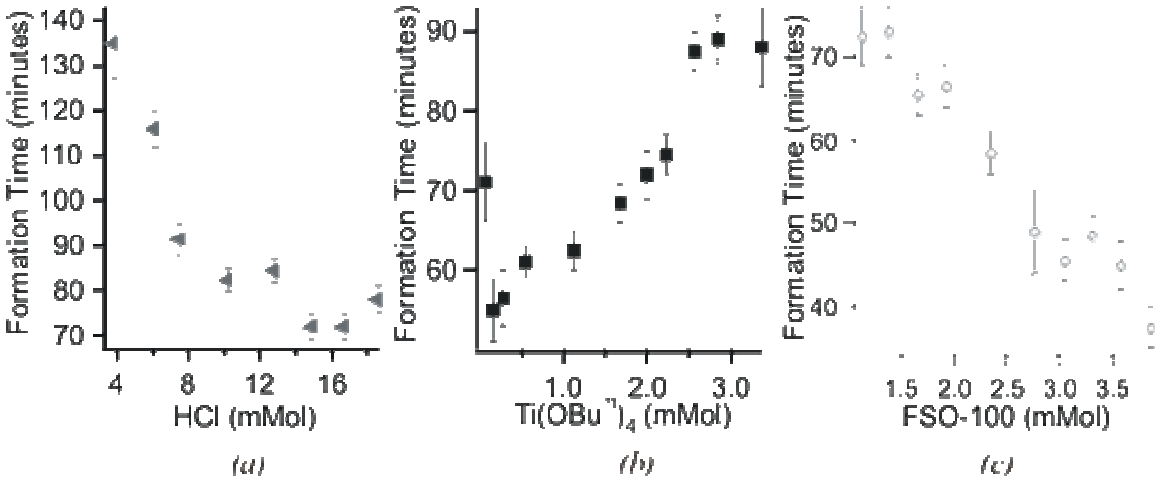

Figure 4-43 : Variation of film formation time for variation of HCl, (a), $Ti(OBu^n)_4$, (b), and FSO-100, (c), observed by Brewster angle microscopy.

Additionally, as the use of anhydrous ethanol makes HCl the only source of water in the reaction solution, the observations of formation time variation for acid and titania precursor variation were combined in order to examine the effect of the H_2O : $Ti(OBu^n)_4$ ratio on formation time. As shown in *Figure 4-44* the film formation was observed to occur faster at higher water contents until a minimum formation time of 55 – 60 minutes was reached.

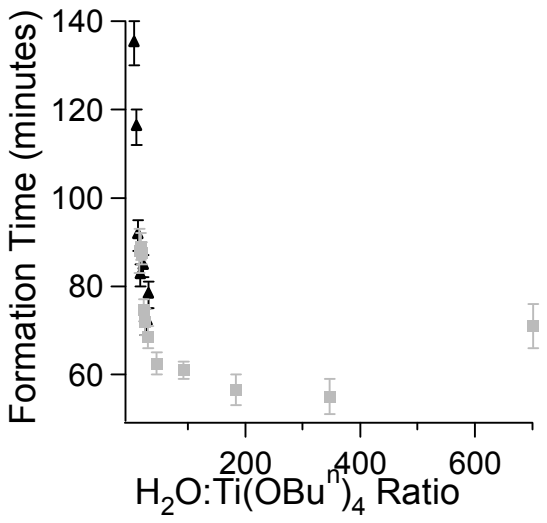

Figure 4-44 : Variation of film formation time with H_2O : $Ti(OBu^n)_4$ ratio. Data combined from HCl, black triangles, and $Ti(OBu^n)_4$, grey squares, variations.

4.2.3 X-ray Reflectometry

Time-resolved off-specular reflectometry and angle dispersive reflectometry experiments were conducted at the ESRF in order to study film formation and film structure respectively. As shown in *Figure 4-45* many of the time-resolved experiments did not give a clear indication of the time of film formation apart from the steady and continuous loss of intensity in the specular peak that corresponds with BAM observations of development.

However, observations of the films by eye showed the films formation time to follow similar trends to those observed in Brewster angle microscopy although the film formation time was lower in all cases. As the PTFE troughs used for reflectometry experiments have a surface area of 60 cm^2 compared to that of the Petrie dishes used during Brewster angle microscopy, 28 cm^2, the consistent reduction in film formation time is attributed to a greater surface area allowing greater surface activity in the precursor solution.

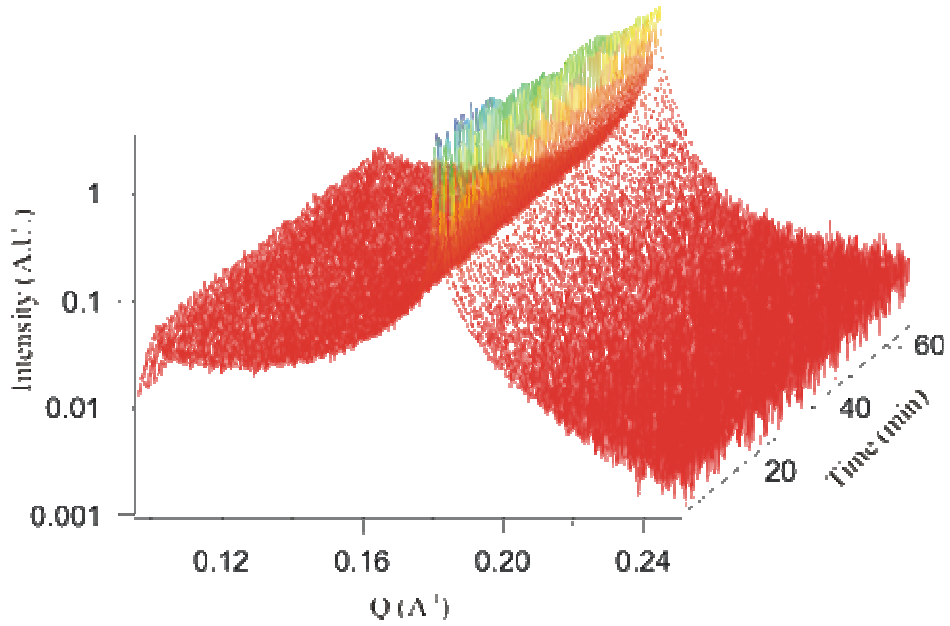

Figure 4-45 : Time-resolved reflectometry of the development of an FSO-100 templated titania film. The specific point of film formation is difficult to identify.

In addition to time-resolved experiments angle dispersive reflectometry was conducted upon developed films to examine the film structure and variations in structure at different reagent concentrations. Evaporation of solvent from the precursor solution left the interface below the edge of the PTFE trough in some cases preventing the collection of data at the lowest *Q* range and some profiles have been truncated in this section to remove misleading data.

As shown in *Figure 4-46* the films were found to have a lamellar structure at all of the acid concentrations studied with peaks at 0.11 $Å^{-1}$ and 0.22 $Å^{-1}$ indicating a *d*-spacing of 57 Å. The peaks were observed to become more sharply resolved for lower HCl concentrations and are most clearly resolved for an acid addition of 7 mMol suggesting a higher degree of order in films generated from low acid precursor solutions. This trend did not extend to solutions without any acid as, although a film was observed to form by eye if no acid was added, the corresponding reflectivity profile shows it to be disordered and no peaks are observed.

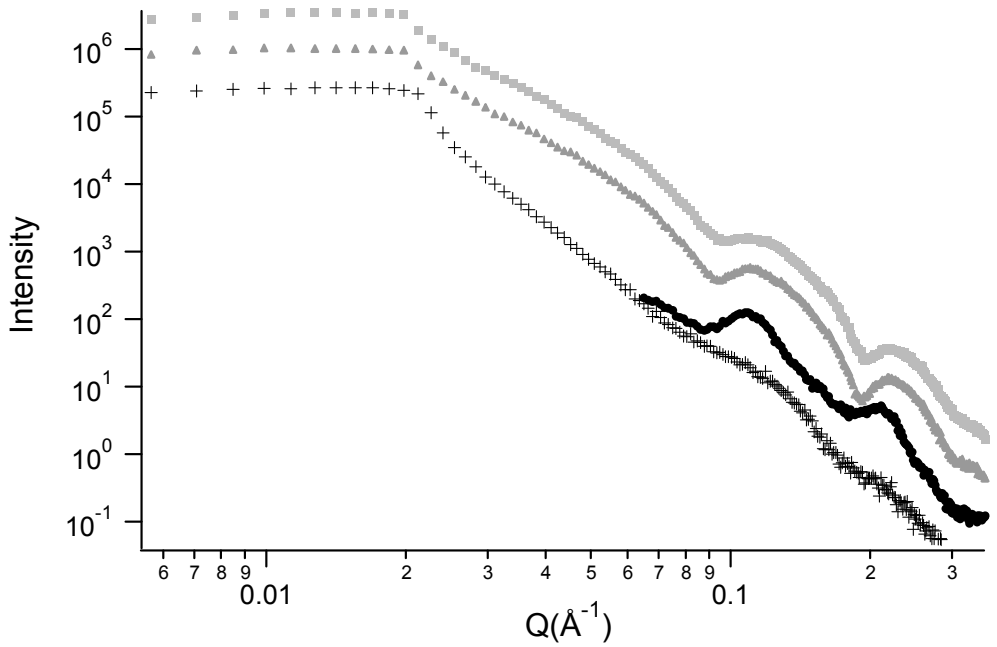

Figure 4-46 : X-ray reflecivity profiles for various acid concentrations. HCl additions of 21 mMol (light grey squares), 15 mMol (dark grey triangles), 7 mMol (black circles) and no acid (black crosses) are shown. Data is offset for clarity.

Structure variation at different FSO-100 surfactant concentrations showed an opposing trend to that for acid addition as shown in *Figure 4-47*. In agreement with acid variation results a lamellar phase with a *d*-spacing of 57 Å is observed at all of the surfactant concentrations studied. Variation in peak resolution is also observed with the peaks at 0.11 Å^{-1} and 0.22 Å^{-1} noted to become more sharply resolved at higher surfactant concentrations. This suggests that either a higher degree of ordering or an increased number of lamellar layers are present at higher surfactant concentrations. This is particularly evident in the relative sharpness of the peaks observed in the reflectivity profile from a film formed using 3.3 mMol of surfactant, 150% of that used in a standard film precursor solution.

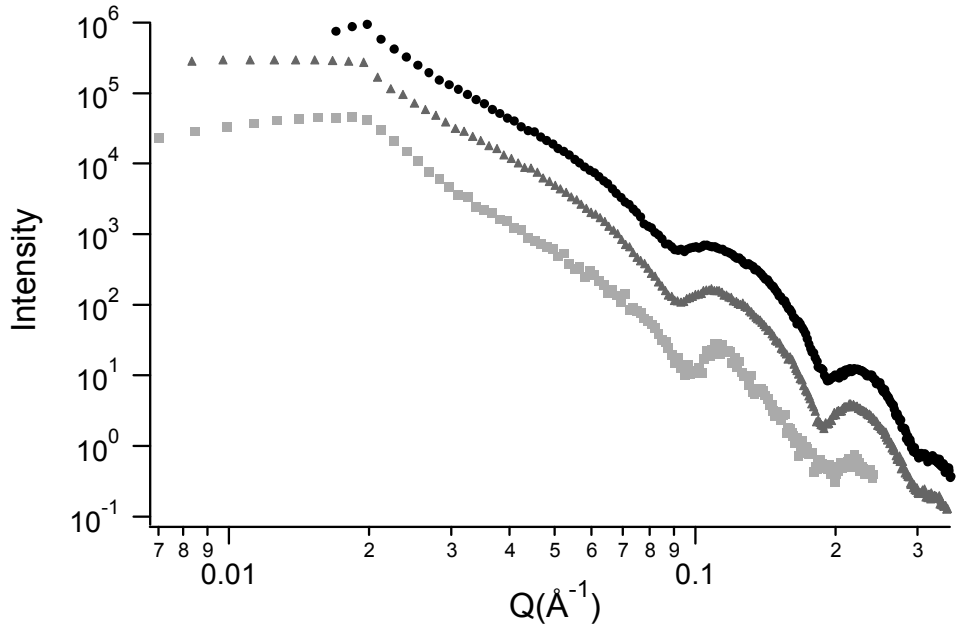

Figure 4-47 : X-ray reflectivity profiles showing variation with FSO-100 content. Additions of 1.7 mMol (black circles), 2.2 mMol (dark grey triangles) and 3.3 mMol (light grey squares) are shown, data is offset for clarity.

Variation for different concentration of titanium precursor are similar to those observed for surfactant variation and acid variation with the peaks noted at 0.11 $Å^{-1}$ and 0.22 $Å^{-1}$ corresponding to a lamellar phase of *d*-spacing 57 Å. The peaks were observed to vary in resolution for different $Ti(OBu^n)_4$ concentrations, becoming better resolved between additions of 0.9 mMol and 2.2 mMol of $Ti(OBu^n)_4$, as shown in *Figure 4-48*.

However, for the addition of 2.9 mMol of titanium precursor the peaks are noted to shift to a lower *Q* of 0.10 $Å^{-1}$ and 0.20 $Å^{-1}$ corresponding to an increase in the interlayer spacing of the lamellae to 62 Å. As shown in the error bars the possibility of peaks at higher *Q* cannot be clearly stated as they are questionably resolved when errors are considered. Additionally, these peaks cannot justifiably be indexed to a different, non-lamellar phase.

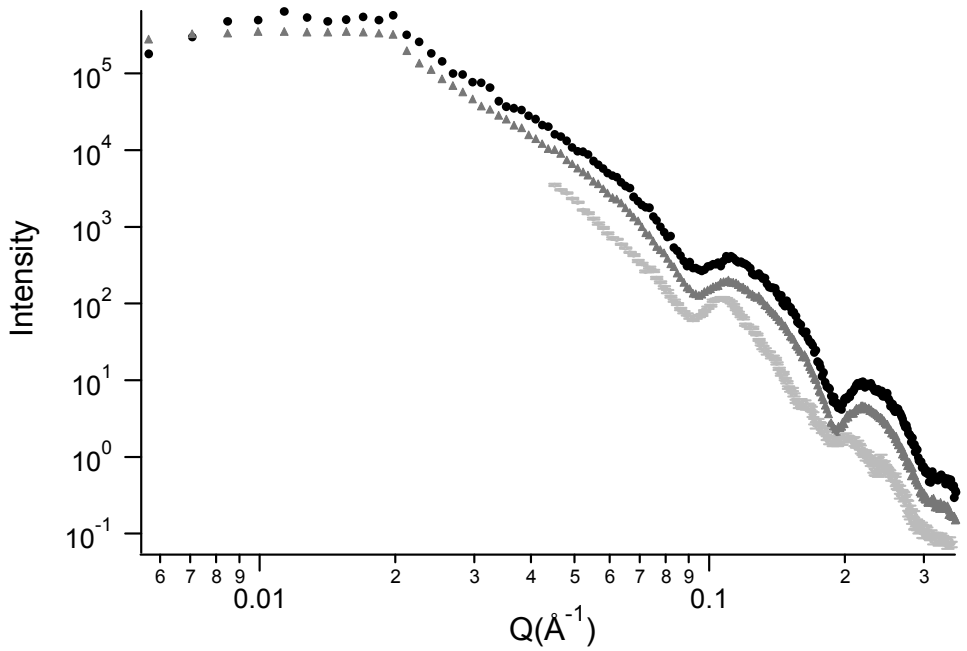

Figure 4-48 : X-ray reflectivity profiles showing variation with Ti(OBu^n)$_4$ content. Additions of 0.9 mMol (black circles), 2.2 mMol (dark grey triangles) are shown and 2.9 mMol (light grey diamonds) is shown with error bars as an example. Ddata is offset for clarity.

Modelling of these reflectivity patterns was undertaken using the Motofit program as detailed in the Experimental chapter, § 2.1.3,[28] however precise fits such as that in *Figure 4-49* were only possible in some cases. For details of the reflectivity modelling, including details of roughness and scattering length densities see *Appendix 1,* § 7.1.

In the case of FSO-100 variation, 2-3 layers of lamellae were adequate to model the data when 1.7 mMol of surfactant was used, while more layers were required at higher concentrations. For HCl variation a similar number of layers were used for acid contents of both 14 mMol and 21 mMol although when no acid was present a monolayer of surfactant at the interface suffices to model the data. Similar observations are made for Ti(OBu^n)$_4$ contents of 2.9 mMol and 2.2 mMol with a comparable number of layers used in modelling. However modelling was not possible in all cases and, due to the truncated nature of the scattering patterns, for 3 mMol of HCl and 2.9 mMol of Ti(OBu^n)$_4$ reliable modelling was not possible in these cases.

In all cases the models indicated a lamellar structure made up of a series of two distinct types of layers. Specifically, 18 – 21 Å fluorocarbon layers, corresponding to a

bilayer of the fluorinated headgroup, and 30 – 35 Å layers of a mixture of PEO and titania. These layers were assessed as a mixture of PEO and titania as the scattering length of the layers was greater than that of PEO alone, suggesting the inclusion of titania, see **Table 2-1**, § 2.1.1. This gives an overall layer thickness of 48 - 56 Å, somewhat smaller than the layer thicknesses derived from the peak positions and suggesting that incomplete ordering of the mesostructure and a small number of repeat units leads to broad, low intensity peaks that do not precisely reflect the existing structure. The continued evaporation of solvent, and therefore lowering of the surface, is also expected to broaden peaks making an accurate assessment of peak position and layer thickness problematic.

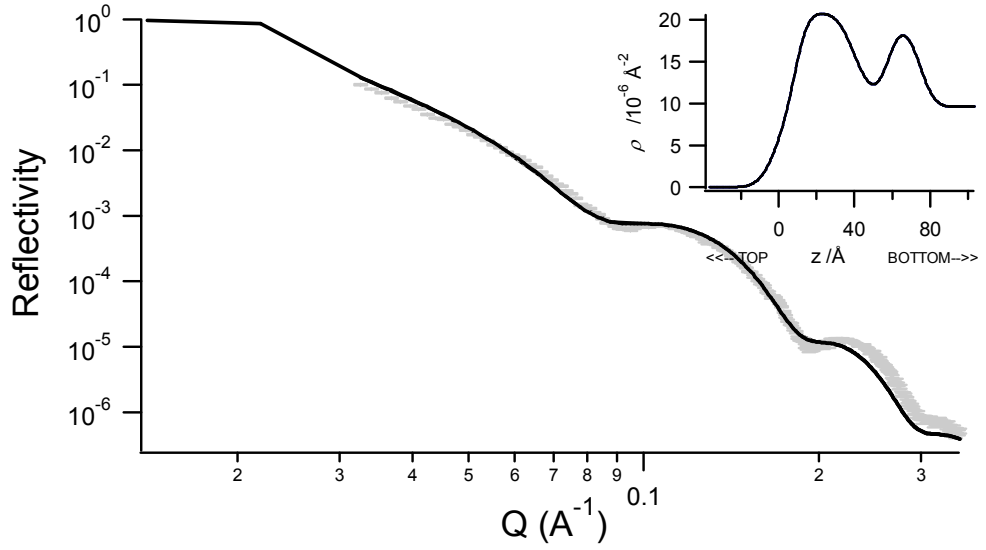

Figure 4-49 : Model of reflectivity data from a FSO-100 templated titania film from a solution using 1.2g of surfactant. Data is shown in grey and the model is shown in black.

Grazing incidence diffraction (GID) was also conducted on some film samples at the air-solution interface when sufficient solution remained to allow collection. However, as in the typical example in *Figure 4-50*, although a peak was observed at 0.1 $Å^{-1}$ no other peaks were observed.

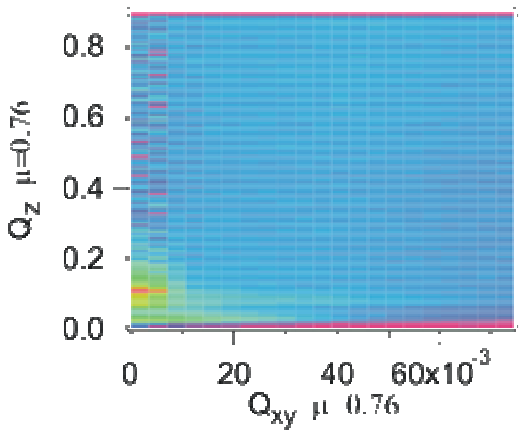

Figure 4-50 : GID pattern for a FSO-100 templated titania film grown on the air-solution interface.

4.2.4 Neutron Reflectometry

Neutron reflectivity experiments were conducted attempting to gain further insight into the film formation at the air-solution interface, however, the 15 minutes required for the collection of each reflectivity profile and rapid evaporation of the ethanol solvent complicated this work. A range of reagent concentrations were studied and, within the errors of the measurements, the results were found to be similar to each other for all reagent concentrations. Typical reflectivity profiles for these experiments are shown in *Figure 4-51* and a shoulder, or broad peak, was observed to appear in the reflectivity profile at approximately 0.1 $Å^{-1}$ in all cases. This is in agreement with observations of the lamellar phase of *d*-spacing 57 – 62 Å observed in X-ray reflectometry. The poor resolution of this peak is probably due to the changing height of the sample as ethanol evaporated during measurement.

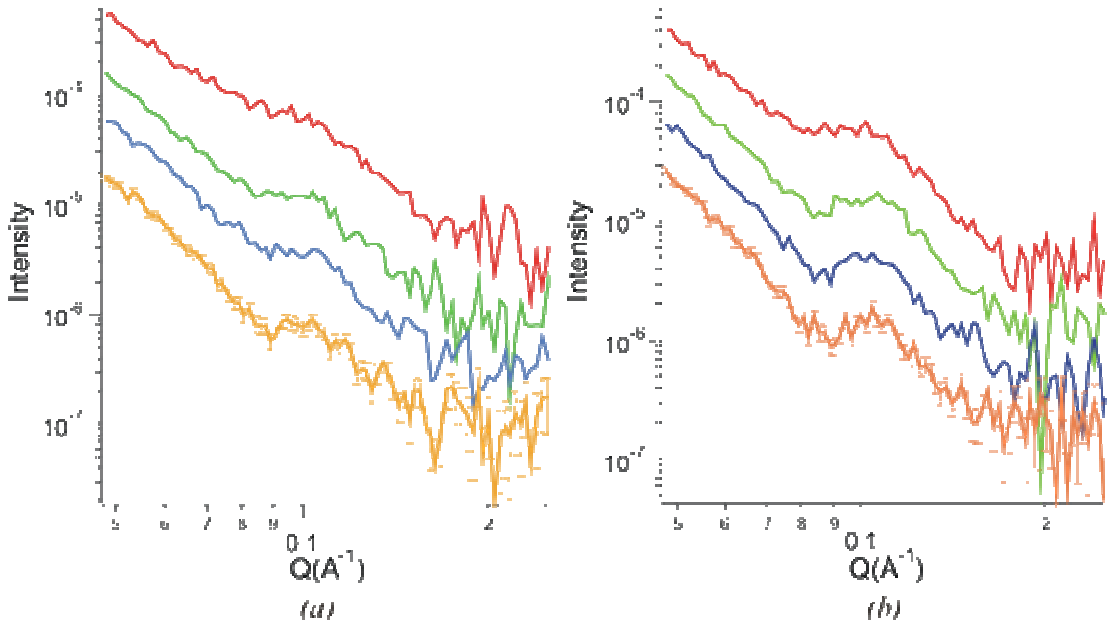

Figure 4-51 : Neutron reflectivity profiles for a standard FSO-100 titania film preparation, (a), and a preparation using 0.35 g of $Ti(OBu^n)_4$, (b). In both cases 15 minute scan beginning 10 (red), 25 (green), 40 (blue) and 55 minutes (orange) after pouring are shown. Data offset for clarity.

Although poorly resolved, the time required for the peak at 0.1 $Å^{-1}$ to appear was found to differ depending on the reagent concentration with the shoulder appearing fully developed within 45 minutes for all concentrations studied. After 45 minutes, the features of the scattering profiles became less defined and the errors more significant, possibly due to roughening of the films.

The variation in time to peak/shoulder development was consistent with Brewster angle microscopy studies of formation time with development occurring faster at higher acid and surfactant concentrations and a lower titania precursor concentrations. In some reflectivity profiles additional small peaks appear to be present however the errors are such that they cannot be identified with statistical confidence.

Data modelling of the neutron reflectivity patterns, detailed in *Appendix 2,* § 7.2, suggests the presence of a growing lamellar structure, however, the broadness of the peak complicates fitting. In all cases the reflectivity patterns could be modelled by a multilayer of consisting of 20 Å thick layers of fluorocarbon and 36 – 39 Å layers of a mixture of PEO chains and titania corresponding to a bilayer of surfactant headgroups and tails respectively. In the case of the PEO layers the inclusion of titania is identified by a

scattering length density that is too high to be due to PEO chains alone. *Figure 4-52* shows an example of such fitting for a film formed from a solution using 0.7g of HCl.

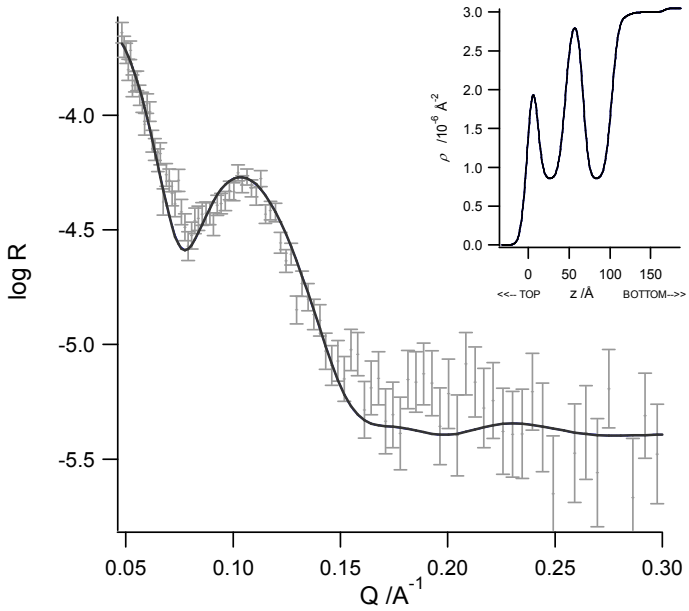

Figure 4-52 : Modeling of neutron reflectivity from a developing FSO-100 templated titania film. Experimental and the model are shown in grey and black respectively.

Reflectivity patterns collected immediately after pouring of the precursor solutions appear to be a mixture of scattering from 1 and 2 repeats of the lamellar system suggesting film development was occurring during collection. Subsequent patterns may be modelled by 2 repeats of the lamellae while patterns collected after 75 minutes appear to be a mixture of scattering from 2 and 3 repetitions. This development is considerably slower than expected and a loss of *Q* resolution due to evaporation is expected to produce artificially broad peaks in the reflectivity profiles that complicate modelling.

4.2.5 Electron Microscopy

Scanning electron microscopy was used to collect secondary electron images of the surface of FSO-100 templated titania films developed at the air-solution interface and removed to a microscope slide substrate and calcined. *Figure 4-53* shows that although most of the film remains smooth, uniform and solid after removal from the interface some areas have cracked and partially peeled from the substrate during drying or

calcination. It is also observed in the higher magnification image, *Figure 4-53 (b)*, that the film appears to consist of a solid network of particles separated by 5 – 20 nm channels suggesting that an open network may exist within the film material.

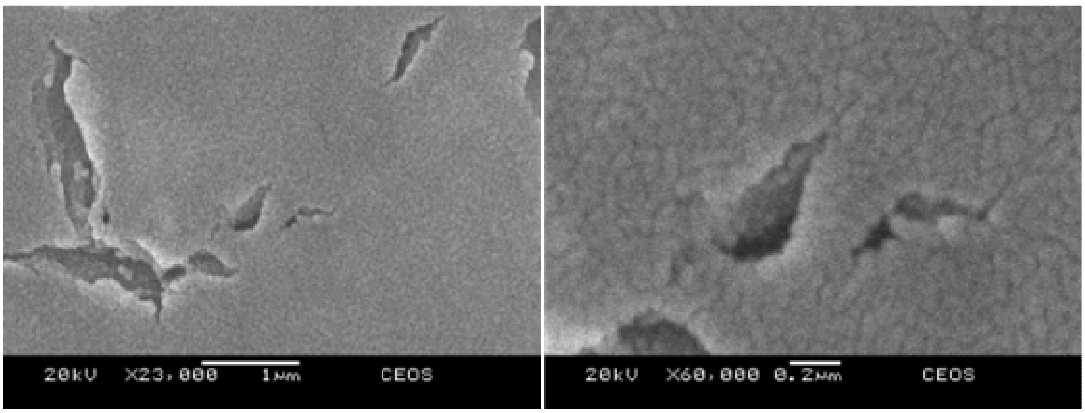

Figure 4-53 : Scanning electron microscopy of FSO-100 templated titania film material on a microscope slide substrate.

In addition to SEM imaging transmission electron microscopy images and electron diffraction patterns were collected for calcined FSO-100 templated titania film material. Although the film material was often too thick for TEM imaging it was possible to image the edges of particles as shown in *Figure 4-54*. These images show a regular, porous matrix of titania particles, the presence of titania confirmed by electron probe microanalysis, held together into a solid film. The pores in the material are observed to be of the order of 10 nm in diameter which is sufficient to allow the diffusion of many organic compounds.

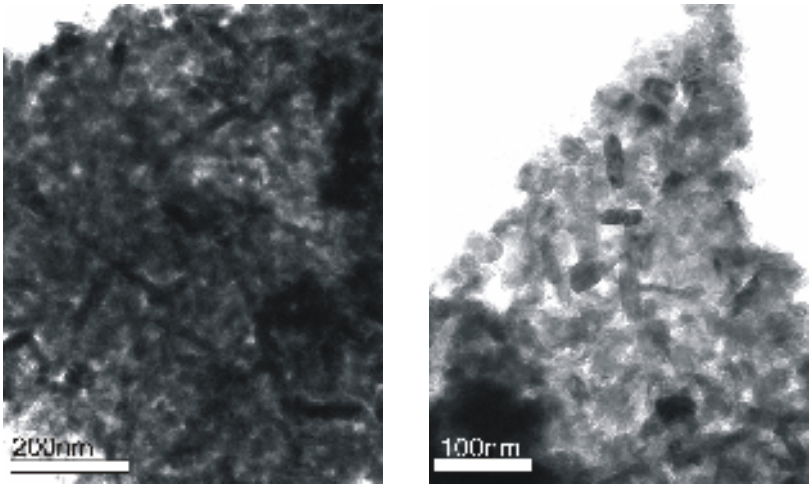

(a) *(b)*

Figure 4-54 : Transmission electron material of film material formed at the air-ethanol interface. Images (a) and (b) are of the edge of film particles in different locations.

An ordered film is also suggested in electron diffraction patterns collected from the same area of film material used for imaging. The diffraction pattern in *Figure 4-55* shows a number of diffraction rings that, although not perfectly resolved, suggest a structured material. Two inner rings and two outer rings are visible, characteristic of the *Ia3d* cubic phase however both TEM images and electron diffraction suggest that this is somewhat disordered in the film material.[29] As the *Ia3d* phase may be considered as a bicontinuous phase of twisted lamellae this suggests a distortion of the lamellar film structure after removal from the interface.

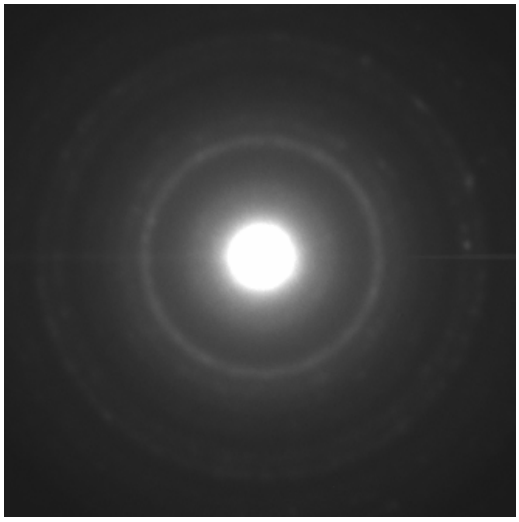

Figure 4-55 : Electron diffraction pattern from FSO-100 templated titania film material

4.2.6 Nitrogen Adsorption

The nitrogen adsorption and desorption isotherm shown in *Figure 4-56* was collected for FSO-100 templated titania film material removed from the air-solution interface, dried at room temperature in air and calcined at 600 °C for template removal. The isotherm was assessed as a Type IV isotherm corresponding to the adsorption and desorption from a mesoporous powder with a characteristic hysteresis loop in the desorption branch of the isotherm, see § 2.1.6. The BET surface area was calculated as 85 m^2g^{-1} using data in the partial pressure range of 0.06 – 0.29. This is considerably larger than the 23 m^2g^{-1} estimated by calculation of randomly packed spherical voids in a titania matrix suggesting that the film material is porous after calcination supporting the presence of a bicontinuous cubic phase such as *Ia3d*.

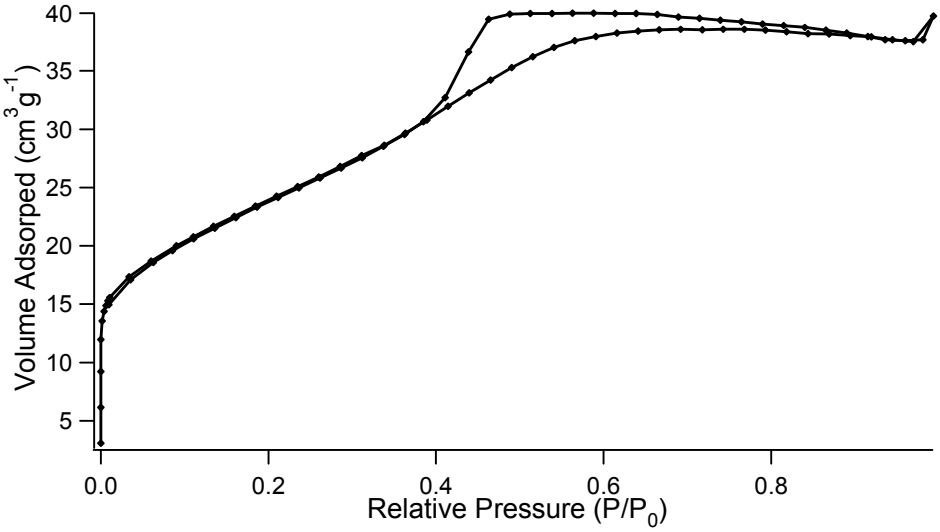

Figure 4-56 : N_2 adsorption and desorption isotherm for calcined FSO-100 templated film material

Additionally, a pore size distribution was calculated from the adsorption and desorption branches of the isotherm as shown in *Figure 4-57*, however calculations from the adsorption branch are considered more reliable. The largest number of pores appears to be in the 16 Å radius range however the distribution of smaller sizes is uncertain as it cannot be reliably calculated with the Kelvin equation, see § 2.1.6.

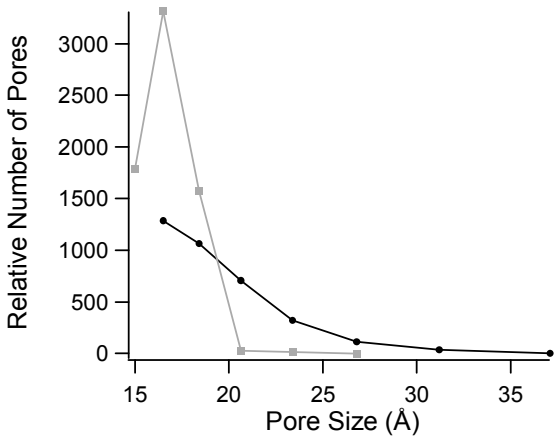

Figure 4-57 : Pore size distribution for FSO-100 templated film material calculated from the adsorption (black) and desorption (grey) branches of the isotherm.

4.2.7 Thermogravimetric Analysis

Thermogravimetric analysis was performed in order to assess the amount of solvent and organic, i.e. surfactant, in film material recovered from the air-solution interface. As shown in *Figure 4-58* the resulting TGA curve did not have plateau regions that would make it possible to clearly identify one evaporation or decomposition stage from another. However, 8% of the original mass remains after calcination at 600 °C indicative that the inorganic content of the films is low.

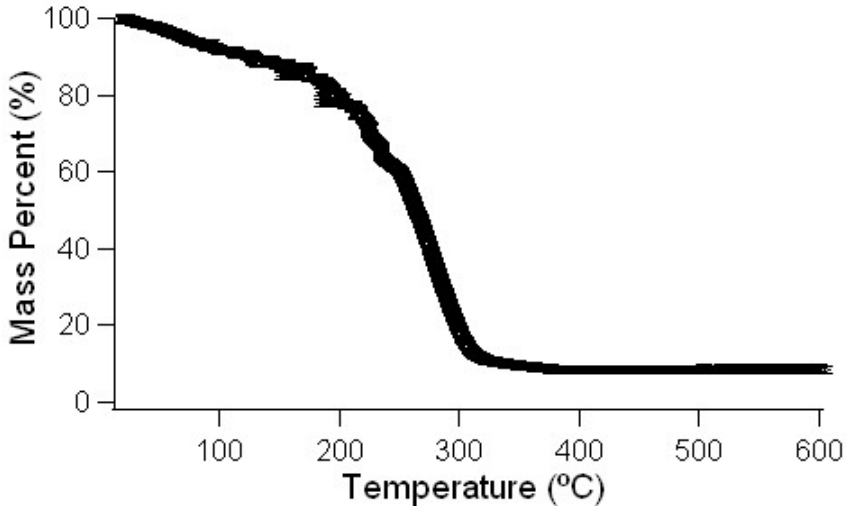

Figure 4-58 : Thermogravimetric analysis of FSO-100 – Titania film material recovered from the air-solution interface. Errors shown are approximate.

4.3 Fluoro-Surfactant Templated Titania Films - Discussion

4.3.1 Titania Film Formation

FSO-100 templated titania film formation at the air-solution interface has been observed to occur gradually, over a period of hours, in Brewster angle microscopy and time-resolved X-ray reflectometry experiments. The presence of titania precursors has been observed to be a requirement for film formation indicating the formation of a self-assembled titania-fluorosurfactant film for the first time, to our knowledge. The gradual loss of the specular peak in time-resolved X-ray reflectometry, the continued development after initial film formation observed in BAM and the growth of peaks observed in neutron reflectometry are all indicative of a gradual formation mechanism.

This gradual development is characteristic of the surface driven formation mechanism in which individual surfactant micelles or molecular species diffuse to the surface and add to a film at the interface that continues to grow in thickness, see § 1.3. Such mechanisms have been reported for the formation of surfactant templated silica materials at specific concentrations with similar reflectometry and BAM observations.[30,31] In this case micelle aggregation prior to film formation did not occur and development of the silica film was reported to be due to individual, coated micelles adding to an initially thin film at the interface and it is likely that a similar mechanism is occurring in the present work.

If, on the other hand, film formation was occurring due to the coalescence of existing micelle aggregates, as has been reported for silica powders and films,[31-33] a rapid transition would be expected in both BAM and reflectometry experiments.[30,34] The absence of sudden interfacial change in BAM observations, or rapid loss of the specular peak, in time-resolved reflectometry both suggest that this is not the case and that development from micelle aggregates is not occurring. No development was observed in SANS experiments to study solution phase development at equivalent concentrations confirming the lack of aggregation in solution.

In the silica case cylindrical micelles coated by silica precursor were reported to add to the film to produce a hexagonally ordered silica-surfactant film. Examination of the FSO-100 – ethanol phase diagram and the highly surface active nature of fluorinated surfactants suggest that spherical micelles exist in the precursor solution prior to film formation and no cylindrical micelle phase was observed, **Table 4-2**. Additionally, the observation of lamellar or bicontinuous structure in developed films, *Figure 4-46*, *4-8* and *4-9*, at the air-solution interface suggests that micelles are not adding to the surface in precisely the same manner as reported for silica films.

Instead it appears that either individual molecular species add to an existing lamellar phase, as has been reported for titania films in aqueous systems,[27] or that micelles adding to the film collapse and add to the lamellar phase. Given that the presence of titania precursors is required for film formation and that a monolayer of fluorinated surfactant is expected to exist at the surface, as is well established for other surfactants at or below the CMC,[35] then a surface development mechanism may be expected. In the case of the FSO-100 surfactant it is expected that the perfluorinated section of the surfactant is uppermost in the monolayer due to its incompatibility with the ethanol solvent and a co-operative, surface driven assembly mechanism is proposed as shown over the page in *Figure 4-59*.

For Pluronic surfactants the separation, due to repulsion, between micelles is due to the entropically unfavoured overlap of PEO sections at the exterior of the micelle rather than electrostatic repulsion for ionic surfactants.[32,36] When such surfactants are used as templates for ordered inorganic materials the coating of surfactant micelles by inorganic precursors provides a barrier to PEO chain overlap and micelle aggregation becomes possible as a result.[34] Interactions between growing inorganic oligomers and PEO chains, hydrogen bonding or hydrophilic – hydrophilic interactions in the case of titania,[37] leads to the envelopment of the surfactant micelle by inorganic material. Although such interactions may be in competition with water in the system it is suggested that the large number of interaction sites available from inorganic oligomers leads to their strong interaction with the surfactant. However, until sufficient inorganic material is bound to the micelles to prevent PEO chain overlap it may be expected that this unfavoured interaction will dominate the structures formed.

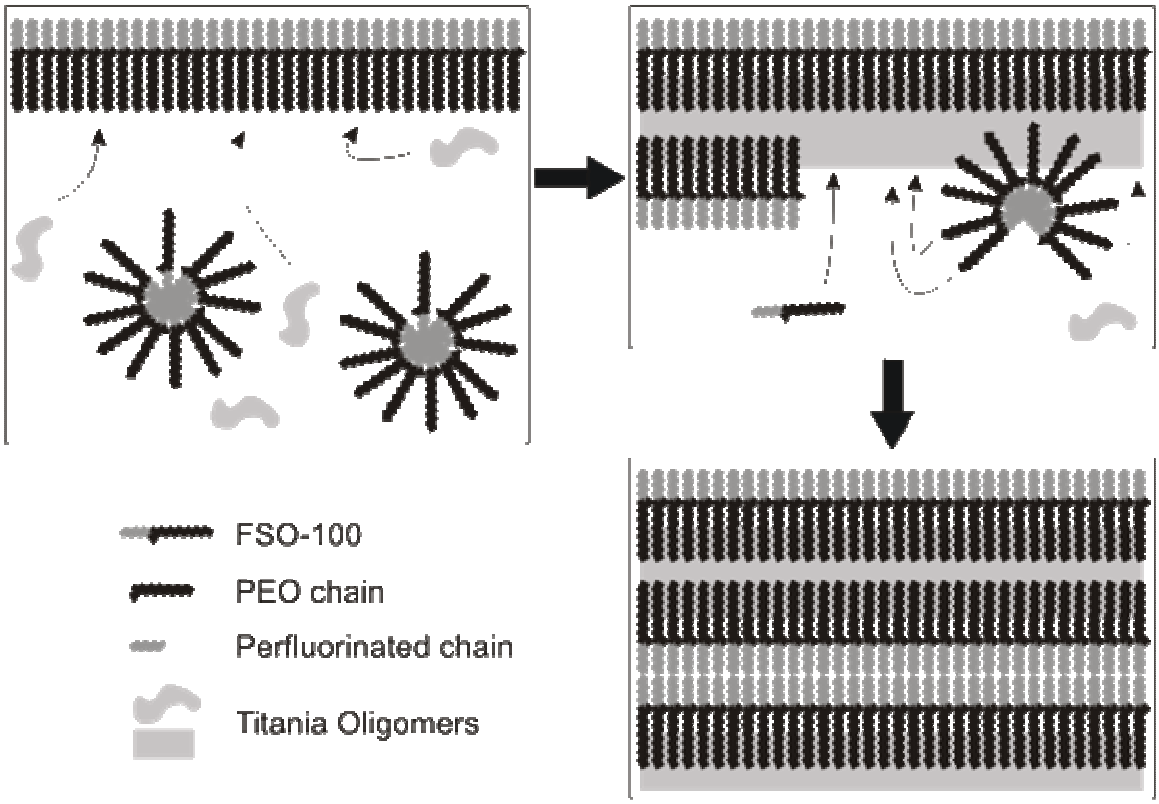

Figure 4-59 : Proposed formation mechanism for FSO-100 templated titania films

Given the PEO section of the FSO-100 surfactant it is likely that the growth of a lamellar phase, although often favoured even for short chain fluorinated surfactants, is prevented by the unfavoured interaction between PEO groups that would result. The addition of an inorganic precursor leads to the formation of a barrier between the PEO sections allowing a bicontinuous/lamellar phase to form of pure layers of perfluorocarbon headgroups and a mixed layers of PEO and titania. Such mixed layers may be expected to contain a small amount of titania, sufficient to provide a barrier to PEO chain overlap but little larger, leading to the low inorganic content in the films observed in thermogravimetric anaylsis experiments.

Data modelling of reflectivity profiles supports these observations as the 20 Å thickness of the fluorocarbon layer observed corresponds to twice the length of the fluorinated section of the surfactant, as expected for a bilayer. The favouring of bilayer structures by flurosurfactants and the established interactions between titania precursors and PEO groups also support the proposed mechanism.[9,37]

This interaction between PEO groups and titania precursors is observed in the decrease in film formation time observed at higher acid concentrations in BAM experiments, *Figure 4-43 (a)*. Although the results of HCl and $Ti(OBu^n)_4$ variation experiments suggest that film formation occurs faster at higher for higher H_2O : Ti ratios the titania precursors are expected to be fully hydrolysed during the premixing of HCl and $Ti(OBu^n)_4$ prior to mixing with the surfactant solution, see § 1.2.2. This suggests that the effect of water content on film formation time is not related to the reactions of the inorganic precursors, as does the observation that formation time decreases in spite of increased acid concentration hindering the condensation reactions of the titania.[10,11,37] However, the interactions between titania species and PEO are known to be greater if acidic water is present[37] and the greater interaction between the species at higher water contents is expected to lead to a faster coating of the PEO layer.

This increased interaction allows faster lamellar formation and faster film formation as observed in BAM experiments. Brewster angle microscopy results also agree with the expectation that film formation will be faster at higher surfactant concentrations as more surfactant will be readily available for the formation of each lamellar layer, *Figure 4-43 (c)*. The addition of greater amounts of $Ti(OBu^n)_4$, on the other hand, may be expected to reduce the H_2O : Ti ratio and, as a result, reduce the interaction with PEO groups leading to slower film formation as observed, *Figure 4-43 (b)*. It may be expected that at sufficiently high concentrations of titania precursor the increased concentration would outweigh the effects of reduced interaction, however, this concentration is not reached in the concentration range studied.

4.3.2 Titania Film Structure

FSO-100 templated titania films are observed to have a lamellar structure during in-situ X-ray reflectometry experiments while electron microscopy images suggest the presence of three dimensional order, *Figure 4-54*, and electron diffraction suggests the film material has a disordered *Ia3d* cubic structure, *Figure 4-55*. The presence of a lamellar film with an interlayer, *d*-spacing of 57 Å at the air-solution interface is observed in reflectivity profiles and data modelling for all reagent concentrations except for the highest $Ti(OBu^n)_4$ concentration when a 62 Å *d*-spacing is observed, *Figure 4-48*.

Furthermore, peaks observed in neutron reflectivity and modelling of this data match the observations of X-ray experiments.

Although these results firmly suggest that the in-situ film has a lamellar structure of uniform thickness, at different concentrations the sharpness of the peaks is observed to vary at different reagent concentrations. Both a higher degree of uniformity in the lamellae or an increased number of layers are expected to produce sharper peaks and it is the latter of these possibilities that is expected to produce the sharper peaks observed for some reagent concentrations in the present work.

Brewster angle microscopy experiments have shown that the films continue to develop at the air-solution interface for a period of hours after the initial formation. As X-ray and neutron reflectivity profiles were collected within 2-3 hours of pouring the precursor solution, a timescale limited by evaporation, it is likely that the films are incompletely developed when reflectivity profiles are collected. It is therefore expected that faster developing films will have formed more lamellar layers, and will feature shaper Bragg peaks in reflectivity profiles, than slower forming films.

This is indeed the case for higher FSO-100 concentrations, *Figure 4-47*, in agreement with faster film formation at higher surfactant concentrations. The presence of additional surfactant in solution can be expected to increase the number of lamellar layers that form in the film as a straightforward result of increased availability within the precursor solution. This is supported by data modelling of reflectivity profiles, detailed in *Appendix 1*, § 7.1, for high and low concentrations of surfactant in which more lamellar layers are observed at high concentration. Data modelling shows a similar trend in the variation of the number of lamellar layers observed for different titania and acid concentrations. For $Ti(OBu^n)_4$ and HCl variation the changes are also expected to be primarily due to the number of lamellar layers, however, increased polydispersity or roughness in the layer thickness may also broaden features in the reflectivity profile.

At higher titania concentrations it may be expected that a larger amount of titania becomes incorporated into the inorganic rich layers of the lamellar structure resulting in a larger number of layers of variable thickness. It is proposed that as the titania layers of the lamellae grow there is competition between the continued incorporation of titania

forming a thicker layer and the coating of surfactant to form a new lamellar layer underneath.

At low titania concentrations the growing inorganic layer is rapidly coated by surfactant, once PEO chain overlap is prevented, resulting in uniform layers. At higher concentrations some areas gain a surfactant coating quickly while titania continues to become incorporated in other areas resulting in layers of polydisperse thickness. Growth of the inorganic is greater at higher concentrations with very high titania concentrations producing films of highly polydisperse and larger average thickness as in the case when 1g of $Ti(OBu^n)_4$ is used. Such layers are expected to generate a higher inorganic content in the film material, above the 8% mass observed for a 'standard' preparation, see *Figure 4-58*, and TGA experiments at different inorganic precursor concentrations are recommended as an area for further research.

The competition between the addition of surfactant and inorganic species to the growing lamellae is also observed for varied acid concentration, as the attractive hydrogen bonding and hydrophilic-hydrophilic interactions between the PEO chains and titania species is greater for higher acid concentrations leading to faster formation.[37] At lower acid concentrations the slower film formation, as observed in BAM, due to lower interaction between titania precursors and PEO groups, is expected to provide a greater opportunity for the material to form into highly uniform layers while fast film formation, at high concentration, is expected to produce greater disorder in the layers as there is little time for adjustment.

Although the films are confidently assigned a lamellar structure in-situ at the air-solution interface the structure of dry, calcined film material removed from the interface appears different in electron microscopy studies. TEM imaging suggests the presence of a porous, three dimensionally structured material and electron diffraction suggests that the film material has the *Ia3d* cubic structure. Additionally, the presence of a mesoporous network in calcined titania film material is supported by nitrogen adsorption and SAXS experiments and modelling shows the presence of oblate ellipsoidal voids in the crystalline titania film material after calcination. This difference between the in-situ and calcined film structure suggests a phase transition may be occurring after a film is removed from the interface to form a cubic, rather than a lamellar, structure.

It has been previously reported that the assignment of a symmetry space group, *Ia3d* in this case, does not unequivocally designate a structure as multiple structures may have similar symmetry.[38] Of particular relevance, the biphasic *Ia3d* structure may be formed by a series of twisted lamellae[39] rather than close packed micelles and, although the mechanism of transition between lamellar and bicontinuous cubic phases remains uncertain, such transition are known in the literature and a bicontinuous *Ia3d* structure has been observed for a partially fluorinated surfactant.[40,41] Therefore it is possible that the cubic structure formed by the FSO-100 – titania film is due to twisting of the existing lamellar phase rather than the formation of a new micelle phase. Surfactant structures existing in equilibrium within the films at the air-solution interface may become disturbed upon removal from the interface due to evaporation.

Synthesis of titania materials using Pluronic surfactants found solvent remained in the product and it is expected that in the solution conditions used in the present work that ethanol and hydrochloric acid will be trapped within the titania – FSO-100 film.[37] The loss of these impurities as the film dries may lead to distortion of the lamellar structure to a favoured bicontinuous cubic phase. This process can be considered similar to changes occurring during the modulable steady state period of evaporation induced self-assembly in which the film has reached a stable equilibrium structure that may be altered to a different structure if the equilibrium is disturbed, see § 3.1.1.[42]

Given that study of the phase diagram of the FSO-100 surfactant did not note the presence of a lamellar phase at, or below, 90% wt. surfactant, see **Table 4-2**, it is probable that the formation of a lamellar phase is encouraged by the presence of a surfactant monolayer at the interface. Instead, at high surfactant concentrations, a high density of ellipsoidal micelles is observed in the surfactant phase diagram that may also correspond to a biphasic structure. After removal from the interface the monolayer effect is removed and a disordered cubic structure of twisted lamellae forms as impurities evaporate from the film material.

This transition gives rise to the disordered cubic structure observed in TEM images as it is recognised in surfactant templating that concurrent inorganic condensation and micelle ordering produce a race between the development of a highly ordered material and setting of the inorganic phase into a non-malleable solid.[43,44] Rapid

condensation can limit ordering as in the setting of a disordered cubic phase due to an incomplete structural transition that has been reported for silica powders[43] and the variation in the size of oblate ellipsoidal voids calculated in SAXS modelling suggests an incomplete phase transition in the present work.

Comparison of the voids sizes from modelling, **Table 4-3**, and formation time variation observed in BAM experiments, *Figure 4-43*, shows that the trend in void size may be related to the formation time. Specifically, smaller voids are observed for material from solutions exhibiting faster film formation. As each film was left for a comparable amount of time (2 hours) after initial formation before material was collected from the interface it is probable, and in agreement with observation by eye, that faster forming films had thicker films at the time of collection. Evaporation of solvent and acid, a requirement for full inorganic condensation,[42] from a thicker film is expected to be slower than in thinner films allowing more time for a phase transition to occur in such cases.

It is therefore suggested that the thicker films allow for a more complete transition from a lamellar phase toward a disordered bicontinuous cubic phase with ellipsoidal units comparable to that observed in study of the FSO-100 phase diagram. It is noted that prolate ellipsoids are observed in surfactant phase studies while oblate ellipsoids are noted after the phase transition however this is expected to be due to an incomplete phase transition in the latter case. An incomplete structural transition is expected to produce a disordered material and may explain the disorder seen in the film material.

This disorder is such that although diffraction rings are observed in electron diffraction experiments the assignment of an *Ia3d* structure is tentative as the rings are not well resolved and it is possible that additional diffraction rings appear absent due to their low intensity. In particular, some *Im3m* cubic structures are reported to have weak (013) and (222) peaks the absence of which may give the appearance of an *Ia3d* structure.[38] Further experiments are therefore recommended to confirm the nature of the cubic structure present in the film material.

The disordered material clearly appears porous in TEM images, an observation confirmed by nitrogen adsorption experiments in that show a clear hysteresis loop characteristic of mesoporous materials.[45] The isotherm is assessed as Type IV, see §

2.1.6, corresponding to mesoporous powders, and as the BET equation is valid for such cases[45] it is possible to calculate the surface area of the film material as 85 m^2g^{-1}. Although this is smaller than the 390 m^2g^{-1} reported for some titania powders[46] it is considerably greater than the 23 m^2g^{-1} calculated for randomly packed 20 nm spheres, based on particle size in TEM images, confirming that the film material is highly porous.

The mesopores of the film appear to be of the order of 10 nm in diameter in TEM images, however, use of the Kelvin equation to calculate a pore size distribution from the adsorption branch of the nitrogen isotherm suggests smaller pores. Pores of a maximum 25 – 30 Å in radius with a larger number of smaller pores are calculated, however the Kelvin equation is recognised to underestimate pore sizes with a 30% error for 20 Å pores.[45] This suggests that the true upper limit of the pore radius is 30 – 35 Å in agreement with modelling of SAXS results from calcined film material. Such a pore size gives an upper diameter of 70 Å comparable to, but slightly smaller than, the pore size observed in TEM images.

As the titania and PEO chains are mixed in the bicontinuous structure it is expected that loss of the PEO material during calcination leads to larger 7 nm pores developing. Additionally, the pores are expected to be of a sufficient size to allow the diffusion of organic molecules such as a photosensitive dye into the pores suggesting that the film material could developed for areas such as photovoltaics or catalysis. Although no precise measurements of film thickness have been possible the films are suggested to be over 300 nm in thickness as TEM imaging found much of the film material too thick for imaging.

4.4 Fluoro-Surfactant Templated Zinc Films – Results

4.4.1 Brewster Angle Microscopy

The formation of zinc films at the air-solution interface using the partially fluorinated surfactant Zonyl FSO-100 was undertaken to observe the film formation effects of different reagent concentrations on formation time. The film formation was observed to proceed in a similar manner to that observed for titania films with an initially highly mobile interface found to progress gradually to a completely stationary interface in approximately 50 minutes for a standard preparation, see § 2.3.3, and the presence of the inorganic precursor was required for film formation to occur. As shown in *Figure 4-60*, immediately after pouring into a Petrie dish the surface was found to be highly mobile with stationary spots due to the FSO-100 surfactant and movement was found to slow gradually before ceasing entirely, indicative of film formation. After a film had formed at the air-solution interface it was observed to continue to develop, appearing clearer and rougher in the BAM images, *Figure 4-60 (c)*.

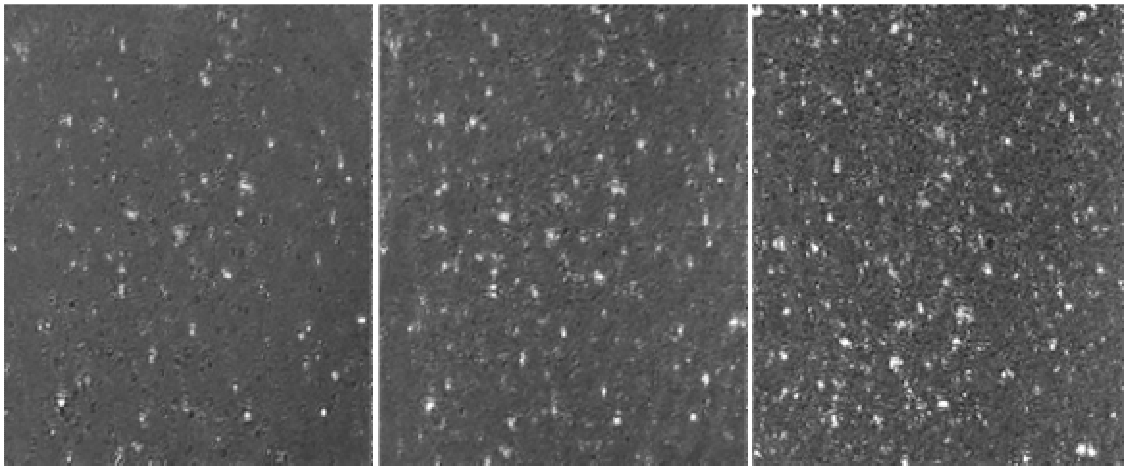

Figure 4-60 : Brewster angle microscopy images of a FSO-100 templated zinc film forming at the air-solution interface. Image (a) shows the surface directly after pouring while images (b) and (c) show the surface after 47 minutes, when a film has formed, and 174 minutes respectively. The BAM images are 477 x 385 μm in each case.

Taking the point at which a completely stationary interface is observed in BAM images as the point of film formation the effect of different reagent concentrations on film formation time was studied in a similar manner to that of titania films, § 4.2.1. The results of these experiments are shown in *Figure 4-61* and it is observed that the formation time decreases for higher FSO-100 concentrations with a minimum formation time of 50 minutes. In comparison, formation time increases for higher $ZnCl_2$ concentrations in a relatively smooth progression from 40 minutes for 1.0 mMol to 100 minutes for 4.0 mMol of $ZnCl_2$. More complex behaviour is observed for acid variation as a minimum formation time is observed for a HCl content of 15.0 mMol in the precursor solution above or below which the formation time is found to increase.

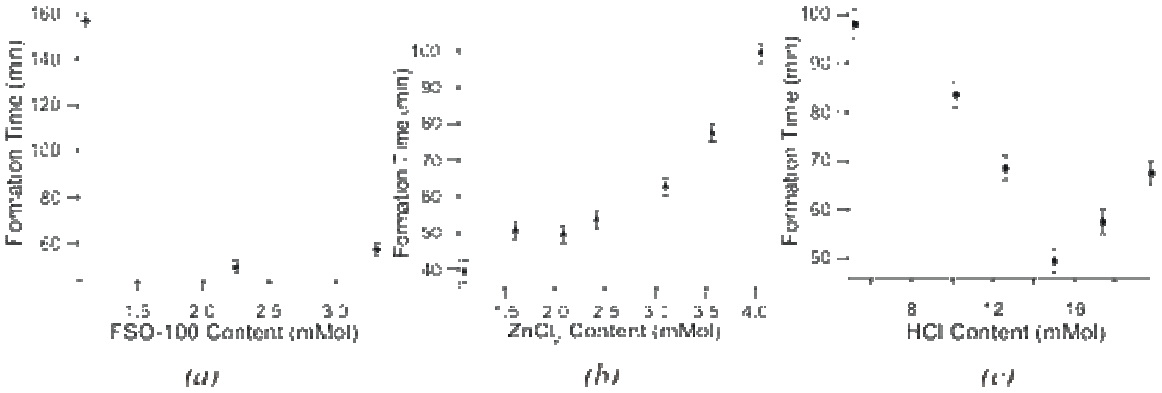

Figure 4-61 : Variation of formation time with reagent concentration observed by BAM. FSO-100, $ZnCl_2$ and HCl variation results are shown in (a), (b) and (c) respectively.

4.4.2 X-ray Reflectometry

Time resolved off-specular reflectometry was conducted at the ESRF, France to observe film formation and structure development at the air-solution interface. The majority of these experiments did not show significant change in the off-specular profile during film development as shown in *Figure 4-62 (a)*, although a gradual reduction in the intensity of the specular peak was observed. However, when 6.2 mMol of $ZnCl_2$ was used, *Figure 4-62 (b)*, a transition in which specular reflection is lost and two peaks grow at 0.090 $Å^{-1}$ and 0.093 $Å^{-1}$ corresponding to 70 Å and 68 Å respectively. After 30 minutes (after pouring) the transition ends and the peak at 0.09 $Å^{-1}$ is lost while specular reflection

is restored. Slow development expected for a high $ZnCl_2$ concentration suggests that development at lower concentration may be too fast to be observed with the 1 minute scans used in the off-specular experiments.

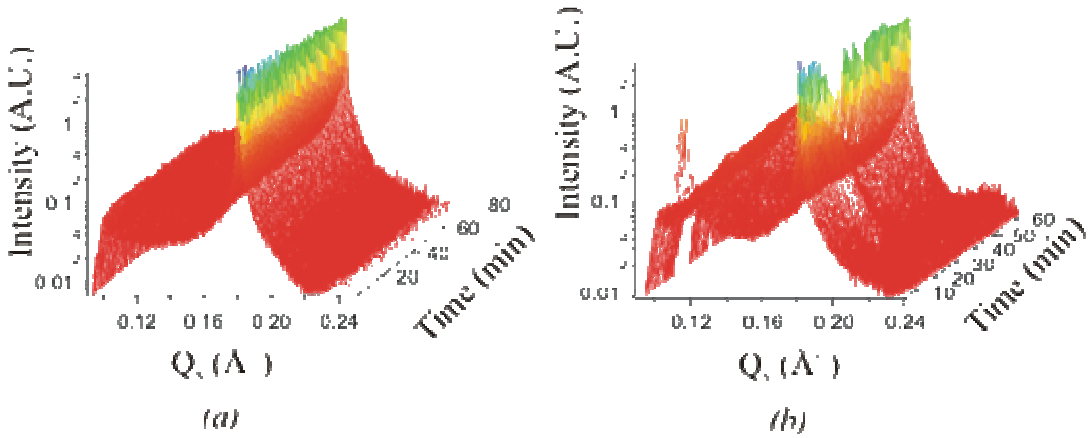

Figure 4-62 : Time resolved off-specular reflectivity from Zn films growing at the air-solution interface. The pattern from a standard preparation (a) is typical for most solutions while (b) shows formation for a solution with 6.2 mMol of $ZnCl_2$.

In addition to time-resolved experiments angle dispersive X-ray reflectometry was used to investigate structural changes in FSO-100 templated zinc films at different reagent concentrations. In some cases the evaporation left the interface below the edge of the PTFE trough preventing data collection at low *Q* values and where applicable reflectivity profiles have been truncated.

In the case of surfactant content variation, peaks are observed at 0.117 $Å^{-1}$ and 0.227 $Å^{-1}$ for each concentration studied as shown in *Figure 4-63*. This is consistent with a lamellar structure with an interlayer *d*-spacing of 54 Å in each case. However, it was observed that the peaks are progressively more sharply resolved at higher surfactant concentrations with the sharpest peaks observed when 3.3 mMol of surfactant was used, 150% of the standard concentration. This observation of sharper peaks suggests greater ordering or an increase in the number of layers present at higher FSO-100 concentrations in a similar manner to that observed for FSO-100 – titania films.

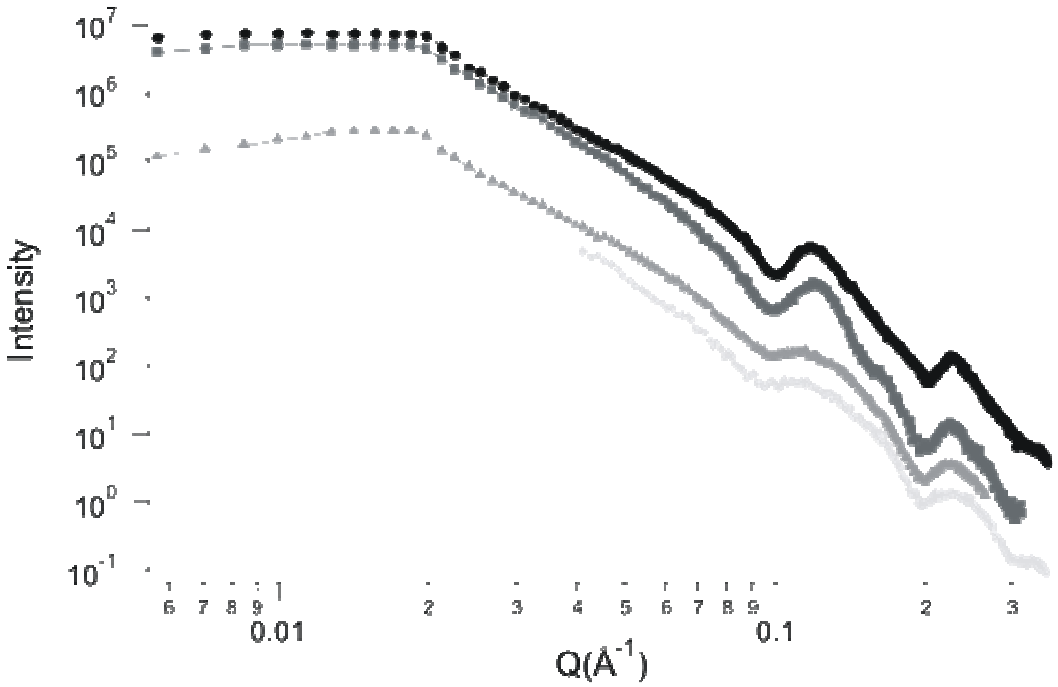

Figure 4-63 : X-ray reflectivity profiles showing changes in zinc oxide films as FSO-100 content is varied. Additions of 1.1 mMol (very light grey), 1.7 mMol (light grey), 2.2 mMol (dark grey) and 3.3 mMol (black) of FSO-100 are shown. Data has been offset for clarity.

For concentration variation of the inorganic precursor, $ZnCl_2$, the effects are less pronounced than for variation of the surfactant as shown in *Figure 4-64 (a)*. A lamellar structure is observed for all concentrations within the 1.0 – 6.2 mMol $ZnCl_2$ range studied with Bragg peaks consistently observed at 0.12 $Å^{-1}$ and 0.23 $Å^{-1}$ corresponding to a *d*-spacing of 54 Å, consistent with observations for surfactant variation. The sharpness of the peaks varied slightly at different $ZnCl_2$ concentrations, however, the changes were neither as pronounced or consistent as for FSO-100 variation.

Variation in the structure of the films is more pronounced in the case of acid variation as shown in *Figure 4-64* (b). In this case similar Bragg peaks are observed from a lamellar structure with a *d*-spacing of 54 Å however they are much more clearly resolved for the addition of 15 mMol of HCl than at either higher or lower concentrations suggesting a greater degree of ordering, or a larger number of lamellar layers, at this concentration. This corresponds to the concentration of fastest film formation in Brewster angle microscopy results and faster formation may lead to an increased number of layers.

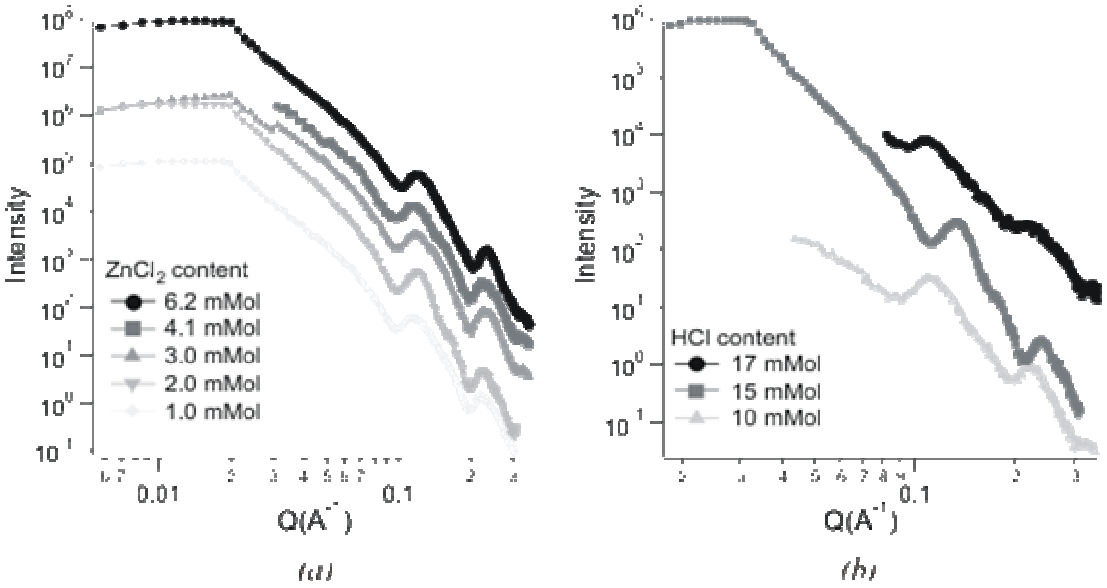

Figure 4-64 : X-ray reflectivity profiles for Zn films with $ZnCl_2$, (a), and HCl, (b) variation. In both cases the additions of reagents are shown on the graph key and data is offset for clarity.

The Motofit reflectivity modelling program was used to fit the X-ray reflectivity data corresponding to various reagent concentrations the full results of which are detailed in *Appendix 3*, § 7.3. The scattering length densities used during modelling are listed in **Table 2-1**, § 2.1.1. It was found that, as shown in *Figure 4-65*, for films featuring broad Bragg peaks such as low FSO-100 concentrations a few lamellar layers provided an adequate fit, however a bicontinuous phase may be present.

For reagent concentrations at which shaper peaks are observed additional lamellar layers were required with 6 – 8 layers used in the case of high FSO-100 concentrations. In the case of $ZnCl_2$ variation 2 – 3 layers were sufficient to model the data in all cases within the 1.0 – 6.2 mMol range studied. The truncated nature of the reflectivity patterns for different acid additions and for a $ZnCl_2$ addition of 4.1 mMol prevented data modelling in these cases as the lack of a critical edge prevents the accurate scaling of the reflectivity.

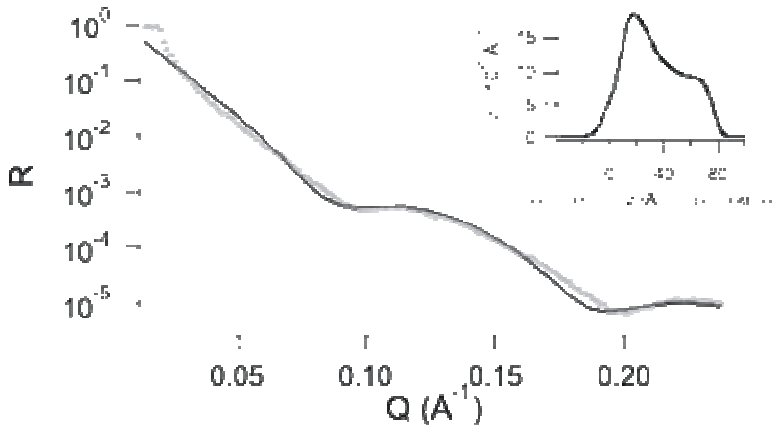

Figure 4-65 : Example of modeling of X-ray reflectivity profile from a FSO-100 templated ZnO film.

The structure of developed FSO-100 templated zinc films at the air-solution interface was also studied using grazing incidence diffraction (GID) to structural peaks. However, as shown in the typical pattern in *Figure 4-66*, these diffraction patterns only showed peaks consistent with a lamellar phase. The single peak at 0.12 $Å^{-1}$ is consistent with angle dispersive reflectometry observations.

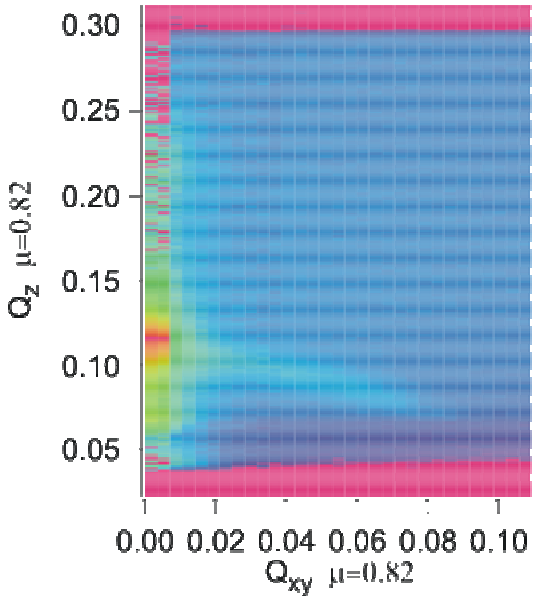

Figure 4-66 : GID pattern for a Zn film developed with 2.4 g FSO-100.

4.4.3 Neutron Reflectometry

Neutron reflectometry experiments were conducted on the SURF reflectometer at ISIS, United Kingdom in order to further investigate the development of the FSO-100 templated zinc films at the air-solution interface, however, limitations on experimental time meant few samples were run. A standard film preparation, see § 2.3.4, and samples utilizing 50% of the normal amounts of $ZnCl_2$ and HCl were studied and the development was observed to be similar in all cases.

As shown in the profiles in *Figure 4-67*, for a standard film preparation, a broad peak was observed to develop at 0.11 $Å^{-1}$ (57 Å) and was observed to continue to develop for up to 70 minutes. This position of this peak was consistent for all samples studied, however delays in between scans make a comparison of the formation time impossible. The poor resolution of the peak may be due to development and evaporation occurring during the 15 minutes required for each measurement.

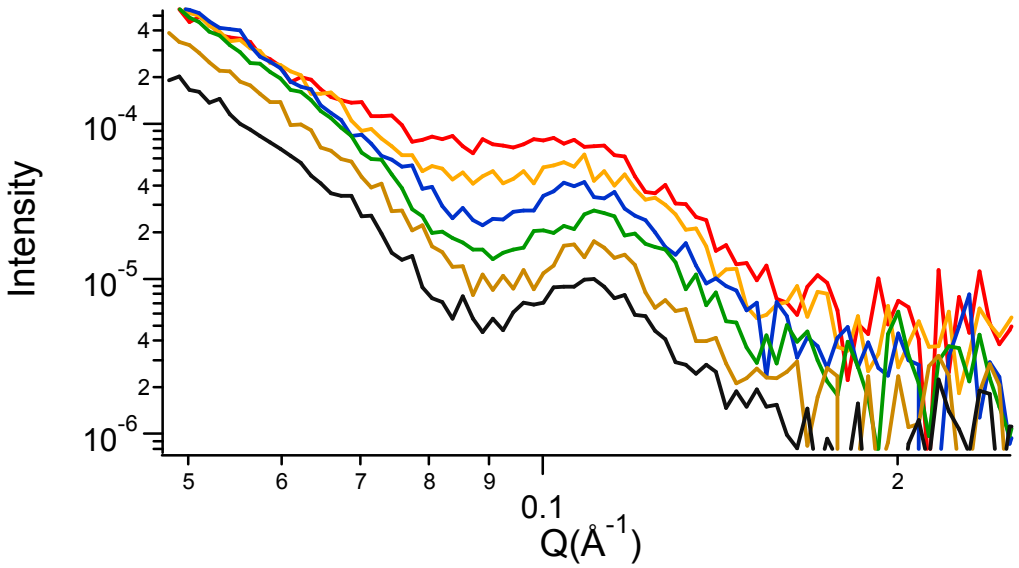

Figure 4-67 : Neutron reflectivity profiles showing the development of a Zn film at the air-solution interface. Data is shown for scans starting 11 (red), 26 (orange), 41 (blue), 56 (green), 71 (brown) and 86 (black) minutes after pouring of the precursor solution. Data is offset for clarity.

As detailed in *Appendix 4*, § 7.4, data modeling of the reflectivity profiles from a standard preparation, for which a complete data series is available, was undertaken using the Motofit program in a similar manner to modeling of the titania film data. The data was found to be accurately modeled by a growing series of lamellar layers with 2 repeat

layers adequate shortly after pouring and a developing to four repeat layers over 40 – 50 minutes. At longer times 3 repeat layers remain sufficient to model the data and it is suggested that the continued evaporation from the solution artificially broadens the peaks giving rise to modeling of fewer layers than are, in fact, present.

In all cases the lamellar layers were found to consist of two blocks, the first being a block of 19 Å of fluorocarbon and the second being a 31 Å block of SLD consistent with a PEO – ZnO mixture, see **Table 2-1**, § 2.1.1. The total lamellar thickness was observed to be 50 Å in reasonable agreement with that derived from the peak position but, as with the titania films, suggesting that the developing peaks give a misleading interlayer spacing. Additionally, the thickness and roughness of the bottom layer suggest that this layer is a disordered mixture of PEO chains and titania precursors as may be expected.

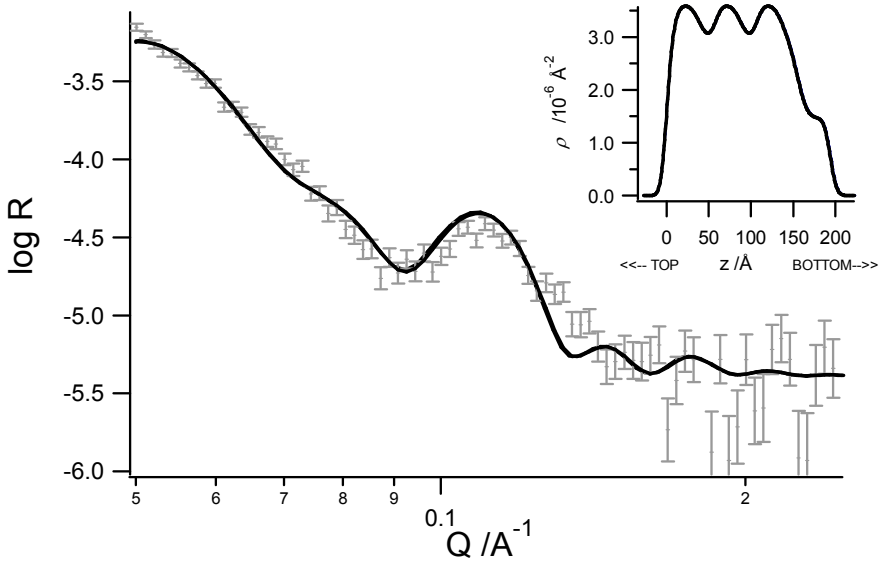

Figure 4-68 : Modeling of neutron reflectivity from a zinc oxide film after 76 minutes development at the air-solution interface using a standard preparation. Data is shown in grey while the model is shown in black.

4.4.4 Small Angle X-ray Scattering

In order to study the structure and robustness of the FSO-100 templated zinc films small angle X-ray scattering patterns were collected from film material recovered from the air-solution interface and dried in air before and after calcination at 600 °C. As shown in *Figure 4-69*, the film material is observed to possess structure before calcination that is found to collapse, suggesting that the zinc oxide is not well condensed, to a disordered powdered material after calcination. However, the structure existing before calcination is indexed to the *Im3m* cubic structure with the peaks assigned as indicated in *Figure 4-69*.[29] It is noted that in the nearby reflections (123), (004) and (233), (224) are not resolved into separate peaks in the scattering pattern appearing instead as broadening of a single peak. However, given recent reports that uniaxial contraction of an *Ia3d* cubic phase may allow the previously forbidden (002) and (112) reflections to be observed the assignment of an *Im3m* structure is tentative.[47]

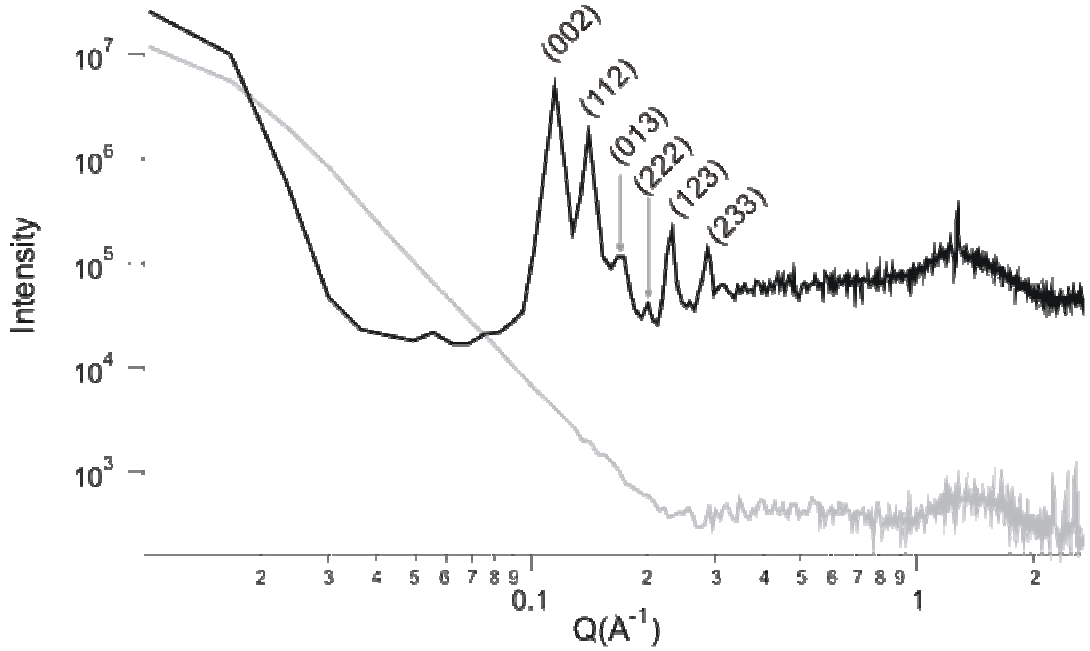

Figure 4-69 : SAXS patterns from FSO-100 templated Zn film material before (black) and after (grey) calcination.

4.5 Fluoro-Surfactant Templated Zinc Films – Discussion

4.5.1 Zinc Film Formation

The formation of FSO-100 templated zinc oxide films at the air-solution interface has been studied by Brewster angle microscopy and time resolved X-ray reflectometry, *Figure 4-62*, in a comparable fashion to the formation of titania – fluorosurfactant films. The observation of gradual film formation in both BAM experiments and time-resolved X-ray reflectometry is indicative that a surface driven mechanism, see § 1.3, is driving film formation in a similar manner to titania film formation. No observations of rapid interfacial change, expected for a bulk driven mechanism,[30] are observed meaning that a bulk driven mechanism cannot be supported.

The continued development of the film after initial formation, observed in BAM, X-ray and neutron reflectometry experiments, supports a surface driven formation mechanism. The X-ray reflectivity observation of lamellar structures for in-situ films indicates a similar mechanism for both zinc oxide and titania films. This suggests that the FSO-100 surfactant has a greater influence on the film formation mechanism than the inorganic precursor species and the formation mechanism proposed in § 4.3.1, *Figure 4-59*, is also proposed for the zinc oxide films. If a comparable mechanism is operating similar trends in film formation time may be expected for reagent concentration variation in both titania and zinc oxide films.

As shown in *Figure 4-61*, similar observations are made for zinc oxide films with formation times observed to decrease at higher FSO-100 concentrations and decrease for higher inorganic precursor concentrations. As in titania films, faster film formation occurring at higher FSO-100 concentration is attributed to the greater availability of FSO-100 surfactant for the formation of lamellae. Slower formation at higher $ZnCl_2$ concentration is attributed to reduced interaction between the inorganic species and PEO chains of the surfactant, however, as no detailed study of interactions between PEO chains and Zn species has been undertaken to our knowledge, this is unconfirmed.

Although formation time observations are comparable to titania film results for FSO-100 and $ZnCl_2$ concentration variation for HCl concentration variation, the observations are only partially comparable. The formation time is found to increase at

low acid concentrations in a comparable fashion to titania films but is also observed to increase at high acid concentration in an opposing fashion to variation in titania films, *Figure 4-61 (c)*.

In the case of titania film formation the slowing of inorganic condensation by acid was observed to have a lesser impact upon film formation than the effect of increased interaction between PEO chains and inorganic precursors.[37] The addition of acid is expected to reduce condensation during zinc oxide film synthesis also and it appears that this creates a more precise balance than in titania film formation. Although higher acid concentration increases PEO - inorganic interactions and reduces the formation time it does so only up to a point.

Once the concentration reaches a certain point film formation is slowed by the reduced rate of inorganic hydrolysis creating smaller inorganic oligomers in solution.[11,48] Although there is greater attraction between the PEO chains and inorganic species more oligomers are required to produce a sufficient inorganic barrier around the surfactant PEO chains and film formation is slowed by the time required for the assembly of this larger number of smaller species. Therefore the two processes of increased attraction and limited condensation are balanced giving rise to a minimum in the film formation time corresponding to an acid concentration at which interactions with PEO outweigh the impact of smaller oligomer size.

4.5.2 Zinc Film Structure

In-situ X-ray and neutron reflectivity profiles of FSO-100 templated zinc oxide films developed at the air – solution interface show them to have a lamellar structure for all reagent concentrations. The interlayer *d*-spacing of the lamellar is found to be 54 Å in all cases except when 1.47g of HCl is utilised when an interlayer spacing of 57 Å is observed. However, small angle X-ray scattering from film material removed from the interface and dried has peaks that may be indexed to the *Im3m* cubic structure, *Figure 4-69*. This suggests that although a lamellar structure exists in the film while at the air-solution interface drying of the film material after removal from the interface induces a phase transition from lamellar to cubic. However, given that the biphasic structure may

be considered as twisted lamellae or close packed micelles the assignment of the space group does not assign a specific structure to the material.

A similar structural transition is observed for FSO-100 templated titania films, although the interlayer spacing of the in-situ lamellar phase was found to be 57 Å in that case (§ 4.3.2). In the titania case it was suggested that the formation of a lamellar phase is favoured due to the development from a surfactant monolayer at the interface and a similar process is proposed here. The number and uniformity of the lamellar layers was found to vary with the reagent concentration in the case of titania films however these effects appear less pronounced in the zinc oxide films. Changes in peak shape observed in the zinc oxide films follow a similar trend to BAM observations of formation time with sharper peaks observed for faster forming films.

As with the titania films the Bragg peaks associated with the lamellar structure are observed to become sharper at higher surfactant concentrations, *Figure 4-63*, attributed to the development of a larger number of lamellae developing for faster reactions, in agreement with BAM experiments. Although observations for the effect of acid variation are limited, these observations agree with proposal that faster formation gives rise to more lamellar layers and it is observed that there is an optimum HCl concentration for the formation of a high degree of order which is matches with the optimum concentration allowing rapid film formation. Studies of formation time suggested that acid is playing a dual role of enhancing interaction between the PEO chains and inorganic precursors and slowing condensation.

However, unlike the titania case, variation of the concentration of inorganic precursor, $ZnCl_2$ in this case, does not appear to have a significant influence on the structure of the film. In the titania case it is suggested that competition between addition to the inorganic layer and formation of a new surfactant layer leads to polydispersity in the layer thickness at higher concentration. If the interaction between the zinc precursors and PEO chains are less significant it is expected that the creation of a new surfactant layer will be favoured and consistent layer thicknesses will be observed at all concentrations.

The presence of a lamellar phase in developed films in-situ at the air-solution interface may be confidently assigned given the results of reflectometry experiments,

however, a bicontinuous cubic structure is assigned from SAXS experiments on material removed from the interface. A transition from lamellar to bicontinuous cubic is observed for titania – FSO-100 film material removed from the interface and given the similarities in the systems it is reasonable to propose a similar transition in the zinc oxide film material.

Phase studies of FSO-100 do not show a lamellar phase at, or below, 90% wt. surfactant, rather a high density of ellipsoidal micelles is observed, see **Table 4-2**. It is probable that, as in the titania case, once the influence of the interface is removed the lamellar sheets twist into a cubic structure as impurities in the recovered material evaporate. It has been noted that some *Im3m* structures have weak (013) and (222) reflection that may lead to an erroneous assignment as *Ia3d*.[38] Additionally, a uniaxial distortion of the *Ia3d* structure, as may be expected for a film contracting orthogonally to the substrate during drying, may allow previously forbidden reflections leading to an incorrect assignment as *Im3m*.[47] Furthermore, neither the zinc oxide nor titania film material appears highly ordered after calcination further complicating comparison.

Therefore, although an *Im3m* cubic structure is observed in the zinc case and an *Ia3d* phase is observed for titania film material neither assignment can be considered absolute. The balance between formation of an *Ia3d* or *Im3m* structure is reported to be delicate in many systems with slight changes leading to the formation of one phase over the other.[38] While the structures remain unconfirmed it is possible that the differences between the zinc oxide and titania systems is sufficient to develop this change.

It is possible that a slower condensation of the zinc oxide material is allowing a more complete phase transition to occur and that titania material would also form the *Im3m* structure if it was not set prematurely by the condensation of the titania phase however this is unconfirmed. Electron microscopy, nitrogen adsorption and further SAXS studies on the zinc oxide film material would provide worthwhile addition to information about this system and allow a more conclusive assignment of the formation processes and structure of the material.

4.6 Conclusion

The partially fluorinated surfactant FSO-100 has been successfully used to template the spontaneous formation of both titania and zinc oxide films at the air-solution interface, from largely non-aqueous solutions, for the first time. Film formation in both cases has been shown in Brewster angle microscopy and time resolved reflectometry to occur via a surface driven formation mechanism in which inorganic precursors are a prerequisite to film formation.

In both titania and zinc oxide films a lamellar structure has been observed by X-ray and neutron reflectivity experiments of in-situ films developed at the air-soltuion. A formation mechanism is therefore proposed in which inorganic precursors interact with the PEO chains of a surfactant monolayer at the air-solution interface and provide a barrier for the progressive development of additional lamellar layers of surfactant and inorganic material at the interface.

Upon removal from the interface and drying the film material is shown to undergo a phase change from lamellar towards a bicontinuous *Ia3d* cubic structure of twisted lamellae similar to that observed in studies of the surfactant phase diagram at high concentration. However, the low resolution of the electron diffraction pattern from which the *Ia3d* structure is assigned and the fact that assigning a symmetry space group does not assign a unique structure suggesting that additional experiments are required to confirm the structure.

It is observed that a highly ordered phase is not achieved in the titania films as condensation of the inorganic phase sets a firm structure before this phase transition is complete. Nonetheless nitrogen adsorption, SAXS data modelling and TEM experiments show that the titania film material is a mesoporous network with pores of the order of 8 nm in diameter.

Small angle X-ray scattering experiments have shown the zinc oxide films develop the *Im3m* cubic structure after removal from the interface, possibly due to a slower condensation of the zinc oxide precursors. However, as changes in allowed reflections due to uniaxial contraction of a structure, as in film drying, may be occurring

further experiments are recommended to confirm the assignment of an *Im3m* structure rather than an *Ia3d* cubic structure.

Additionally, this film material is not robust to calcination of the film material and further experiments are required to establish the presence or absence of porosity. Transmission electron microscopy, electron diffraction and nitrogen adsorption are suggested as three worthwhile areas for further investigation of the zinc oxide film material.

In assessing the potential for the future application of these materials study of dye adsorption would be relevant for solar cell application. Additionally testing of the film material in the photodecomposition of dyes of other organic compounds is a recommended test for the utility of these materials as photocatalysts and as a more general test of their photoactivity.

4.7 References

(1) Beck, J. S.; Vartuli, J. C.; Roth, W. J.; Leonowicz, M. E.; Kresge, C. T.; Schmitt, K. D.; Chu, C. T.-W.; Olson, D. H.; Sheppard, E. W.; McCullen, S. B.; Higgins, J. B.; Schienker, J. L. *Journal of the American Chemistry Society* **1992**, *114*, 10834-10843.

(2) Bagshaw, S. A.; Prouzet, E.; Pinnavaia, T. J. *Science* **1995**, *269*, 1242-1244.

(3) Blin, J.; Lesieur, P.; Stebe, M. *Langmuir* **2004**, *20*, 491-498.

(4) Stallings, W. E.; Lamb, H. H. *Langmuir* **2003**, *19*, 2989-2994.

(5) Mele, S.; Ninham, B. W.; Monduzzi, M. *Journal of Physical Chemistry B* **2004**, *108*, 17751-17759.

(6) Meng, X.; Lu, D. L.; Tatsumi, T. *Chemistry Letters* **2007**, *36*, 670-671.

(7) Abe, M. *Current Opinion in Colloid & Interface Science* **1999**, *4*, 354-356.

(8) Kekicheff, P.; Tiddy, G. *Journal of Physical Chemistry* **1989**, *93*, 2520-2526.

(9) Ravey, J.; Stebe, M.; Sauvage, S.; Elmoujahid, C. *Colloids and Surfaces A* **1995**, *99*, 221-231.

(10) Soler-Illia, G. d. A.; Sanchez, C.; Lebeau, B.; Patarin, J. *Chemical Reviews* **2002**, *102*, 4093-4138.

(11) Brinker, C. J.; Scherer, G. W. *Sol-Gel Science*; 1 ed.; Academic Press: London, 1990; Vol. 1.

(12) Blin, J.; Stebe, M. *Microporous and Mesoporous Materials* **2005**, *87*, 67-76.

(13) Patel, N.; Marlow, M.; Lawrence, M. J. *Journal of Colloid and Interface Science* **2003**, *258*, 345-353.

(14) Han, Y.; Li, D.; Zhao, L.; Song, J.; Yang, X.; Li, N.; Di, Y.; Li, C.; Wu, S.; ZXu, X.; Meng, X.; Lin, K.; X, F.-S. *Angewandte Chemie International Edition* **2003**, *42*, 3633-3637.

(15) Meng, X.; Di, Y.; Zhao, L.; Jiang, D.; Li, S.; Xiao, F.-S. *Chemistry of Materials* **2004**, A-I.

(16) Di, Y.; Meng, X.; Li, S.; Xiao, F.-S. *Microporous and Mesoporous Materials* **2005**, *82*, 121-127.

(17) Rodriguez-Aberu, C.; Botta, P. M.; Rivas, J.; Aramaki, K.; Quintela, M. A. L. *Journal of Non-Crysatlline Solids* **2008**, *354*, 1074-1079.

(18) Huo, Q.; Margolese, D. I.; Ciesla, U.; Feng, P.; Gier, T. E.; Sieger, P.; Leon, R.; Petroff, P. M.; Schuth, F.; Stucky, G. D. *Nature* **1994**, *368*, 317-321.

(19) Zhu, H.; Hagfeldt, A.; Boschloo, G. *Journal of Physical Chemistry C* **2007**.

(20) Afzaal, M.; Malik, M. A.; O'Brien, P. *New Journal of Chemistry* **2007**, *31*, 2029-2040.

(21) Keis, K.; Vayssieres, L.; Lindquist, S.-E.; Hagfeldt, A. *Nanostructured Materials* **1999**, *12*, 487-490.

(22) Peiro, A.; Ravirajan, P.; Govender, K.; Boyle, D.; O'Brien, P.; Bradley, D.; Nelson, J.; Durrant, J. *Journal of Materials chemistry* **2006**, *16*, 2088-2096.
(23) Vendamme, R.; Onoue, S.-y.; Nakao, A.; Kunitake, T. *Nature Materials* **2006**, *5*, 494-501.
(24) Angerer, P.; Yu, L. G.; Khor, K. A.; Krumpel, G. *Materials Science and Engineering A* **2004**, *381*, 16-19.
(25) Kline, A. R. *Journal of Applied Crystallography* **2006**, *39*.
(26) Henderson, M. J.; Gibaud, A.; Bardeau, J.-F.; White, J. W. *Journal of Materials Chemistry* **2006**, *16*, 2478-2484.
(27) Henderson, M. J.; King, D.; White, J. W. *Langmuir* **2004**, *20*, 2305-2308.
(28) Nelson, A. *Journal of Applied Crystallography* **2006**, *39*, 273-276.
(29) MacGillavry, C. H.; Rieck, G. D. e. *International tables for X-ray crystallography, Volume 3, Physical and chemical tables*; 2nd ed.; Dordrecht: London, 1968; Vol. 3.
(30) Edler, K.; Brennan, T.; Roser, S. J.; Mann, S.; Richardson, R. M. *Microporous and Mesoporous Materials* **2003**, *62*, 165-175.
(31) Edler, K. *Australian Journal of Chemistry* **2005**, *58*, 627-643.
(32) Flödstrom, K.; Wennerstrom, H.; Alfredsson, V. *Langmuir* **2004**, *20*, 680-688.
(33) Linton, P.; Alfredsson, V. *Chemistry of Materials* **2008**, *20*, 2878-2880.
(34) Fernandez-Martin, C.; Roser, S. J.; Edler, K. *Journal of Materials Chemistry* **2008**, *18*, 1222-1231.
(35) Lee, E. M.; Thomas, R. K.; Penfold, J.; Ward, R. C. *Journal of Physical Chemistry* **1989**, *93*.
(36) Epping, J. D.; Chmelka, B. F. *Current Opinion in Colloid & Interface Science* **2006**, *11*, 81-117.
(37) Soler-Illia, G. d. A.; Sanchez, C. *New Journal of Chemistry* **2000**, *24*, 493-499.
(38) Finnefrock, A. C.; Ulrich, R.; Toombes, G. E. S.; Gruner, S. M.; Wiesner, U. *Journal of the American Chemistry Society* **2003**, *125*, 13084-13093.
(39) Schwarz, U. S.; Gompper, G. *Physical Review E* **1999**, *59*, 5528-5541.
(40) Conn, C. E.; Ces, O.; Mulet, X.; Finet, S.; Winter, R.; Seddon, J. M.; Templer, R. H. *Physical Review Letters* **2006**, *96*, 108102.
(41) Ropers, M. H.; Stebe, M. *Physical Chemistry Chemical Physics* **2001**, *3*, 4029-4036.
(42) Grosso, D.; Cagnol, F.; Soler-Illia, G. d. A.; Crepaldi, E. L.; Amenitsch, H.; Brunet-Bruneau, A.; Bourgeois, A.; Sanchez, C. *Advanced Functional Materials* **2004**, *14*, 309-322.
(43) Flödstrom, K.; Wennerstrom, H.; Teixeira, C. V.; Alfredsson, V.; Linden, M.; Amenitsch, H. *Langmuir* **2004**, *20*, 10311-10316.
(44) Soler-Illia, G. d. A.; Crepaldi, E. L.; Grosso, D.; Sanchez, C. *Current Opinion in Colloid & Interface Science* **2003**, *8*, 109-126.
(45) Gregg, S. J.; Sing, K. S. W. *Adsorption, Surface Area and Porosity*; 2nd ed.; Academic Press: London, 1982.
(46) Peng, T.; Hasegawa, A.; Qiu, J.; Hirao, K. *Chemistry of Materials* **2003**, *15*, 2011-2016.

(47) Toombes, G. E. S.; Finnefrock, A. C.; Tate, M. W.; Ulrich, R.; Wiesner, U.; Gruner, S. M. *Macromolecules* **2007**, *40*, 8974-8982.
(48) Bradley, D. C.; Mehotra, R. C.; Guar, D. P. *Metal Alkoxides*; Academic Press: London, 1978; Vol. 1.

Chapter 5
Diblock Copolymer Surfactant Templated Films
Use of the novel di-block copolymer $PEPEG_{2250}$ in film self assembly

5.1 Block Copolymers as Film Templates

Block copolymers are defined as copolymers (polymers derived from more than one monomer species) that are block polymers, a block being a group of many constitutional units that has at least one feature not present in adjacent units.[1] Typical block copolymers have either two or three blocks, diblock and triblock respectively, and the different properties of each block can give rise to interesting activity in the polymer. If, as is relevant to the present research, the blocks differ in their hydrophobicity the amphiphilic block copolymer will be surface active giving rise to a wide array of block copolymer surfactants.

Such surfactants may be used to template the formation of mesoporous materials in a similar manner to that for short chain ionic surfactants, see § 1.2.2, and have been noted to produce materials with larger pores and thicker inorganic walls than may be achieved with ionic surfactants.[2,3] These factors and the cheapness and environmentally benign nature of many block copolymers have made them a topic of considerable research interest since their first use in mesoporous silica formation in 1995.[4]

This research used diblock and triblock surfactants, available under many tradenames and of the structure $PEO_xPPO_yPEO_x$, in which the surface activity arises from hydrophobicity differences between the poly(ethylene oxide) and polypropylene blocks. Such surfactants and other block copolymers have subsequently become highly successful in mesoporous material and film formation. However, the formation mechanism has remained less clearly understood than for ionic surfactants for some years[3,5] and it is only recent work that has begun to clearly elucidate the mechanism.

A counter ion mediated $(S^0X^-)(I^+)$ mechanism, comparable to the $S^+X^-I^+$ mechanism for ionic surfactants,[6] was among those initially proposed for the block

copolymer templating of mesoporous materials.[3,4] However, more recent research has found insufficient evidence to justify assigning such a mechanism and the templating of materials is now understood to be due to hydrogen bonding and hydrophilic – hydrophilic interactions between the surfactant and inorganic precursors.[5,7,8] Both of these interactions occur in competition with water in the system however inorganic oligomers may offer more binding sites and greater interactions that favour their interaction with the surfactant.

As detailed in § 1.2.2, investigation into the block copolymer templated formation of mesoporous silica particles has noted that there is no aggregation of micelles initially an observation assigned to the entropically unfavoured overlap of PEO groups.[8] Instead, hydrolyzed silica species adsorb at the palisade region of the micelles until a coating is developed that allows coated micelles to gather into conglomerates without overlap of PEO groups.[5,8,9] Collisions between micelles and conglomerates leads to the formation a larger aggregates and particles in solution as inorganic condensation binds them together.[9]

The development of larger aggregates leads to phase separation and precipitation of the materials in solution and the final structure of the particles is determined by competition between the free energy of mesophase formation and surface free energy.[10,11] The structure of materials produced often corresponds to a liquid crystal phase not present in the initial solution, however, as inorganic condensation and structure formation occur concurrently a disordered structure may be set if condensation is too rapid.[3,11] Indeed, such competition has been reported in the formation of a disordered cubic phase in silica materials in which a hexagonal phase is otherwise expected.[11]

The mesostructure of block copolymer templated materials varies greatly with the reaction conditions and of particular importance are the size of the respective hydrophilic and hydrophobic blocks and the surfactant concentration.[12,13] A very large EO headgroup has been found to produce disordered wormlike structures, a very small EO group produces materials with small pores and no order while at sizes in between ordered phases may be formed.[13,14] The choice of solvent also influences structure formation as differences between the blocks of the copolymer surfactant may be less significant in different systems.[12]

In the aqueous and high water solvent mixtures most commonly used in block copolymer templated material formation the hydrophobicity difference between PEO and PPO blocks, commonly sold under the tradename Pluronic surfactants, among others, is sufficient for surfactant activity and micelle formation. However, the difference in hydrophobicity between these blocks is insufficient to generate significant surface activity and micelle formation in high alcohol systems and different block copolymers must be considered if such systems are to be used.[12,15]

Increasing the hydrophobicity of a block in the copolymer is a recommended method to increase the surface activity of the block copolymer.[15] This has been achieved for Brij surfactants, $CH_3(CH_2)_mCH_2(CH_2CH_2O)_nOH$ $m,n \leq 16$, triblock copolymers replacing the polypropylene block with a polybutylene block, and KLE surfactants, poly(ethylene-co-butylene)-b-poly(ethylene oxide), and all of these surfactants have been successful in mesoporous material formation.[16-20] However, the use of high alcohol systems remains relatively rare and the use of long polyethylene – poly(ethylene oxide) block copolymers is a new area of research.

As the use of non-aqueous conditions offers a method to control the reactivity of transition metal precursors,[21-23] see § 1.4, and given the desirability of mesoporous transition metal materials the development of high alcohol systems has potential for functional material design.[23] Additionally, the use of non-aqueous solvents has been reported as more promising than aqueous systems.[24] The development of mesoporous titania materials is of particular interest for photochemical applications and the use of block copolymers in alcohol solvents represents a potential pathway for their development. The larger pores formed by block copolymers and their relatively benign nature make them particularly attractive.

In the case of titania the use of a pure alcohol solvent is not ideal as the micelle formation of PEO containing block copolymers is enhanced in the presence of acid and some water.[12,15,25] Furthermore acidic water enhances the interaction between titania precursors and PEO groups encouraging the formation of the inorganic coating required for aggregation into larger particles and films.[9,15] Therefore a system using a small, controlled amount of acid and water is likely to be the most promising for the formation of mesoporous titania from high alcohol solvent systems.

5.2 PEPEG$_{2250}$ Templated Titania Films and Their Development at the Air-Solution Interface

5.2.1 Brewster Angle Microscopy

The formation of PEPEG$_{2250}$ templated films at the air-solution interface has been studied in BAM experiments to observe the effect of different reagent concentrations on the film formation time. For all reagent concentrations a regular series of changes were observed in the surface during film formation as shown in *Figure 5-70*.

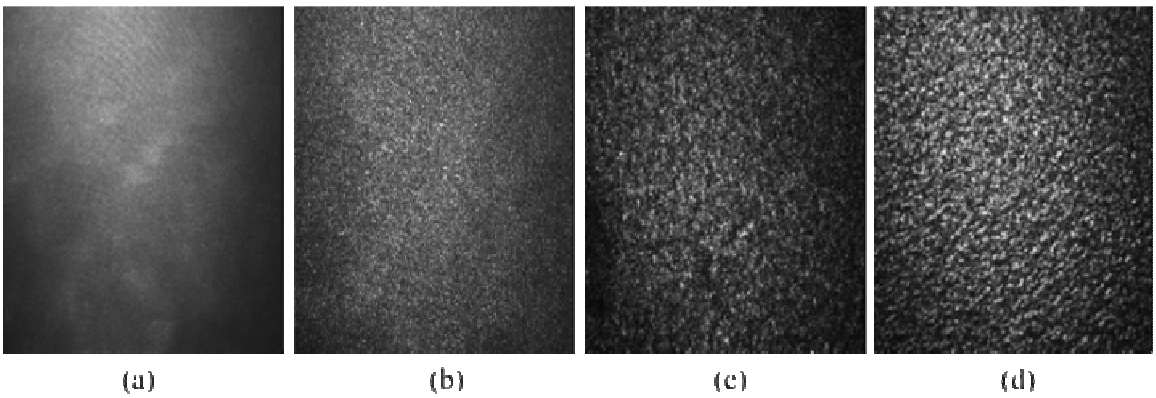

Figure 5-70 : Progression from a highly mobile surface to a stationary, uniform film observed by Brewster angle microscope. A highly mobile surface is seen after 4, (a), and 27 minutes, (b), while a stationary surface and increased intensity are seen after 42, (c), and 47 minutes, (d), when a film has developed at the interface.

After the film precursor solution was poured into a Petri dish, a highly mobile surface was visible in the live image of the Brewster angle microscope that had no apparent structure. This remained unchanged until a rapid increase in the light intensity was accompanied by the cessation of movement and a significant reduction in solvent evaporation. This point was defined as the point of film formation. After a film had formed the stationary, uniform surface was observed to continue to give a gradually increasing reflected intensity over time. The intensity variation observed in the live image of the BAM is not observed in *Figure 5-70* due to an automatic gain adjustment prior to image collection.

As a similar transition was observed for all reagent concentrations, it was possible to plot the observed changes in film formation time against the respective reagent

concentrations as in *Figure 5-71*. It was observed that both higher HCl and higher $PEPEG_{2250}$ surfactant concentrations reduced the film formation time. However, for titanium precursor, $TiCl_4$, variation about an optimum concentration giving a minimum formation time was observed. At concentrations above and below this optimum concentration the formation time was significantly longer.

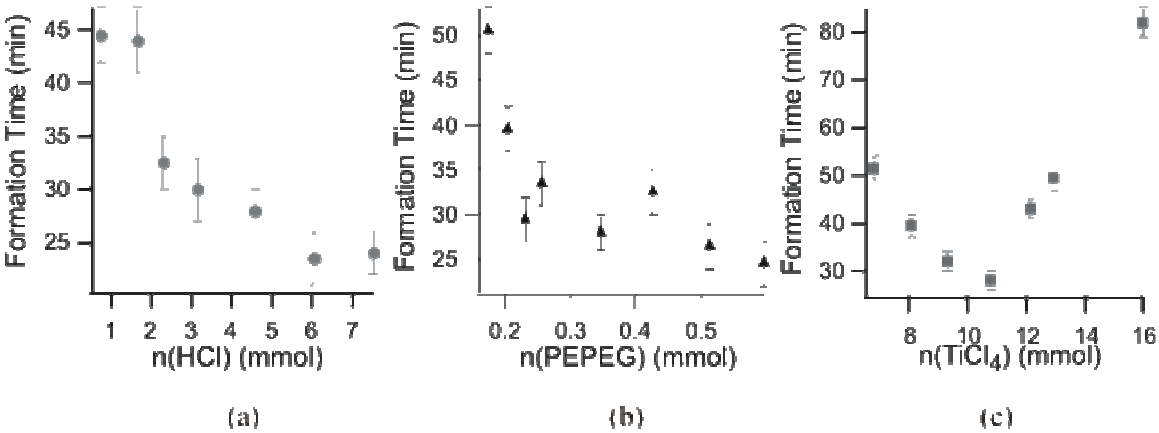

Figure 5-71 : Variation of film formation time due to variation of reagent concentrations. Plots are shown for HCl, (a), $PEPEG_{2250}$, (b), and $TiCl_4$, (c), variation.

In all cases it was attempted to collect the readily visible opaque, white film developed under BAM observation from the interface using either a microscope slide or a plastic mesh with 1 cm^2 holes. Although the lowest $TiCl_4$ concentrations produced thin films that could not be recovered intact, the majority of the films were observed to be robust. The films collected on the mesh were observed to remain intact and self supporting as they dried in air and in some cases large sections of self supporting titania film could be recovered intact as shown in *Figure 5-72*. Films collected on microscope slides were also found to remain intact as they dried.

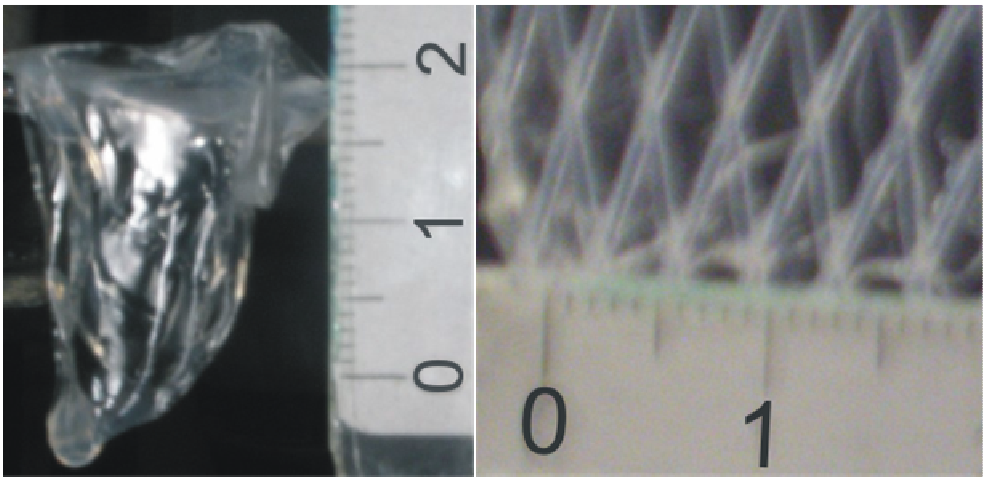

Figure 5-72 : Pictures of $PEPEG_{2250}$ templated, self supporting titania films removed from the air-solution interface to a mesh. Image (a) shows a film using 1 g of surfactant while (b) used 1.5 g and the rulers are in cm in each case.

5.2.2 X-ray scattering

Film development at the air-solution interface was studied using both time-resolved off-specular reflectometry and angle-dispersive specular reflectometry at the ESRF, France. Film formation in time-resolved reflectometry experiments was observed as the loss of the specular peak as shown in *Figure 5-73*. After the loss of the specular reflection no further development was observed in the time-resolved reflectometry and when inspected by eye the films were observed to be macroscopically rough within minutes of formation.

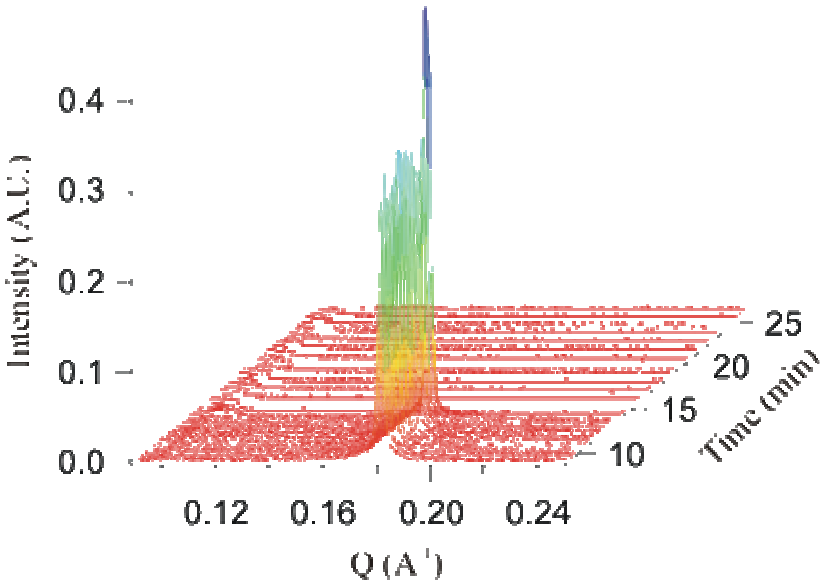

Figure 5-73 : Time-resolved (20 second scans) off-specular reflectivity pattern for the development of a PEPEG$_{2250}$ templated film developing at air-solution interface. Loss of the specular peak is observed to occur within two scans, data is shown against a linear scale in the interest of clarity of the loss of specular reflection.

For all reagent concentrations the specular peak was observed to vary for some time prior to the rapid loss of the specular peak that was observed to occur within 30 seconds. It is possible that the formation of a monolayer of surfactant at the interface is occurring prior to film formation leading to increased reflectivity or that an initial formation of the film leads to increased reflection before loss due to full development.

However, unlike the BAM experiments a direct comparison of the film formation times is not possible as the conditions were changed for some experiments by partially covering the sample with a lid attempting to slow development. It was also attempted to develop a film with a lid completely sealing the system although no film development was recorded in these cases while the lid remained. Upon subsequent removal of the lid film formation was recorded within a few minutes and within one minute in some cases in which surface activity was visible by eye also.

After film formation angular-dispersive reflectometry experiments were used to collect reflectivity profiles from developed films at the air-solution interface. Although some variation with reagent concentration was observed in these reflectivity profiles they were typically observed to be similar to those in *Figure 5-74*. Due to the rapid development of the films these profiles are also considered unreliable due to being

disrupted by the macroscopic roughness of the films during the 30 minutes required for data collection.

In many cases, as in *Figure 5-74* (b), a broad peak is observed in the reflectivity pattern due to evaporation lowering the solution and film below the lip of the PTFE trough used for these reflectometry experiments. At low angles in such cases some of the incident beam hits the trough rather than the surface artificially lowering the reflected intensity until the incident angle is such that the edge of the trough is avoided. Attempts to use the Motofit program to model these reflectivity profiles have been unsuccessful.

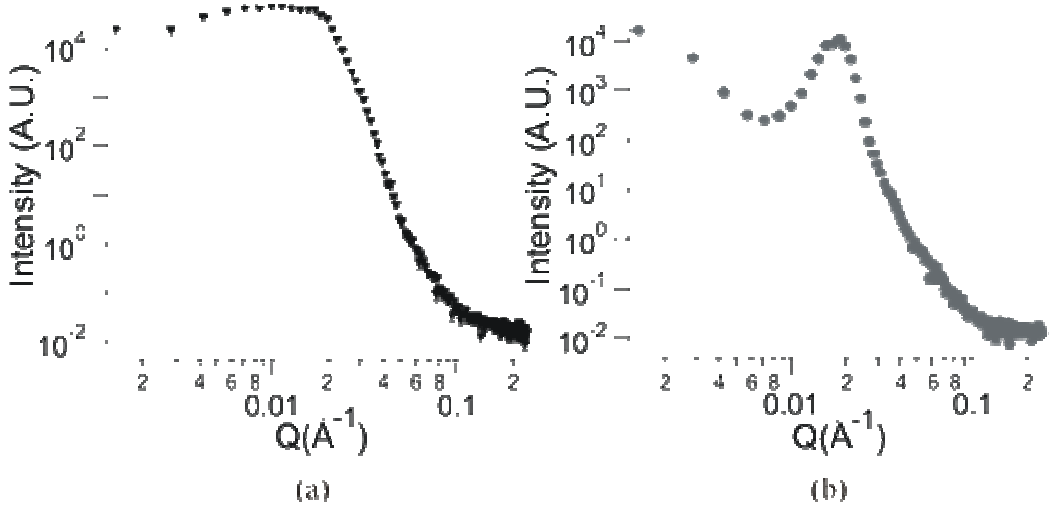

Figure 5-74 : X-ray scattering profiles from PEPEG$_{2250}$ templated titania films at the air solution interface. A complete pattern is shown in (a) while an artificial peak due to evaporation below the trough lip is seen in (b).

In addition to reflectometry studies small angle X-ray scattering patterns were collected from the PEPEG$_{2250}$ surfactant in ethanol at different concentrations and from film material collected from the interface after BAM observation of film formation, dried at room temperature and calcined. A scattering pattern was also collected for film material collected from the interface and dried prior to calcination to observe the effect of calcination upon the film structure.

Surfactant solutions were studied in the concentration range of 2.5% wt. to 60% wt. in ethanol and, as shown in *Figure 5-75*, the scattering patterns were found to vary subtly in shape/slope and for all concentrations no low angle peaks related to a liquid crystal phase were observed. At surfactant concentrations above 25% wt. the high angle

peaks that are observed in the scattering pattern at 1.36, 1.48 and 1.66 $Å^{-1}$ that are assigned to a crystalline phase of the solid surfactant. However, at concentrations above 60% by weight, solutions of the $PEPEG_{2250}$ surfactant in ethanol were found to be too viscous for comparable study in the capillary of the SAXS instrument.

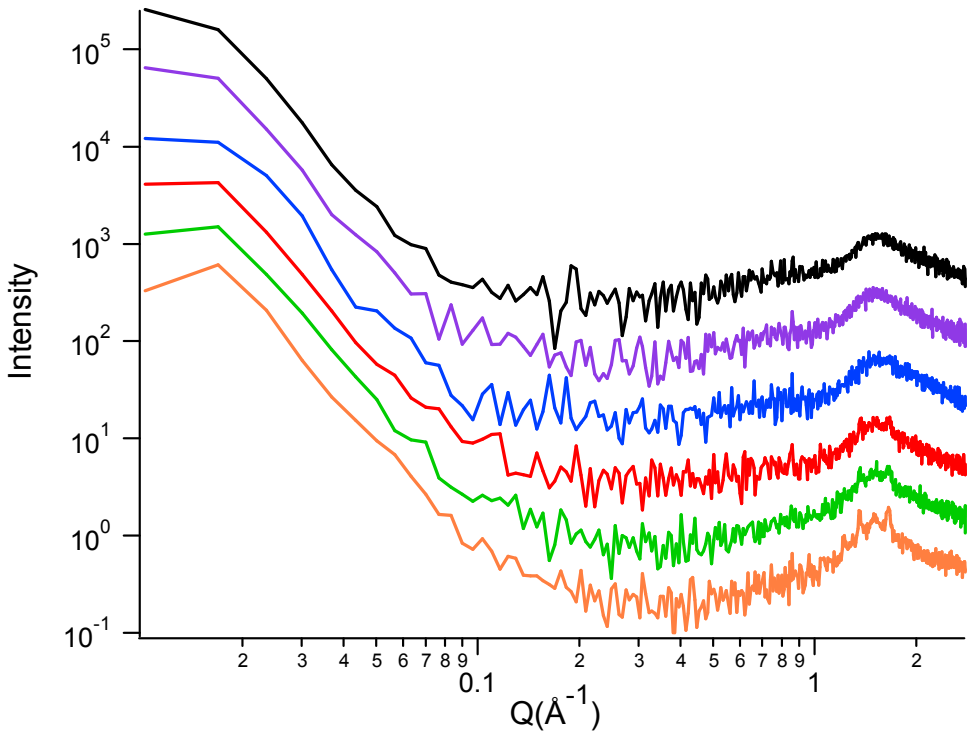

Figure 5-75 : SAXS patterns for the $PEPEG_{2250}$ surfacant in ethanol for 2.5% (black), 5% (blue), 10% (purple), 25% (red), 40% (green) and 60% (orange) by weight. Data offset for clarity.

In all cases Guinier analysis and calculations of the Porod slope were attempted, however, in all cases no reliable information was available as the results for calculated radius of gyration, R_g, were outside the valid range of the analysis. It was not possible to interpret the Porod slope with confidence as the analysis is only valid at high Q and the background in reached in the scattering patterns before this level is reached.

During the fitting undertaken for each scattering pattern data modelling was attempted using polydisperse models of core shell spheres, cylinders and lamellae and monodisperse prolate and oblate ellipsoids. The micelle shape and size corresponding to

the best fits for each sample are shown in **Table 5-4** and it is observed that as concentration increases the micelle shape varies with surfactant concentration as follows:

Spheres ⟶ Prolate Ellipsoids ⟶ Cylinders ⟶ Lamellae

Table 5-4 : Size and shape of $PEPEG_{2250}$ micelles in ethanol. R_a is the rotation axis, R_b is the minor axis and R_t is the shell thickness or bilayer thickness in the case of lamellar. PD is the polydispersity.

$PEPEG_{2250}$ Wt. %	**Micelle shape**	**R_a (Å) ± 2**	**R_b (Å) ± 2**	**R_t (Å) ± 2**	**PD ± 0.05**	**χ^2**
2.5	Spherical	43	-	44	0.29	13.3
5	Spherical	42	-	43	0.21	24.7
10	Spherical	44	-	48	0.22	32.0
25	Ellipsoidal	142	81	-	-	18.1
40	Cylindrical	332	77	-	0.37	6.7
60	Lamellar	-	-	319	0.33	15.0

In addition to study of surfactant micelles SAXS was also used to examine the structure of the films prepared in Brewster angle microscopy experiments. After collection from the air-solution interface film material was dried and calcined and SAXS patterns collected from the resulting powders to observe changes in film structure at different reagent concentrations. As seen in *Figure 5-76* the scattering patterns from the film material vary with the $PEPEG_{2250}$ concentration with variation observed to be similar for HCl and $TiCl_4$ variation (data not shown). The peak observed at high angle, $Q = 1.81$ $Å^{-1}$, is assigned to the anatase phase of crystalline titania,[26] that may be expected to form during calcination as it is typically associated with higher temperatures than the rutile phase of titania.

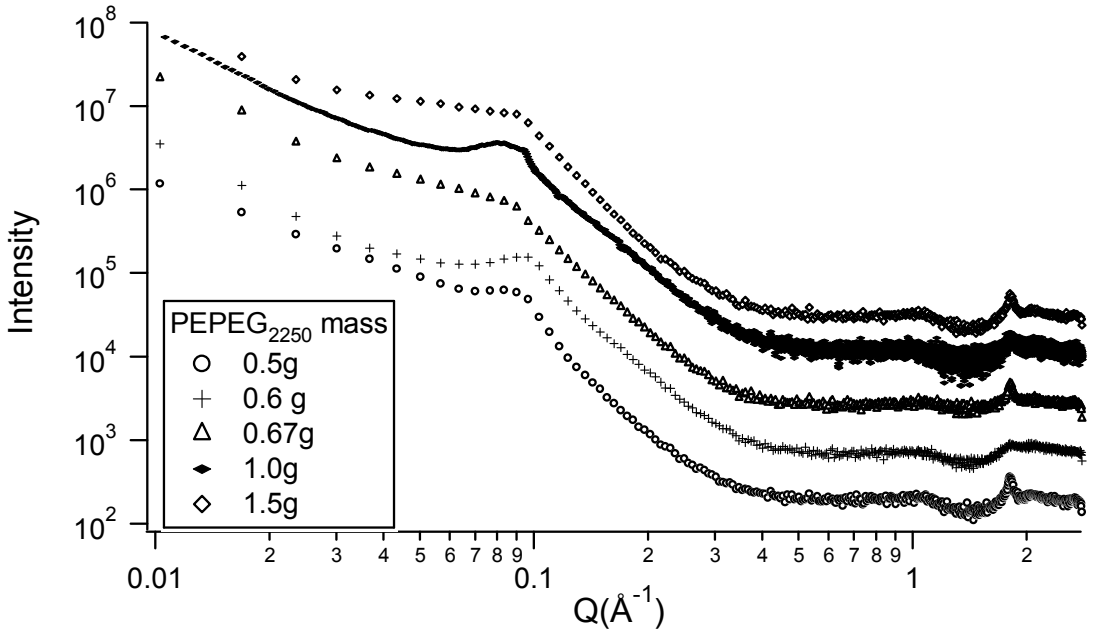

Figure 5-76 : Variation in SAXS patterns of dried, calcined films formed using different $PEPEG_{2250}$ additions as per the key on the graph.

In all cases a broad shoulder or peak appears in the scattering pattern in the range 0.083 – 0.091 $Å^{-1}$ corresponding to a distance within the range 69 – 75 Å. However the variation of the underlying shape of the scattering patterns are unclear as attempts to model the data from calcined film materials were unsuccessful. Attempts at a Guinier or Porod analysis of the data were similarly unsuccessful as the results lay outside the range of validity of the analysis.

In order to check the robustness and thermal stability of the film material a small angle X-ray scattering pattern was also collected from dried film material without calcination. A shown in *Figure 5-77* it was observed that the removal of the surfactant led to a considerable change in the structure of the material and the amount of material was greatly reduced after calcination suggesting a high surfactant content in the film. It is also observed that peaks at 1.36, 1.50 and 1.66 $Å^{-1}$ are present in the film material before calcination but not afterward in agreement with their assignation to a crystalline surfactant phase.

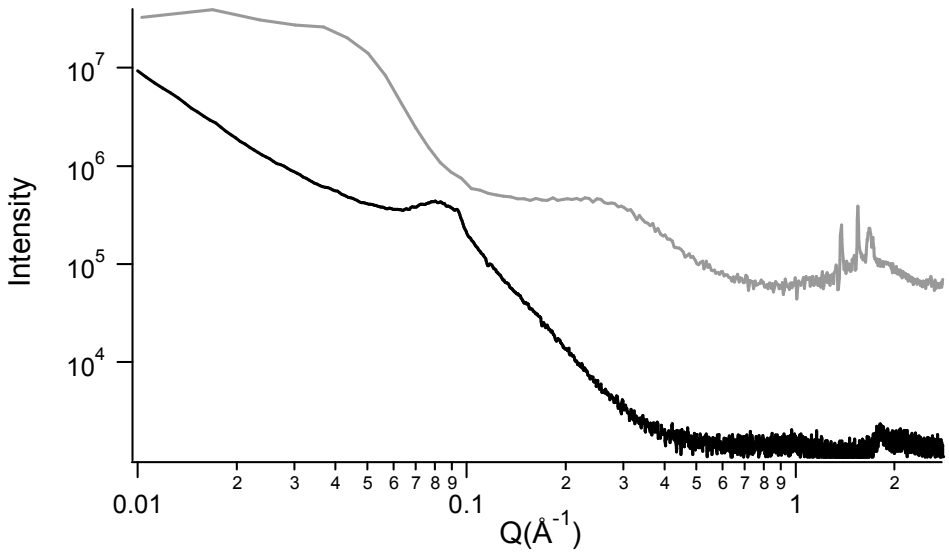

Figure 5-77 : SAXS patterns of film material before (grey) and after (black) calcination.

Furthermore while modelling of the full data range was not successful modelling within the range 0.01 – 0.35 $Å^{-1}$, comparable to the range of modelling of micelles in solution, gave an ellipsoidal structure for the uncalcined film material. Attempts at modelling core-shell or uniform particles showed that the uncalcined $PEPEG_{2250}$ – titania film material was best treated as ellipsoids in a titania matrix and the oblate polyethylene ellipsoids were found to have a rotation axis of 33 ±1 Å and a minor axis of 54 ±1 Å.

5.2.3 Neutron Scattering

In addition to small angle neutron scattering to observe development in the subphase SANS patterns were collected from developed, dried and powdered film material. As seen in *Figure 5-78* a peak at 0.0377 $Å^{-1}$, corresponding to a 167 Å structural distance, was observed in the scattering pattern from the titiania material in air. Although experiments were conducted with D_2O to provide data at a second contrast, data was not collected due to the high scattering saturating the detector and preventing collection. Attempts to establish the scattering length density of the powdered film material using the limited data from three contrasts collected were unsuccessful.

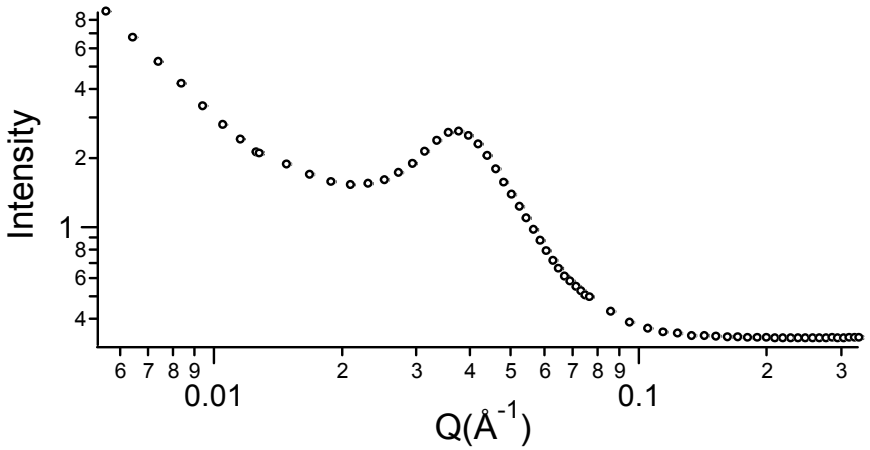

Figure 5-78 : SANS pattern collected from dried, powdered film material removed from the air-solution interface.

Unfortunately, neutron reflection that was conducted attempting to observe film formation and structure at the air-solution interface was also unsuccessful, albeit for different reasons. A typical reflectivity profile is shown in *Figure 5-79* and is clear that no significant information can be derived from the profile. Although peaks may be present in the profile none are of sufficient size in comparison to the errors to be considered significant. As X-ray scattering shows the films to be rough and as 15 minute scan times were required for these experiments it is likely that the sample undergoes significant change during profile collection distorting the data.

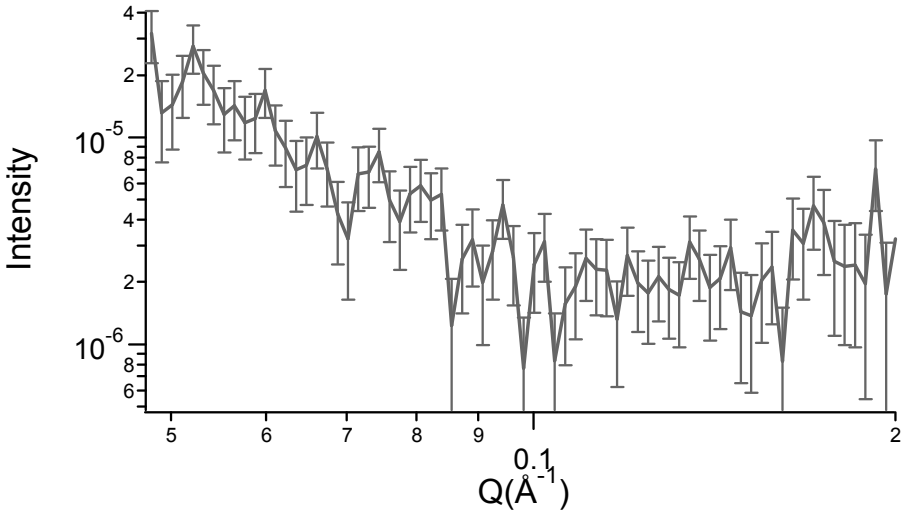

Figure 5-79 : A typical neutron reflectivity pattern for a $PEPEG_{2250}$ film at the air-solution interface. Rapid development and roughness of the film mean that little information can be gained from such profiles as indicated by the large error bars.

5.2.4 Nitrogen Adsorption

The nitrogen adsorption and desorption isotherm shown in *Figure 5-80* was collected for film material removed from the interface, dried at room temperature in air and calcined for template removal. The isotherm was assessed as a Type III isotherm corresponding to the characteristic adsorption and desorption from a non-porous powder with very low interaction between the gas and the adsorbate, see § 2.1.6. The BET surface area was calculated as 40 m^2g^{-1} using data in the partial pressure range of 0.06 – 0.31.

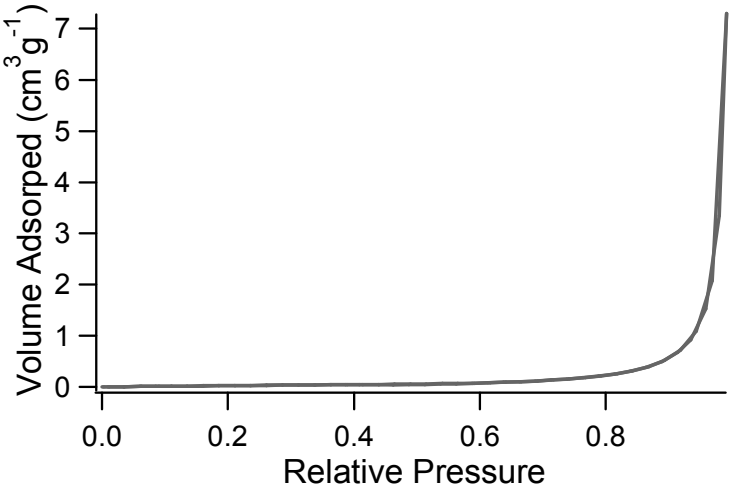

Figure 5-80 : N_2 adsorption and desorption isotherm for calcined $PEPEG_{2250}$ templated film material

5.2.5 Thermogravimetric Analysis

The inorganic content of film material, recovered from the air-solution interface and allowed to dry in air, was assessed by thermogravimetric analysis as shown in *Figure 5-81*. Samples were tested for material recovered from precursor solutions of surfactant to titania precursor molar ratios of 0.048 : 1, 0.032 : 1 and 0.032 : 1.5 and the temperature of decomposition and inorganic content were found to vary with the titania content. The decomposition temperature was observed to be lower when a higher surfactant content was present in the precursor solution suggesting that the surfactant is less protected from decomposition. At higher titania concentrations the inorganic content, indicated by the mass remaining at 500 – 600 °C, increases as shown in **Table 5-5**, suggesting that more titania, relative to surfactant, becomes integrated into the films.

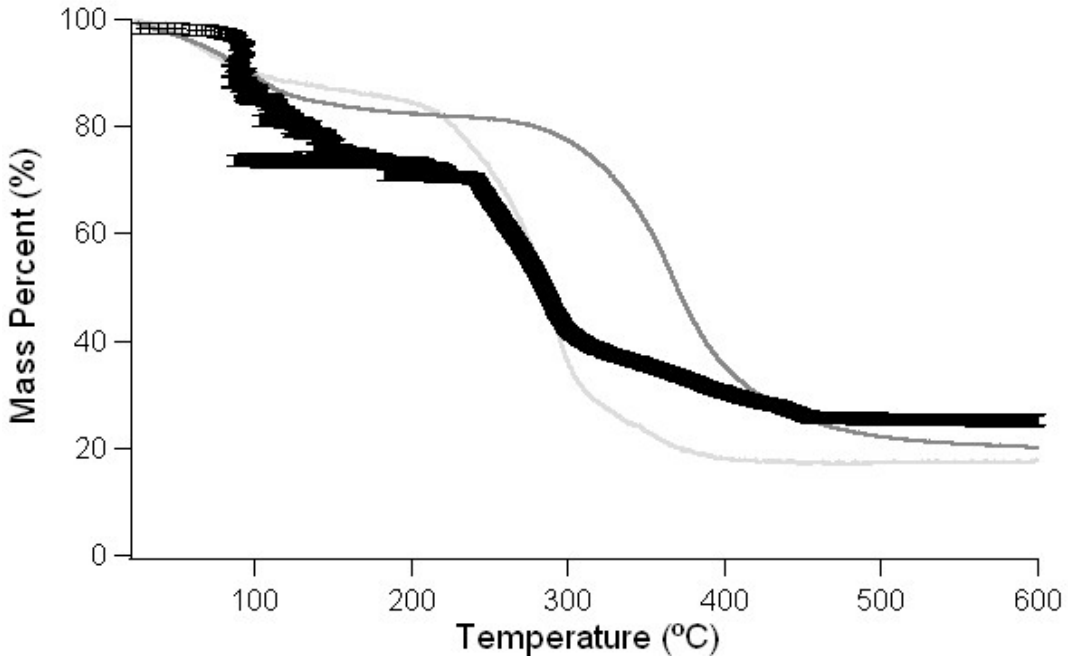

Figure 5-81 : Thermogravimetric analysis of $PEPEG_{2250}$ – titania film material. Results are shown for surfactant to titania mass ratios of 0.032:1.5 (black), 0.032:1 (dark grey) and 0.048:1 (light grey). Errors are shown for 0.032:1.5 ratio data as an example.

Table 5-5 : Mass % inorganic material for $PEPEG_{2250}$ – titania films.

Ti : PEPEG mole ratio	0.048 : 1	0.032 : 1	0.032 : 1.5
Mass % inorganic	17%	20%	25%

5.3 Discussion

5.3.1 Film Formation at the Air-Solution Interface

Film formation at the air-solution interface has been observed in Brewster angle microscopy and X-ray reflectometry to occur within 60 seconds, after a period in which no development occurs at the interface. Although this rapid formation presents challenges, due to the time required to collect scattering patterns and images, it is characteristic of a bulk driven formation mechanism, see § 1.3. Similar rapid formation at the air-solution interface after a period of no development has been reported for silica films templated with copolymer surfactants, shorter than those used in this work.[27] In this case the formation mechanism was reported as the development of silica coated micelles and aggregates of micelles in solution, followed by the migration of aggregates to the interface leading to rapid film formation. It is probable that a similar bulk driven formation process is occurring in the present work.

If film formation were occurring gradually at the interface, by the addition of individual micelles below the film, the formation of a uniform, static film in BAM and loss of specular reflection in reflectometry would be expected to be gradual as has been reported previously.[27-29] The rapid changes observed here do not reflect such a process and are, instead, suggested to be due to development in solution prior to formation at the interface.

A requirement of this mechanism is that surfactant micelles exist free in solution prior to the introduction of inorganic precursors, otherwise the transition to film development would be less pronounced. Unlike the electrostatic interactions of ionic surfactant micelles the repulsion between block copolymer surfactant micelles is due to the entropically unfavoured overlap of the PEO chains at the exterior of the micelles.[8,30] Thus, although micelles form in solution, at the concentrations used in these film preparations, < 5% wt., micelles are expected to be spherical and are not expected to exist in a highly ordered phase in solution. This is confirmed in SAXS patterns in which spherical micelles are observed below 10% wt. $PEPEG_{2250}$, see *Figure 5-75*. As micelles are formed in solution but are not aggregated or ordered the subsequent development of a

film may be described in stages comparable to those reported for formation of surfactant templated silicas:[3,7,9]

- Titania precursors bind to the surfactant micelles
- Associative phase separation creates a concentrated surfactant and inorganic phase in which titania – coated micelles aggregate
- Aggregates rise to the surface, possibly due to increasing hydrophobicity as the inorganic phase condenses, and bind together into a film

A number of surfactant – inorganic precursor interactions have been suggested,[3] however, specific research on the mechanism reports attraction between PEO blocks and silica precursors and oligomers in acidic conditions as due to hydrophilic – hydrophilic interactions.[7] This is enhanced by the development of positive charge on growing silica oligomers in acidic conditions below the isoelectric point and by greater surfactant activity and hydrogen bonding of PEO blocks in acidic conditions.[15,25,29,31] Similar effects can be expected between titania precursors and oligomers and the PEO groups of the $PEPEG_{2250}$ surfactant as titania species are expected to be charged in the acidic conditions used, below its isoelectric point of a pH of 4.3.[32] Furthermore the acid and water present in the film precursor solution is expected to enhance the ordering and hydrogen bonding of PEO groups and be sufficient to prevent disruption of micelles by chelation of PEO groups by titania species.[31]

The effect of acid enhancing micelle formation is indirectly observed in the reduction in film formation time at higher acid concentrations, see *Figure 5-71* (a). Similar observations of faster formation times for silica templated by ionic surfactant suggested that the increasing concentration of Cl^- counter ions had a greater influence than increasing acid.[27] This is unlikely to be the case in the present work as, although a counter-ion-mediated mechanism has been suggested for copolymer surfactant templating there is little evidence for it in the literature and a hydrogen bonding mechanism is accepted.[5,7] Furthermore, as $TiCl_4$ is used as the titania source the concentration of Cl^- in solution is more dependent upon the amount of precursor used rather than the amount of HCl added initially. Cl^- ions may have a different role in aiding film formation, however,

as the limited solubility of NaCl in ethanol led to a lack of success in the experiments undertaken to test this in the present work it is not possible to suggest a role of the ions in the reaction solution. Therefore, a separate and specific investigation of ion effects utilising different inorganic precursors is suggested is recommended as an area for future research.

Similarly the use of acid to control condensation does not explain the reduction in formation time as the quantity of HCl added to the initial solution of $PEPEG_{2250}$ in ethanol is small compared to that generated by the addition of $TiCl_4$. Use of an acidic solution is a recognised way to control the rapid condensation of titania precursors, as acid retards the condensation of precursors and encourages the formation of longer, linear chains rather than branched chains.[3,21] Although this work utilises acid in this role it does not explain the effect of the initial HCl concentration on formation time.

However, the addition of acidic water to a solution of copolymer surfactant in alcohol is known to encourage micelle formation and increase hydrogen bonding in PEO headgroups.[15,25,31] Additionally, it is likely that the effect of the initial HCl concentration is due to its effect on the initial surfactant solution prior to the addition of the titiania precursor. Therefore the observed effect of reduced formation times at higher HCl concentrations is suggested to be due to the aqueous acid encouraging $PEPEG_{2250}$ micelle formation and enhancing the initial interaction with titania precursors. This early enhancement of the inorganic – surfactant interactions and encouragement of micelle formation accelerates subsequent associative phase separation leading to a reduction in film formation time.

Although interactions between the $PEPEG_{2250}$ block copolymer surfactant micelles are initially repulsive, once a coating of titania surrounds and integrates with the PEO chains the entropically unfavoured interaction no longer inhibits micelle interaction.[8,27] Furthermore, the coating of the micelles may create an attraction between micelles that favours the formation of a concentrated phase.[30] Associative phase separation has been reported during the formation of block copolymer surfactant templated silica materials and is required for the formation of some materials.[9,11,27,33] The formation of a phase containing a higher concentration of inorganic precursor coated micelles allows for greater interaction between them enabling or enhancing

agglomeration, mesophase ordering and film formation. As the initial aggregation of silica coated micelles is suggested to occur through the collision of micelles in solution and inorganic condensation sticking them together, the existence of a concentrated phase may be a requirement for aggregation and film formation.[9,34,35] The joining of micelles into aggregates and then into a film becomes favoured once the inorganic condensation is sufficiently progressed and once this point is reached formation can occur very rapidly in the concentrated phase, as is observed in BAM and reflectometry.[27,33]

Formation of such a phase through associative phase separation is expected to be encouraged at higher surfactant concentrations and the larger number of micelles present to increase micelles collisions leading to faster formation times. As in *Figure 5-71* (b) this has been observed in BAM, as higher $PEPEG_{2250}$ concentrations lead to a reduction in the film formation time. However, the effects of different titania concentrations in the film precursor solution is less straightforward as observed in the U – shaped curve of film formation time vs. $TiCl_4$ concentration, *Figure 5-71 (c)*.

The formation of a titania coating around the $PEPEG_{2250}$ micelles is required for associative phase separation to occur as it is otherwise prevented by the entropically unfavoured interactions of PEO chains. As the development of a coating is expected to be faster at higher titania concentrations this is expected to be accompanied by a reduction in formation time. However, as the polymerising titania is expected to be charged in the acidic conditions used, the presence of more charged titania at the surface of the micelles is expected to lead to greater repulsion and an increase in the formation time.

It is this balance that leads to the U – shaped curve observed for variation of titania concentration. As the concentration increased, the coating of $PEPEG_{2250}$ micelles occurs faster, eliminating the repulsion due to PEO chain overlap and leading to faster formation times and outweighing charge considerations. Above a certain concentration the change in coating time is no longer significant and the increased repulsions between micelles due to greater charge inhibit aggregation, leading to an increase in the formation time. A similar balance has been recently reported for non-ionic surfactant templated silica films.[27]

This increased binding of titania to the PEO groups of the surfactant is also observed in the thermogravimetric analysis of film material recovered from the air-

solution interface, see **Table 5-5**. The higher mass of inorganic material, titania, relative to surfactant at higher titania precursor concentrations shows that more titania is being incorporated into the film material under these conditions. As the titania oligomers are expected to be charged this increased binding is expected to lead to electrostatic repulsion giving rise to the U-shaped dependence of formation time with titania precursor concentration as detailed above.

However, no U – shaped curve is observed when the surfactant FSO-100 is used, see Chapter 4, even though it is a similar non-ionic surfactant in acidic solutions. Although both $PEPEG_{2250}$ and FSO-100 have PEO sections giving rise to surface activity these sections are considerably shorter in the FSO-100 surfactant. It is therefore proposed that fewer inorganic oligomers interact with the micelles and that less charge builds up on the hybrid micelles with the result that the effects of overcharging are not observed. Increased inorganic binding is also suggested in TGA results that show a higher inorganic content in the $PEPEG_{2250}$ templated films rather than the FSO-100 templated films.

Of particular importance in this mechanism is the formation of a concentrated phase through associative phase separation allowing greater micelle interaction and more frequent micelle collision. The lack of film formation when a trough or dish is sealed with a lid suggests that evaporation is required for this phase separation, and film formation, to occur. It is suggested that evaporation leading to a locally higher concentration at the interface encourages further phase separation as additional micelles add to this phase. Thus no phase separation and therefore no film formation occurs when evaporation is restricted in a sealed container.

5.3.2 Film Structure

Films grown at the air-solution interface and templated by the block copolymer surfactant $PEPEG_{2250}$ do not appear to form a highly ordered phase such as cubic or hexagonal in X-ray or neutron reflectometry experiments, see *Figure 5-74* and *Figure 5-79*. The films are expected to grow and change considerably within the time required for the collection of either type of reflectivity profile and, therefore, the experiments suffer from the rapid formation and development of the films. However, previous observations of surfactant templated silica films growing at the air-solution interface show peaks

related to film structure growing during time-resolved off-specular reflectometry.[27,33,36] The lack of similar development in these titania films, *Figure 5-73*, further suggests a lack of order in the developed films.

Given the micelle behaviour of the $PEPEG_{2250}$ surfactant in ethanol and the suggested formation mechanism of micelle coating followed by micelle aggregation and aggregate combination to form a film this lack of order is explicable. Although the bulk-driven mechanism is known to produce cubic and hexagonal particles and films in silica materials, the development of order is reported to occur after combination of aggregates during this mechanism.[5,10,11,27,30] Additionally, it is recognised that structural organisation and inorganic condensation are concurrent processes in such surfactant templated syntheses and that the formation of a highly ordered material is effectively a race between these two processes.[3,30] If inorganic condensation occurs too quickly a disordered structure may be set.

At the surfactant concentrations of less than 5% wt. used during film synthesis, the surfactant has been observed by SAXS to form polydisperse spherical micelles in solution, **Table 5-4**, while SAXS patterns from developed film material show an oblate ellipsoidal structure, *Figure 5-77*. However, peaks observed at 1.36, 1.50 and 1.66 $Å^{-1}$ are assigned to a crystalline surfactant phase, due to crystallisation of the polyethylene segment, which is also observed for high concentrations of surfactant in solution. An ellipsoidal structure is observed to form in solution at higher surfactant concentrations (25% wt.) suggesting that micelle changes are occurring during agglomeration of titania coated micelles after associative phase separation has occurred.

However, the micelle growth and ordering do not produce an ordered film as the rapid condensation of the titania sets a solid film structure before ordering can be completed. This is in contrast to film formation using the FSO-100 surfactant in which the film remains modulable during growth at the interface and structural changes occur after removal from the interface, see § 4.3. As the fluorinated sections of the surfactant are expected to lead to greater phase separation it is possible that the condensing titania is less able to fix a solid structure when the fluorinated surfactant is used, allowing structural development that is prevented for the $PEPEG_{2250}$ surfactant.

It is widely recognised that the rapid condensation of transition metal precursors presents a considerable challenge to the formation of surfactant templated materials.[15,21,23] Uncontrolled condensation can lead to precipitation of random particles, but can also limit the establishment of order by preventing full micelle organisation. This effect has been reported for the formation of P-123 copolymer surfactant templated silica particles in which a disordered cubic phase of slightly elongated spherical micelles is formed.[11] Here micelles expected to elongate to form cylinders in a hexagonal structure, were prevented by silica condensation occurring too quickly, setting the disordered phase before organisation was complete.

A lack of observed order in templated materials is also expected in the case of considerable polydispersity as structural peaks and features become smoothed out, see § 2.1.2. As the $PEPEG_{2250}$ surfactant micelles are observed to be highly polydisperse, **Table 5-4**, considerable polydispersity in the encapsulated micelles may also be expected to remain present in the films formed at the air-solution interface and any structural peaks in reflectivity or scattering profiles are expected to be broadened or lost altogether.

Therefore, the lack of order observed in the $PEPEG_{2250}$ templated titania films at the air-solution interface is suggested to be due to the rapid condensation of titania preventing the development of an ordered phase and polydispersity in the size of titania coated micelles. Structure is also noted to be lost upon calcination with the lack of order in calcined film material, *Figure 5-78*, also due to a loss of ordering as the surfactant is burnt away as the film is observed to collapse to a powder during calcination. As the titania is expected to be well condensed prior to calcination this collapse is somewhat surprising. However it is expected that the long PEO sections of the surfactant are heavily interwoven in the titania walls of the material, as has been reported for silica systems.[3] The calcination may lead to collapse of the walls as the loss of the PEO segments in the material destroy the walls of the material leaving a non-porous material after calcination.

As an ordered material is expected to be porous the lack of order in the calcined film material is supported by the nitrogen adsorption isotherm that is assessed as a Type III isotherm, typical of non-porous powders with weak interactions between the adsorbate and gas, § 2.1.6.[37,38] Although this confirms the loss of structure during calcination the BET surface area of 40 m^2g^{-1} cannot be considered accurate as the BET theory is only

valid for type II and type IV isotherms where the asorbate – gas interactions are greater.[37,39]

Although structure is largely lost in calcined film material, the presence of a shoulder or broad peak in the calcined material SAXS patterns, *Figure 5-76*, corresponding to a distance of 70 – 76 Å is encouraging. As modelling of this data was not successful it is not possible to assign a firm structure to the material, however it is expected to correspond to the size of hybrid surfactant-titania micelles in the film. As the radius of the polyethylene micelle core is 40 Å in solution, **Table 5-4**, this suggests a PEO – titania wall thickness of approximately 40 Å all of which is expected to be a mixture of PEO and titania and may not provide great thermal stability. Although TGA experiments suggest that thicker walls may exist at higher titania concentrations they are not observed to be stable to calcination.

In stable block copolymer templated materials further titania is found to bind to the exterior of the micelles, forming walls between micelles in the developed film, to a thickness of 20 – 30 Å.[3,40] The limited thickness of 40 Å for titania around the polyethylene micelle core is a good match to the thickness observed in SAXS, however, no pure titania walls appear to be present for calcined material supporting the suggestion that although the films are not highly ordered and that a lack of thicker walls between titania coated $PEPEG_{2250}$ micelles means the material collapses upon calcination. It is also likely that incomplete ordering of the micelles creates varied thickness of the inorganic wall, increasing the broadening of any peaks present due to micelle disorder.

Improvement of micelle ordering and structural robustness may be possible through further reduction of the rate of condensation, at very high acid concentration or using competing ligands, to allow greater structural development.[23] This would need to be followed by thermal treatment of the films after removal from the air-solution interface as this is expected improve order and cross linking in the inorganic phase. Such treatment is noted in silica systems to further condense the inorganic phase and produce separation from the PEO chains forming solid, robust walls[3] and is predicted to be beneficial in the present work also. Additional strengthening of the inorganic phase may also be possible by the addition of further titania into the pre-assembled films by direct addition via vapour deposition.

5.4 Development in the Solution Subphase

5.4.1 Small Angle Neutron Scattering

Time-resolved development of the titania and surfactant in the solution subphase has been studied using small angle neutron scattering conducted on the D11 beamline at the ILL, France as detailed in the Experimental section. It was observed that within 3 minutes after the addition of the titania precursor, $TiCl_4$, the scattering patterns show a clear transition from one structure to another, as shown in *Figures 5-1 & 5-2*. Multiple contrasts were used by varying the deuteration of the solvent and the transitions were found to be consistent regardless of the deuterium content of the ethanol solvent. However, the transition from one state to another was found to be non-linear with respect to time as illustrated in *Figure 5-87.* Transitions were also found to vary depending upon the relative concentrations of polymer surfactant, $PEPEG_{2250}$, and inorganic precursor, $TiCl_4$.

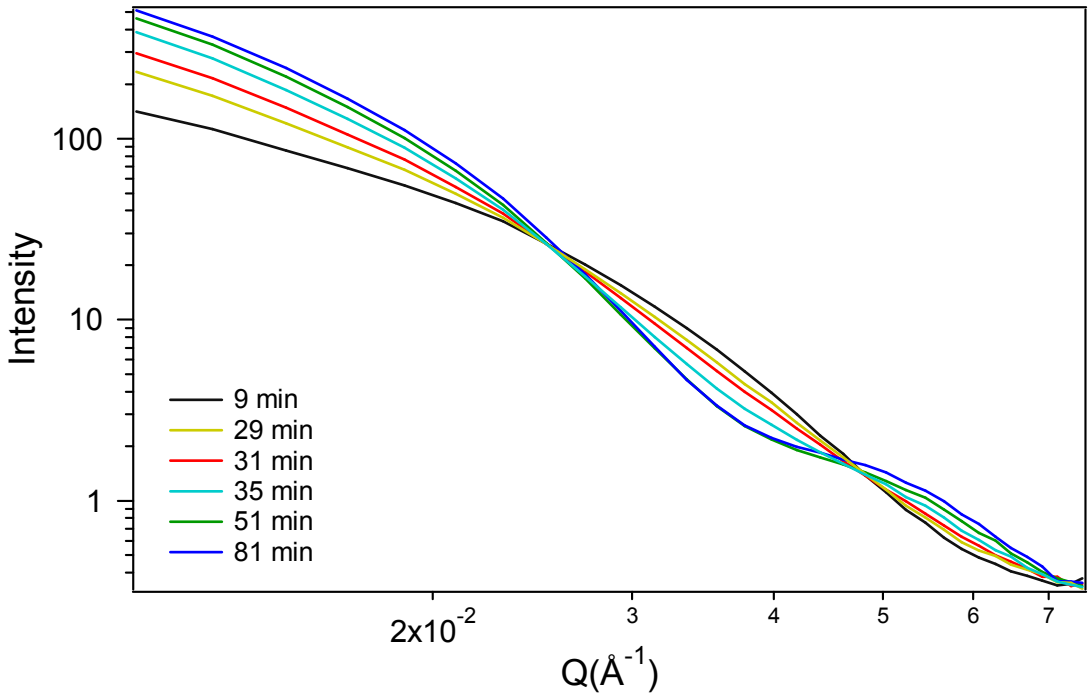

Figure 5-82 : Small Angle Neutron Scattering patterns from a reaction solution with a 1.5 $PEPEG_{2250}$: 2 $TiCl_4$ ratio. A steady transition from one structure to another is observed. Development is slow for the first 20 minutes and after 50 minutes.

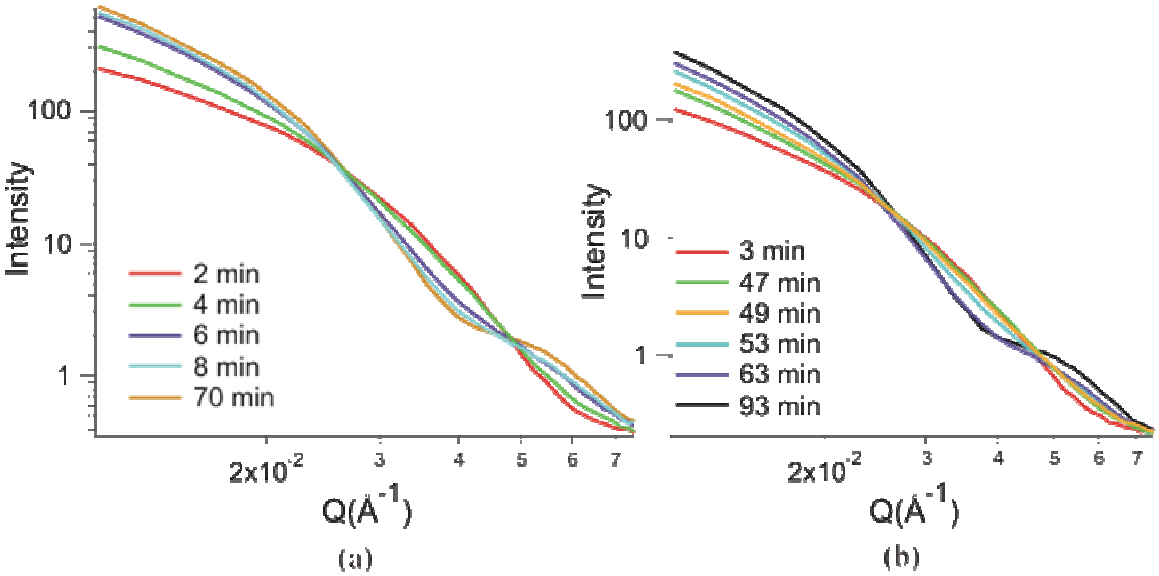

Figure 5- 83 : SANS patterns collected from, (a), 1 : 1.25 and, (b), 1 : 3 $PEPEG_{2250}$: $TiCl_4$ ratio solutions. Transition begins quickly in the low ratio case and is delayed in the high ratio case. Steady transitions are observed in both cases.

At all reagent concentrations, an initially slow development was followed by a period of rapid transition that was again followed by slow change. The duration of the initial slow reaction stage was found to vary with reagent concentration of lower concentrations of $TiCl_4$ which were found to react somewhat faster than high concentrations. The transitions themselves were also different for the different reagent concentrations and it was possible to gain an understanding of the changes occurring through data modelling of the solutions at different stages through the transition. Full details of the data modelling may be found in *Appendix 5*, § 7.5.

As reactions were conducted using both 100% and 70% deuteration of the ethanol solvent data modelling was conducted by calculating a global fit for both sets of data to increase confidence in the model. Scattering length densities used during modelling may be found in **Table 2-1**, § 2.1.1. In some cases scattering patterns for a solvent deuteration of 50% were also collected and included in the global modelling. In all cases the data was modelled with a polydisperse core-shell model in which the polydispersity of core radius and shell thickness followed a Schulz distribution as described in § 2.1.3. The majority of experiments were conducted with observations covering a Q range of 0.01 – 0.07 $Å^{-1}$ and

fitting was conducted within the same range. Such fitting provided good fits for all of the data considered, as shown in the example in *Figure 5-84*.

Not all of the data could be modelled in this manner as it required similar SANS patterns for both the 100% and 70% deuterated cases. As scan collection for each sample did not begin at precisely the same time sufficient similarity in the scattering pattern was only available at a limited number of times during the reaction. Particularly during the period of rapid transition a delay of 30 seconds in the start of the 2 minute scans makes direct comparison of scans difficult. In all cases the data was modelled by the Form Factor only as inclusion of a Scale Factor was not found to provide any significant improvement in the quality of the fits and was thus excluded to reduce the number of variables in the modelling. This is justifiable due to the dilute nature of the solutions and the difficulty of micelle formation in a high ethanol content solvent meaning that the volume fraction of micelles will be low and the structure factor will be negligible.

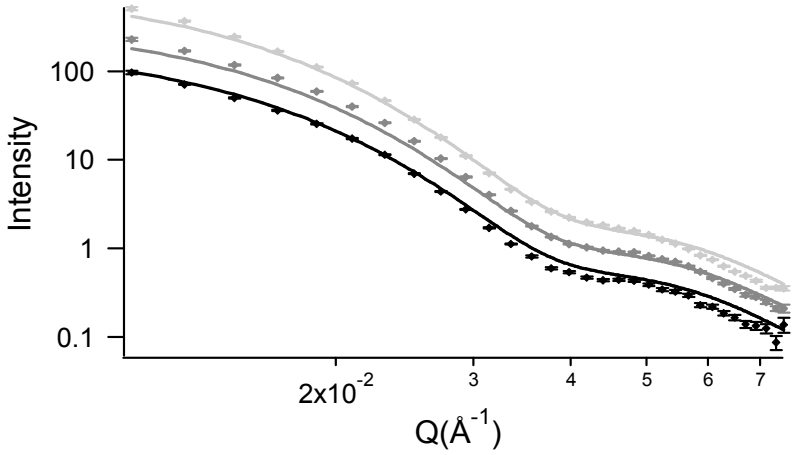

Figure 5-84 : Example of modeling for data from a 1.5 $PEPEG_{2250}$: 2$TiCl_4$ solution over a 0.01 – 0.07 $Å^{-1}$ range. SANS data is shown by markers and models by solid lines for both 100% (light grey), 70% (dark grey) and 50% (black) deuteration of the solvent.

For some reagent ratios data was also collected, and development observed, in a Q range of 0.05 – 0.33 $Å^{-1}$. To further test the validity of the modelling global fitting was conducted on the data from this angular range. In addition to separate modelling the data for the beginning and end of the reaction for both Q ranges were combined and global fitting conducted over the full range of 0.01 – 0.33 $Å^{-1}$. As shown in *Figure 5-85*, these

scattering profiles could also be well modelled by the polydisperse core-shell sphere model used for the other experiments.

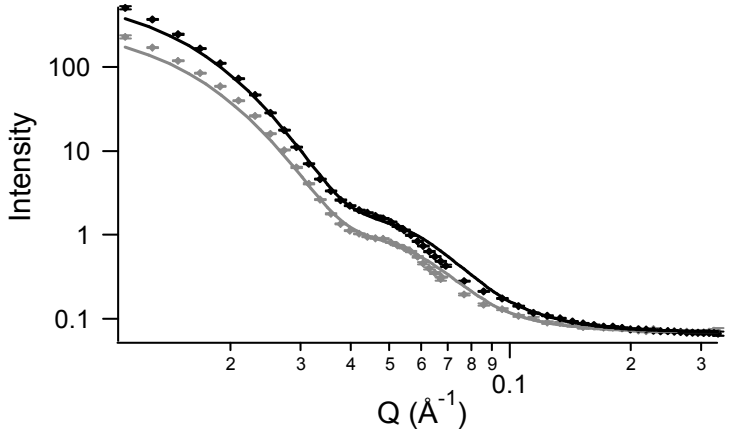

Figure 5-85 : Example of a polydisperse core-shell sphere model for combined data from a 1 $PEPEG_{2250}$: 1.25 $TiCl_4$ solution at the end of the reaction and over the total Q range of 0.01 – 0.33 $Å^{-1}$. Data is shown by markers and models by solid lines for both 100%, black, and 70%, grey, deuteration of the solvent. Errors are shown in both cases.

Attempts were also made to model the data with core-shell ellipsoid models however these did not provide fits that agreed with the data. This model could provide a rough fit for some experiments in the 0.01 – 0.07 $Å^{-1}$ range but the ellipsoid model could not provide an adequate fit to data in the 0.05 – 0.33 $Å^{-1}$ *Q* range and, as seen in *Figure 5-86*, fits were very poor for combined data in the full range of 0.01 – 0.33 $Å^{-1}$.

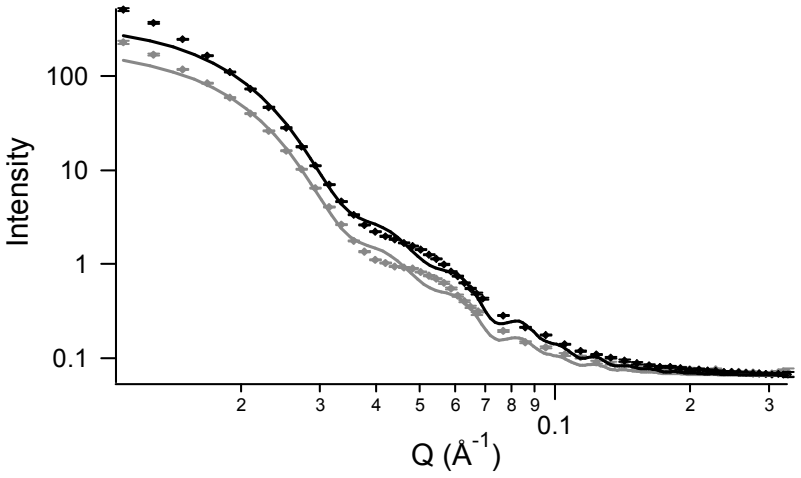

Figure 5-86 : Core-shell ellipsoid model for combined data over the 0.01 – 0.33 $Å^{-1}$ range. The model is a poor fit compared the core-shell sphere model. Data is shown by markers and models by solid lines for both 100%, black, and 70%, grey, deuteration of solvent. Errors are shown in both cases.

The modelling of different reagent concentration at different stages during the reactions allowed the comparison of the core radii, shell thicknesses and volume fractions shown in **Table 5-6**.

Table 5-6 : Comparison of model parameters corresponding to SANS patterns from different reagent concentrations and reaction times.

$PEPEG_{2250}$: $TICl_4$	Time (min)	VF ± 0.001	R_c (Å) ± 2	R_t (Å) ± 2	PD ± 0.003
0.019 : 1	3	0.015	42	38	0.33
	49	0.034	41	49	0.40
	53	0.058	41	58	0.44
	93	0.088	42	78	0.30
0.05 : 1	9	0.022	40	36	0.35
	33	0.068	40	52	0.49
	41	0.112	40	73	0.34
	81	0.141	40	78	0.31
0.089 : 1 0.01 – 0.07 $Å^{-1}$	2	0.035	41	41	0.28
	6	0.142	41	64	0.37
	68	0.175	41	76	0.29
0.089 : 1 0.01 – 0.33 $Å^{-1}$	3	0.031	40	36	0.38
	80	0.140	40	76	0.32

Core radius, R_c, was observed to be similar for all reagent concentrations and reaction times while shell thickness, R_t, and volume fraction, VF, both increased throughout the reaction. As observed in changes in the scattering profiles in *Figure 5-82* the reaction is found to be non-linear with respect to time and a period of rapid shell growth is observed, as shown below in *Figure 5-87*. Polydispersity was found to be similar for different reagent concentrations but was observed to increase during the period of rapid transition before falling back to the initial level, around 0.35, when the reaction slows again.

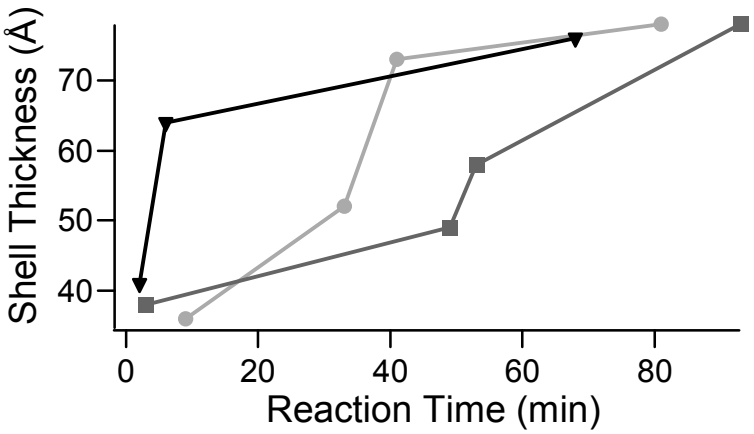

Figure 5-87 : The non-linear growth of shell thickness of particles in the solution subphase over time. 0.019 : 1 (squares) is found to react slowest while 0.089 : 1 (triangles) reacts very quickly and 0.05 : 1 (circles) is in between the two.

Furthermore, it was possible to calculate compositional changes occurring in the particles during the reaction by using changes in the scattering length density to calculate the distribution of surfactant, inorganic and solvent species. The total volume of each component of the shells may be calculated and the results of the calculations detailed below are shown in **Table 5-7** while full details of the fitted parameters may be found in *Appendix 5*, § 7.5.

As the core radius and shell thickness vary between experiments and at different reaction times the volumes also vary but may be calculated for each scattering pattern. In each case the core volume, V_{core}, and shell volume, V_{shell}, of an individual hybrid core-shell micelle are calculated from the formula for the volume of sphere as

$$V_{core} = \frac{4}{3}\pi R_c^{\,3} \text{ and } V_{shell} = \frac{4}{3}\pi\left(R_s^{\,3} - R_c^{\,3}\right) \qquad (5\text{-}1)$$

where R_c is the core radius and R_s is the combined radius of the core and shell. It is then possible to calculate both the number of micelles in solution and the number of surfactant molecules per micelle by considering the volume occupied by the surfactant in solution. Published analysis of the $PEPEG_{2250}$ surfactant gives a molecular weight of 2939 $gmol^{-1}$ and a poly(ethylene oxide) content of 81% that corresponds to molecular structure of a 54 PEO repeat unit headgroup and a tail of 20 polyethelene repeat units.[41] Given the

published volume of a PEO unit[41] of 38.8 cm^3mol^{-1} and published density of polyethylene,[42] 0.92 $gmol^{-1}$ it is straightforward to calculate the headgroup volume, V_{head}, and tail volume, V_{tail}, as 3479 $Å^3$ and 1008 $Å^3$ respectively. Assuming that the hybrid micelle core contains only surfactant tails the number of surfactant molecules per micelle, $N_{molecules}$, is then calculated as

$$N_{molecules} = \frac{V_{core}}{V_{tail}} \tag{5-2}$$

The further assumption that all surfactant molecules are in micelles and consideration of the polyethylene density allows the calculation of the number of micelles, $N_{micelles,}$ in solution as

$$N_{micelles} = \frac{m_{PEPEG} \times 0.19 \times 10^{24}}{0.92 \times V_{core}} \tag{5-3}$$

where m_{PEPEG} is the mass of surfactant in the sample solution. It is then possible to calculate the total volume of PEO chains in all shells, V_{PEO}, as

$$V_{PEO} = N_{micelles} \times N_{molecules} \times V_{head} \tag{5-4}$$

Additionally, assuming that the shell consists only of TiO_2, surfactant PEO tails and solvent the volume of all of the hybrid micelle shells may also be defined as

$$V_{all\_shells} = V_{TiO_2} + V_{PEO} + V_{EtOH} \tag{5-5}$$

where V_{TiO2}, V_{PEO} and V_{EtOH} are the volumes of TiO_2, PEO tails and ethanol solvent in all shells respectively. Recalling Equation (2-2), § 2.1.1 also allows the definition of scattering length density of the shell, ρ_{shell}, as

$$\rho_{shell} = \frac{n_{TiO_2}\rho_{TiO_2} + n_{PEO}\rho_{PEO} + n_{EtOH}\rho_{EtOH}}{n_{TiO_2} + n_{PEO} + n_{EtOH}} \quad (5\text{-}7)$$

where n_{TiO2}, n_{PEO}, and n_{EtOH} are the number of moles of TiO_2, PEO tails and ethanol solvent and ρ_{TiO2}, ρ_{PEO} and ρ_{EtOH} are the scattering length densities of TiO_2, PEO and ethanol respectively, as detailed in **Table 2-1**, § 2.1.1. This may be rearranged more usefully as

$$n_{PEO}(\rho_{shell} - \rho_{PEO}) = n_{TiO_2}(\rho_{TiO_2} - \rho_{shell}) + n_{EtOH}(\rho_{EtOH} - \rho_{shell}) \quad (5\text{-}8)$$

Consideration of the fact that the number of moles may be derived from the density, volume and molecular weight of a species allows us to redefine Equation (5-8) in terms of these quantities as

$$\frac{d_{PEO}(\rho_{shell} - \rho_{PEO})}{MW_{PEO}} = V_{TiO_2}\frac{d_{TiO_2}(\rho_{TiO_2} - \rho_{shell})}{MW_{TiO_2}} + V_{EtOH}\frac{d_{EtOH}(\rho_{EtOH} - \rho_{shell})}{MW_{EtOH}} \quad (5\text{-}9)$$

in which d_{TiO2}, d_{PEO} and d_{EtOH} are the densities of TiO2, PEO and ethanol respectively and MW_{TiO2}, MW_{PEO} and MW_{EtOH} are their respective molecular weights. The straightforward calculation of V_{EtOH} is then achieved using the equation

$$\frac{d_{PEO}(\rho_{shell} - \rho_{PEO})}{MW_{PEO}} = (V_{all\_shells} - V_{PEO} - V_{EtOH})\frac{d_{TiO_2}(\rho_{TiO_2} - \rho_{shell})}{MW_{TiO_2}} + V_{EtOH}\frac{d_{EtOH}(\rho_{EtOH} - \rho_{shell})}{MW_{EtOH}}$$

reached by combination of Equations (5-5) and (5-9) as all other values in the equation are available from the model or literature. Equation (5-5) may then be used alone to calculate the total volume of TiO_2 in all shells, V_{TiO2}. The results of these calculations of shell component volumes and the mole ratios of ethanol to TiO_2 in the shells are shown in **Table 5-7** below.

Table 5-7 : Comparison of total shell component volumes
for different reagent concentrations and reaction times.
Errors are based upon the effects of manual variation of the volume calculations.

$PEPEG_{2250}$:$TiCl_4$	Time	V_{PEO} (cm^3) ± 0.005	V_{EtOH} (cm^3) ± 0.005	V_{TiO2} (cm^3) ± 0.005	EtOH : TiO_2
0.019 : 1	3 min	0.036	0.008	0.017	0.15 : 1
	49 min	0.036	0.046	0.018	0.85 : 1
	53 min	0.036	0.082	0.018	1.5 : 1
	89 min	0.036	0.153	0.042	1.3 :1
0.05 : 1	33 min	0.053	0.103	0.017	2 : 1
	41 min	0.053	0.235	0.045	1.7 : 1
	54 min	0.053	0.283	0.059	1.6 : 1
0.089 : 1	2 min	0.071	0.038	0.034	0.36 : 1
	6 min	0.071	0.218	0.037	1.9 : 1
	70 min	0.071	0.302	0.078	1.3 : 1

5.4.2 Subphase Development

The time-resolved development of block-copolymer surfactant templated titania particles has been observed by small angle neutron scattering for the first time to our knowledge. Previous studies investigating the formation of surfactant templated silica particles using small angle scattering have been reported,[10,27] however, equivalent studies with titania are made more challenging due to the higher reactivity of the titanium precursors.[5,21,31] The use of an ethanol solvent and a high level of acidity are both recognised methods to reduce the uncontrolled condensation of transition metal precursors and both methods have been used to successfully control the reaction of the titania precursor $TiCl_4$ in this work.[21,23]

As shown in **Table 5-6**, formation of the templated polydisperse core-shell spheres in solution is observed to occur with a layer of titania condensing around spherical micelles of the $PEPEG_{2250}$ surfactant. This agrees with the expectation of spherical micelles at the concentration of less than 5% wt. surfactant used, see **Table 5-4**. It is noted that the radius of the core and, therefore, the surfactant micelle size remains unchanged throughout the reaction, while the titania rich shell of the particle grows in thickness throughout the reaction. Shell growth is noted in silica systems also although the maintenance of a constant micelle size is in contrast to some silica results utilising PEO-PPO-PEO block copolymer templates.[11] The use of silica alkoxides as inorganic

precursors is known to liberate alcohol as the alkoxides undergo hydrolysis that is able to penetrate into a PPO micelle core and swell particles,[5] however this is not expected to occur when a polyethylene – PEO surfactant such as $PEPEG_{2250}$ is used due to the non-polar micelle core.

Studies of developing silica particles templated by a non-ionic surfactant report that initially spherical particles become elongated as the formation reaction proceeds, becoming ellipsoidal and, eventually, cylindrical.[10] This development during in-situ SAXS studies was attributed to the aggregation of particles in solution leading to the development of larger, elongated micelles prior to the formation of an ordered phase. In this work, however, no particle aggregation is observed and no strong interparticle interactions are noted in the reaction solutions. As the structure factor was found to have little influence in the modelling, which would not be the case if interparticle interactions were significant, see § 2.1.2, it is concluded that no strong interactions are present. It is therefore probable that the spherical particles develop individually and unchanged in the subphase solution.

Similar results have also been reported for other silica systems that develop as oblate ellipsoid particles in the subphase solution.[27] These particles retained their shape, albeit with a size increase in the major axis, throughout the reaction as is observed for the spherical particles here. This work also noted a discrepancy between film development and solution development at high silica : surfactant ratios, above 10.8.[27] In this case it was observed that although such ratios form films if a large interface is available no development of order is reported in solution. It was concluded that these high silica content solutions require the air-solution interface to form ordered structures.

As a reagent ratios of above 10 Ti : 1 $PEPEG_{2250}$ are used in this work it is probable that a similar effect is responsible for the discrepancy between film and subphase formation in this work. The film formation is attributed to the formation of aggregates in solution that rise to the surface and condense into a solid film at the air-solution interface. However, in the film formation reactions a large surface area is available for this process to occur that was not available in the cuvettes used for subphase studies. As it has additionally been noted that no film formation occurs if the solution is in a sealed container it is suggested that the formation of a continuous mesophase

requires evaporation from the solution surface to occur. An evaporation driven process is further supported by the lack of aggregation in the subphase studies and it is reasonable to suggest that evaporation is required for particle aggregation and film formation.[42] It is possible that the film precursor solutions are too dilute for the aggregation of hybrid micelles to occur in solution and, as a result, film formation is forced to occur in a coacervate phase below the air-solution interface in which the local concentration is higher.

In the solution subphase the growth of the titania shell likely occurs through the migration of individual precursor species or small oligomers to the particle surface. It is noted that although the $TiCl_4$ precursor rapidly undergoes conversion to an ethoxide species in the ethanol solvent and that these species rapidly become hydrolysed in the acidic conditions, used subsequent condensation is greatly inhibited.[21,23,43] Condensation is further restricted by the presence of stable species such as $Ti_3(OCH_2CH_3)_{12}$ in solution that resist both hydrolysis and condensation.[44] It has been previously reported that titania precursors interact preferentially with the PEO blocks of copolymer surfactants, as observed in this case, however, the nature of these interactions varies with the amount of water present.[5,31,45]

In the reaction conditions used there is expected to be sufficient water present that the disruption of surfactant phases reported for very low hydrolysis ratios, due to chelation interactions, is not expected to occur. Rather, the higher water content of the solutions studied in this work correspond to the region for which interactions between titania precursor species and PEO groups is reported as due to hydrogen bonding interactions.[31] As acidic conditions are known to increase hydrogen bonding interactions and surface activity of PEO chains,[25] it is reasonable to expect them to be strong in the present work. In such cases the inorganic precursors are noted to gather around surfactant micelles that are not inhibited from forming in solution, as observed in this work. The hydrogen bonding and hydrophilic-hydrophilic interactions responsible for the core-shell particle formation are strong between the surfactant PEO groups and inorganic species, but do not lead to particle aggregation limiting development to growth of the titania shell. Additionally, as the number of micelles is expected to be relatively low at the

concentrations used, the micelle collisions that may be expected to give rise to aggregation are expected to be infrequent.

In addition to observing the increasing shell thickness it has been possible to examine the compositional changes within the shell through consideration of the scattering length density with results shown in **Table 5-7**. Initial volumes of surfactant, ethanol and titania in the shells appear to depend upon the reagent concentrations used with a 1 $PEPEG_{2250}$: 3 $TiCl_4$ ratio giving an initial ethanol to titania ratio less than half that calculated when a 1 $PEPEG_{2250}$: 1.33 $TiCl_4$ is used. This is consistent with the interaction between inorganic precursors and surfactant as a greater relative concentration of $TiCl_4$ would be expected to lead to a greater presence of titania precursors in the initial particle shell. Unfortunately the lack of data for the initial period of the 0.05 $PEPEG_{2250}$: 1 $TiCl_4$ case prevents comparison with this case.

As expected given the unchanging micelle core in the particles, the PEO volume in the shell remains constant while the volumes of ethanol and titania both increase over time. They do not increase at the same rate though and it is noted that the molar ratio of ethanol to titania progresses toward approximately 1.3 : 1 over time. The progressive increase in the inorganic content in the shell has been reported for the formation of core-shell silica particles. [27] In this case it was attributed to the condensation of an existing silica layer around surfactant micelles and progressive exclusion of solvent and was accompanied by a reduction in shell thickness. Unlike the silica case in the present work condensation of titania precursors in the shell is concurrent with additional titania precursors coming to shell surface, particularly during the period of rapid reaction, see *Figure 5-87*.

As additional inorganic precursors migrate to and become incorporated into the shell the content of both inorganic material and organic material increases if incompletely hydrolysed precursors bring organic ligands with them. Titania is recognised to form stable trimeric species in solution such as $Ti_3(OCH_2CH_3)_{12}$ that are expected to be present in these reactions.[22,44] The migration of such species to the shell would raise the ethanol to titania ratio. At later times the titania precursors condense due to their greater proximity in the particle shell and ethanol begins to be excluded from the shell with the ethanol to titania ratio dropping in a comparable situation to that for the silica system.[27]

Additionally, it is reported that a considerable amount of ethanol can become bound into copolymer templated titania materials formed in acidic conditions and it is likely that such processes are also occurring in the present work.[31]

Therefore these results indicate that the particle formation in the subphase solution of the $PEPEG_{2250}$ templated titania films occurs through the formation of a titania shell around spherical micelles of the surfactant due to hydrogen bonding and hydrophilic – hydrophilic interactions. As titania is incorporated into the shells the solvent content also increases due to binding of precursors that have retained ethoxide ligands however the shells progress toward purer titania as the precursors condense. This increased condensation is expected to increase the hydrophobicity of the core-shell particles as Ti-OH groups are lost from the exterior as condensation proceeds and may contribute towards a higher concentration of micelles forming at the interface.

Similar processes are expected to occur prior to film formation although no micelle aggregation is observed in the subphase due to the lack of evaporation during these experiments. It is possible that, as reported for silica films, lower titania ratio preparations may form ordered materials in solution and this is recommended as a direction for future research.

5.5 Results of Polymer Addition to Titania - $PEPEG_{2250}$ Films

5.5.1 Benchtop Observations

Although the $PEPEG_{2250}$ templated titania films could be removed from the interface observation of some film cracking, see *Figure 5-72*, during drying led to the inclusion of additional polymers in an attempt to reinforce the films. PEI, and two different lengths of PEO (10,000 and 600,000 MW) were tested as additions of 10% - 20% wt. vs. surfactant to improve film order and robustness. Film formation appeared unchanged in all cases, however once removed from the interface the polymers appeared to affect the films.

The addition of PEI had no observable impact upon films removed from the interface, and its use therefore discontinued, while the addition of PEO of either length affected the films as they dried after removal from the interface. Previous observations had shown the films to change from opaque white to transparent as they dried with some cracking observed after several hours. As shown in *Figure 5-88*, the addition of 10,000 MW PEO was found to make the films more robust, allowing them to dry fully to a clear material without cracking. The addition of 600,000 MW PEO, on the other hand, appeared to destabilise the films as they were found to pull away from the supporting mesh and to remain opaque rather than drying to a transparent material.

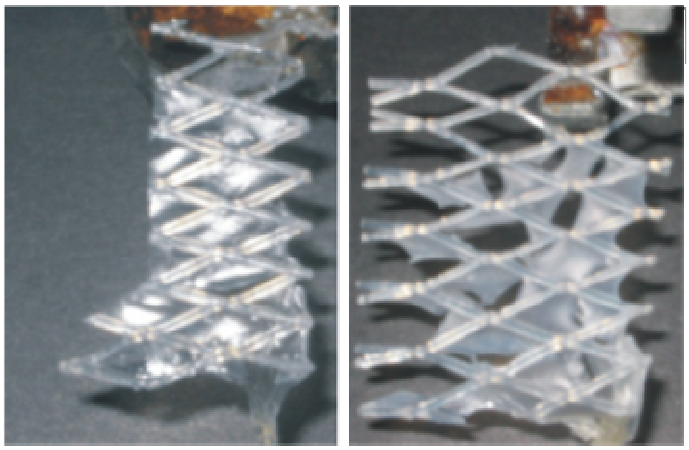

Figure 5-88 : Pictures of $PEPEG_{2250}$ - titania films removed from the air-solution interface and showing the effects of 10,000 MW PEO, (a), and 600,000 MW PEO, (b).

5.5.2 X-ray Reflectivity

As in the case of the normal $PEPEG_{2250}$ films time resolved off-specular X-ray reflectometry was used to observe film formation at the air-solution interface and angle dispersive X-ray reflectometry was used to observed the in-situ film structure of films after development. The time resolved reflectivity profile shown in *Figure 5-89* is typical of the observations of film development during with the addition of polymer and is observed to be similar to that observed when pure $PEPEG_{2250}$ is used. Film formation, identified by the loss of the specular reflection peak, is observed to occur within 30 seconds with the specular peak being lost completely from one scan to the next.

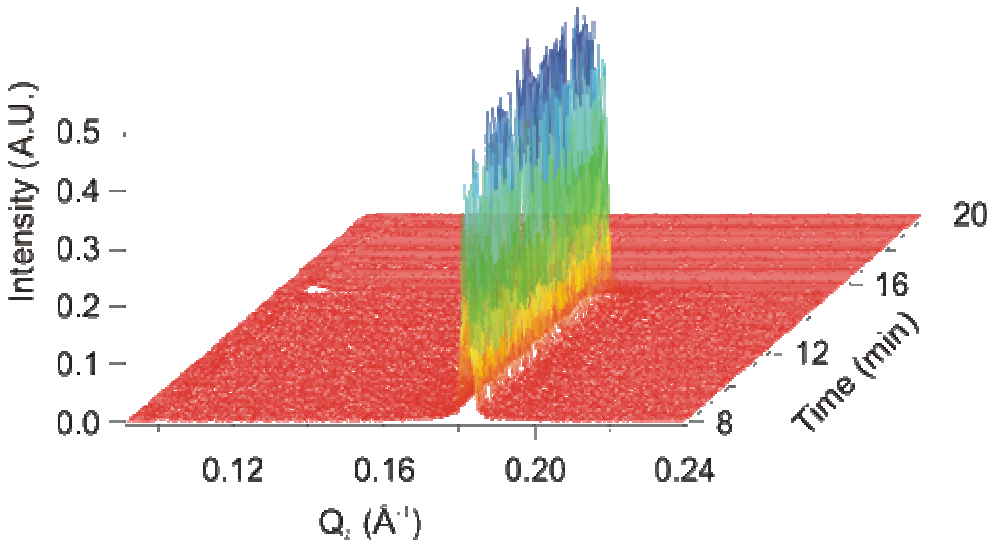

Figure 5-89 : Time resolved reflectometry showing the formation of a $PEPEG_{2250}$ templated titania film with the addition of 20% wt. 10,000 MW PEO.

Observations of the in-situ film structure by angle dispersive reflectometry are also similar whether additional PEO polymer is present in the system or not and it is noted that similar problems arise due to solvent evaporation lowering the solution surface below the edge of the sample trough. In all cases no structural peaks were observed in the reflectivity patterns and the films appear to have no structure at the air-solution interface as is the case for films templated without additional polymer. This lack of structure is observed in the typical reflectivity profile shown in *Figure 5-90*.

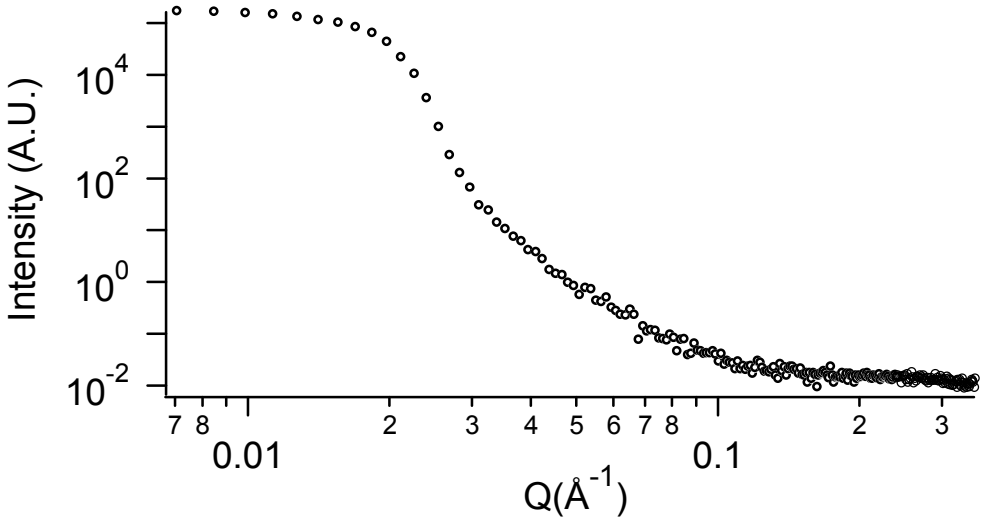

Figure 5-90 : Reflectivity profile from a titania film templated with 1g $PEPEG_{2250}$ and 0.1g 10,000 MW PEO. This profile is typical of those observed for all PEO additions.

5.5.3 Small Angle X-ray Scattering

In addition to X-ray reflectivity on in-situ films small angle X-ray scattering was used to observe the structure of titania film material after removal from the interface. In each case films were allowed to develop at the air-solution interface for two hours before collection on a mesh and drying in air. Dry film material was removed from the mesh and SAXS patterns collected and a summary of these patterns is shown in *Figure 5-91*.

It is observed that although polymer addition does not change film formation or in-situ structure the structure of the dried film material changes with polymer addition, in agreement with benchtop observations of films as they dry. However, in all cases no structural peaks are observed in the SAXS profiles suggesting that, as in the case when no additional PEO is present, the films do not possess a highly ordered structure.

Although a diffraction peak may be present at 0.065 $Å^{-1}$ in the case of the addition of 20% wt. 600,000 MW PEO it is not possible to note any other peaks, expected for a highly ordered phase, when the errors are considered, see *Figure 5-91*. Peaks observed at high Q (1.37, 1.53 and 1.66 $Å^{-1}$) are assigned a crystalline surfactant phase as in the case when no additionally polyethylene oxide is present in the film material, see the end of § 5.1.2.

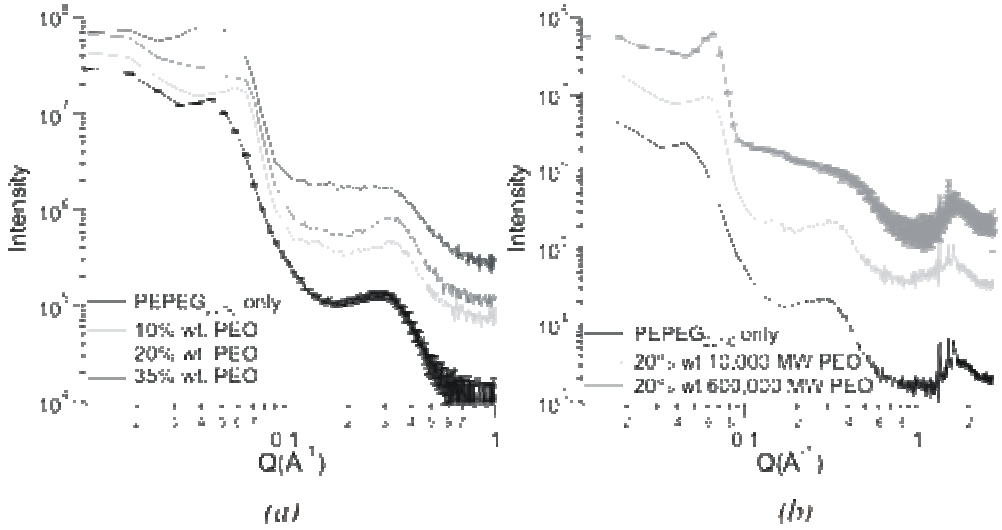

Figure 5-91 : SAXS patterns showing the effect of PEO polymer addition to $PEPEG_{2250}$ templated titania films. (a) shows the effect of different lengths of polymer while (b) shows the effect of different weight percentages of added 10,000 MW PEO. Error bars are shown on one pattern in both (a) and (b) and are comparable in all other cases.

Guinier analysis and consideration of Porod slopes was not possible as no Guinier or Porod region was visible in the scattering patterns. In addition to such analysis the SAXS profiles were modelled in the same manner as that used to model data when no additional polymer was present in the system. Modelling was tried using spherical, ellipsoidal and cylindrical particle models and using core-shell and homogenous models. As in the case without polymer the best model for the system was found to be ellipsoidal polyethylene particles in a titania matrix as shown in ***Figure 5-92***.

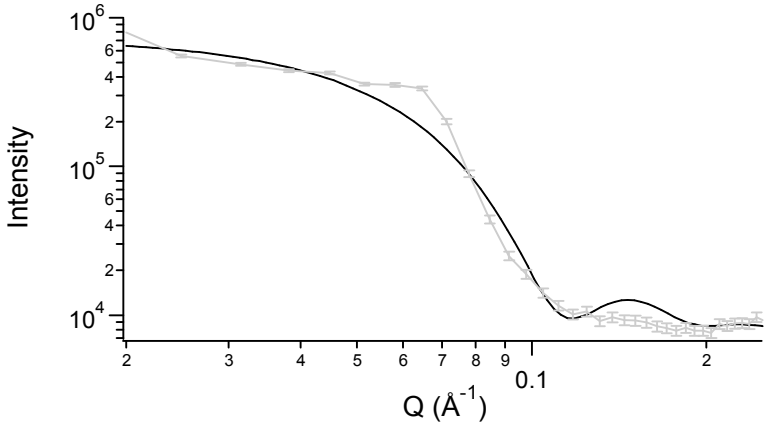

Figure 5-92 : SAXS model for a $PEPEG_{2250}$-titania film with 20% wt. PEO 10,000 MW

As summarised in **Table 5-8**, the results of the modelling of the SAXS data shows the impact of the addition of PEO to the film precursor solution. Whereas film material using a purely $PEPEG_{2250}$ template has an oblate ellipsoidal structure films containing additional 10,000 MW PEO are found to be near spherical in shape and were found to become more spherical when more 10,000 MW PEO was present in the system.

Table 5-8 : Summary of SAXS modeling for films using additional PEO

PEO MW ($gmol^{-1}$)	PEO % wt.	Shape	R_a (Å) ± 2	R_b (Å) ± 2
N/A	0%	Ellipsoidal	33	54
10,000	5%	Ellipsoidal	32	55
	10%	Ellipsoidal	35	47
	20%	Ellipsoidal	33	42
	35%	Ellipsoidal	39	40
600,000	10%	Ellipsoidal	32	40

5.6 Discussion of Polymer Addition to Titania – $PEPEG_{2250}$ Films

Examination of $PEPEG_{2250}$ templated titania films using 10-20% wt. additions of 10,000 and 600,000 MW PEO suggests that although polymer addition influences the dried film material it does not alter the mechanism of film formation. Bench-top observations of film during formation so not show any differences when additional PEO is present and time resolved X-ray reflectometry experiments show a comparable, rapid development of the films at the air-solution interface.

Such a rapid formation is what is expected in a bulk driven mechanism in which particles develop in solution prior to combining to rapidly form a film at the interface suggesting that this mechanism is in operation with or without additional PEO.[36] No precipitation was observed, however, suggesting that the bulk driven mechanism nonetheless requires the presence of the interface for aggregation and film formation. Additional PEO may act to bridge between the titania-rich shells of coated micelles and assist formation of aggregates and development into a full film.

However, no BAM experiments have been conducted to observe surface development and no small angle scattering experiments have been conducted to observe development in the subphase. Both of these techniques may be expected to provide useful additional information on the formation mechanism and are recommended as areas for future investigation.

Although no differences in film formation are observed, benchtop observation and small angle X-ray scattering from dried film material recovered from the interface shows the effect of additional PEO polymer on the films. Films with additional 10,000 MW PEO are observed to be more robust upon drying that films templated by $PEPEG_{2250}$ alone while the addition of 600,000 MW PEO is found to produce films that crack severely upon drying. It is possible that additional polymer produces a more robust film by long chains holding the film together, however if this were the case it is expected that 600,000 MW would produce a more robust material that is not observed. Therefore it appears that the stabilising influence of 10,000 MW PEO and indifferent influence of 600,000 MW PEO are due to structural differences in the film materials.

SAXS modelling shows 33 x 54 Å oblate ellipsoidal particles, corresponding to the micelle core of polyethylene groups of the surfactant, when only $PEPEG_{2250}$ is used as a film template. As the weight percentage of 10,000 MW PEO is increased the particle size is observed to become progressively more spherical, see **Table 5-8**, from 32 x 55 Å particles at 5% wt to 39 x 40 Å at 35% wt. However, the addition of the longer 600,000 MW PEO is found to produce particles of dimensions 32 x 40 Å that are both smaller and more spherical. As purely spherical particles may be expected to pack more precisely into an ordered material it is possible that closer packing of the micelles leads to improved film stability. However, no increase in film ordering is observed in reflectometry or small angle scattering experiments and this does not explain the increase in robustness for 10,000 MW but not 600,000 MW.

Alternatively, the increased robustness of the films may be due to thicker inorganic walls that are reported to provide increased durability in other materials.[3,5] In the acidic reaction conditions used the reported interaction between titania precursors and PEO groups may be expected is occur between both PEO groups of the surfactant and PEO groups of the added polymer.[31] Although the added polymer and $PEPEG_{2250}$ micelles are expected to remain separate initially, due to the entropy considerations,[8,30] once a sufficient titania coating is present to allow micelle aggregation coated PEO polymers are expected to become included in the aggregating film material.

The inclusion of titania coated polymers during aggregation is expected to increase film durability by producing thicker inorganic walls and by providing a long, continuous section binding the film together. Increased durability is not observed in the case of the longer, 600,000 MW as it may be expected that the inclusion of the much larger species is limited by diffusion considerations, or coils around the titania-rich micelle shell too much, particularly given the very rapid film formation. However, it is not possible to confirm that this proposed process is occurring with the present experimental data. TEM study of film material may show changes in the film structure due to the inclusion of polymer and time-resolved study of formation in the subphase may also confirm the proposed mechanism and both studies are recommend for further study.

5.7 Conclusions and Further Work

Titania films have been made at the air-solution interface by templating with the block copolymer surfactant $PEPEG_{2250}$. The films have been found to form via a bulk driven mechanism in which titania precursors initially bind to surfactant micelles allowing an associative phase separation followed by micelle aggregation and film development that is evaporation dependant. The films are observed to be disordered due to fast formation and condensation prematurely halting micelle ordering and due to the high polydispersity in micelle size. Films do not appear well ordered before or after removal of the surfactant phase and TEM study is recommended to more clearly observe film structure, or lack thereof.

The addition of PEO polymer to the film precursor solution is found to produce no increase in ordering within the film but is found to promote the formation of more spherical micelles, possibly by restricting the space available for larger micelles. Long chain, 600,000 MW, PEO is found to have no positive influence on the film stability while shorter 10,000 MW PEO significantly increases the robustness of the titania films upon drying. This is suggested to be due to the diffusion limted incorporation of titania precursor coated PEO polymers into the film providing structural support over longer distances in the film. As longer chain polymers are unable to freely diffuse, or unwind from a globular conformation, for incorporation into the film their influence is limited compared to the shorter polymer. However, the further evidence is needed to support this mechanism and TEM study and examination of solution phase development are recommended for further study.

Study of solution phase development, without additional PEO, has allowed the development of block copolymer templated titania particles in solution to be observed for the first time. The particles are observed to consist of a growing titania shell in and around the palisade region of the $PEPEG_{2250}$ micelles and a critical point appears to exist at which development is very rapid, however no phase separation or aggregation is observed. The suggestion of an evaporation induced phase separation during film formation is strengthened by the observation of a lack of particle aggregation or organisation in solution.

5.8 References

(1) *IUPAC Compendium of Chemical Terminology, Electronic version,http://goldbook.iupac.org/B00683.html*, 1996.

(2) Guo, Q.; Thomann, R.; Gronski, W. *Polymer* **2007**, *48*, 3925-3929.

(3) Soler-Illia, G. d. A.; Crepaldi, E. L.; Grosso, D.; Sanchez, C. *Current Opinion in Colloid & Interface Science* **2003**, *8*, 109-126.

(4) Bagshaw, S. A.; Prouzet, E.; Pinnavaia, T. J. *Science* **1995**, *269*, 1242-1244.

(5) Edler, K. *Australian Journal of Chemistry* **2005**, *58*, 627-643.

(6) Huo, Q.; Margolese, D. I.; Ciesla, U.; Demuth, D.; Feng, P.; Gier, T. E.; Sieger, P.; Firouzi, A. *Chemistry of Materials* **1994**, *6*, 1176-1191.

(7) Egger, C. C.; Anderson, M. W.; Tiddy, G. J. T.; Casci, J. L. *Physical Chemistry Chemical Physics* **2005**, *7*, 1845-1855.

(8) Epping, J. D.; Chmelka, B. F. *Current Opinion in Colloid & Interface Science* **2006**, *11*, 81-117.

(9) Linton, P.; Alfredsson, V. *Chemistry of Materials* **2008**, *20*, 2878-2880.

(10) Flödstrom, K.; Teixeira, C. V.; Amenitsch, H.; Alfredsson, V.; Linden, M. *Langmuir* **2004**, *20*, 4885-4891.

(11) Flödstrom, K.; Wennerstrom, H.; Teixeira, C. V.; Alfredsson, V.; Linden, M.; Amenitsch, H. *Langmuir* **2004**, *20*, 10311-10316.

(12) Soni, S.; Brotons, G.; Bellour, M.; Narayanan, T.; Gibaud, A. *Journal of Physical Chemistry B* **2006**, *110*, 15157-15165.

(13) Blin, J.; Leonard, A.; Su, B. L. *Chemistry of Materials* **2001**, *13*, 3542-3553.

(14) Palmqvist, A. *Current Opinion in Colloid & Interface Science* **2003**, *8*, 145-155.

(15) Soler-Illia, G. d. A.; Scolan, E.; Louis, A.; Albouy, P.; Sanchez, C. *New Journal of Chemistry* **2001**, *25*, 156-165.

(16) Coleman, N.; Attard, G. S. *Microporous and Mesoporous Materials* **2001**, *44-45*, 73-80.

(17) Yu, C.; Yu, Y.; Zhao, D. *Chemical Communications* **2000**, 575-576.

(18) Thomas, A.; Schlaad, H.; Smarsly, B.; Antonietti, M. *Langmuir* **2003**, *19*, 4455-4459.

(19) Fattaakhova-Rohlfing, D.; Wark, M.; Brezesinski, T.; Smarsly, B.; Rathousky, J. *Advanced Functional Materials* **2007**, *17*, 123-132.

(20) Brezesinski, T.; Fischer, A.; Iimura, K.; Sanchez, C.; Grosso, D.; Antonietti, M.; Smarsly, B. *Advanced Functional Materials* **2006**, *16*, 1433-1440.

(21) Brinker, C. J.; Scherer, G. W. *Sol-Gel Science*; 1 ed.; Academic Press: London, 1990; Vol. 1.

(22) Bradley, D. C.; Mehotra, R. C.; Guar, D. P. *Metal Alkoxides*; Academic Press: London, 1978; Vol. 1.

(23) Soler-Illia, G. d. A.; Sanchez, C.; Lebeau, B.; Patarin, J. *Chemical Reviews* **2002**, *102*, 4093-4138.

(24) Antonietti, M.; Niederberger, M.; Smarsly, B. *Dalton Transactions* **2008**, 18-24.

(25) Yang, B.; Guo, C.; Chen, S.; Ma, J.; Wang, J.; Liang, X.; Zheng, L.; Liu, H. *Journal of Physical Chemistry B* **2006**, *110*, 23068-23074.

(26) Angerer, P.; Yu, L. G.; Khor, K. A.; Krumpel, G. *Materials Science and Engineering A* **2004**, *381*, 16-19.

(27) Fernandez-Martin, C.; Roser, S. J.; Edler, K. *Journal of Materials Chemistry* **2008**, *18*, 1222-1231.

(28) Henderson, M. J.; King, D.; White, J. W. *Langmuir* **2004**, *20*, 2305-2308.

(29) Brennan, T.; Hughes, A. V.; Roser, S. J.; Mann, S.; Edler, K. *Langmuir* **2002**, *18*, 9838-9844.

(30) Flödstrom, K.; Wennerstrom, H.; Alfredsson, V. *Langmuir* **2004**, *20*, 680-688.

(31) Soler-Illia, G. d. A.; Sanchez, C. *New Journal of Chemistry* **2000**, *24*, 493-499.

(32) Barringer, E. A.; Bowen, H. K. *Langmuir* **1985**, *1*, 420-428.

(33) Edler, K.; Brennan, T.; Roser, S. J. *Thin Solid Films* **2006**, *495*, 2-10.

(34) Buxton, G. A.; Clarke, N. *EPL* **2007**, *78*, 56006.

(35) Jones, R. A. L.; Norton, L. J.; Kramer, E. J.; Bates, F. S.; Wiltzius, P. *Physical Review Letters* **1991**, *66*, 1326-1329.

(36) Edler, K.; Brennan, T.; Roser, S. J.; Mann, S.; Richardson, R. M. *Microporous and Mesoporous Materials* **2003**, *62*, 165-175.

(37) Gregg, S. J.; Sing, K. S. W. *Adsorption, Surface Area and Porosity*; 2nd ed.; Academic Press: London, 1982.

(38) Brunauer, S.; Deming, L. S.; Deming, W. E.; Teller, E. *Journal of the American Chemistry Society* **1940**, *62*, 1723-1732.

(39) Brunauer, S.; Emmett, P. H.; Teller, E. *Journal of the American Chemistry Society* **1938**, *60*, 309-319.

(40) Sanchez, C.; Boissiere, C.; Grosso, D.; Laberty, C.; Nicole, L. *Chemistry of Materials* **2008**, *20*, 682-737.

(41) Rajzer, B. *Certificate of Analysis: Polyethylene - block - poly(ethylene glycol)*; Sigma-Aldrch [online], 2005.

(42) Manekar, N. C.; Puranik, P. K.; Joshi, S. B. *Journal of Microencapsulation* **1992**, *9*, 63-66.

(43) Grosso, D.; Cagnol, F.; Soler-Illia, G. d. A.; Crepaldi, E. L.; Amenitsch, H.; Brunet-Bruneau, A.; Bourgeois, A.; Sanchez, C. *Advanced Functional Materials* **2004**, *14*, 309-322.

(44) Sanchez, C.; Livage, J. *New Journal of Chemistry* **1990**, *14*, 513-521.

(45) Yang, P.; Zhao, D.; Margolese, D. I.; Chmelka, B. F.; Stucky, G. D. *Chemistry of Materials* **1999**, *11*, 2813 - 2826.

6. Conclusion & Future Directions

Surfactant templated, mesostructured titania films have been made using three different methods with a range of surfactants. Film formation has been studied using Brewster angle microscopy, reflectometry while film structure has been studied by reflectometry, small angle scattering, electron microscopy and nitrogen adsorption. Additionally, in the case of $PEPEG_{2250}$ templated titania solution phase development has been studied by small angle neutron scattering. Data modelling of small angle scattering and reflectivity profiles was undertaken to provide further detail on the film structure during and after formation.

6.1 Dip-Coated Films

Repetitive dip-coating was used in the formation of mesoporous titania films for development as dye sensitized solar cells and it was found to be possible to generate porous film of cubic *Pm3n* structure using the Pluronic surfactants P-123 or F-127. In each case four depositions were used and the P-123 templated films were successfully developed into DSSCs by the Peter research group at the University of Bath with an IPCE of 60%, comparable to that achieved in current literature but with a relatively poor photocurrent density of 1.17 $mAcm^{-2}$. The films produced are relatively thin compared to those reported in the literature but the results of the present work demonstrate the potential of the dip-coated method.

However, the F-127 templated films were not successful as solar cells and it was found that in this case repeated dip-coating did not lead to a linear increase in layer thickness as expected. Surface profilometry revealed that each subsequent deposition was thinner than the proceeding one and electron diffraction found a loss of order in film material after a second deposition. It is proposed that these effects were due to the penetration of film precursor solution into the film pores during subsequent deposition.

These results pose additional problems for the development of the repetitive dip coating technique as additional care must be taken to ensure that subsequent depositions do not compromise existing film layers.

6.2 Fluorosurfactant Templated Films

In contrast to dip-coated films, mesostructured titania films were developed at the air solution interface using a high alcohol content solvent and using two different surfactants. Such conditions allow greater control of the reactions of titania precursors, however, the self assembly of such films from high alcohol solvents remains difficult due to limited surface activity of many surfactants in such solvents. Surfactant templating has been enabled in the present work by the use of the novel partially fluorinated surfactant Zonyl FSO-100 and di-block copolymer surfactant $PEPEG_{2250}$.

In the case of FSO-100 templated films, the film development was observed to occur via a surface driven templating mechanism with individual inorganic oligomers and surfactant molecules found to add to the growing film front. Film growth occurred by the progressive addition of layers of titania precursors and surfactant molecules beneath an existing surfactant monolayer at the air-solution interface. Spherical micelles are expected to exist in solution prior to film formation as the surfactant is unable to form the bilayer structure, favoured by fluorinated surfactants, due to the unfavoured overlap of PEO chains that would result. Attraction between PEO groups of the surfactant and titania precursors led to the formation of a barrier beneath the monolayer that allowed the development of a second surfactant layer that prevented the entropically unfavoured overlap of PEO chains.

This mechanism produced a lamellar structure at the air-solution interface, however, after removal from the interface and drying the film material was observed in electron microscopy and SAXS to have a disordered *Ia3d* space group corresponding to a bicontinuous cubic phase. It is proposed that after removal from the interface a structural phase transition from lamellar to bicontinuous cubic, due to distortion of the existing lamellar layers, occurs in the film material as the recovered film material dries and the titania continues to crystallise.

The bicontinuous cubic phase is found to be preserved during calcination and produces mesoporous titania film material upon removal of the FSO-100 surfactant with a surface area of 85 m^2g^{-1} and pores of approximately 8 nm diameter. Such pores are suitable for the diffusion of organic compounds, such as the dye molecules used in dye sensitized solar cells. The mesoporous structure of the material and pore dimensions suggest the possible utility of the material in catalysis or photochemical applications. Testing of film material in photovoltaic applications and for the photochemical decomposition of organic compounds would be interesting experiments to further study the potential of these materials for specific applications.

In addition to titania films the FSO-100 surfactant was used to template the formation of zinc oxide films at the air-solution interface for which film formation was found to occur by a comparable surface driven mechanism to that of the titania films. Film formation using zinc chloride was found to be more sensitive to the acid concentration than in titania film formation with film formation slowed at high acid concentrations.

After removal from the interface and drying the zinc films, SAXS showed the dried material to be *Im3m* cubic in agreement with, but more highly ordered than, the bicontinuous structure developed in FSO-100 – titania films. Although a different structure appears when zinc precursors are used, recently published results showing that contraction of an *Ia3d* space group can allow previously forbidden reflections, mean that the assignment of an *Im3m* phase is uncertain. In either case it is expected that distortion of existing lamellar layers is responsible for the formation of a bicontinuous cubic phase after removal from the air-solution interface.

However, additional study of the zinc oxide material is required and transmission electron microscopy and electron diffraction are recommended for imaging the film material and examining its structure respectively. Nitrogen adsorption is also suggested for study of film porosity and similar tests for photochemical activity may also be undertaken for detailed examination of the applicability of the film material. Zinc oxide materials are also of interest in photochemical applications and the development of zinc oxide films at the air-solution interface is highly novel and suggests future potential for use of the FSO-100 surfactant as a template.

6.3 Block-copolymer Templated Films

Also using a high alcohol content solvent, but in contrast to the surface driven mechanism observed for FSO-100 templated films, use of the di-block copolymer $PEPEG_{2250}$ was observed to produce films at the air-solution interface by a bulk driven formation mechanism. In both FSO-100 and $PEPEG_{2250}$ templated films, the film formation was found to be faster at higher acid concentrations, due to increased inorganic – PEO interaction. Film formation was also faster at higher surfactant concentrations in both cases, due to the increased availability of the surfactant for formation. However, formation time increased at higher titania precursor concentrations for FSO-100 films while it followed a U-shaped dependence for $PEPEG_{2250}$ templated films.

When $PEPEG_{2250}$ was used as a film template, the film formation was initially faster as the titania precursor concentration increased, as the precursors were able to more rapidly coat the surfactant micelles. At higher concentrations, however, it is suggested that the addition of a large number of charged titania species to the micelle creates an electrostatic repulsion between the hybrid micelles leading to slower film formation although it is unclear if it is significant in solution prior to film formation.

Small angle neutron scattering studies of development in the solution subphase allowed the time-resolved observation of the development of titania-surfactant particles in solution for the first time. It was found that the titania precursors form a shell around spherical $PEPEG_{2250}$ micelles extant in solution and that this become thicker and enriched with titania over time. Higher titania precursor concentrations were found to develop a more titania rich shell around the surfactant micelles, however, no electrostatic repulsion was observed in the dilute solutions used for SANS. Given the novelty of these observations, further study of solution phase development under different reaction conditions and over a larger concentration range is recommended as an area of further research, to examine formation mechanisms in titania – surfactant materials. In particular further experiments at higher titania precursor concentrations are suggested as a method to test the development of electrostatic repulsion at high precursor concentrations or whether such effects are only apparent during film formation. Similarly, higher surfactant

concentrations may give rise to stronger interparticle interactions that can be observed in SANS studies.

A lack of evaporation, or the lack of a sufficiently large air-solution interface, during study of the subphase prevented phase separation in the cuvettes used for solution phase experiments. However, during film formation the development of core-shell surfactant-titania particles occurred in solution is followed by the formation of a concentrated micelle phase by liquid-liquid phase separation in which interparticle interactions are expected to be larger. Film development was observed to occur very rapidly after the formation of this concentrated phase, although the film appeared disordered in-situ at the air-solution interface.

Upon removal from the interface the film material was found to be thick and robust and the material was self supporting when removed on a $1cm^2$ mesh. The robustness of the films was found to be increased by the addition of 10,000 MW PEO and it is suggested that the integration of the polymer within the film provides binding over a longer distance. The addition of longer, 600,000 MW, PEO did not improve film robustness and in this case it is suggested that the long polymer is limited by diffusion considerations from integrating into the film given the very rapid film formation.

After removal from the interface and drying the film was found to be formed of ellipsoidal particles, in agreement with the $PEPEG_{2250}$ / ethanol phase diagram at high concentration. Addition of PEO polymer was found to produce more spherical micelles in the film, possibly due to the space occupied by the titania coated polymer restricting micelle development.

However, with or without the addition of PEO polymer, the $PEPEG_{2250}$ – titania film was not stable to calcination and nitrogen adsorption found the material to be a non-porous powder after calcination suggesting a low degree of titania condensation or a lack of robust titania walls in the film. It is also possible that the large amount of PEO expected to be present in the walls of the $PEPEG_{2250}$ – titania films leads to the destruction of the films as the organic content is removed upon calcination. Transmission electron microscopy has not been undertaken on these film materials and is recommended for further study of the film material before and after calcination as this may confirm the presence, or lack of, an ordered structure in both cases.

6.4 Concluding Discussion and Further Work

In both FSO-100 and $PEPEG_{2250}$ templating film formation increased at higher acid concentrations due to the increased interactions between titania precursors and PEO groups of the surfactant that results. Similarly, high surfactant concentrations sped up film formation in both cases due to the greater availability of the surfactant in solution. However, the mechanism of film formation differed between the surfactants and while higher titania concentrations increased formation times for FSO-100 surfactant, due to a lower water : titania ratio, variation of titania concentration produced a U-shaped dependence when $PEPEG_{2250}$ was used.

Although acidic, high alcohol solvent conditions are used for both surfactants the $PEPEG_{2250}$ surfactant, with a much longer PEO section, is used at a lower concentration and much higher titania : surfactant ratio than the FSO-100 surfactant. The development of a lamellar film in the surface driven mechanism of the FSO-100 surfactant allows the formation of a bilayer structure favoured by fluorinated surfactants while the $PEPEG_{2250}$ surfactant is expected to be less surface active and more stable as micelles in solution. It is also expected that the lower $PEPEG_{2250}$ surfactant concentration reduces the availability of the $PEPEG_{2250}$ surfactant for film formation until development in solution leads to a liquid-liquid phase separation that allows film formation by a bulk-driven, rather than a surface driven, mechanism.

Additionally, a larger amount of titania is expected to be present in hybrid-micelles and films when $PEPEG_{2250}$ is used due to the higher titania : surfactant ratio and longer PEO sections in the $PEPEG_{2250}$ surfactant. Electrostatic repulsion between hybrid micelles, due to charged titania oligomers, is therefore expected to be greater when the block-copolymer surfactant is used and it is suggested that this overcharging gives rise to the U-shaped dependence of formation time with titania precursor concentration. In summary, higher titania concentrations in $PEPEG_{2250}$ containing solutions lead to an excess of charged titania in the hybrid micelles. However, in FSO-100 solutions such a high a titania content at which the binding of titania oligomers leads to electrostatic repulsion is not reached.

6.5 Overall Summary

In conclusion the repetitive dip-coating technique was tried for the production of films for solar cell applications, however, although promising results were obtained the thickness of the films was insufficient for solar cell applications. Alternative methods using a partially fluorinated surfactant and block-copolymer in surfactant templated self-assembly at the air-solution interface, from a high alcohol solvent system, produced novel surfactant-titania films with interesting structures and morphologies. It was found to be possible to produce not only porous titania materials but also zinc oxide materials and these methods show good potential for producing materials suitable to photochemical applications.

7. Appendices

7.1 Appendix 1

FSO-100 – Titania film X-ray reflectivity fitting details

Data was modelled using the Motofit program as detailed in § 2.2.5 and was modelled as a mutilayer lamellar phase as detailed in *Figure 7-93*. A monolayer of the fluorinated section of the surfactant was modelled above the multilayer and a monolayer of the PEO section of the surfactant was modelled below the multilayer to reflect the termination of the lamellar phase. The number of repeat units of the monolayer was varied manually. The details of each fit are shown in **Table 7-9, 7-2** and **7-3** with each table corresponding to the variation of a single reagent in the film precursor solution and the concentration of all other reagents is as per a standard preparation, see § 2.3.3. In all cases the SLD above the sample was fixed at zero and the SLD of the base, corresponding to the precursor solution, was held at 9.6 x 10^{-6} $Å^{-2}$. The modelling of other parameters was constrained to be within a physically realistic range.

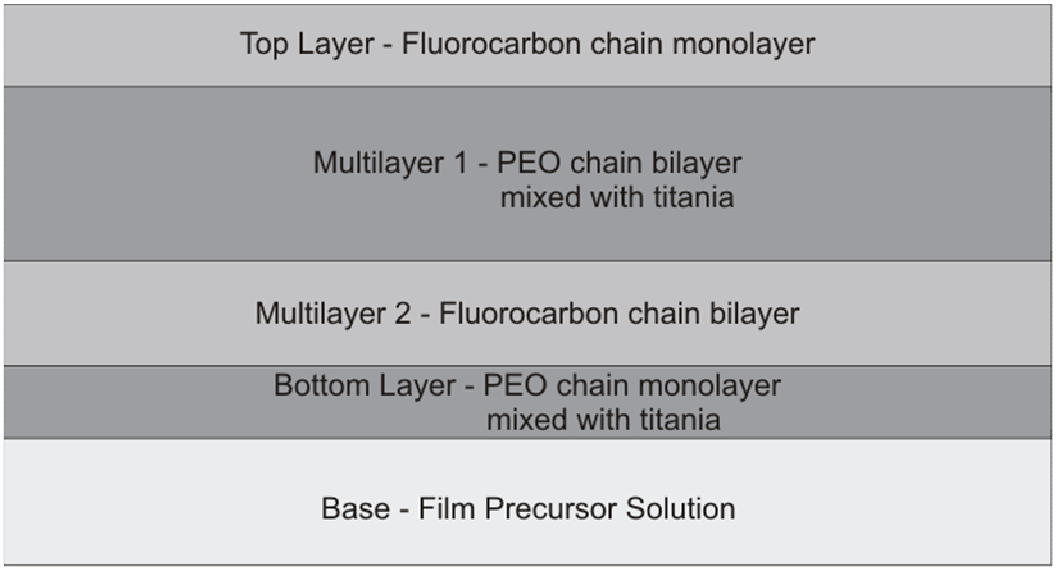

Figure 7-93 : Diagram of how X-ray reflectivity models were modeled. The number of repeats of the multilayer was adjusted manually while variables within each layer, e.g. layer thickness, were fitted by computer.

Table 7-9 : Details of the modeling of reflectivity profiles for FSO-100 variaton. Layers Top, Multi 1, Multi 2 and Bottom refer to the layers of the model as in *Figure 7-93*.

FSO-100 content	Multilayer Repeats	Layer	Thickness (Å) ± 2 Å	SLD (x10^{-6} Å^{-2}) ± 1 Å^{-2}	Roughness (Å) ± 1 Å
3.3 mMol	6	Top	10	11.1 (fixed)	5
		Multi 1	36	16	5
		Multi 2	21	11.1 (fixed)	6
		Bottom	25	18	9
2.2 mMol	2	Top	10	11.1 (fixed)	5
		Multi 1	32	16	8
		Multi 2	19	11.1 (fixed)	5
		Bottom	20	16	5
1.7 mMol	1	Top	10	11.1 (fixed)	6
		Multi 1	32	18	5
		Multi 2	19	11.1 (fixed)	7
		Bottom	17	19	5

Table 7-10 : Details of the modeling of reflectivity profiles for HCl variation.

HCl content	Multilayer Repeats	Layer	Thickness (Å) ± 2 Å	SLD (x10^{-6} Å^{-2}) ± 1 Å^{-2}	Roughness (Å) ± 1 Å
21 mMol	2	Top	10	11.1 (fixed)	7
		Multi 1	32	19	5
		Multi 2	19	11.1 (fixed)	7
		Bottom	16	17	6
15 mMol	2	Top	10	11.1 (fixed)	5
		Multi 1	32	16	8
		Multi 2	19	11.1 (fixed)	5
		Bottom	20	16	5
No Acid	0	Top	10	11.1 (fixed)	6
		Multi 1	-	-	-
		Multi 2	-	-	-
		Bottom	25	10	6

Table 7-11 : Details of the modeling of reflectivity profiles for $Ti(OBu^n)_4$ variation.

$Ti(OBu^n)_4$ content	Multilayer Repeats	Layer	Thickness (Å) ± 2 Å	SLD (x10^{-6} Å^{-2}) ± 1 Å^{-2}	Roughness (Å) ± 1 Å
2.1 mMol	2	Top	10	11.1 (fixed)	5
		Multi 1	32	16	8
		Multi 2	19	11.1 (fixed)	5
		Bottom	20	16	5
0.9 mMol	2	Top	10	11.1 (fixed)	8
		Multi 1	32	18	5
		Multi 2	19	11.1 (fixed)	5
		Bottom	16	19	5

7.2 Appendix 2

FSO-100 – Titania film neutron reflectivity fitting details

Data was modelled using the Motofit program in a comparable manner to that for X-ray reflectivity and data was modelled as a mutilayer lamellar phase as detailed in *Figure 7-93*. A monolayer of the fluorinated section of the surfactant was modelled above the multilayer and a monolayer of the PEO section of the surfactant was modelled below the multilayer to reflect the termination of the lamellar phase. The number of repeat units of the monolayer was varied manually. Data modelling was only undertaken for a standard preparation as a full data series was available in this case and the loss of resolution due to evaporation limits the use of additional data fitting. The details of each fit, each corresponding to a different time in the reaction, are shown in **Table 7-12**. In all cases the SLD above the sample was fixed at zero while the SLD of the subphase was held held at 3.1 $Å^{-2}$ for as this sample was made using 65% d_6-ethanol and the modelling of the other parameters was constrained to be within a physically realistic range.

Table 7-12 : Details of the modeling of neutron reflectivity from a developing sample of FSO-100 – titania film from a standard reaction solution.

Time after pouring	Multilayer Repeats	Layer	Thickness (Å) ± 2 Å	SLD ($x10^{-6}$ $Å^{-2}$) ± 0.5 $Å^{-2}$	Roughness (Å) ± 1 Å
10 min	1	Top	9	2.9 (fixed)	6
		Multi 1	36	0.8	7
		Multi 2	21	2.9 (fixed)	7
		Bottom	30	0.7	6
25 min	2	Top	10	2.9 (fixed)	6
		Multi 1	37	0.8	6
		Multi 2	22	2.9 (fixed)	6
		Bottom	25	2.7	6
40 min	2	Top	10	2.9 (fixed)	6
		Multi 1	35	0.9	7
		Multi 2	21	2.9 (fixed)	6
		Bottom	30	2.6	6
70 min	2	Top	10	2.9 (fixed)	7
		Multi 1	38	0.8	8
		Multi 2	19	2.9 (fixed)	8
		Bottom	40	2.7	7

7.3 Appendix 3

FSO-100 – ZnO film X-ray reflectivity fitting details

Data was modelled using the Motofit program as detailed in § 2.2.5 and was modelled as a mutilayer lamellar phase as detailed in *Figure 7-93*, where ZnO is present rather than titania. A monolayer of the fluorinated section of the surfactant was modelled above the multilayer and a monolayer of the PEO section of the surfactant was modelled below the multilayer to reflect the termination of the lamellar phase. The number of repeat units of the monolayer was varied manually. The details of each fit are shown in **Table 7-13, 7-6** and **7-7** with each table corresponding to the variation of a single reagent in the film precursor solution and the concentration of all other reagents is as per a standard preparation, see § 2.3.4. In all cases the SLD above the sample was fixed at zero and the SLD of the base, corresponding to the precursor solution, was fixed at 9.6 x 10^{-6} $Å^{-2}$. The modelling of the other modelled parameters was constrained to be within a physically realistic range.

Table 7-13 : Details of the modeling of reflectivity profiles for FSO-100 variaton. Layers Top, Multi 1, Multi 2 and Bottom refer to the layers of the model as in *Figure 7-93*.

FSO-100 content	Multilayer Repeats	Layer	Thickness (Å) ± 2 Å	SLD (x10^{-6} $Å^{-2}$) ± 1 $Å^{-2}$	Roughness (Å) ± 1 Å
3.3 mMol	6	Top	9	11.1 (fixed)	7
		Multi 1	34	16.7	6
		Multi 2	19	11.1 (fixed)	6
		Bottom	17	13.9	8
2.2 mMol	3	Top	10	11.1 (fixed)	7
		Multi 1	30	15.6	5
		Multi 2	18	11.1 (fixed)	7
		Bottom	25	11.6	6
1.7 mMol	1	Top	10	11.1 (fixed)	7
		Multi 1	26	19.8	4
		Multi 2	20	11.1 (fixed)	7
		Bottom	24	9.3	5

Table 7-14 : Details of the modeling of reflectivity profiles for $ZnCl_2$ variation.

$ZnCl_2$ content	**Multilayer Repeats**	**Layer**	**Thickness (Å) ± 2 Å**	**SLD ($x10^{-6}$ $Å^{-2}$) ± 1 $Å^{-2}$**	**Roughness (Å) ± 1 Å**
6.2 mMol	2	Top	10	11.1 (fixed)	4
		Multi 1	28	16.5	8
		Multi 2	20	11.1 (fixed)	5
		Bottom	19	16.9	5
2.1 mMol	3	Top	10	11.1 (fixed)	7
		Multi 1	30	15.6	5
		Multi 2	18	11.1 (fixed)	7
		Bottom	25	11.6	6
1.0 mMol	2	Top	10	11.1 (fixed)	4
		Multi 1	28	15.7	8
		Multi 2	20	11.1 (fixed)	4
		Bottom	21	14.6	5

Table 7-15 : Details of the modeling of reflectivity profiles for a HCl content of 15 mMol. Fitting was not possible for other HCl additions due to the truncated nature of the reflectivity patterns in these cases.

HCl content	**Multilayer Repeats**	**Layer**	**Thickness (Å) ± 2 Å**	**SLD ($x10^{-6}$ $Å^{-2}$) ± 1 $Å^{-2}$**	**Roughness (Å) ± 1 Å**
15 mMol	3	Top	10	11.1 (fixed)	7
		Multi 1	30	15.6	5
		Multi 2	18	11.1 (fixed)	7
		Bottom	25	11.6	6

7.4 Appendix 4

FSO-100 – ZnO film neutron reflectivity fitting details

Data was modelled using the Motofit program in a comparable manner to that for X-ray reflectivity and data was modelled as a mutilayer lamellar phase as detailed in *Figure 7-93*, although ZnO is present, and was modelled, rather than titania. A monolayer of the fluorinated section of the surfactant was modelled above the multilayer and a monolayer of the PEO section of the surfactant was modelled below the multilayer to reflect the termination of the lamellar phase. The number of repeat units of the monolayer was varied manually. Data modelling was only undertaken for a standard preparation as a full data series was available in this case and the details of each fit, each corresponding to a different time in the reaction, are shown in **Table 7-16**. In all cases the SLD above the sample and of the subphase was fixed at zero as the solution was contrast matched to air.

Table 7-16 : Details of the modeling of neutron reflectivity data from a developing FSO-100 – ZnO film at the air-solution interface.

Time after pouring	Multilayer Repeats	Layer	Thickness (Å) ± 2 Å	SLD ($x10^{-6}$ $Å^{-2}$) ± 0.5 $Å^{-2}$	Roughness (Å) ± 1 Å
11 min	1	Top	10	2.9 (fixed)	5
		Multi 1	30	4.2	5
		Multi 2	18	2.9 (fixed)	7
		Bottom	28	2.8	6
26 min	2	Top	10	2.9 (fixed)	8
		Multi 1	35	3.9	5
		Multi 2	21	2.9 (fixed)	5
		Bottom	34	2.7	7
41 min	3	Top	10	2.9 (fixed)	4
		Multi 1	30	3.9	5
		Multi 2	20	2.9 (fixed)	8
		Bottom	32	1.6	9
56 min	3	Top	10	2.9 (fixed)	4
		Multi 1	29	3.7	5
		Multi 2	20	2.9 (fixed)	8
		Bottom	35	1.5	8
71 min	3	Top	9	2.9 (fixed)	6
		Multi 1	30	3.6	7
		Multi 2	19	2.9 (fixed)	7
		Bottom	36	1.5	8

7.5 Appendix 5

Details of SANS modelling for subphase development in $PEPEG_{2250}$ – Titania film precursor solutions

Data was modelled using fitting routines from the NCNR, NIST and a polydisperse core-shell sphere model was found to be the best although ellipsoid and cylindrical models were also tested. As shown in *Figure 7-94*, the model consisted of a polyethylene core surrounded by a shell made of a mixture of polyethylene oxide and titania. Global fitting was used to simultaneously fit data of different solvent contrasts to increase confidence in the fitted results. The full details of the results for precursor solutions of different surfactant to titania ratio and different times during the reaction are shown in **Table 7-17** in which VF is the volume fraction, PD is the polydispersity, R_C is the core radius and R_T is the shell thickness. In all cases the SLD of the core was fixed at -0.33×10^{-6} Å^{-2} and the solvent SLD was fixed as appropriate for the level of deuteration. For other parameters a limited number of the modelled variables were allowed to vary at any time.

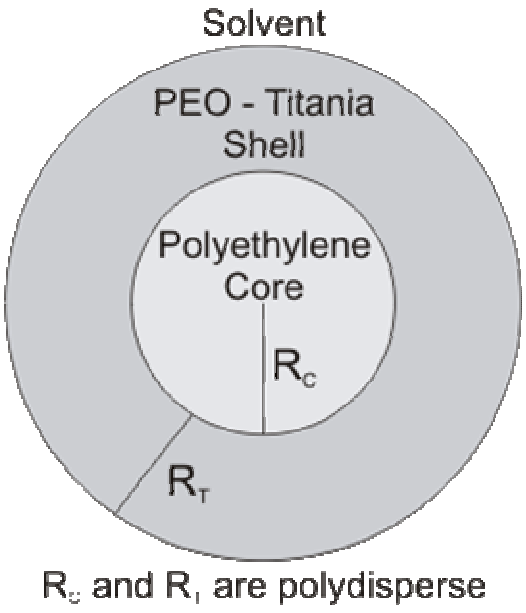

Figure 7-94 : Diagram of the model used to for development of $PEPEG_{2250}$ – titania particles in the solution subphase. R_C and R_T are the core radius and shell thickness respectively and both have polydispersity following a Schulz distribution.

Table 7-17 : Details of the modeling of SANS patterns corresponding to subphase development in $PEPEG_{2250}$ – Titania film precursor solutions. Data covers a range of 0.01 – 0.07 $Å^{-1}$, data marked by * corresponds covers a range of 0.01 – 0.33 $Å^{-1}$.

$PEPEG_{2250}$: Titiania (Reaction Time)	Solvent D_6 (%)	VF ±0.001	R_C (Å) ±2Å	R_T (Å) ±2Å	PD ±0.003	SLD_{Core} ($x10^{-6}Å^{-2}$) ± 0.02	SLD_{Shell} ($x10^{-6}Å^{-2}$) ± 0.02	$SLD_{Solvent}$ ($x10^{-6}Å^{-2}$) ± 0.02
0.019 : 1 3 min	100	0.015	42	38	0.33	-0.33	1.84	5.39
	70	0.015	42	38	0.33	-0.33	1.76	3.99
0.019 : 1 49 min	100	0.034	41	49	0.40	-0.33	2.67	5.39
	70	0.034	41	49	0.40	-0.33	2.24	3.99
0.019 : 1 53 min	100	0.058	41	58	0.44	-0.33	3.17	5.39
	70	0.058	41	58	0.44	-0.33	2.59	3.99
0.019 : 1 93 min	100	0.088	42	78	0.30	-0.33	3.49	5.39
	70	0.088	42	78	0.30	-0.33	2.88	3.99
0.05 : 1 9 min	100	0.022	40	36	0.35	-0.33	2.02	5.39
	70	0.022	40	36	0.35	-0.33	1.66	3.99
	50	0.022	40	36	0.35	-0.33	1.62	3.05
0.05 : 1 33 min	100	0.068	40	52	0.49	-0.33	3.07	5.39
	70	0.068	40	52	0.49	-0.33	2.48	3.99
	50	0.068	40	52	0.49	-0.33	2.03	3.05
0.05 : 1 41 min	100	0.112	40	73	0.34	-0.33	3.62	5.39
	70	0.112	40	73	0.34	-0.33	2.92	3.99
	50	0.112	40	73	0.34	-0.33	2.22	3.05
0.05 : 1 81 min	100	0.141	40	78	0.31	-0.33	3.65	5.39
	70	0.141	40	78	0.31	-0.33	2.99	3.99
	50	0.141	40	78	0.31	-0.33	2.24	3.05
0.089 : 1 2 min	100	0.035	41	41	0.28	-0.33	2.14	5.39
	70	0.035	41	41	0.28	-0.33	1.95	3.99
0.089 : 1 6 min	100	0.142	41	64	0.37	-0.33	3.43	5.39
	70	0.142	41	64	0.37	-0.33	2.76	3.99
0.089 : 1 68 min	100	0.175	41	76	0.29	-0.33	3.50	5.39
	70	0.175	41	76	0.29	-0.33	2.88	3.99
0.089 : 1* 3 min	100	0.031	40	36	0.38	-0.33	2.71	5.39
	70	0.031	40	36	0.38	-0.33	2.22	3.99
0.089 : 1* 80 min	100	0.140	40	76	0.32	-0.33	3.42	5.39
	70	0.140	40	76	0.32	-0.33	2.94	3.99